# Dielectric Materials for High Power Energy Storage

**Chuying Yu**

**Submitted in partial fulfilment of the requirements of the Degree of Doctor of Philosophy**


**School of Engineering and Materials Science,**

**Queen Mary, University of London**

**London, United Kingdom**

**October 2016**

# Declaration

I declare that this thesis has been composed solely by myself during the course of my PhD studies in Queen Mary, University of London. It has not been submitted, in whole or in part, in any previous application for a degree or professional qualification.

The data presented in this thesis was obtained in experiments carried out by myself or with collaboration with other research institutes. I played a major role in the preparation and execution of the experiments. The data analysis and interpretation are entirely my own work. Any contributions from colleagues and other research institutes in the experiment processing, data analysis and results discussion are acknowledged below.

I am aware of and understand the university's policy on plagiarism and I certify that this thesis is my own work, except where indicated by referencing.



Chuying Yu

01/10/2016

# Abstract

Energy storage is currently gaining considerable attention due to the current energy crisis and severe air pollution. The development of new and clean forms of energy and related storing devices is in high demanded. Dielectric capacitors, exhibiting high power density, long life and cycling life, are potential candidates for portable devices, transport vehicles and stationary energy resources applications. However, the energy density of dielectric capacitors is relatively low compared to that of traditional batteries, which inhibits their future development. In the current work, three types of dielectrics, namely antiferroelectric samarium-doped $BiFeO_3$ ($Bi_{1-x}Sm_xFeO_3$), linear dielectric (potential antiferroelectric) $BiNbO_4$ and incipient ferroelectric $TiO_2$, have been investigated to develop their potential as energy storage capacitors.

For the samarium-doped $BiFeO_3$ ($Bi_{1-x}Sm_xFeO_3$) system, the effect of samarium content in the A-site (x=0.15, 0.16, 0.165 and 0.18) on the structural phase transitions and electrical properties across the Morphotropic Phase Boundary (MPB) were studied. A complex coexistence of rhombohedral *R3c*, orthorhombic *Pbam* and orthorhombic *Pnma* was found in the selected compositions. The *R3c* phase is the structure of pure $BiFeO_3$, the *Pbam* phase has a $PbZrO_3$-like antiferroelectric structure and the *Pnma* phase has a $SmFeO_3$-like paraelectric structure. The presence of the $PbZrO_3$-like antiferroelectric structure was confirmed by the observation of the $\frac{1}{4}\{110\}, \frac{1}{4}\{001\}$, $\frac{1}{2}\{011\}$ and $\frac{1}{2}\{111\}$ superlattice reflections in the transmission electron microscopy diffraction patterns. The weight fractions of the three phases varied with different

calcination conditions and Sm substitution level. By increasing the calcination temperature, the weight fractions of the *Pbam* increased, while that of the *R*3*c* decreased. The fraction of the *Pnma* phase is mainly derived by the Sm concentration and is barely affected by the calcination temperature. The increase of Sm concentration, determined an increase of the weight fraction of the *Pnma* phase and a decrease of the *Pbam* and the *R3c* phases. Temperature dependent dielectric measurements and high temperature XRD of $Bi_{0.85}Sm_{0.15}FeO_3$ revealed several phase transitions. The drastic weight fraction change between the *Pbam* and the *Pnma* phase around 200 °C is assumed as the Curie transition of the antiferroelectric *Pbam* phase. The transition at 575 °C is related to the diminishing of the *R3c* phase and is suggested as the Curie transition of the ferroelectric *R3c* phase. The Curie point of the antiferroelectric *Pbam* phase and the ferroelectric *R3c* phase in the $Bi_{1-x}Sm_xFeO_3$ ceramics shifted towards lower temperature with an increase of the Sm concentration. Current peaks were obtained in current-electric field loops in $Bi_{0.85}Sm_{0.15}FeO_3$, which are correlated to domain switching in the *R3c* phase. The ferroelectric behavior was suppressed in $Bi_{1-x}Sm_xFeO_3$ (x=0.16, 0.165, 0.18), which is due to the gradually diminished contribution from the *R*3*c* phase. The system $Bi_{0.82}Sm_{0.18}FeO_3$ showed the highest energy density of 0.64 J $cm^{-3}$ (error bar ±0.02).

For the $BiNbO_4$ system, single phase α-$BiNbO_4$ (space group *Pnna*) and β-$BiNbO_4$ (space group *P*-1) powder and ceramics were produced. The longstanding issue related to the sequence of the temperature-induced phase transitions has been clarified. It is demonstrated that the β phase powder could be converted back to the α phase when annealed in the temperature range 800 °C -1000 °C with certain incubation time. The β

to $\alpha$ phase transition is a slow kinetic process because sufficient temperature and time are required for the transition. In bulk ceramics with β phase, this transformation is impeded by inner stress, while it is favored by graphite-induced reducing atmosphere.

A high temperature $\gamma$ phase has been revealed and the structure has been resolved. The structure of the $\gamma$ phase is monoclinic with a space group of $P2_1/c$. The lattice parameters are: $a$ = 7.7951(1) Å, $b$ = 5.64993(9) Å, $c$ = 7.9048(1) Å, $\beta$ = 104.691(2)° Z=4. The volume is 336.76 (2) $Å^3$. The calculated density is 7.217 g $cm^{-3}$. The phase relationships among $\alpha$, $\beta$ and $\gamma$ phases have been clarified. It was found that the $\alpha$ phase (for both powder and ceramic) transforms into the $\gamma$ phase at 1040 °C on heating, and that the $\gamma$ phase always transforms into the $\beta$ phase at 1000 °C on cooling. Meanwhile, a reversible first-order $\beta$ to $\gamma$ phase transition is observed at *ca.* 1000 °C for both powder and ceramic if no incubation is processed on heating. The electric properties of both α- and β- $BiNbO_4$ have been investigated. The breakdown field of both ceramics were too low to observe any possible field-induced transition. As a result, linear P-E loops were obtained in each phase. The energy densities of α- and β- $BiNbO_4$ ceramics are 0.03 and 0.04 J $cm^{-3}$ (error bar ±0.001), respectively.

For the $TiO_2$ system, ceramics were produced by conventional sintering and spark plasma sintering (SPS). Compared to conventional sintering, SPS technique produced dense ceramics without using sintering aids and avoided abnormal grain growth. Relaxation behavior related to the oxygen hopping among vacant sites is observed in the temperature range of 200 to 600 °C. $TiO_2$ exhibits ultra-low loss at terahertz frequencies due to the reduced contribution of oxygen vacancies relaxation. $TiO_2$ has a

high breakdown field, but still has low polarization. The highest energy density obtained in$TiO_2$ ceramics is 0.3 J $cm^{-3}$ (error bar ±0.01).

# Acknowledgements

First of all, I would like to sincerely thank my supervisor Dr. Haixue Yan for his continuous support of my PhD study, for his patience, motivation, and immense knowledge. He guided me not only in my research but also in my life. He taught me to think what great people would think and do what successful people would do. I couldn't achieve what I have now without his help.

Besides my supervisor, I would like to thank the rest of my thesis committee: Prof. Mike Reece, Dr. Isaac Abrahams, Dr. Giuseppe Voila, for their insightful comments and encouragement, but also for harsh questions which incented me to view my research in a deeper and wide perspective.

My sincere thanks also goes to Dr. Rory Wilson for the help in XRD characterization, Dr. Nadja Tarakina for the help in TEM, Dr. Russell Bailey for the help with SEM, Dr. Baogui Shi and Dr. Haitao Ye for their expertise in XPS. Dr. Amit Mahajan for the guidance with Raman, Dr. Salvatore Grasso for the guidance in SPS technique.

I am also grateful for all my colleagues for their kind help. They are: Dr. Baoli Du, Dr. Peter Tatarko, Dr. Harshit Porwal, Dr. Xiaojing Zhu, Dr. Chen Chen, Dr. Ruth Mckinnon, Theo Saunders, Zheng Li, Kan Chen, Nan Meng, Jiyue Wu.

I would like to acknowledge China Scholarship Council. I couldn't come to London to pursue my PhD degree without their financial support.

In the end, I would like to thank my family, friends and my boyfriend Yang Zeng for their support and endless love.

# Table of Contents

# List of Figures

# List of Tables

# Chapter Ⅰ. Dielectrics for Energy Storage

## 1.1 Dielectric behavior of materials

Dielectric materials are a class of electric insulators that can be polarized under external electric field. Polarization ($P_i$), defined as the finite displacement of the bound charges or orientation of the dipoles per unit volume in response to the applied electric field $E_i$ (equation 1.1.1), is introduced to describe the induced or switched level of charges, also called polarized level [1].

$$P_i = \chi_{ij} E_j \tag{1.1.1}$$

Where $\chi_{ij}$ is the electric susceptibility of the dielectric.

Permittivity (ε) is to describe how the electrostatic field or flux is produced per unit charge in dielectrics and is related to electric susceptibility which measures how easily a dielectric can be polarized in response of an electric field [2]. The total surface charge density that is induced by external field can be expressed by the electric displacement [1]:

$$D_i = \varepsilon_0 E_i + P_i \tag{1.1.2}$$

Where $D_i$ is the electric displacement, $\varepsilon_0$ is the permittivity of free space.

It follows from equations (1.1.1) and (1.1.2) that

$$D_i = \varepsilon_0 E_i + \chi_{ij} E_j = \varepsilon_0 \delta_{ij} E_j + \chi_{ij} E_j = (\varepsilon_0 \delta_{ij} + \chi_{ij}) E_j = \varepsilon_{ij} E_j \tag{1.1.3}$$

Where $\delta_{ij}$ is Kronecker's symbol ($\delta_{ij} = 1 \text{ for } i = j, \delta_{ij} = 0 \; for \; i \neq j$) and $\varepsilon_{ij}$ is the dielectric permittivity of the material [2]. Thus the permittivity can be expressed as $\varepsilon = D/E$.

For an ideal dielectric, the application of a sinusoidal voltage will result in a charging current. However, as an alternating voltage is applied on the dielectric, the direction of the current will change every half cycle, which results in a change of polarization direction. The alternation of the polarization direction under AC field leads to a production of heat through dielectric loss. Thus the total current $I_{tot}$ can be divided into two parts: one is charging current $I_{chg}$, the other is loss current $I_{loss}$. The relationship is shown in Fig. 1.1.1 [1].

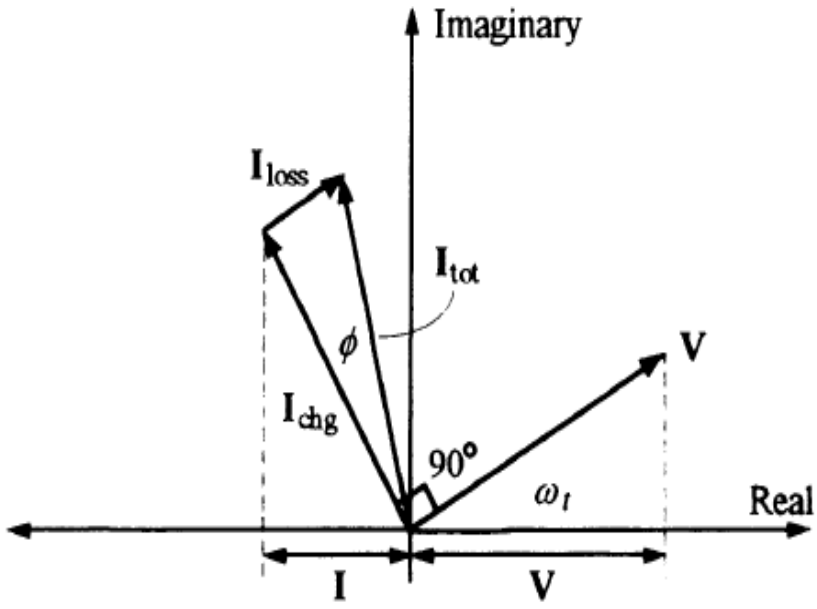


Fig. 1.1.1 The relationship of $I_{tot}$, $I_{chg}$ and $I_{loss}$ to the applied voltage $V$ [1].

As can be seen, there is an angle ϕ between $I_{chg}$ and $I_{loss}$, which is the loss angle. Loss tangent (equation 1.1.4) is used to describe the dissipated energy transformed from

electromagnetic energy of dielectric per unit time per volume. The physical meaning is the phase difference of the electric displacement and the electric field.

$$\tan\phi=\frac{I_{loss}}{I_{chg}}=\frac{\varepsilon''}{\varepsilon'} \quad (1.1.4)$$

where ε' is the real part and ε'' is the imaginary part of the complexed permittivity. More energy is dissipated as a form of heat in ceramics with higher dielectric loss. It is of great importance to minimize the dielectric loss of the materials for energy storage applications.

To further understand the dielectric properties of the materials, polarization mechanisms are studied. Polarization mechanisms can be classified into four types, namely space charge polarization, dipolar polarization, ionic polarization and electronic polarization [1]. Space charge polarization is produced by charge carriers which can migrate in short distance through the dielectric. The carriers could easily be trapped by surfaces, grain boundaries or interphase boundaries and are called space charges [1]. The positive charges will tend to take positions relative to negative charges along the direction of the electric field. The dipolar polarization involves the displacements of ions between several equilibrium sites and the occupancy probability of each site depends on the strength of the external electric field. For ferroelectric materials, it results in spontaneous displacement and nonlinear polarization. Dipole polarization is the dominant contribution to the permittivity in ferroelectric due to the relative large displacement [1]. Ionic polarization is the displacement between positive and negative ions towards the negative and positive electrodes. For electronic polarization, the electronic cloud is displaced to the nucleus it is surrounding under an

applied electric field [1]. Both ionic polarization and electronic belong to displacement polarization which is an elastic and energy save polarization and can be done in a moment. The contribution of different polarization mechanisms to the permittivity and loss values as a function of frequency is given in Fig. 1.1.2 [1].

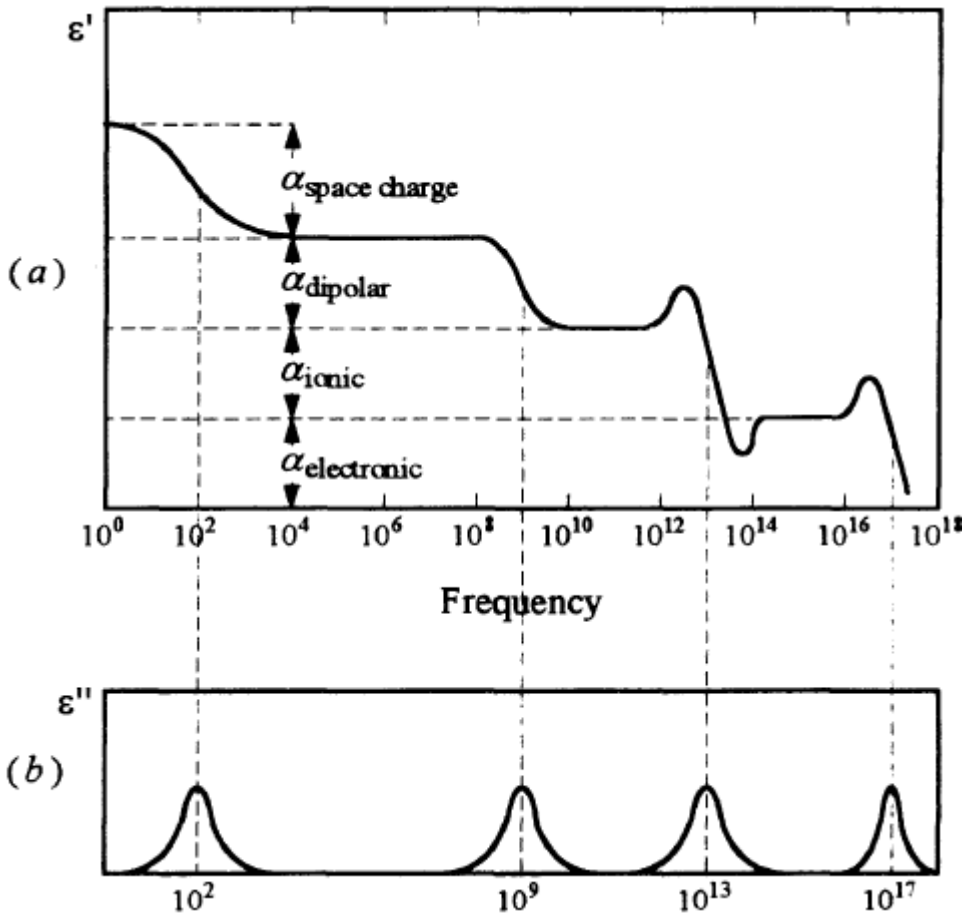


Fig. 1.1.2 The frequency dependence of permittivity and dielectric loss spectrum different polarization mechanism [1].

## 1.2 Jahn-Teller Effect

Jahn-Teller effect, also known as Jahn-Teller distortion, describes the geometrical distortion of nonlinear molecules and ions with spatially degenerate electron ground state [3]. It also emphasizes that the stability and the degeneracy could not simultaneously exist unless in a linear molecule. Hermann Arthur Jahn and Edward Teller state that the energy of the system could be lowered by geometrical distortion [3]. The Jahn-Teller effect is widely observed in octahedral complexes such as six-coordinate copper (II) complexes in which the $d^9$ electronic configuration of Cu gives three electrons in two degenerate $e_g$ orbitals [4]. The double degenerate ground state of Cu leads to the complexes distortion along *z* axis. The Jahn-Teller distortion indicates the spontaneous symmetry breaking of the system.

Group theory is adopted to prove this theorem as the electronic states can be classified by symmetry [4]. The ionic distortions which lift the degeneracy could also be classified by symmetry using irreducible representations. The pertinent potential energy surfaces (PES) and energy levels of the nuclear motion (also termed vibronic energy level) could be obtained from identifying the degree of degeneracy and symmetry [3]. Meanwhile, adiabatic approximation is applied in the equation of the electronic motions to provide an effective potential energy, which is termed adabatic potential energy sheet (APES) [3]. The Jahn-Teller effect of small molecules could directly be obtained by calculating the electronic structure of the APES. The development of the Jahn-Teller effect has been largely promoted by the application of the density functional theory to calculate larger systems such as solids [3].

## 1.3 Background of energy storage

Electric energy storage (EES) refers to a process that the energy can be transformed from the electric network into a medium, which serves as a secondary supplier for further releasing the energy [5]. It has enormous applications in practical fields like portable devices, transport vehicles, stationary energy resources [6, 7]. Focus has been put on developing hybrid electric vehicles due to the current energy crisis and severe environment pollution [6]. Dielectric capacitors, as potential EES media in the electric vehicles industry, have quite high power density (~$10^8$ W $kg^{-1}$) and extremely long life time and cycle life (>50,000) comparing to that of the batteries [8]. Capacitors are applicable for power storage quality with large discharge rate and fast responses, which make them capable for instant accelerating [5]. However, capacitors exhibit relative low energy density, which is the biggest drawback in the practical applications. Therefore, it is important to look for new materials with improved energy density so that it can be used for commercial applications.

## 1.4 Development of dielectrics for energy storage

Dielectric capacitors can be divided into three types, according to their performance under the external electric field, namely linear dielectrics, ferroelectrics and antiferroelectrics [9]. Fig. 1.4.1 shows the schematic for the electric behavior of the three types of dielectrics under the external electric field [10].

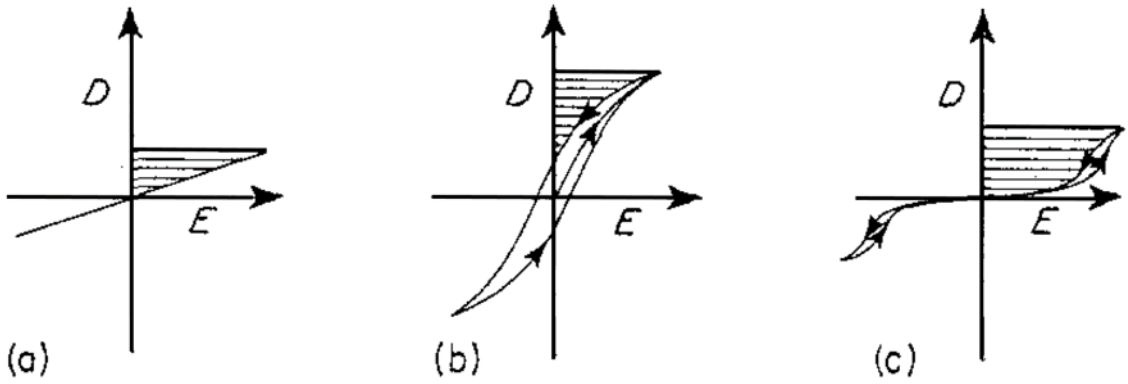


Fig. 1.4.1 Schematic of electric displacement vs. electric field (D-E) behavior on (a) linear dielectric; (b) ferroelectric; (c) antiferroelectric [10].

The energy stored per unit volume in the linear dielectrics can be expressed as equation (1.2.1) [10].

$$\mathrm{J} = \int_0^{D_{max}} E dD \tag{1.4.1}$$

Where $E$ is the external electric field and $D_{max}$ is the electric displacement in the maximum electric field. The shaded area in the schematic is the energy that can be released during discharge. As permittivity ($\varepsilon$) can be defined as d$D$/d$E$, the energy can be given in an alternative form as shown in equation (1.4.2).

$$\mathrm{J} = \int_0^{Emax} \varepsilon E dE \tag{1.4.2}$$

It can be deduced that high permittivity and high electric breakdown field are the key factors to get high energy density in the linear dielectrics [10].

For ferroelectrics, the electric displacement is attributed to both vacuum polarization and spontaneous polarization, according to the equation (1.4.3) [11].

$$D = \varepsilon_0 E + P \tag{1.4.3}$$

The main contribution comes from spontaneous polarization. The polarization is not zero at zero electric field due to the electric hysteresis. The energy density function can be expressed as equation (1.4.4)

$$\mathrm{J} = \int_{P_r}^{P_s} E dP \tag{1.4.4}$$

Where $P_s$ is the saturated polarization and $P_r$ is the remnant polarization. The spontaneous polarization should be high enough and meanwhile the remnant polarization should be low enough to enlarge the shaded area.

For antiferroelectrics, as long as the $P_s$ is large and $P_r$ is low and the electric breakdown field is high, it can store a lot more energy than that of linear dielectrics and ferroelectrics at certain electric field [12].

The state-of-art research showed that ferroelectric $Pb_{0.92}La_{0.08}Zr_{0.52}Ti_{0.48}O_3$ thin film [13] and $PbZrO_3$-based antiferroelectric thin films exhibited high energy density (~45 J $cm^{-3}$) [14, 15]. However, lead is harmful to the environment and its use has been restricted from many commercial applications, such as in electronic devices [16]. Interests have been transformed into lead-free materials. Meanwhile, ceramics and thick films are

favored as they require much lower cost and exhibit larger effective volume for energy storage, comparing to thin films. Dielectric polymers and dielectric ceramics are the main commercialized ferroelectric-capacitor materials, with relatively low energy densities (<1 J $cm^{-3}$) [8]. The development of appropriate lead-free antiferroelectric materials, having high breakdown field and large saturated polarization, for the energy storage application is the present need of the industries.

## 1.5 Aim and objective of the dissertation

Rare-earth-doped $BiFeO_3$ (*e.g.* Sm-$BiFeO_3$) has the potential to be antiferroelectric, which is supported by the double polarization-electric field hysteresis loops obtained in thin films [17]. However, the structure transitions in rare-earth-doped $BiFeO_3$ system is still an open question [18]. Moreover, the origin of the double hysteresis loops in thin films is not well understood and cannot be observed for counterpart ceramics [19]. The investigation of $Bi_{1-x}Sm_xFeO_3$ ceramics is of great importance to identify the antiferroelectric nature, also of other rare-earth doped systems.

Linear dielectric material $BiNbO_4$ (α-phase) is reported to be antiferroelectric, with the appearance of double hysteresis loops in a thin film as well as the permittivity/loss peaks at elevated temperature in a single crystal and ceramics. However, there is no clear structural information and no evidence of a double hysteresis loop in ceramics to support the presence of antiferroelectricity. Meanwhile, the β-$BiNbO_4$ is also regarded as a possible antiferroelectric based only on a structural hypothesis [20]. The relationship between α- and β- phase $BiNbO_4$ is under debate, so is their antiferroelectric nature [21, 22].

Rutile $TiO_2$ is an incipient ferroelectric with high permittivity and high breakdown field. The potential of $TiO_2$ being used as energy storage material has seldom been reported.

In the current chapter, a brief view on the dielectric materials for energy storage is included. An extensive review of published work on the rare-earth-doped $BiFeO_3$, linear dielectric $BiNbO_4$, and incipient ferroelectric $TiO_2$ (rutile) is given in chapter II. An overview on the experimental process used in this work has been listed in chapter III.

The results of antiferroelectric Sm-doped $BiFeO_3$ ($Bi_{1-x}Sm_xFeO_3$), linear dielectric $BiNbO_4$, and incipient ferroelectric $TiO_2$ (rutile) have been discussed in chapters IV, V and VI, respectively. Conclusions and future work are presented in chapter VII.

# Chapter Ⅱ. Literature Review

## 2.1 Antiferroelectric: Rare-earth-doped $BiFeO_3$ in the Morphotropic Phase Boundary (MPB) zone

### 2.1.1 Crystal structure and conductivity mechanism of $BiFeO_3$

$BiFeO_3$ is a room temperature multiferroic which can be potentially used as multi-state memory storage element, sensor, actuators, *etc*. [23]. It has a ferroelectric and an antiferromagnetic ordering with a ferroelectric Curie point $T_c$=830 °C and antiferromagnetic Néel temperature $T_N$=370 °C [24]. $BiFeO_3$ has a rhombohedrally distorted perovskite structure with the *R*3c space group. The lattice parameter is $a_{rh}$=3.965 Å and rhombohedral angle is $\alpha_{rh}$=89.3° [25]. $BiFeO_3$ shows 8 possible spontaneous polarization directions along [111] axis. According to theoretical calculations, the spontaneous polarization of $BiFeO_3$, can be as high as *ca*. 90-100 μC $cm^{-2}$ [26]. The large polarization mainly comes from the large displacement of $Bi^{3+}$ ion, as the active 6s lone pair electrons act as the driving force for the ferroelectric distortion [27].

The phase diagram of $Bi_2O_3$-$Fe_2O_3$ has been mapped out [28, 29] and is shown in Fig. 2.1.1 [30]. $BiFeO_3$ is formed by mixing $Bi_2O_3$ to $Fe_2O_3$ in 1:1 ratio. Pure $BiFeO_3$ is really difficult to be synthesized due to the volatilization of Bi at high temperature and the reduction of $Fe^{3+}$ into $Fe^{2+}$ [31, 32]. There is a narrow temperature window where monophasic $BiFeO_3$ can be formed but dependent on various extrinsic factors such as precursor purity, atmospher and so on. This makes it very difficult to obtain single

phase BFO. It is nearly always accompanied with the secondary phases such as $Bi_2Fe_4O_9$, $Bi_{25}FeO_{39}$ (or $Bi_{25}FeO_{40}$ [33]), as shown in equation (2.1.1), due to a competitive formation energy [34].

$$BiFeO_3 \leftrightarrow 1/49\ Bi_{25}FeO_{39} + 12/49 Bi_2\ Fe_4O_9 \quad (2.1.1)$$

It is also difficult to obtain a saturated polarization hysteresis loop because $BiFeO_3$ normally exhibits high electrical conductivity. The high leakage current is attributed to the reduction of $Fe^{3+}$ to $Fe^{2+}$ and the formation of oxygen vacancies during synthesis [32].

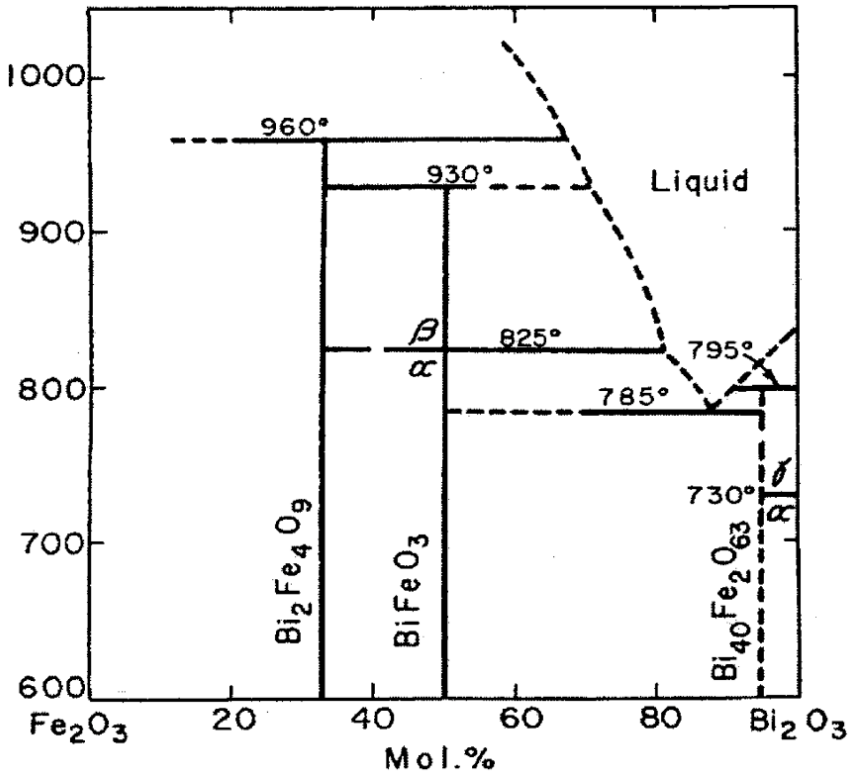


Fig. 2.1.1 The phase diagram of $Fe_2O_3$-$Bi_2O_3$ [30].

The evaporation of Bi, the reduction of $Fe^{3+}$ and the formation of oxygen vacancies can be expressed by equation (2.1.2) and (2.1.3), according to the Kröger-Vink notation [35].

$$2Fe^{\times} + O^{\times} \Leftrightarrow 2Fe^{'} + \frac{1}{2}O_2 \uparrow + V_O^{\cdot\cdot} \quad (2.1.2)$$

$$2Bi^{\times} + 3O^{\times} \Leftrightarrow Bi_2O_3 \uparrow + 2V_{Bi}^{'''} + 3V_O^{\cdot\cdot} \quad (2.1.3)$$

Moreover, $BiFeO_3$ could become a p-type semiconductor under an oxygen-rich atmosphere (e.g. $O_2$ or air) [36]. Bi vacancies and Fe vacancies are energetically favored. These vacancies would easily be ionized to release holes, as displayed in equation (2.1.4) and (2.1.5).

$$Bi_{Bi}^{\times} \rightarrow V_{Bi}^{'''} + 3h^{\cdot} \quad (2.1.4)$$

$$V_{Fe}^{\times} \rightarrow V_{Fe}^{'''} + 3h^{\cdot} \quad (2.1.5)$$

Numerous methods were investigated to produce single phase $BiFeO_3$. Single crystalline $BiFeO_3$ powder was obtained by Achenbach *et. al* [37] using 100% excess $Bi_2O_3$ as raw material to avoid the formation of $Bi_2Fe_4O_9$. The residual $Bi_2O_3$ was then washed by multiple-step concentrated $HNO_3$ leach. Rapid liquid sintering could also prevent the formation of second phases [38]. Mixed raw materials $Bi_2O_3$ and $Fe_2O_3$ are directly pressed into pellet and sintered at high temperature (*ca*. 880 °C) with high heating rate. $Bi_2O_3$, in a form of liquid phase (melting point 817 °C), could accelerate the synthesis to avoid second phases.

Meanwhile, A-site or B-site substitution were also adopted to reduce the leakage current. Bi volatilization is widely observed in Bi-based ferroelectrics, such as bismuth ferrite ($BiFeO_3$), strontium-bismuth titanate ($SrBi_2Ta_2O_9$, SBT) and bismuth titanate ($Bi_4Ti_3O_{12}$, BIT) [39]. Equivalent A-site rare-earth element dopants like $La^{3+}$ or $Nd^{3+}$ were reported to be able to stabilize the Bi evaporation and suppress the formation of oxygen vacancies and thus reduce the electrical conductivity in $BiFeO_3$ [40, 41]. The

acceptor and donor A-site doping were also investigated to have a complete understanding of the conductive mechanism. Brinkman *et al.* [42] observed that $Ca^{2+}$ or $Sr^{2+}$ substitution could remove the second phases. However, the leakage current increased, as oxygen vacancies were formed to balance the charge. Maso *et al.* [43] claimed that the electric properties of Ca doped $BiFeO_3$ depend on the oxygen partial pressure $p(O_2)$. The electrical conductivity of sample sintered in high partial pressure ($O_2$ or air) was quite high [43]. This suggested that a hole-conduction mechanism is dominant, according to the reaction presented in equation (2.1.6) [43].

$$V_O^{\cdot\cdot} + \frac{1}{2}O_2 = O_O^{\times} + 2h^{\cdot} \qquad (2.1.6)$$

While sample sintered in $N_2$ atmosphere was dominated by oxygen vacancies and acted as an oxide ion conductor, according to the reaction (2.1.7) [43].

$$O_O^{\times} \rightarrow V_O^{\cdot\cdot} + O_2 \uparrow \qquad (2.1.7)$$

The conduction mechanism changes from p-type semiconductor to an oxide ion conductor by decreasing the oxygen partial pressure $p(O_2)$ during sintering [43].

On the other hand, donor dopants with comparable ionic radius were chosen to compensate $Fe^{2+}$ and therefore decrease the amount of charge carries. Donor dopants are restricted to B-site, because ions with valence 4+ and above are not large enough to fit in the A-site [19]. Kalantari *et al.* [19] found that the electrical conductivity could be largely reduced by a small amount of Ti doping (<5 mol%), while an incommensurate structure was generated at Ti concentrations higher than 5 mol%. Singh *et al.* [44] managed to decrease the leakage current and produce saturated hysteresis loop with

remnant polarization $P_r$=100 μC/cm$^2$ in a thin film by a level of 3-5 mol% of Mn substitution (Fig. 2.1.2).

To balance both Bi volatilization and Fe reduction, A-site/B-site co-substitution has also been proposed. Low leakage current density and improved ferroelectric properties were shown in a series of A-site/B-site co-doped $BiFeO_3$ systems for example, $Bi_{0.95}La_{0.05}Fe_{0.95}Ti_{0.05}O_3$ [32] and $Bi_{0.85}La_{0.15}Fe_{0.97}V_{0.03}O_3$ [35]. Fig. 2.1.3 displays the P-E loops of pure $BiFeO_3$ (BFO), $BiFe_{0.95}Ti_{0.05}O_3$ (BFT), $Bi_{0.95}La_{0.05}FeO_3$ (BLF), $Bi_{0.95}La_{0.05}Fe_{0.95}Ti_{0.05}O_3$ (BLFT) films on the Pt (111)/Ti/$SiO_2$/Si (100) substrate [32].

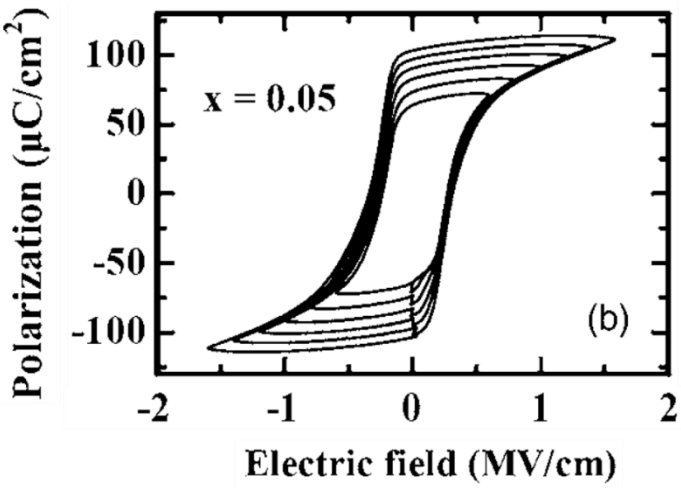


Fig. 2.1.2 P-E hysteresis loop of $BiFe_{0.95}Mn_{0.15}O_3$ film on Pt/Ti/$SiO_2$/Si (100) structure [44].

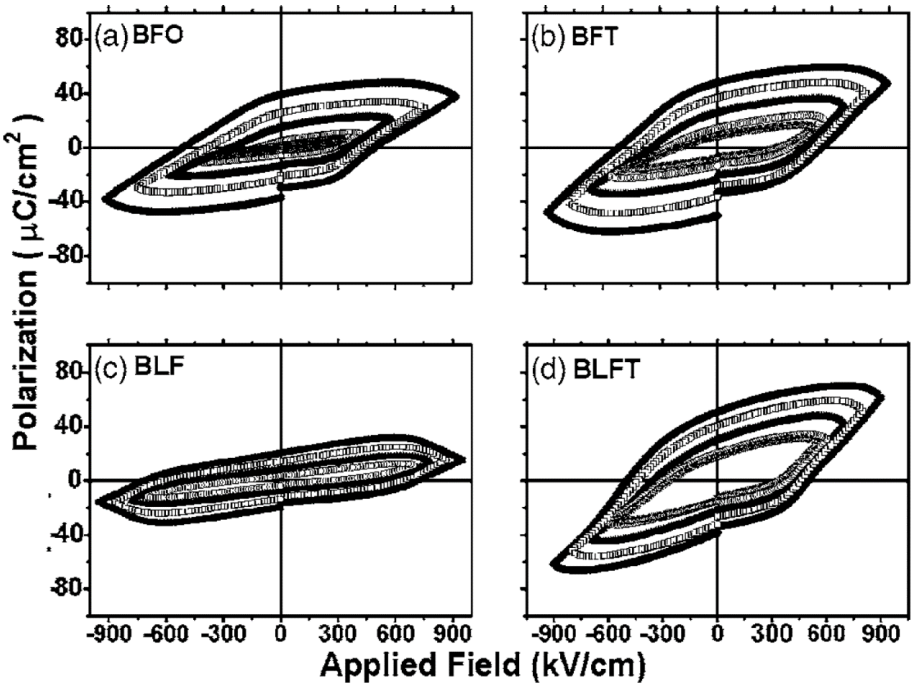


Fig. 2.1.3 P-E loops of (a) pure $BiFeO_3$ (BFO); (b) $BiFe_{0.95}Ti_{0.05}O_3$ (BFT); (c) $Bi_{0.95}La_{0.05}FeO_3$ (BLF); (d) $Bi_{0.95}La_{0.05}Fe_{0.95}Ti_{0.05}O_3$ (BLFT) films on the Pt (111)/Ti/$SiO_2$/Si (100) substrate. [32]

### 2.1.2 Rare-earth doped $BiFeO_3$ as potential antiferroelectric materials

The concept of antiferroelectric systems was first proposed by Kittel as crystals with spontaneous polarization, but of antiparallel orientation in adjacent molecular units [45]. According to Lines and Glass, an antiferroelectric phase could be obtained by condensation of a nonpolar lattice mode near the transition temperature, with the appearance of large dielectric anomalies, and it could be transformed to an induced ferroelectric phase by applying external electric field [46, 47]. Shirane defined it as an antipolar crystal, of which the free energy is comparable to that of the polar crystal with aligned polarization in the sublattice [48-50].

It is reported that rare-earth doping in $BiFeO_3$ could not only reduce the electrical conductivity, but also manipulate the structure into an orthorhombic *Pbam* phase, which has a antiferroelectric structure symmetry. Rare-earth ions are isovalent to Bi ion, but with smaller radius. The Goldschmid tolerance factor (t) [51] of the rare-earth doped $BiFeO_3$ will decrease comparing to that of the pure $BiFeO_3$, according to equation (2.1.8).

$$t=(R_A+R_O)/\ [\sqrt{2}(R_B+R_O)] \qquad (2.1.8)$$

where $R_A$, $R_B$, $R_O$ are the ionic radii of A-, B-site atoms and oxygen atoms, respectively. The tolerance factor is an indicator of crystal stability and distortion. The structure becomes more distorted as the tolerance factor decreases, in which case the phase transition would possibly take place [23]. Reaney *et al.* [52] has derived a relationship between octahedral tilting and tolerance factor. This relationship predicts that the structure is untilted when $0.985<t<1.06$, while it undergoes an anti-phase tilting at

0.964<t<0.985 and both in-phase and anti-phase tilting at t<0.964. The ionic radius of $Fe^{3+}$ in 6-fold coordination is 0.645 Å. The ionic radii of the A-site cations are listed in Table 2.1.1 [53]. The tolerance factors of rare-earth-doped $BiFeO_3$ can be calculated.

Table 2.1.1 The ionic radii in twelve coordination [53]

| Cation | $Bi^{3+}$ | $La^{3+}$ | $Nd^{3+}$ | $Sm^{3+}$ | $Gd^{3+}$ | $Dy^{3+}$ |
|---|---|---|---|---|---|---|
| Radius (Å) | 1.36 | 1.36 | 1.31 | 1.28 | 1.27 | 1.24 |

The concept of morphotropic phase boundary (MPB) was first introduced by Jaffe *et al.* [54] to describe phase transitions, as a result of composition changes or mechanical pressure. Ferroelectric ceramics usually exhibit giant dielectric response and high electromechanical coupling constant in MPB region, due to the coexistence of different phases and the increased amount of possible polarization switching directions [55]. MPB is widely studied in lead zirconate titanate ($PbZr_{1-x}Ti_xO_3$) and lead magnesium niobate-lead titanate ($(1-x)PbMg_{1/3}Nb_{2/3}O_3$-$xPbTiO_3$) solid solutions [56, 57].

The phase separation and related phase transitions in rare-earth substituted $BiFeO_3$ are still under debate [18]. Multiple structure models have been proposed for certain dopant concentrations. Meanwhile, the phase diagrams for $BiFeO_3$-$MFeO_3$ (M=rare earth element) remain vague [23, 58, 59].

### 2.1 3 Structure evolution in La-$BiFeO_3$

For the La-doped system, it is agreed that the structure of $Bi_{1-x}La_xFeO_3$ is rhombohedral *R*3*c* at x<0.1 [60, 61]. However, the introduction of a larger amount of La ions (x>0.1) leads to higher structural complexity. Gabbasova *et al.* [62] reported that (1-x)$BiFeO_3$-

$xLaFeO_3$ solid solution experienced the following composition-driven phase transitions from *R*3*c* to *P*1, *C*222, $C222_1$, $Pbn2_1$ and *Pnma* at x=0.06, 0.24, 0.4, 0.55 and 0.7, respectively. Troyanchuk *et al.* [63] claimed that $Bi_{1-x}La_xFeO_3$ owned a *R*3*c* structure at x≤0.15 while a mixed *R*3*c* and *Imma* phase at 0.15<x<0.45, *Imma* phase at 0.45≤x<0.5 and *Pnma* phase at x≥0.5. Rusakov *et al.* [60] preferred four structure modifications: *R*3*c* (x<0.1), mixed *R*3*c* and *Pnam* ($PbZrO_3$-related structure with $\sqrt{2}a_c \times 2\sqrt{2}a_c \times 4a_c$, where $a_c$ =4 Å is the lattice parameter of pseudocubic subcell structure (0.1<x<0.18), pure *Pnma* (x=0.18), incommensurate *Imma* (0.19≤x≤0.3), mixed *Imma* and *Pnma* phase (0.3<x<0.5) and pure *Pnma* phase for higher La concentrations. Karimi *et al.* [23] found the existing of MPB at x=0.2 for La-doped system, with a *R*3*c* structure at x<0.2 and a pseudocubic structure at x>0.2. An antiferroelectric structure similar to that of $PbZrO_3$ was traced as a minor phase at x=0.3 as well.

### 2.1.4 Structure evolution in Sm-$BiFeO_3$

The investigation of the Sm substituted $BiFeO_3$ system has turned out to be of great interest, due to the observation of an anti-polar $PbZrO_3$-like *Pbam* structure and the double polarization-electric field hysteresis loops, in a certain composition range in thin films [17, 64]. $PbZrO_3$ is a prototype antiferroelectric structure, whose lattice parameter can be described as $\sqrt{2}a_c \times 2\sqrt{2}a_c \times 2a_c$. The $PbZrO_3$ can be better interpreted using a pseudo-cubic structure, as shown in Fig. 2.1.4 [65].

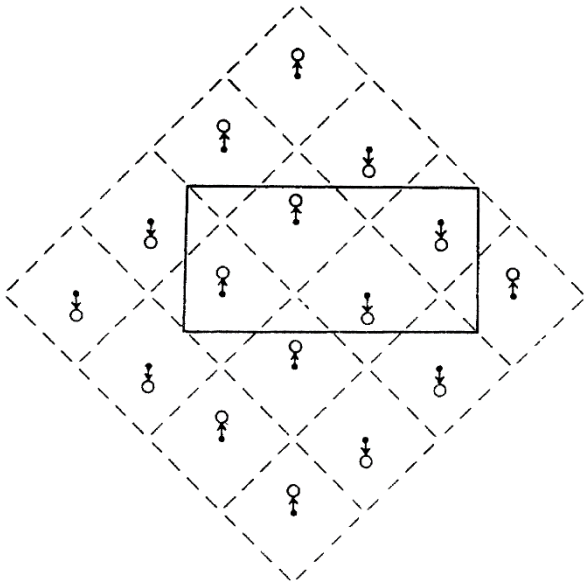

Fig. 2.1.4 Schematic of 2D structure of the antiferroelectric $PbZrO_3$. The arrows represent the polarization of Pb ion and solid lines refer to an orthorhombic unit cell [64, 65].

The observation of a MPB region in $Bi_{0.86}Sm_{0.14}FeO_3$ epitaxial thin film, on a (100) $SrTiO_3$ substrate, was first reported by Fujino *et al.* [17]. The (002) spot became mixed (002), (020) and (200) spots beyond x=0.13, as a results of twinning. Extra diffraction spots $(2\ 0\ \frac{1}{2})$ and $(2\ 0\ -\frac{1}{2})$ seen in two dimensional XRD in $Bi_{1-x}Sm_xFeO_3$ ($x \geq 0.14$) indicated the cell doubling, as shown in Fig. 2.1.5. The $Bi_{1-x}Sm_xFeO_3$ thin film undergoes a rhombohedral to pseudo orthorhombic phase transition and then becomes paraelectric beyond x=0.27.

Karimi *et al.* [23] found that the $Bi_{1-x}Sm_xFeO_3$ ceramics owned a major polar *R*3*c* structure at $x<0.15$ and $PbZrO_3$-like orthorhombic structure at $x \geq 0.15$, as coincident to Fujino's results [17]. A mixed $PbZrO_3$-like and orthoferrite *Pnma* structure were obtained at $x>0.175$ (Fig. 2.1.6). Second phases like $Bi_2Fe_4O_9$ or $Bi_{25}FeO_{39}$ were always formed at $x<0.1$ but disappeared at $x>0.1$, as a result of Sm doping.

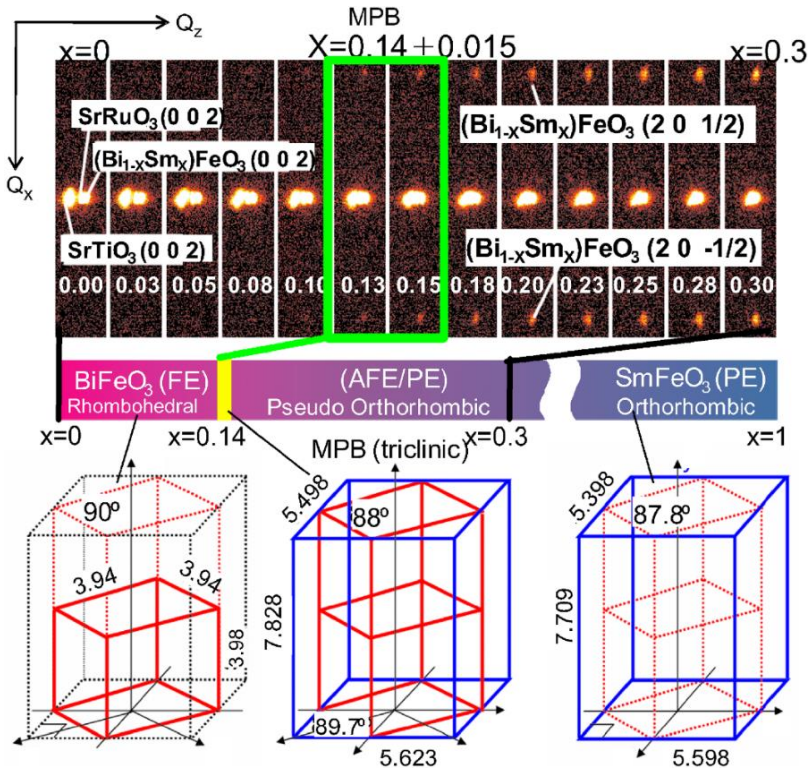


Fig. 2.1.5 Two-dimensional XRD of the $Bi_{1-x}Sm_xFeO_3$ ($0 \le x \le 0.3$) composition spread. Structure changes from rhombohedra (red unit cell) to orthorhombic (blue unit cell) [17].

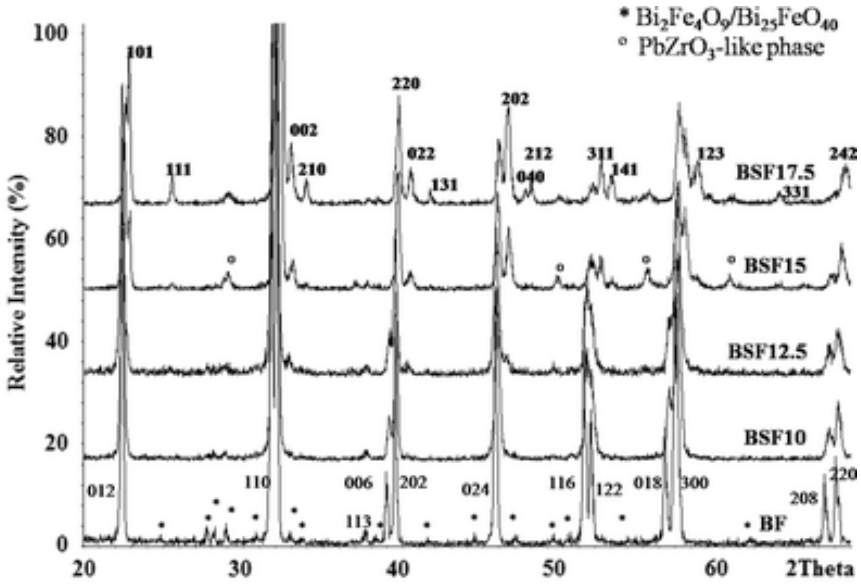


Fig. 2.1.6 XRD spectra of $Bi_{1-x}Sm_xFeO_3$ with $0<x<0.4$ [23].

It is reported that calcination conditions could also influence the phase distribution in the $BiFeO_3$-$SmFeO_3$ system. Khomchenko *et al.* [66] found that a low calcination temperature of 850 °C would lead to the formation of mixed three phases in $Bi_{0.85}Sm_{0.15}FeO_3$ ceramics, including the *Pbam,* the *Pnma* and the *R*3*c* phases. The phase separation was explained as an inhomogeneous distribution of $Bi^{3+}$ and $Sm^{3+}$ cations caused by the insufficient calcination temperature [66]. The fraction of the main *Pbam* phase would increase with the increase of calcination temperature. A calcination at 950 °C led to 93 wt% of the *Pbam* phase. A further increase of the calcination temperature would lead to the formation of impurities like $Bi_2Fe_4O_9$/$Bi_{25}FeO_{39}$. It was suggested that antiferroelectric *Pbam* single phase was really difficult to obtain.

A more detailed structural study on the ferroelectric-to-antiferroelectric phase boundary in the $Bi_{1-x}Sm_xFeO_3$ thin film has been carried out by Cheng *et al.* [64]. Fig. 2.1.7 shows the TEM images of $Bi_{0.9}Sm_{0.1}FeO_3$ thin film. The $\frac{1}{4}\{011\}$ superstructure reflections were spotted.

It was suggested that these are due to the quadrupling of unit cell along the <011> direction, which originated from the antiparallel displacement of A-site cations [64]. Meanwhile, anti-phase octahedral tilting was deduced from the appearance of the $\frac{1}{2}\{011\}$ reflection in Fig. 2.1.7b. However, these superstructure reflections existed only in localized region within a ferroelectric matrix [64].

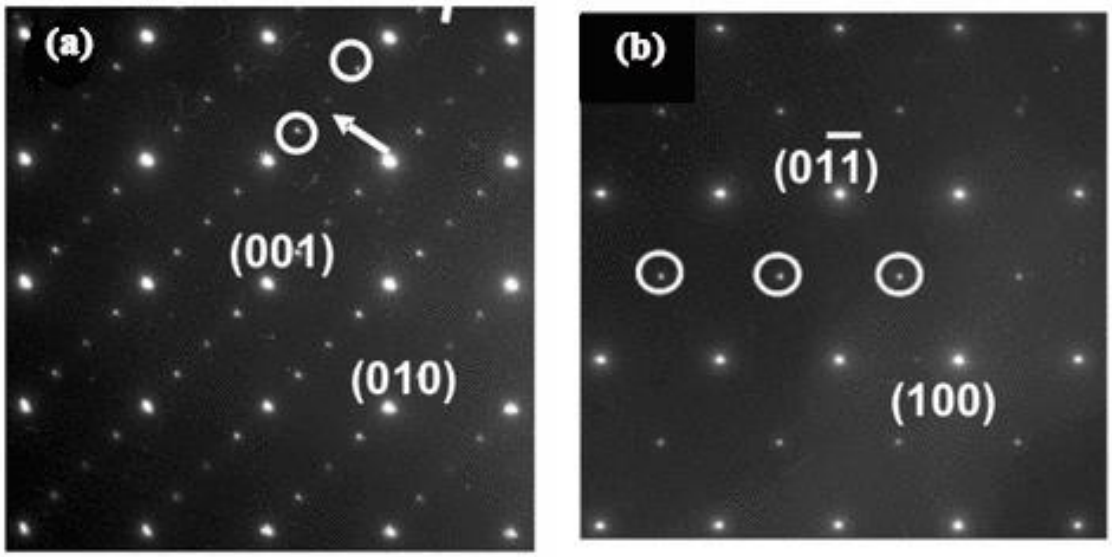


Fig. 2.1.7 TEM images of $Bi_{0.9}Sm_{0.1}FeO_3$ (a) [100] zone axis diffraction pattern (ZADP) with $\frac{1}{4}\{011\}$ (circle) and $\frac{1}{2}\{011\}$ (arrow) superstructure reflections; (b) [011] ZADP with $\frac{1}{2}\{11\bar{1}\}$ reflections [64].

The structure of the $Bi_{0.86}Sm_{0.14}FeO_3$, where the FE-AFE phase boundary resides, is very complex; not only $\frac{1}{4}\{011\}$ and $\frac{1}{2}\{011\}$ spots, but also $\frac{1}{2}\{010\}$ spots were detected (Fig. 2.1.8) [64]. The antiparallel shift of cations was severely suppressed according to the decreased intensity of $\frac{1}{4}\{011\}$ reflections. The $\frac{1}{2}\{010\}$ spots are related to the $Sm^{3+}$ doping and $\frac{1}{2}\{011\}$ spots are related to structural twinning. Moreover, incommensurate reflections along $[01\bar{1}]$ direction (appearing as satellite spots near main reflections) were also observed. The incommensuration phenomenon was expected as a competition between the antipolar *Pbam* phase and polar *R*3*c* phase, which is often associated with the enhanced electromechanical properties [67, 68].

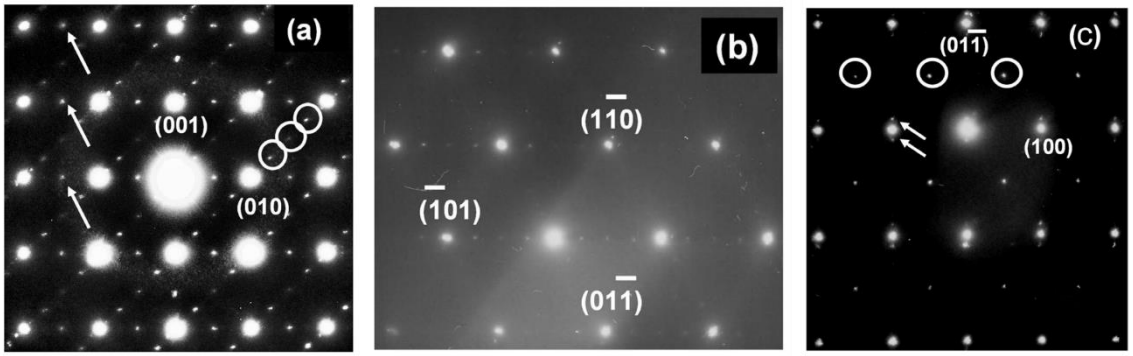


Fig. 2.1.8 TEM images of $Bi_{0.9}Sm_{0.14}FeO_3$ (a) [100] ZADP with circled $\frac{1}{4}\{011\}$ and $\frac{1}{2}\{011\}$ superstructure reflections and arrowed $\frac{1}{2}\{010\}$ reflections; (b) [111] ZADP with weakened $\frac{1}{4}\{011\}$ reflections; (c) [011] ZADP with $\frac{1}{2}\{11\bar{1}\}$ reflections (circle) and incommensurate reflections (arrow) [64].

Meanwhile, a large density of nanodomains with the appearance of twinning structures in size of 20-50 nm were also observed by TEM. Nanodomains were claimed to be responsible for the outstanding piezoelectric properties, as smaller domains are easier to be perturbed by electric field [69]. Fig. 2.1.9 shows the dielectric (Fig. 2.1.9a) and piezoelectric (Fig. 2.1.9b) properties as a function of Sm concentration. A maximum permittivity value was observed at x=0.14, due to the existence of complex incommensurent structure and nanodomains [17]. Moreover, an indication of polarization rotation from the [111] direction in $BiFeO_3$ to the [001] direction in the $Bi_{1-x}Sm_xFeO_3$ (x=0.14) was proposed by Kan *et al.* [70]. The polarization rotation was also responsible for the enhancement of $d_{33}$ along the [001] direction at the structure boundary. For films grown on (110) and (111) substrate, the $d_{33}$ value decreased with increasing Sm concentration.

The $\frac{1}{4}\{011\}$ reflections disappeared as the Sm dopant increased to 0.2, which indicates the vanishing of the antiparallel cation displacement. The fundamental reflections of paraelectric $SmFeO_3$ phase were the only observed reflections as the Sm dopant increased to 0.3, indicating the fully transition to $SmFeO_3$ type structure.

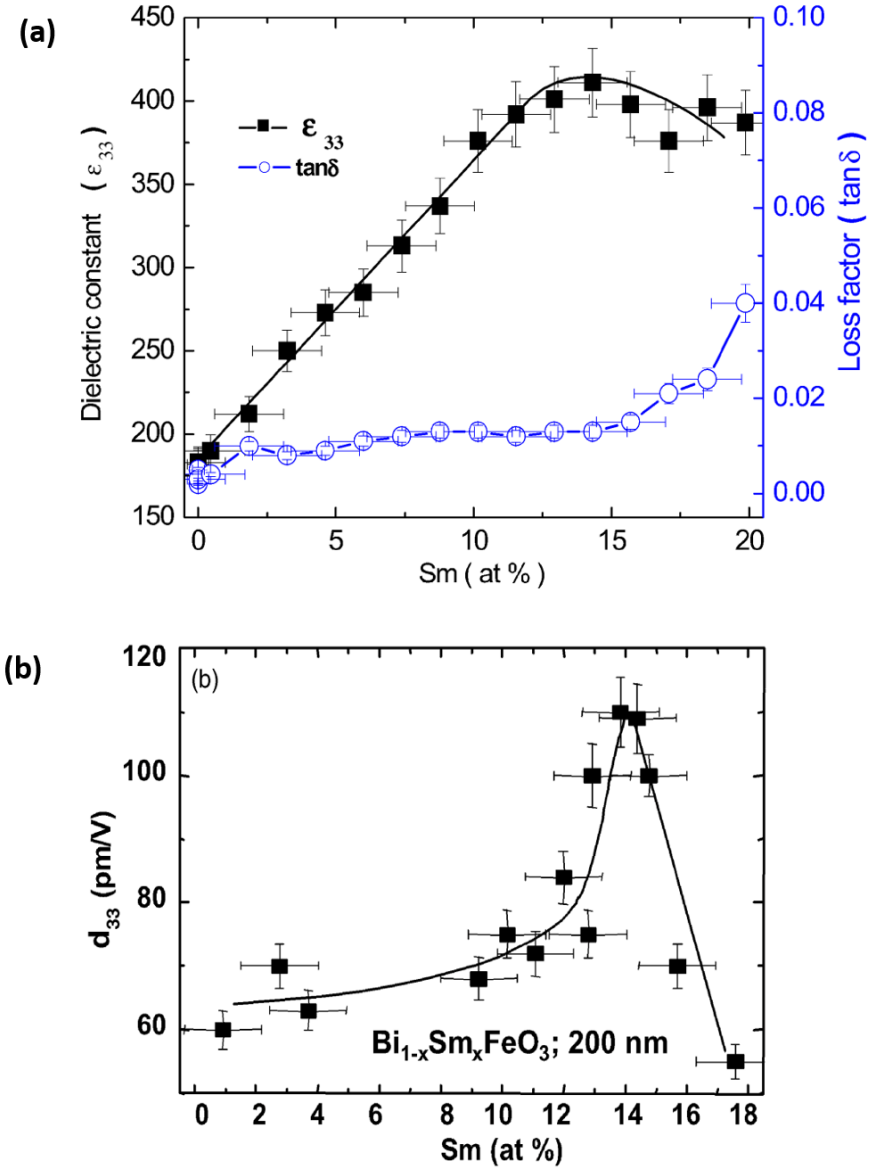


Fig. 2.1.9 Enhanced electromechanical properties of $Bi_{1-x}Sm_xFeO_3$ ($0 \le x \le 0.2$) thin film at MPB region (a) Dielectric properties at 1 MHz; (b) high field $d_{33}$ determined from piezoelectric hysteresis loop [17].

### 2.1.5 Structure evolution in Nd-$BiFeO_3$

As another member of rare-earth family, the Nd-doped $BiFeO_3$ has been investigated as well. Yuan *et al.* [71] reported that in $Bi_{1-x}Nd_xFeO_3$ ceramics the rhombohedral structure transforms to a triclinic structure, *P*1 space group, at x=0.05-0.15 and then it changes to a pseudo-tetragonal phase at x=0.175-0.2. It was indicated that the triclinic structure contained a single cell with mixed Bi/Nd atoms on the A-site rather than a supercell. The $Bi_{1-x}Nd_xFeO_3$ compositions were suggested as ferroelectric at x≤0.175 and paraelectric at x=0.2, based on the observation of the typical polarization-electric field (P-E) loops. Karimi *et al.* [72] reported that peak splitting and superlattice reflections were obtained in $Bi_{1-x}Nd_xFeO_3$ ceramics (x=0.15, 0.2). XRD Rietveld refinement of $Bi_{1-x}Nd_xFeO_3$ (x=0.15, 0.2) resulted in an orthorhombic structure with the *P*bam space group. The orthoferrite *Pnma* phase would be dominant at x=0.25 for the $Bi_{1-x}Nd_xFeO_3$ ceramics with a minor trace of $PbZrO_3$-like phase. A TEM study of $Bi_{0.8}Nd_{0.2}FeO_3$ (BNF20) ceramics (Fig. 2.1.10) also revealed the $\frac{1}{4}\{110\}$, $\frac{1}{4}\{001\}$, $\frac{1}{2}\{011\}$ and the $\frac{1}{2}\{111\}$ superlattice reflections, suggesting an antipolar order.

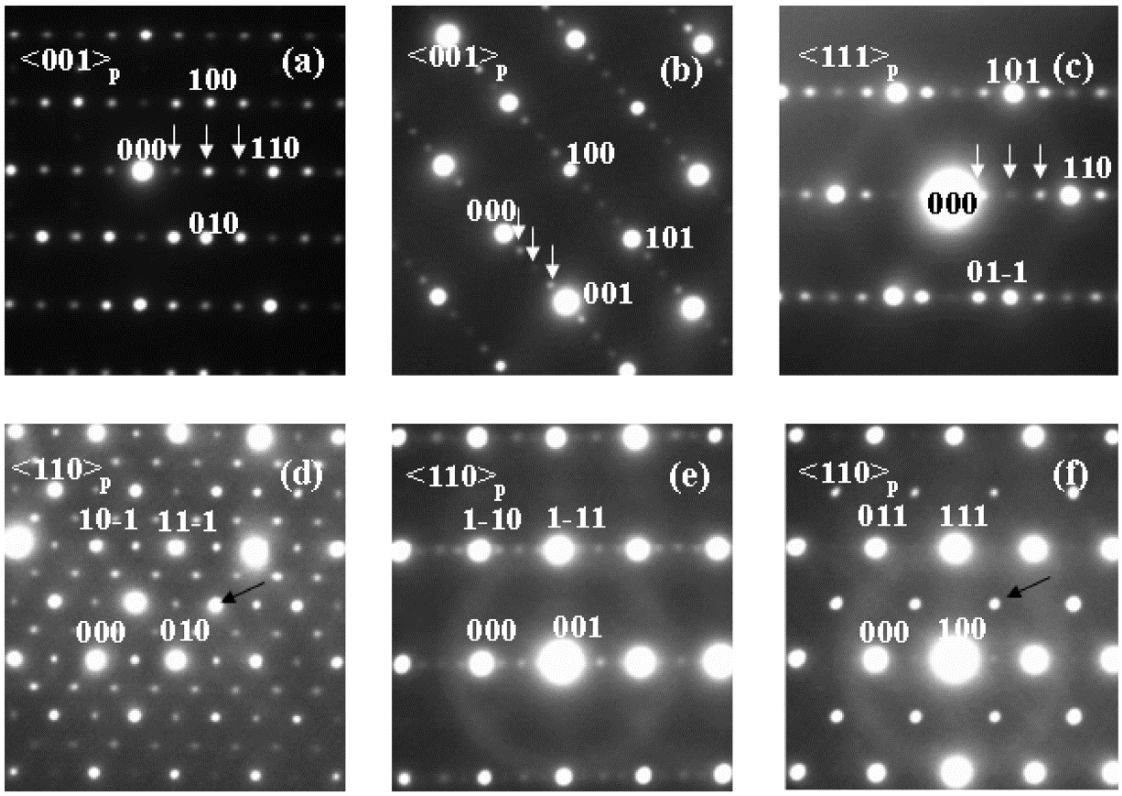


Fig. 2.1.10 Electron diffractions of BNF20 ceramic (a-b) zone axes in <001>p; (c) zone axes in <111>p; (d-f) zone axes in <110>p. The $\frac{1}{4}\{001\}$ and the $\frac{1}{4}\{110\}$ are arrowed in (a-c), The $\frac{1}{2}\{011\}$ and the $\frac{1}{2}\{111\}$ reflections are arrowed in (d) and (f) [72].

### 2.1.6 Universal behavior of Rare-earth doped $BiFeO_3$

Kan *et al.* [58] reported a universal behavior of structural phase transition in rare-earth-substituted (Sm, Gd, Dy) $BiFeO_3$. Fig. 2.1.11 has illustrated the changes of normalized intensity of the $\frac{1}{4}\{011\}$ and the $\frac{1}{2}\{010\}$ XRD spots as a function of substitution (Sm, Gd, Dy) concentration.

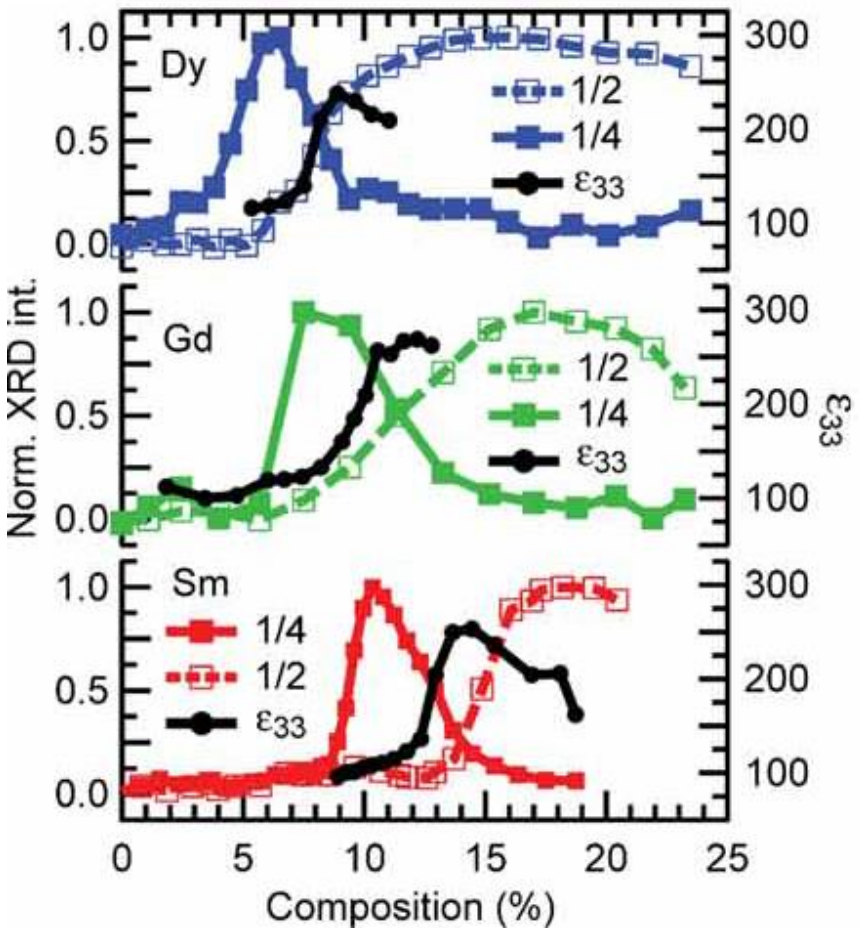


Fig. 2.1.11 Normalized XRD intensities of $\frac{1}{4}\{011\}$ (filled square) and $\frac{1}{2}\{010\}$ (open square) superstructure spots and $\varepsilon_{33}$ at zero bias field as a function of RE-doped $BiFeO_3$ (RE=Sm, Gd, Dy) concentration [58].

It was found that the intensity of the $\frac{1}{4}\{011\}$ spots decreased and that of the $\frac{1}{2}\{010\}$ spots increased with the increasing of RE concentration. Meanwhile, the study of the dielectric properties at zero bias field indicated that permittivity reached a maximum value at the structural phase transition boundary, as previously reported [17]. Furthermore, the phase boundary shifted towards the higher RE concentration with larger RE ionic radius.

A universal phase transition behavior has been revealed by replacing the dopant composition with the average A-site ionic radius ($R_{ave}$). The average A-site ionic radius in $Bi_{1-x}M_xFeO_3$ (M represents rare-earth element) can be easily calculated using equation 2.1.9.

$$R_{ave}=(1-x)\ R_{Bi} + x\ R_M \quad (2.1.9)$$

The relationship between the rare-earth element concentration and the average A-site ionic radius is listed in Table 2.1.2.

Table 2.1.2 Relationship between the rare-earth element concentration and the average A-site ionic radius ($R_{ave}$)

| $R_{ave}$ (Å) | 1.353 | 1.352 | 1.349 | 1.348 | 1.345 |
|---|---|---|---|---|---|
| $x_{Sm}$ | 0.09 | 0.1 | 0.14 | 0.15 | 0.19 |
| $x_{Gd}$ | 0.08 | 0.09 | 0.12 | 0.13 | 0.17 |
| $x_{Dy}$ | 0.06 | 0.07 | 0.09 | 0.1 | 0.125 |

The re-organization of data is shown in Fig. 2.1.12. The phase transition is found irrelevant to the types of rare-earth elements, but correlates to the average ionic radius. This is explained as a hydrostatic pressure effect caused by chemical substitution [58].

The distortion of the system, such as the oxygen octahedral tilting, destabilize rhombohedral *R*3*c* phase and stabilize orthorhombic *Pnma* phase. The shrinkage of the lattice parameter and unit cell volume would stabilize the distorted system. Kan *et al.*

[73] suggested that enhanced electromechanical properties were not observed in La substituted system because the chemical pressure effect created by La is too weak to manipulate the local structure.

In addition, the transformation of ferroelectric polarization hysteresis loop to the double hysteresis loop is also $R_{ave}$ dependent, as shown in Fig. 2.1.13.

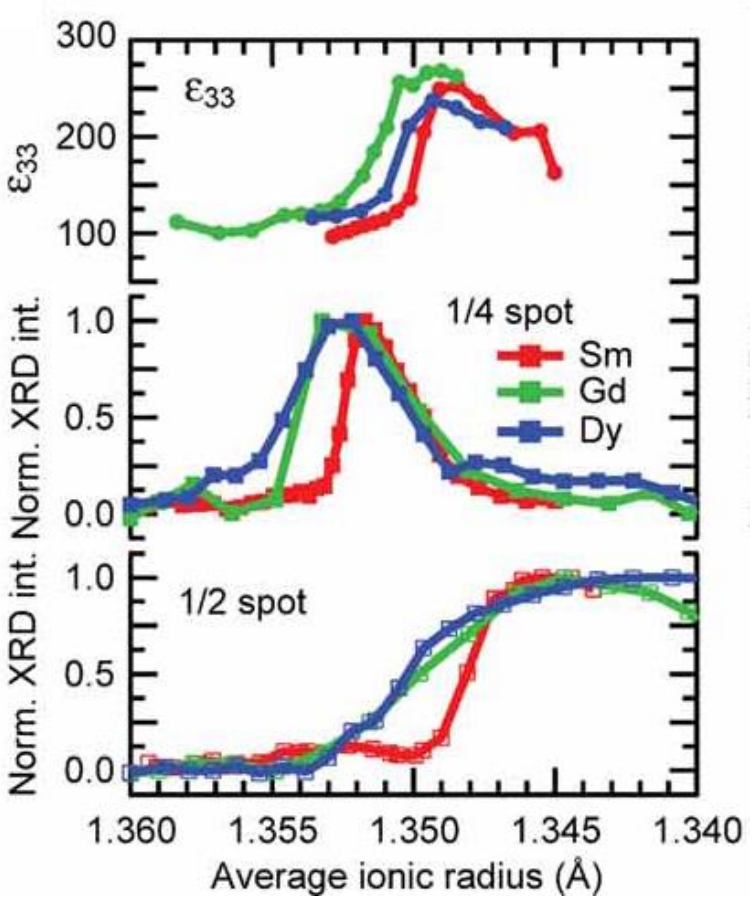


Fig. 2.1.12 Normalized XRD intensities of $\frac{1}{4}\{011\}$ (filled square) and $\frac{1}{2}\{010\}$ (open square) superstructure spots and $\varepsilon_{33}$ at zero bias field as a function of $R_{ave}$ (ionic radius of $Bi^{3+}$ is 1.36 Å, $Sm^{3+}$ is 1.28 Å, $Gd^{3+}$ is 1.27 Å, $Dy^{3+}$ is 1.24 Å in twelve coordination) [58].

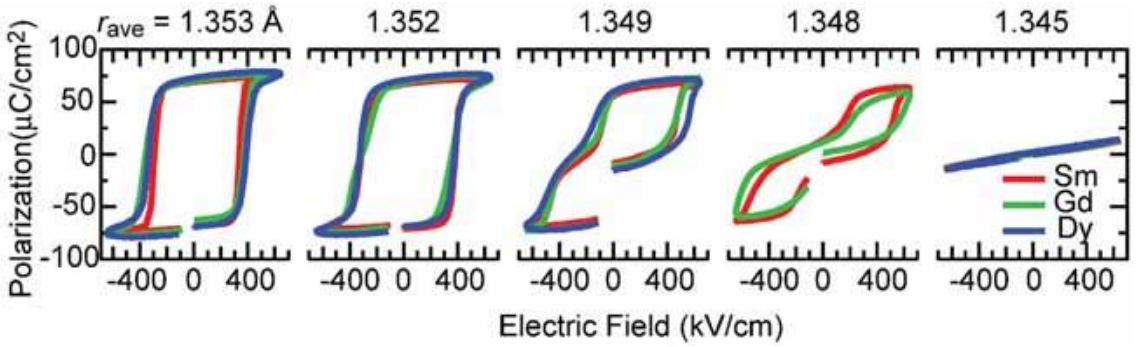


Fig. 2.1.13 Polarization hysteresis loops of RE-$BiFeO_3$ (RE= Sm, Gd, Dy) thin film as a function of $R_{ave}$ [58].

The transition started at $R_{ave}$=1.349 ($x_{Sm}$=0.14) where the permittivity reached the maximum. Double hysteresis loops were observed at $R_{ave}$=1.348 ($x_{Sm}$=0.15). Linear hysteresis loops were observed at $R_{ave}$=1.345 ($x_{Sm}$=0.19). However, according to Fujino's results [17], the square loop was observed at x=0.14 in Sm-doped $BiFeO_3$ thin film with a much lower coercive field. The double hysteresis loops were observed in a composition range of 0.15≤x≤0.27, which covers a much larger Sm range than that was observed in Kan's report [58]. Moreover, the universal behavior with different rare-earth dopants could not be revealed in ceramics [74]. It is explained as the influence of the chemical homogeneity, substrates in the thin films as well as the elastic and electric grain boundary conditions in ceramics [74].

### 2.1.7 Phase diagram of rare-earth-doped $BiFeO_3$

The phase evolution of rare-earth-doped $BiFeO_3$ with various compositions and elevated temperature has been widely studied. Preliminary phase diagrams have been built up although visible discrepancies can be found in the references [18, 23, 58]. For La-doped $BiFeO_3$, Karimi et al. [23]proposed a two-phase (*R*3*c*-*Pnma*) diagram as single

phase PZ-like structure could not be obtained. Transition temperatures were detected by DSC and structures were analyzed by XRD. The diagram is shown in Fig. 2.1.14a. The *R*3*c* phase is stable at low temperature and the *Pnma* phase is stable at high temperature. The transformation temperature from the *R*3*c* phase to the *Pnma* phase decreased with the increase of La content. The *Pnma* phase became the stable phase at room temperature at *ca.* x=0.2.

However, Kan *et al.* [73] proposed a three-phase model for La-doped $BiFeO_3$ composites (Fig. 2. 14b), due to the observation of the $\frac{1}{4}\{011\}$ supercell reflections from x=0.1 to x=0.3 at room temperature. The $\frac{1}{4}\{011\}$ spots disappeared at T=360 °C for the $Bi_{0.9}Sm_{0.1}FeO_3$ composition and the transformation temperature kept decreasing with the increasing of the La substitution.

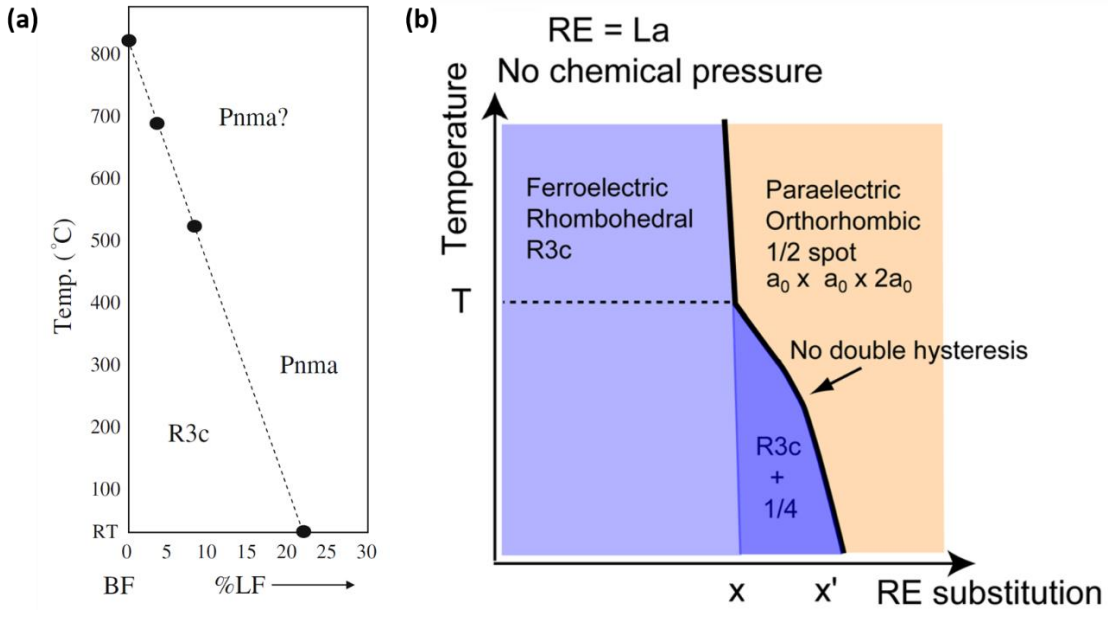


Fig. 2.1.14 Preliminary phase diagram of $Bi_{1-x}La_xFeO_3$ based on (a) two-phase model [23]; (b) three-phase model [73].

For Sm- and Nd-doped $BiFeO_3$, a reasonable agreement has been achieved on the existence of the PZ-like *Pbam* structure. Karimi *et al.* [23] claimed the observation of PZ-like structure in the $Bi_{1-x}Nd_xFeO_3$ at x=0.15-0.25 (discussed in section 2.1.5) and the $Bi_{1-x}Sm_xFeO_3$ at x=0.125-0.175 (discussed in Fig. 2.1.6). Fig. 2.1.15a shows the schematic phase diagrams of the $BiFeO_3$-$NdFeO_3$ system. The phase transition temperature between the PZ-like structure and the *Pnma* structure decreased from 325 °C to 170 °C and to room temperature for a Nd mole concentration of 0.15, 0.2 and 0.25, respectively. The phase diagram of (1-x) $BiFeO_3$-x $SmFeO_3$ solid solution is shown in Fig. 2.1.15b. The transition temperature for x=0.15 is 309 °C and decreased to room temperature for that of x=0.175. However, Kan *et al.* [73] found that the PZ-like structure coexisted with the fundamental *R*3*c* structure from x=0.1 to x=0.14, rather than an intermediate phase. The structure gradually changed to the *Pnma* phase beyond x=0.14, as shown in Fig. 2.1.15c. The disappearance of the $\frac{1}{4}$ spots in Sm-doped $BiFeO_3$ (x=0.1) occurred at T=280 °C.

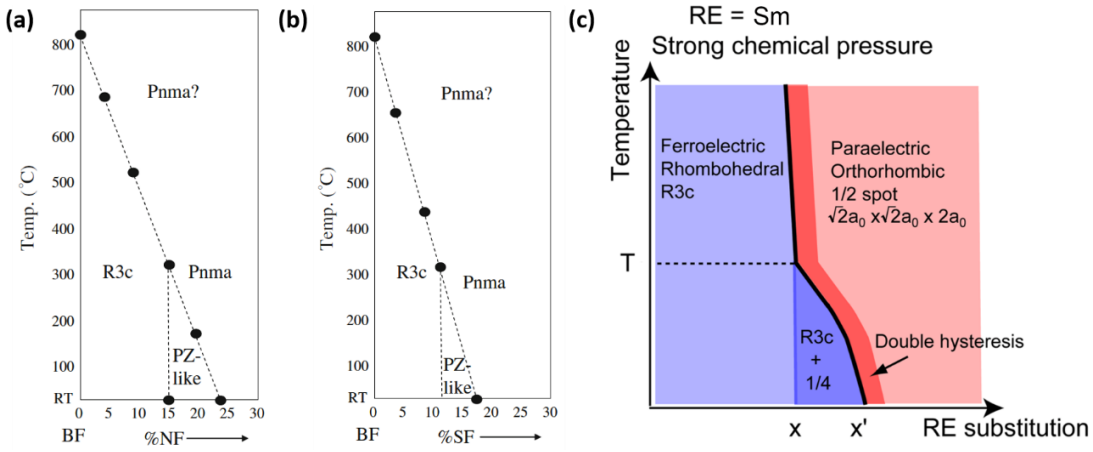


Fig. 2.1.15 The preliminary phase diagram of (a) $BiFeO_3$-$NdFeO_3$ ceramic system; (b) $BiFeO_3$-$SmFeO_3$ ceramic system [23]; (c) $BiFeO_3$-$SmFeO_3$ thin film system [73].

A systematic phase diagram of rare-earth-doped $BiFeO_3$ is summarized in Fig. 2.1.16 by Arnold [18].

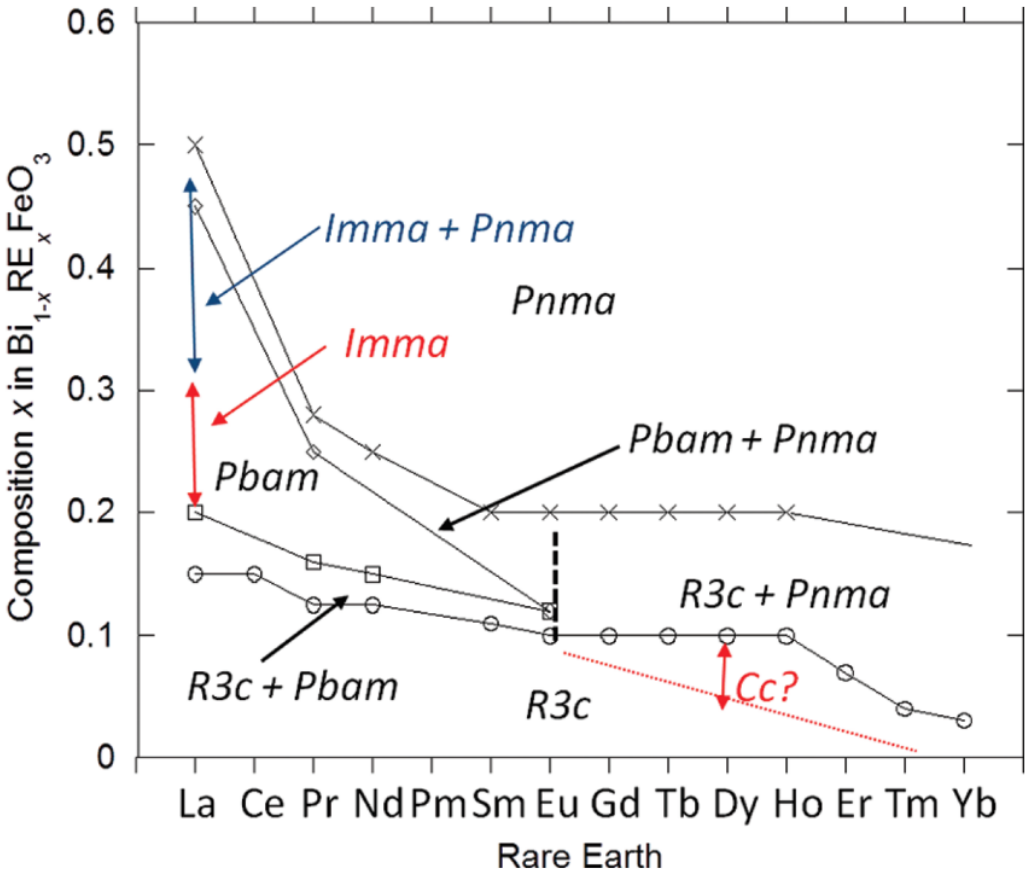


Fig. 2.1.16 Systematic phase diagram of rare-earth-doped $BiFeO_3$ [18].

### 2.1.8 The origin of double hysteresis loops

Double polarization-electric field hysteresis loops were obtained in Sm-doped $BiFeO_3$ thin films [17]. However, this has not been seen in ceramics yet, probably due to the high leakage current and low breakdown field. The origin of the double hysteresis loop has been widely discussed. Previous researches considered it as an evidence of an electric field-induced antiferroelectric to ferroelectric phase transition, based on the observation of PZ-like superstructure.

Kan *et al.* [70] claimed that the chemical pressure caused by rare-earth doping was accounted for this unique electric behavior. A universal behavior unrelated to the element types was obtained with the presentation of average ionic radius (Fig. 2.1.13). Double hysteresis loop doesn't exist in La-doped system, as the chemical pressure effect from the La ions is too weak.

For the other rare-earth elements, double hysteresis loop was observed at the structure boundary where the $\frac{1}{4}$ spots gradually disappeared and the $\frac{1}{2}$ spots appeared. It is suggested that the formation of double hysteresis loop was not related to the field-induced AFE-FE transition, as the $\frac{1}{4}$ spots diminished before the formation of the double P-E hysteresis loops. Kan *et al.* [58] proposed that it could be related to the paraelectric (*Pnma*) to ferroelectric (*R3c*) phase transition at the structure boundary (Fig. 2.1.15c).

The first-principles total-energy calculation revealed the possible low-energy structures of the $BiFeO_3$ that are favorable with A-site doping [58]. Attention has been paid on the zone-center polar $\Gamma_4^-$ mode, the alternating polar displacement related $M_{AFE}$ and $X_{AFE}$ modes, and the oxygen octahedron rotation related $R_4^+$ and $M_3^+$ modes, as shown in Fig. 2.1.17a. The ferroelectric bulk ground state *R*3*c* phase is obtained with a combination of the $\Gamma_4^-$ [111] and $R_4^+$ [111] modes [58]. The alternative structures are specified in Table 2.1.3 with the calculated combination of modes. Lattice parameters and volume of the formula unit (f.u.) are listed as well [58]. The energy difference ($\Delta U$) between alternative structures and ground state *R*3*c* indicated that orthorhombic

*Pnma* phase owns a closer energy to the *R*3*c* ground state, compared to the *Pbam* structure.

The *Pnma* structure exhibited lower energy than the rhombohedral phase at zero field, as shown in Fig. 2.1.17b. At high electric field (E>Ec), the *Pnma* structure acted as a conventional antiferroelectric and proceeded a discontinuous transition to polar phase, the cations with alternative displacements aligned towards the same direction [58].

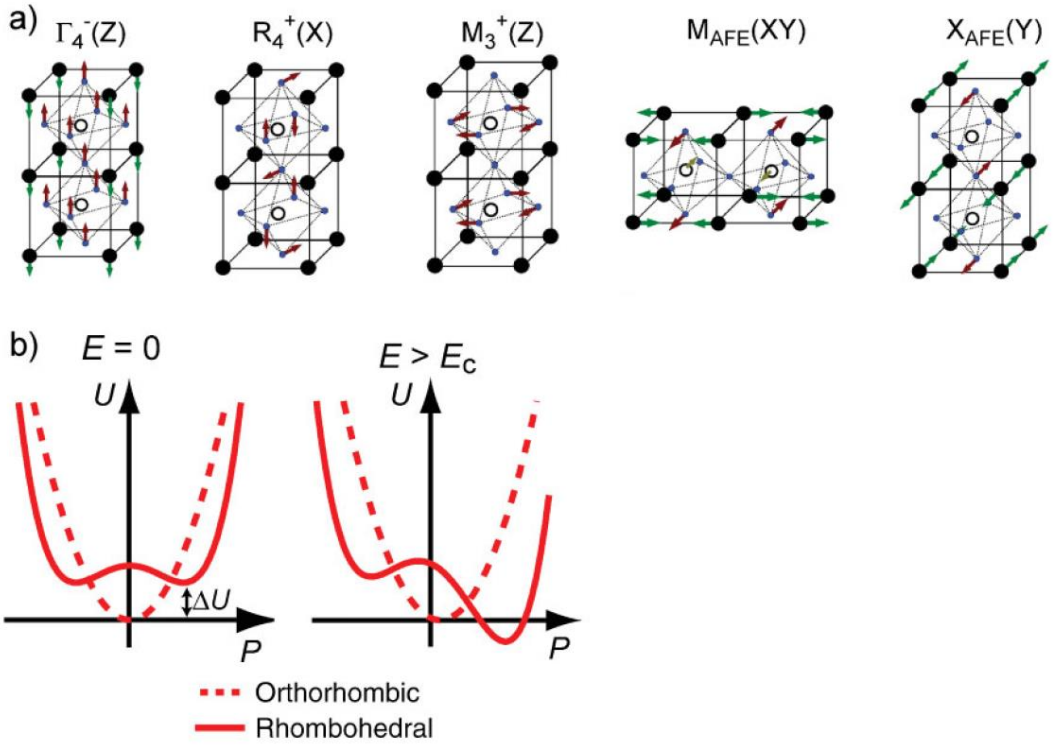


Fig. 2.1.17 (a) selected unstable modes of the $BiFeO_3$. Solid blue circles are oxygen atoms, open circles are Fe atoms, solid black circles are Bi atoms. Green arrows show Bi displacements and red arrows show oxygen displacements (not to scale). (b) scheme of the energy profile of ferroelectric *R*3*c* phase (solid line) and the nonpolar orthorhombic phase (dashed line) versus polarization (P) near $R_{ave}$-critical [58].

Table 2.1.3 Low energy alternative structure of $BiFeO_3$ [58].

| Space group | Modes | Lattice parameters (Å) | V [Å$^3$ f.u.$^{-1}$] | ΔU [meV f.u.$^{-1}$] |
|---|---|---|---|---|
| *Pbam* | $\Gamma_{25}$, $R_{25}$, $\left(\frac{1}{2}\frac{1}{2}0\right)\frac{\pi}{a}\Sigma_3$, $(110)\frac{\pi}{a}M_5'$ | (5.480, 11.162, 7.68) | 58.73 | 153 |
| *Pnma* | $M_3^+([001])$, $R_4^+([110])$, | (5.372, 5.589, 7.690) | 57.71 | 14 |
| *R3c* | $\Gamma_4^-$ [111], $R_4^+$ [111] | (5.525, 5.525, 5.525) α=β=γ=59.8 | 59.31 | 0 |

Interestingly, Fig. 2.1.18 shows that double hysteresis loop was only observed in thin films with (001) substrate but not in films with (110) or (111) substrates. As previously mentioned, the polarization would rotate to the [001] direction in the Sm-doped $BiFeO_3$ thin film at x=0.14 [70]. The induced paraelectric to ferroelectric phase transition under electric field will result in a polar phase with a [001] polarization direction due to a lower energy needed for rotation of domains. Maximum energy stability can be achieved when the electric field is applied along this polarization direction as well. As a result, the double hysteresis loop was the most prominent in (001) film. This is also a possible reason why double hysteresis loop has not been observed in ceramic.

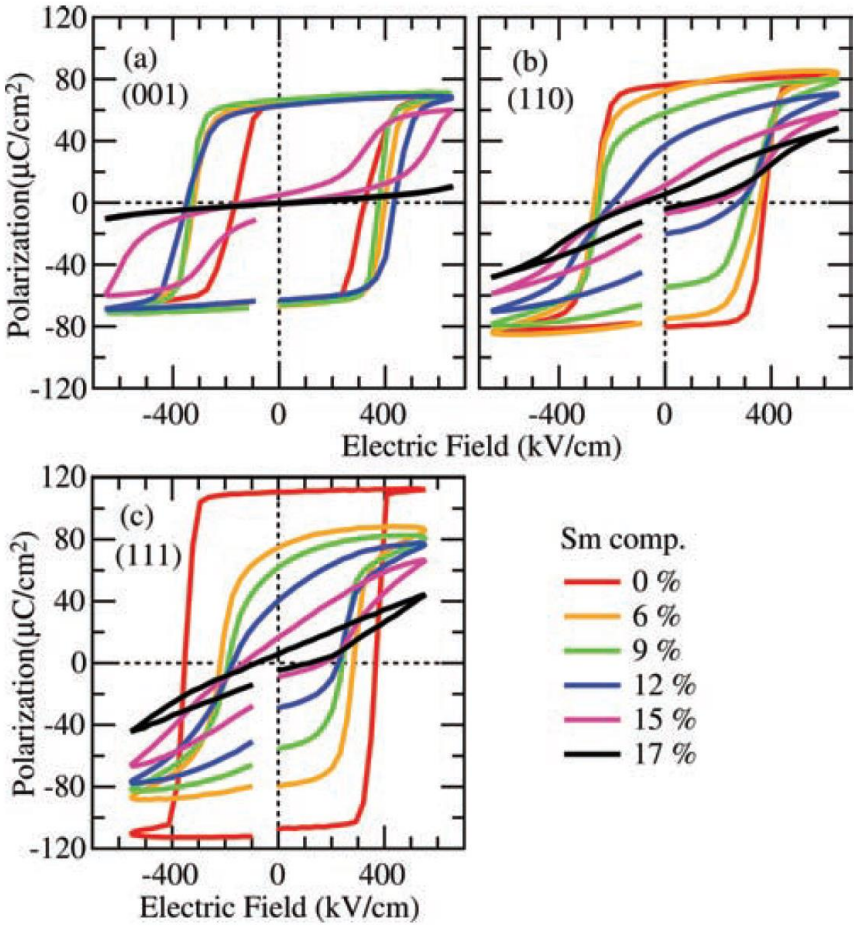


Fig. 2.1.18 Polarization-electric hysteresis loops of 400 nm-thick Sm-doped $BiFeO_3$ films with (a) (001); (b) (110); (c) (111) $SrTiO_3$ substrates as a function of Sm concentration [70].

## 2.2 Linear dielectric: $BiNbO_4$ as a possible antiferroelectric candidate

### 2.2.1 Basic structure of $BiNbO_4$

The $BiNbO_4$ system exhibits two crystal structures, one with orthorhombic structure which was first reported by Roth [75] and the other with triclinic structure found by Aurivillus [76]. The orthorhombic phase, commonly referred to as the α phase, owns a centrosymmetric *Pnna* space group and is normally formed below 1000 °C. The cell dimensions are *a*=5.67 Å, *b*=11.71 Å, *c*=4.97 Å and Z=4 [77]. The α-$BiNbO_4$ belongs to the stibiotantalite structured $ABO_4$ family of compounds (A=Sb or Bi, and B=Nb, Ta, Sb), where the B-site atom is placed inside an octahedron formed by six oxygen atoms and A-site atom connects to six oxygen atoms as well.

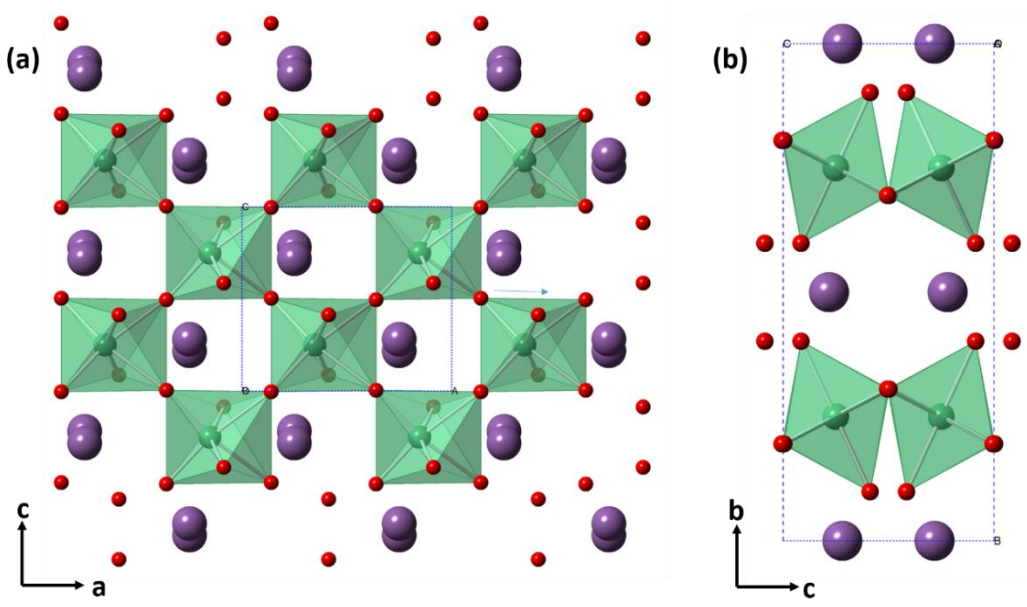


Fig. 2.2.1 Schematic of α-$BiNbO_4$ structure showing (a) $NbO_6$ octahedral network along *ac* plan; (b) the $NbO_6$ octahedral layers separated by Bi layers (green atoms denote Nb, purple atoms denote Bi and red atoms denote oxygen).

The Nb-O octahedra in the α-$BiNbO_4$ are connected by four corners along *ac* plane, as shown in Fig 2.2.1a. The Bi atom forms distorted octahedra with oxygen atoms in an edge sharing connection along a direction. The octahedral layers are separated by Bi layers in the *b* direction (Fig. 2.2.1b).

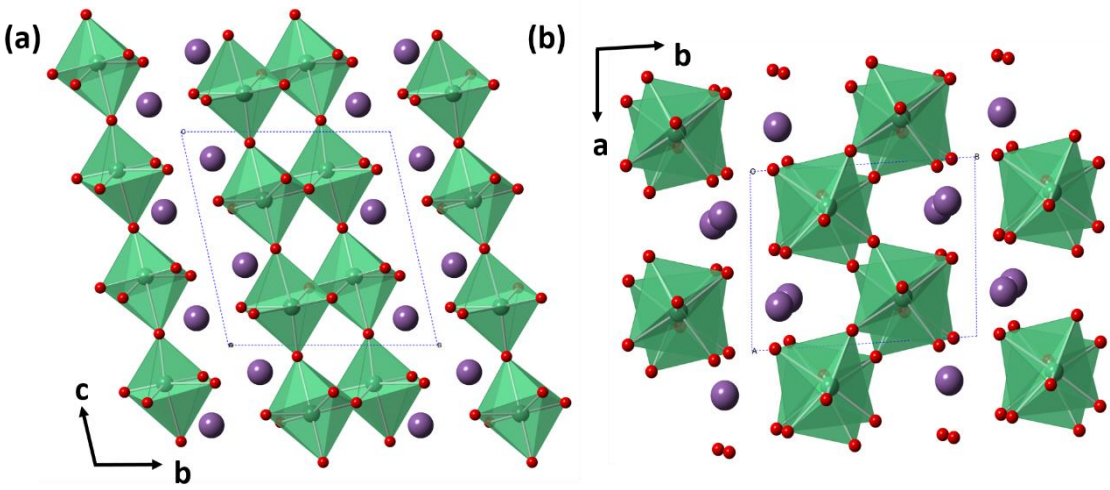


Fig. 2.2.2 Schematic of the β-$BiNbO_4$ structure showing (a) two-layers of $NbO_6$ octahedra joined by four vertices with two adjacent free atoms in *bc* plane; (b) the $NbO_6$ octahedra layers separated by Bi layers (green atoms denote as Nb, purple atoms denote as Bi and red atoms denote as oxygen).

The triclinic phase, referred to as the β phase, exhibits a centrosymmetric *P*-1 space group and is always formed above 1050°C. The cell dimension is *a*=7.61 Å, *b*=5.53 Å, *c*=7.91 Å, α=89.88°, β=77.43°, γ=87.15° and Z=4 [20]. The structure of the β phase is totally different from that of the α phase. Fig. 2.2.2 illustrates the structure of the β phase as octahedra joined by four vertices with another two adjacent oxygen atoms. This type of structure was first reported in the β-$BiNbO_4$. The Bi atom forms a distorted square antiprism with the nearest eight oxygen atoms [20].

### 2.2.2 Vibration spectra of $BiNbO_4$

The vibrational characteristics of the α-$BiNbO_4$ have been studied based on Raman scattering and Infrared absorption [78]. Raman activity modes refer to the modes by which the electron polarizability can be changed during vibration. Infrared activity modes refer to the modes by which the molecular dipole moment can be changed during vibration. The α-$BiNbO_4$ belongs to the *Pnna* ($D_{2h}^6$) structure, thus it is expected to have four $Bi^{3+}$ cations occupying $C_2^z$ sites and four $Nb^{5+}$ cations occupying $C_2^x$ sites and $O^{2-}$ ions occupying $C_1$ sites [78]. The optical phonons can be classified as:

$$\Gamma=8A_g+8A_u+9B_{1g}+8B_{1u}+10B_{2g}+9B_{2u}+9B_{3g}+8B_{3u}$$

All the *gerade* modes are Raman active while all the *ungerade* modes except $A_u$ are Infrared active [78]. Table 2.2.1 lists the vibrational spectrum of $BiNbO_4$ and the assignment of the observed peaks to the symmetry species of $NbO_6$ octahedra [78].

The vibrational spectrum includes the vibrations within the $NbO_6$ octahedra and vibrations between cation and octahedra. The vibrations in $NbO_6$ octahedra can be classified as: i) two pure bond-stretching vibrations ($A_{1g}$+$E_g$), ii) two inter bond angle-bending vibrations ($F_{2g}$+$F_{2u}$), and iii) a remaining $F_{1u}$ mode with a combination of vibration types Fig. 2.2.3 shows the correlations of vibration spectra in the α-$BiNbO_4$ [78]. The $A_{1g}$ ($\nu_1$) stretching mode is at *ca.* 620 $cm^{-1}$. The $E_g$ ($\nu_2$) stretching mode is at *ca.* 540 $cm^{-1}$. The $F_{2g}$ ($\nu_5$) bending mode is at *ca.* 270 $cm^{-1}$. The $F_{1u}$ ($\nu_3$) stretching mode appears at *ca.* 600 $cm^{-1}$ and $\nu_4$ bending mode at *ca.* 350 $cm^{-1}$. The $F_{2u}$ ($\nu_6$) mode locates in low frequency region (190-200 $cm^{-1}$).

Table 2.2.1 Vibration spectra of α-$BiNbO_4$ and assignment of observed peaks to the symmetry species of $NbO_6$ octahedra [78]

(s=strong, m=medium, w=weak, b=broad, sh=shoulder, db=doublet, v=very)

| Frequency of Raman active modes [$cm^{-1}$] | Frequency of Infrared active modes [$cm^{-1}$] | Symmetry assignment |
|---|---|---|
| | 28 w-m | |
| 60 s | 35 w-m | |
| 84 s | 83 m | |
| 93 w | | |
| 108 m, db | 120 m | |
| 110 m, db | | |
| 139 vs | 130 m | |
| 153 vs | 156 vs | |
| | 165, 174 db | |
| 199 m | 198 m | $F_{2u}$ ($\nu_6$) |
| 220 w-m | 208 m | |
| 255 m | 232 s | |
| 272 s | | $F_{2g}$ ($\nu_5$) |
| | 289 s | |
| 336 m-s | 328 w, sh | |
| | 347 sh | |
| | 356 vs | $F_{1u}$ ($\nu_4$) |
| 368 m-s | 374 w, sh | |
| 382 w | | |
| 424 w | 422 m | |
| | 433 m | |
| | 442 m | |
| 537 w-m | | $E_g$ ($\nu_2$) |
| | 580 vs, vb | $F_{1u}$ ($\nu_3$) |
| 624 vs, b | | $A_{1g}$ ($\nu_1$) |
| | 642 s, b | |
| 730 w | 716 s,b | |
| 883 w | | |

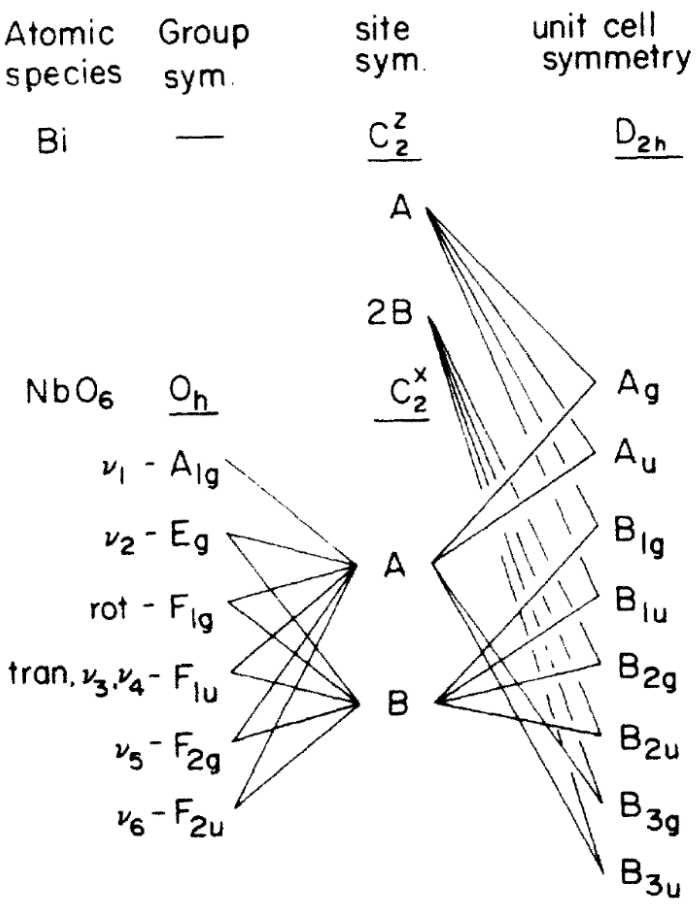


Fig. 2.2.3 Correlations of $BiNbO_4$ vibration spectra [78].

The vibrational spectrum of the β-$BiNbO_4$ has barely been studied. Yu *et al.* [79] accidently obtained the polarized Raman spectroscopy of the β-$BiNbO_4$ single crystal. Table 2.2.2 lists the vibration modes of X(ZZ)Y, X(YX)Y, X(ZX)Y geometries and nonpolar Raman spectrum of the β-$BiNbO_4$ single crystal [79]. Scattering geometry X(YX)Y, for example, represents that the polarized radiation comes from the X-direction with an electric vector vibrating parallel to the Y-axis, while the Raman scattering is observed in the Y-direction with a polarization along X-direction [80].

Table 2.2.2 Vibration modes of X(ZZ)Y, X(YX)Y, X(ZX)Y geometries and nonpolar Raman spectrum of the β-$BiNbO_4$ single crystal [79]

| X(ZZ)Y $cm^{-1}$ | X(YX)Y $cm^{-1}$ | X(ZX)Y $cm^{-1}$ | Nonpolar Raman $cm^{-1}$ |
|---|---|---|---|
| 51 | 50 | 49 | 51 |
| 60 | 62 | 60 | 63 |
| | 73 | 73 | 75 |
| 91 | 92 | 91 | 92 |
| 101 | 101 | 101 | 103 |
| 119 | 119 | 117 | 120 |
| 134 | 132 | 132 | 134 |
| 157 | 155 | 153 | 157 |
| 176 | 178 | 175 | 176 |
| 198 | 202 | | |
| 216 | 219 | 218 | |
| 236 | 238 | 234 | 240 |
| 249 | 252 | | |
| 270 | 270 | 270 | 270 |
| 291 | 292 | 291 | 291 |
| 305 | 307 | | 307 |
| 325 | 325 | 324 | 323 |
| 358 | 356 | 355 | 359 |
| 381 | 387 | | 390 |
| 422 | 420 | 419 | 420 |
| 453 | 453 | 451 | 452 |
| 485 | 483 | 488 | 483 |
| 527 | 519 | 518 | 519 |
| 609 | 605 | 606 | 610 |
| 688 | 688 | 687 | 691 |
| 891 | 891 | 892 | 891 |

### 2.2.3 Antiferroelectricity of $BiNbO_4$

Popolitov *et al.* [81, 82] studied the temperature dependence of the dielectric properties of α-$BiNbO_4$ single crystal and ceramics. It is reported that a loss peak at 360 °C and a permittivity peak at 570 °C as a function of temperature were found in single crystal, as shown in Fig. 2.2.4 [82]. The temperature dependent of the dielectric properties of α-$BiNbO_4$ ceramics showed a slight relaxation behavior with the peak shifting towards higher temperature at higher frequency. It is explained as the contribution of relaxation component to the overall polarization.

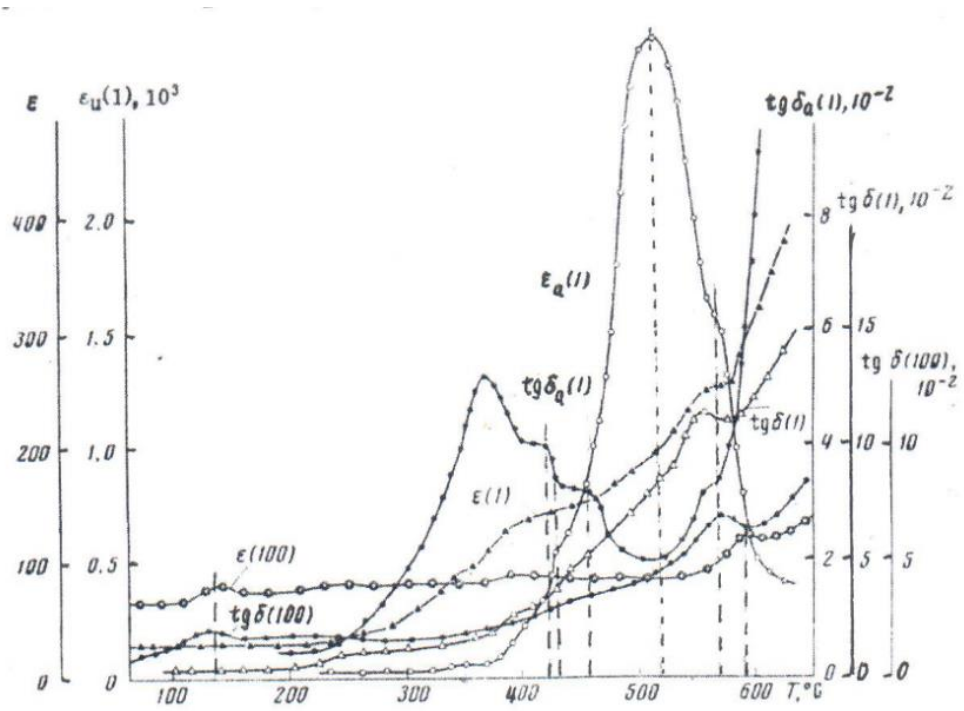


Fig. 2.2.4 Temperature dependence of dielectric properties for the α-$BiNbO_4$ single crystal and ceramics. The presented $\varepsilon_a(1)$ and $tg\delta_a(1)$ are relative to single crystal in [100] direction at 1 kHz frequency; the ε(1) and tgδ(1) were obtained on a ceramic sample at 1 kHz frequency; the ε(100) and tgδ(100) were obtained from a ceramic sample at 100 kHz frequency [82].

It has been mentioned that unsaturated polarization-electric field hysteresis loop was generated between 360 °C and 570 °C which were regarded as an evidence of a possible ferroelectric or ferrielectric state. However, the hysteresis loops were not presented. Additionally, the temperature dependence of second harmonic generation failed to prove the existence of ferroelectric phase because the signal intensity dropped out of the instrument sensitivity from 360 °C to 570 °C [82]. However, from this study [70] it was concluded that the α-$BiNbO_4$ is antiferroelectric at room temperature and it transforms into ferroelectric at 360 °C and to a paraelectric phase at 570 °C.

More research has been carried out on the other compounds in stibotantalite structure family, such as $SbNbO_4$ and $BiTaO_4$, to further understand their intrinsic electrical nature [22, 81, 83]. The $SbNbO_4$ compound has been demonstrated as ferroelectric with polarization along the *c* axis using structure analysis and electrical properties measurements [83]. The temperature dependence of dielectric properties of $SbNbO_4$ revealed a permittivity peak and a loss shoulder at 410 °C and 605 °C, respectively. Meanwhile, temperature dependent second harmonic generation test showed intense signal below 410 °C with a subsequently dramatic drop to 20-fold diminution. It was then deduced that ferroelectric $SbNbO_4$ transformed to antiferroelectric at 410 °C and to paraelectric at 605 °C [22]. The $BiTaO_4$ is isostructural to the $BiNbO_4$, in which similar phase transitions at 360 °C and 570 °C were observed in temperature dependence dielectric measurement. As a result, the $BiTaO_4$ is anticipated to be an antiferroelectric as well. Table 2.2.3 lists the polar state of stibotantalite compounds at variable temperatures [22].

Table 2.2.3 Polar state of stibotantalite compounds [22]

| Single crystals | Temperature region (°C) | State |
|---|---|---|
| $SbNbO_4$ | Below 410 | Ferroelectric |
| | 410-605 | Antiferroelectric |
| $SbTaO_4$ | Below 400 | Ferroelectric |
| | 400-600 | Antiferroelectric |
| $BiNbO_4$ | 20-360 | Antiferroelectric |
| | 360-570 | Ferroelectric |
| $BiTaO_4$ | 20-360 | Antiferroelectric |
| | 360-570 | Ferroelectric |
| $SbSbO_4$ ($Sb_2O_4$) | 20-560 | Antiferroelectric |
| $BiSbO_4$ | 20-550 | antiferroelectric |

Even though various phase transitions were observed within the compounds of stibotantalite family, more efforts should be taken to further verify the existence of antiferroelectricity. Ayyub *et al.* [84] studied the polarization-electric field hysteresis loops in the α-$BiNbO_4$ thin film. Ferroelectric hysteresis loops were observed with a film thickness below 240 nm while double hysteresis loops were observed in films with a thickness above 600 nm. Fig. 2.2.5 shows the ferroelectric hysteresis loops of films at a thickness of 240 nm and antiferroelectric hysteresis loop at a thickness of 900 nm [85]. It was suggested that the α-$BiNbO_4$ is antiferroelectric and the appearance of the ferroelectric hysteresis loop was related to the interfacial pinning effect by the semiconductor substrate [86]. However, the current-electric field loops have not been

provided to support the existence of the antiferroelectric or ferroelectric state. The antiferroelectricity nature of the α-$BiNbO_4$ is still an open question and until now, double hysteresis loop has not been found in ceramics.

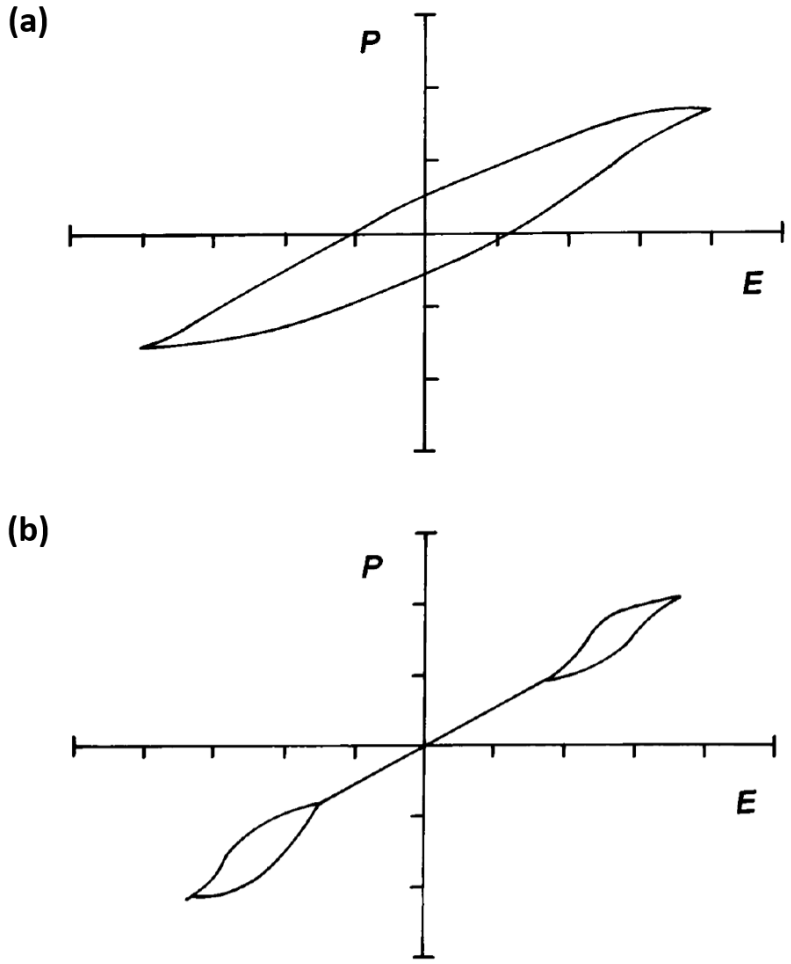


Fig. 2.2.5 Polarization-electric field hysteresis loops for the α-$BiNbO_4$ films with a film thickness of (a) 240 nm (each division -41.6 kV $cm^{-1}$ along x and 28.0 μC $cm^{-2}$ along y) and (b) 900 nm (each division -2.2 kV $cm^{-1}$ along x and 28.0 μC $cm^{-2}$ along y) [85].

Keve *et. al* presumed that the centrosymmetric β-$BiNbO_4$ was also antiferroelectric [20]. It is considered that the β-$BiNbO_4$ shared the same structure prototype with that of the $BaMnF_4$. Both of them are made of corner sharing octahedra, with two free adjacent B-

site atoms connected to one A-site atom only [20, 87, 88]. The $NbO_6$ octahedra are connected as -O-Nb-O-Nb- chains in the β-$BiNbO_4$, while the $MnF_6$ are linked by a lattice translation. Pyroelectric $BaMnF_4$ has a polarization direction along *a* axis, which cannot be reversed by the external field [87, 88]. The atom arrangement in $BaMnF_4$ is shown in Fig. 2.2.6.

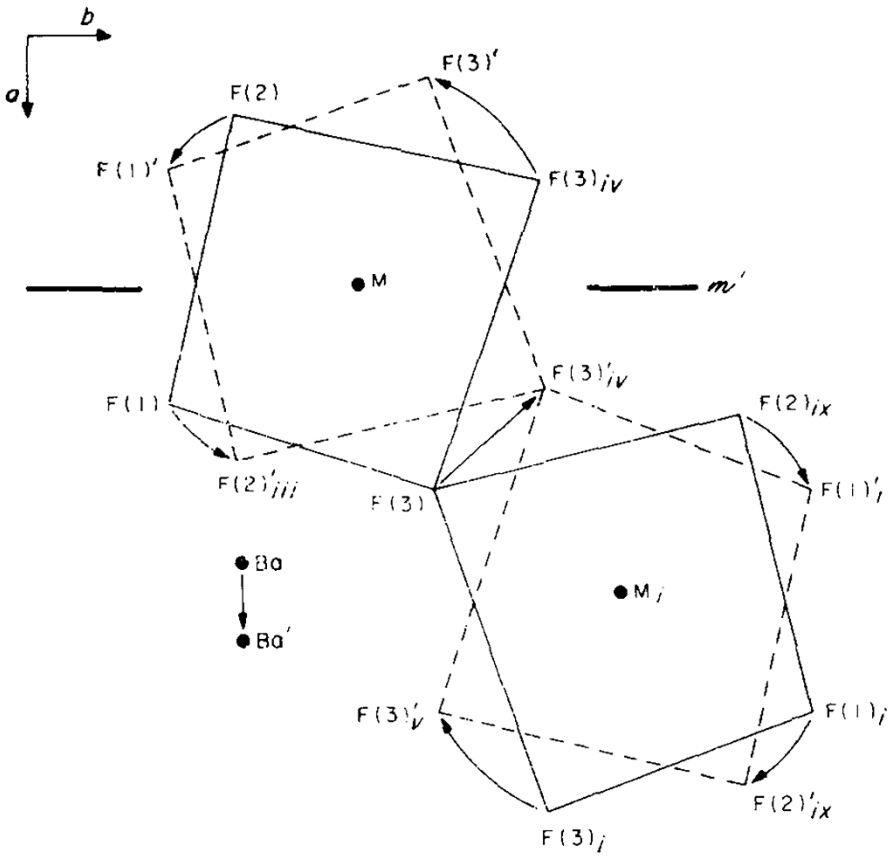


Fig. 2.2.6 Atom arrangement of $BaMnF_4$. The solid lines join fluorine atoms (x,y,z) and the broken lines join the primed atoms (1-x,y,z). The two sets are related by a mirror plane m'. The arrows represent the atom translations required to reverse the polarity [89].

In $BiNbO_4$ which can be constructed with the same prototype, the polarization direction should be alternate in adjacent unit cells along the *c*-axis to satisfy its centrosymmetric characteristics; as a consequence, the β-$BiNbO_4$ matched the

definition of an antiferroelectric material [20, 88]. Despite of the structure assumption, no other structural evidence or dielectric properties have ever been provided to support its antiferroelectric nature.

### 2.2.4 Phase transitions in $BiNbO_4$

The α-$BiNbO_4$ is synthesized below 1000 °C and the β-$BiNbO_4$ is formed above 1050 °C, thus it is considered that the α phase could transform to the β phase by heating. However, Keve *et al.* convinced that the β phase could not be transformed back to the α phase by heating once it is generated, due to its lower symmetry and denser atom packing [20, 77, 90].

In recent research, Zhou *et al.* [21] reported that the β to α phase transformation was reversible in bulk by heat treatment at a temperature range of 700 °C to 1030 °C (Fig. 2.2.7). Such transition could not be observed in powder as the transition was suggested to be favored by internal stresses. The longer dwelling time would also favor the transformation. However, the bulk prepared by Zhou *et al.* was actually crushed ceramic powder which technically can only be regarded as a powder form instead of bulk (ceramic).

Subsequently, Zhai *et al.* [91] synthesized the β phase powder at 700 °C and 1050 °C separately by a citrate method. The powder calcined at 700 °C is named as low-temperature β phase and the powder calcined at 1050 °C is named as high-temperature β phase. The powder synthesized between 900 °C and 1040 °C was identified as the α phase. The powder produced at 850 °C was a combination of the β phase and the α phase, which indicated the existence of a transition between low-

temperature β phase and the α phase. The low-temperature β phase to the α phase transition was also observed by annealing low-temperature β phase powder at 1000 °C. However, such transformation was not obtained in the high-temperature β phase powder. The phase transition between the low-temperature β phase and the α phase is assumed to be related to the thermodynamically metastable state of the low-temperature β phase and the grain size effect.

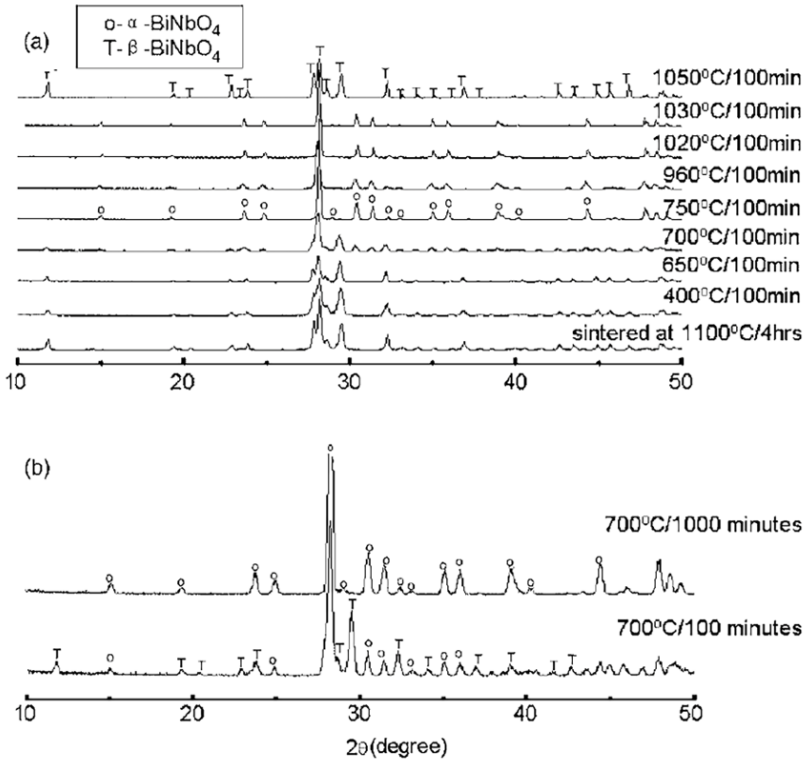


Fig. 2.2.7 XRD of crushed $BiNbO_4$ ceramics (a) annealed at different temperatures for 100 min; (b) annealed at 700 °C for 100 min and 1000 min.

A high pressure and high temperature study has been carried out by Xu *et al.* [92]. Both the α and β phase $BiNbO_4$ could be converted to a new high pressure phase (HP-$BiNbO_4$) with a pressure above 3 GPa. The transformation temperature is pressure dependent. The relationship of the α phase and β phase to HP phase under different

pressure and annealing temperature is sketched in Fig. 2.2.8. Meanwhile, this HP phase could be converted back to the α phase and the β phase at 730 and 1040 °C, respectively [93].

The phase transitions in $BiNbO_4$ are still under debate and the transition mechanisms have not been completely understood. Further research is needed to clarify the phase relationships in the $BiNbO_4$.

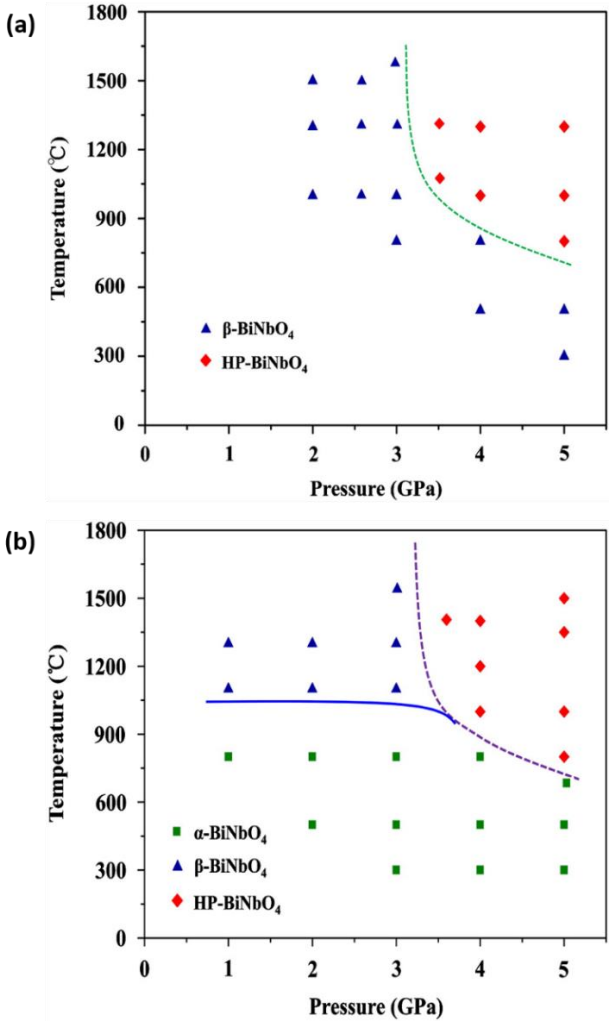


Fig. 2.2.8 Pressure and annealing temperature dependent phase transition of (a) β-$BiNbO_4$ to HT-$BiNbO_4$; (b) α-$BiNbO_4$ to HT-$BiNbO_4$ and β-$BiNbO_4$ [92].

### 2.2.5 Discovery of the new γ phase in $BiNbO_4$

Sleight *et al.* in 1975 [94] studied the high temperature stability of the β-$BiNbO_4$ and β-$BiTaO_4$, using high temperature X-ray diffraction (HTXRD) and differential thermal analysis (DTA). DTA transition peaks were observed in the β-$BiTaO_4$ at temperatures of 740 °C on heating and 715 °C on cooling. Similar transitions were observed in β-$BiNbO_4$ at a temperature of 1009 °C on heating and 1002 °C on cooling. High temperature XRD identified the phase transformations in the $BiTaO_4$ and a high temperature γ phase was discovered. The cell dimension of the γ-$BiTaO_4$ was *a*=7.681 Å, *b*=5.627 Å, *c*=7.749 Å, α=90°, β=78.55°, γ=90°. The structure is assumed to be isostructural to monoclinic $LaTaO_4$, whose lattice parameters are *a*=7.651 Å, *b*=5.577 Å, *c*=7.823 Å, α=90°, β=78.48°, γ=90°. However, no structure information has been reported for γ-$BiNbO_4$. Meanwhile, no more efforts have been made to further study the high temperature γ phase of $BiTaO_4$ and $BiNbO_4$.

## 2.3 Incipient ferroelectric: $TiO_2$ (rutile)

### 2.3.1 Basic structure of $TiO_2$

Titanium oxide $TiO_2$ can exist in three structural forms, namely, anatase, brookite and rutile. Anatase and brookite are low temperature phases that can be irreversibly transformed into the rutile phase in the temperature range 700 °C -920 °C [95]. Rutile owns the highest permittivity among the three forms. This is the reason why it is predominantly discussed in the current work. Rutile phase $TiO_2$ has a tetragonal structure with a space group $P\,4_2/mnm$. The cell dimension is $a$=$b$=4.59 Å, $c$=2.96 Å and Z=2 [96]. The theoretical density is 4.23 g $cm^{-3}$. It has a di-tetragonal and bi-pyramid body centered structure as illustrated in Fig. 2.3.1.

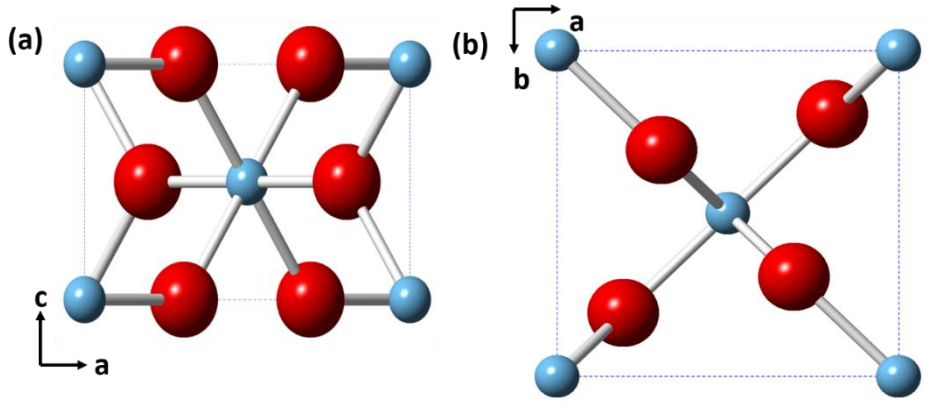


Fig. 2.3.1 Schematic of the rutile structure (a) *b* direction; (b) *c* direction (blue atoms denote Ti and red atoms denote oxygen).

### 2.3.2 Vibration spectra of $TiO_2$

The vibration modes of the rutile $TiO_2$ have been calculated based on the $D_{4h}^{14}$ - $P\,4_2/mnm$ space group [97]. The optical phonons can be classified as:

$$\Gamma=1A_{1g}+1A_{2g}+1A_{2u}+1B_{1g}+1B_{2g}+2B_{1u}+1E_g+3E_u$$

Four vibration modes ($A_{1g}$, $B_{1g}$, $B_{2g}$, $E_g$) are Raman active [98] and two vibration modes ($A_{2u}$, $E_u$) are Infrared active [99], as classified in Table 2.3.1.

Table 2.3.1 Classification of vibration modes of Rutile $TiO_2$ [97, 100]

| Vibration mode | Degree of freedom | | Number of vibration | Optic activity | Vibration frequency ($cm^{-1}$) |
|---|---|---|---|---|---|
| | Ti site | O site | | | |
| $A_{1g}$ | 0 | 1 | 1 | Raman active | 614.52 |
| $A_{2g}$ | 0 | 1 | 1 | Inactive | |
| $B_{1g}$ | 0 | 1 | 1 | Raman active | 141.18 |
| $B_{2g}$ | 0 | 1 | 1 | Raman active | 819.15 |
| $E_g$ | 0 | 1 | 1 | Raman active | 466.28 |
| $A_{2u}$ | 1 | 1 | 1 | Infrared active | 797 |
| $B_{1u}$ | 1 | 1 | 2 | Inactive | |
| $E_u$ | 2 | 2 | 3 | Infrared active | 189; 377; 491 |

Each Raman vibration mode has been illustrated in Fig. 2.3.2 [98]. The $E_g$ mode, as a double degenerated mode, has been interpreted in one possible state. A second-order Raman scattering was always obtained at *ca.* 240 $cm^{-1}$.

The Infrared spectrum with the scheme of each vibration mode is shown in Fig. 2.3.3 [100]. The $A_{2u}$ mode is of special interest because it consists of a displacement of Ti atom against O atom along *c* axis and considered as the soft mode for the incipient ferroelectric.

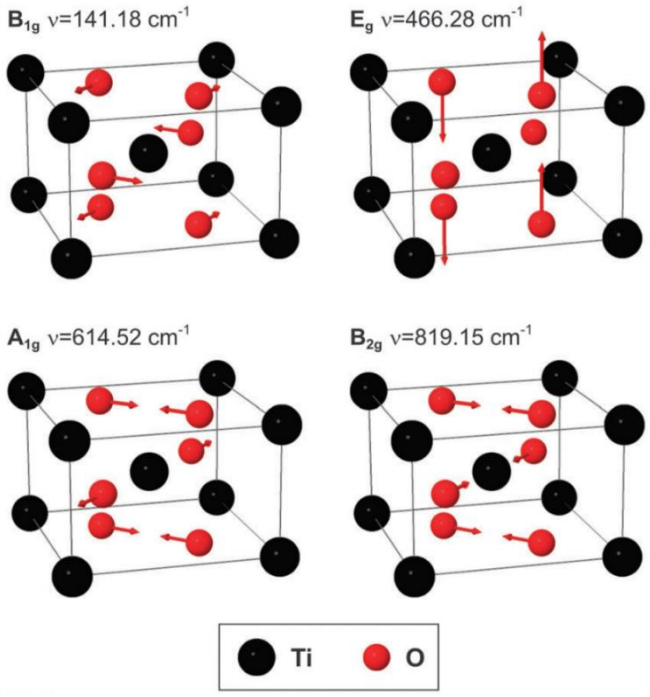


Fig. 2.3.2 Illustration of Raman vibration modes for rutile $TiO_2$. Arrows represent the amplitude and direction of the vibrations [98].

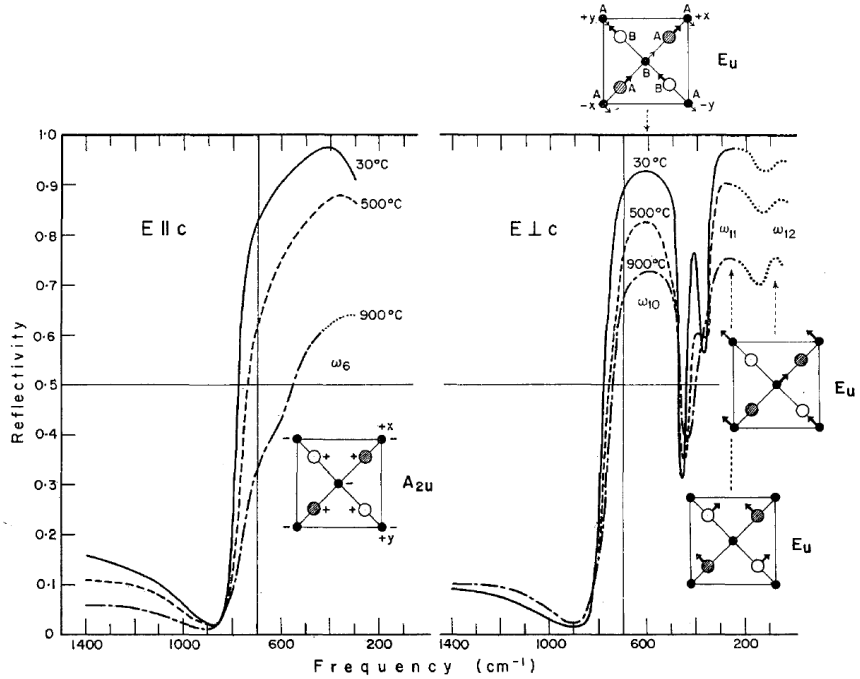


Fig. 2.3.3 Infrared spectroscopy of $TiO_2$ crystal with E∥*c* and E⊥*c* respectively. Infrared active vibration modes are illustrated with arrows indicating the vibration direction [100].

### 2.3.3 Non-stoichiometry of $TiO_2$

Pure $TiO_2$ is an insulator with a band gap of *ca.* 3 eV from a full 2*p*-band of $O^{2-}$ to an empty 3*d*-band of $Ti^{4+}$ [100]. However, the synthesis of $TiO_2$ is very sensitive to temperature and oxygen partial pressure. It is easily reduced to an oxygen-deficient non-stoichiometric $TiO_{2-x}$ (where x is the oxygen deficiency $O_d$) at high temperature and low oxygen partial pressure. The defects structure of reduced rutile, which acted as donor centers, have been extensively studied for decades, but are still under debate [101-105]. Two main types of defects as oxygen vacancy and Ti interstitials were proposed. The point defects are described , according to the Kröger-Vink notation [95], as shown in equations (2.3.1)-(2.3.3):

$$O_O^{\times} \Leftrightarrow V_O^{\cdot\cdot} + 2e' + \frac{1}{2}O_2 \quad (2.3.1)$$

$$Ti_{Ti}^{\times} + 2O_O^{\times} \Leftrightarrow Ti_i^{\cdot\cdot\cdot\cdot} + 4e' + O_2 \quad (2.3.2)$$

$$Ti_{Ti}^{\times} + 2O_O^{\times} \Leftrightarrow Ti_i^{\cdot\cdot\cdot} + 3e' + O_2 \quad (2.3.3)$$

The equilibrium constants $K_i$ of reactions (2.3.1) - (2.3.3) can be expressed as equation (2.3.4) to (2.3.6) [106].

$$K_1 = [V_O^{\cdot\cdot}]e'^2 p(O_2)^{1/2} \quad (2.3.4)$$

$$K_2 = [Ti_i^{\cdot\cdot\cdot\cdot}]e'^4 p(O_2) \quad (2.3.5)$$

$$K_3 = [Ti_i^{\cdot\cdot\cdot}]e'^3 p(O_2) \quad (2.3.6)$$

The relationship of the $V_O^{\cdot\cdot}$ , $\mathrm{Ti}_i^{\cdot\cdot\cdot}$ and $\mathrm{Ti}_i^{\cdot\cdot\cdot\cdot}$ concentration and the oxygen partial pressure can be deduced from the above defect equilibria, as shown in equation (2.3.7) – (2.3.9) [106].

$$[V_O^{\cdot\cdot}] = (\frac{1}{4}\mathrm{K}_1)^{1/3} p(\mathrm{O}_2)^{-1/6} \quad (2.3.7)$$

$$[\mathrm{Ti}_i^{\cdot\cdot\cdot\cdot}] = (\frac{1}{256}\mathrm{K}_2)^{1/5} p(\mathrm{O}_2)^{-1/5} \quad (2.3.8)$$

$$[\mathrm{Ti}_i^{\cdot\cdot\cdot}] = (\frac{1}{27}\mathrm{K}_2)^{1/4} p(\mathrm{O}_2)^{-1/4} \quad (2.3.9)$$

Indirect methods like electric conductivity measurement, thermoelectric power measurement and thermogravimetric measurement have been extensively carried out as a function of temperature and oxygen partial pressure on $TiO_2$ to study the defect structure.

Kofstad *et al.* [107] and Yahia *et al.* [108] found that the conductivity was proportional to $p(\mathrm{O}_2)^{-1/6}$, which suggested that the oxygen vacancies are the dominant source for the electrical conductivity, based on equation (2.3.7). It was also demonstrated that oxygen vacancies were the dominant defects at high oxygen pressure (>0.001 atm), while Ti interstitials dominated at low oxygen pressure (<0.001 atm) [108]. Haul *et al.* [109] proved the existence of oxygen vacancy by the $O^{18}$ labelled oxygen diffusion measurements.

However Blumenthal *et al.* [110] supported the Ti interstitials model at an oxygen partial pressure from 1 to $10^{-15}$ atm and a temperature from 1000 °C to 1500 °C. Hurlen *et al.* [101] pointed out that the arrangement of octahedral chains in rutile resulted in the

formation of an 'open' channel along *c* axis, as shown in Fig. 2.3.4. Meanwhile, there is a Ti interstitial site ($\frac{1}{2}$ 0 $\frac{1}{2}$) in the open channel, where the Ti atoms could easily place.

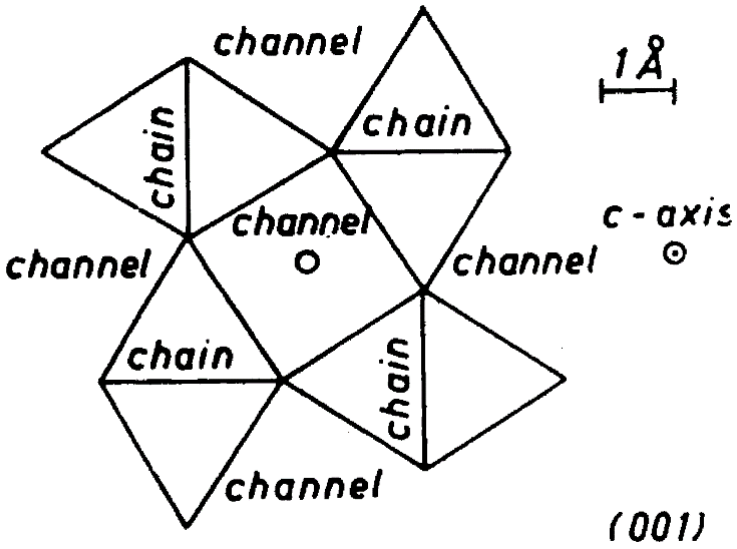


Fig. 2.3.4 The open channel surrounded by octahedral in rutile, with the circle in the channel represented Ti interstitial site [101].

The Ti interstitials were first identified by Chester *et al.* [111] using electron spin resonance (ESR). A paramagnetic center was detected at 2K within the liquid helium temperature range and termed '*A* spectrum'. The paramagnetic centers, such as well-known F-center, can be identified by *g* factor value. The appearance of *A* spectrum is shown in Fig. 2.3.5 [111]. It was explained using four possible models, namely (a) the $Ti^{3+}$ interstitial in ($\frac{1}{2}$ 0 $\frac{1}{2}$) site; (b) an electron trapped by $Ti^{4+}$ in lattice site; (c) an electron trapped by oxygen vacancies; (d) unidentified center that is related to the incorporation of hydrogen in rutile lattice when the sample was prepared in hydrogen atmosphere [111]. However, the *A* spectrum was found in four-fold, three-fold and two-fold multiplicity state when varying the angle between the magnetic field (*H*) and the *a* axis, as shown in Fig. 2.3.6 [111].

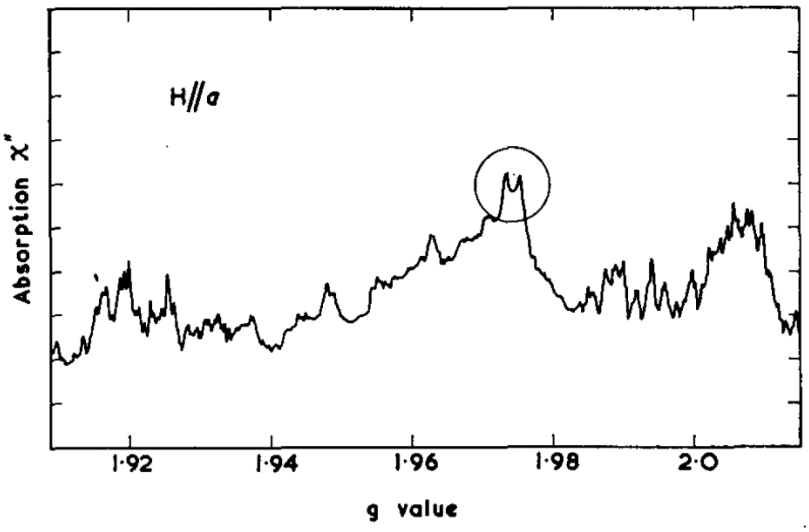


Fig. 2.3.5 The ESR spectrum of rutile crystal at 2K with *H*||*a*. The circle portion correlated to the *A* spectrum [111].

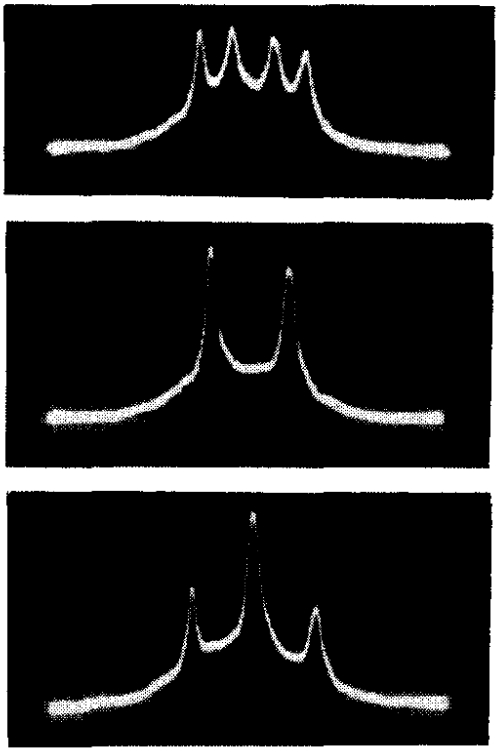

Fig. 2.3.6 The *A* spectrum observed in partially re-oxidized rutile crystal, *H*⊥*c*, 2.16K. The angle between *H* and the *a* axis are $\varphi$=9°, 0° and 18° from top to bottom, respectively [111].

Subsequently, Kingsbury *et al.* [112] and Hasiguti *et al.* [113] performed more detailed ESR investigation on rutile. The *A* spectrum was well explained as the $Ti^{3+}$ in the $(\frac{1}{2}\ 0\ \frac{1}{2})$ interstitial site. It is reported that the evidence of the four-fold multiplicity of the *A* spectrum (Fig. 2.3.6) excluded the above mentioned models *(b)* and *(c)*, which only gave two-fold multiplicity. Meanwhile, the *A* spectrum can be produced by interstitial-diffusion doping of Li and Na as well as hydrogen, which ruled out the model *(d)*. Yagi *et al.* [114] in 1977 further confirmed the existence of $Ti^{3+}$ interstitials in the open channel by channeling method. Fig. 2.3.7 showed the angular backscattering scan of Ti ions (Ti dip) in both oxidized $TiO_2$ and reduced $TiO_{2-x}$ [114].

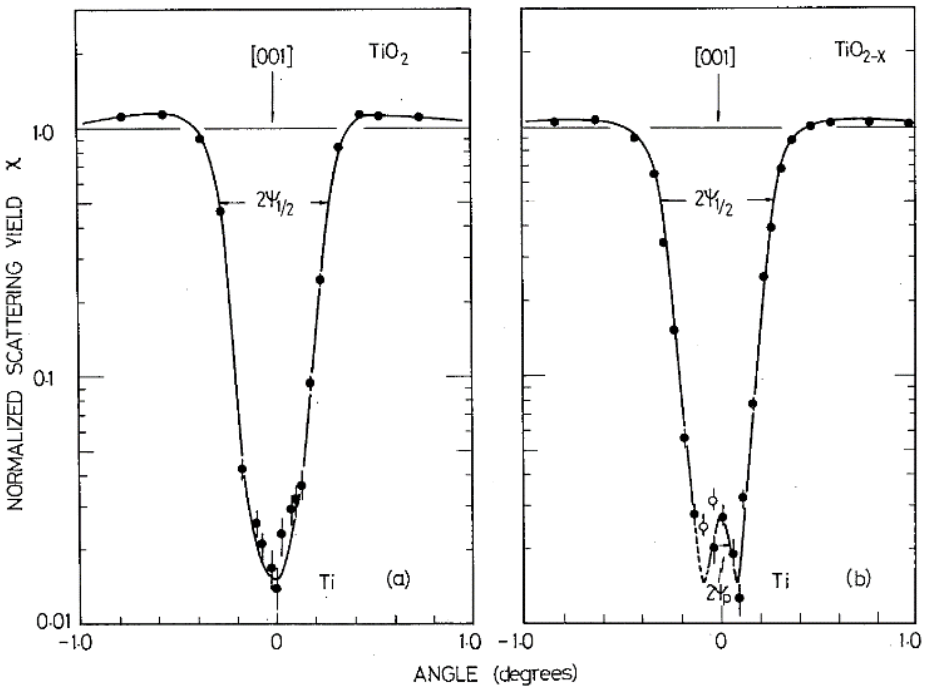


Fig. 2.3.7 The backscattering yield from Ti ion in (a) stoichiometric $TiO_2$; (b) reduced $TiO_{1-x}$ *vs.* the angle θ between the incident beam direction and *c* axis [114].

The channeled beam flux density would have a higher value with an incidence beam parallel to a main axis than that with a random direction. When the Ti atoms are

located in the interstitial sites in open channel where none of them were shadowed by other atoms, it would generate a peak with higher scattering yield with an incident direction along the *c* axis. The small peak observed in Ti dip at θ=0 indicated the existence of Ti interstitials.

Meanwhile, crystallography shear planes were observed in non-stoichiometric $TiO_2$. Defect clusters would be formed if the number of point defects increase. The collapse of the defect clusters could produce the crystallography shear planes. The point defects are eliminated by shear planes, when the apex-sharing is replaced by (a) edge-shearing and (b) edge-shearing is replaced by plane-shearing, as described in Fig. 2.3.8 [115].

Three basic models were proposed to explain the formation of crystallography shear planes based on oxygen vacancies elimination [115]. The schematic of three models are shown in Fig. 2.3.9.

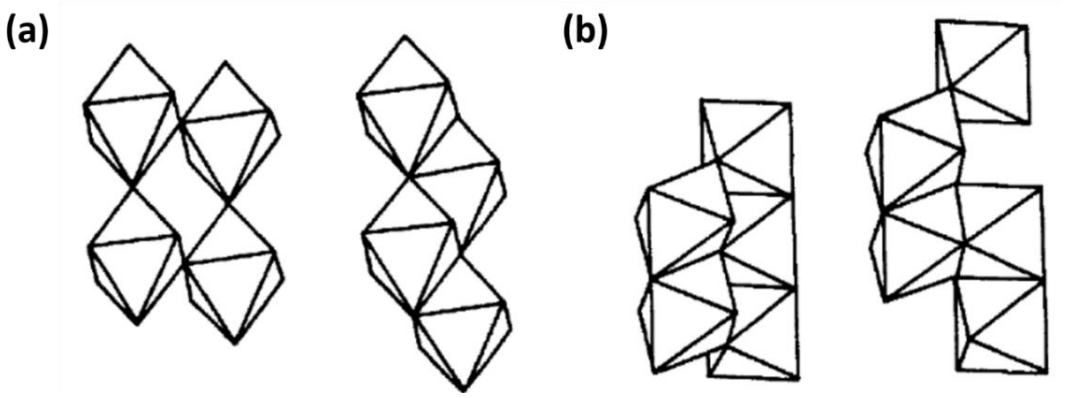


Fig. 2.3.8 The schematic of the formation of crystallography shear planes (a) replacing of apex-sharing by edge-shearing; (b) replacing of edge-shearing by plane-shearing [115].

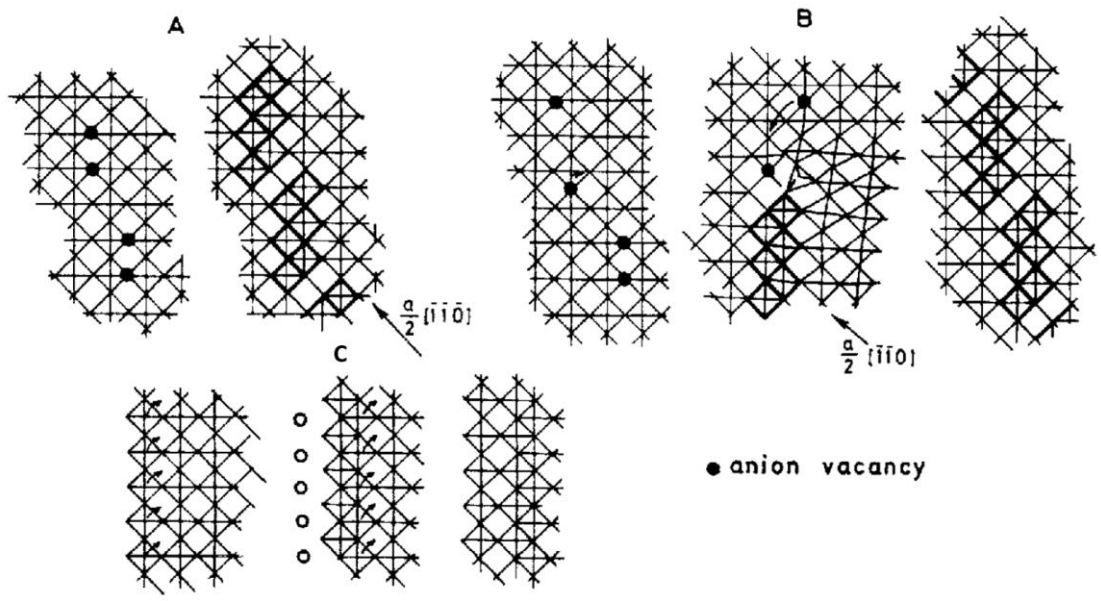


Fig. 2.3.9 Schematic shows the mechanism for the formation of crystallography shear planes (a) Gado model; (b) Anderson and Hyde model; (c) Anderson and Wadsley model [115].

Gado *et al.* suggested that the oxygen vacancies undergo an ordering of zigzag 'walls', where the crystals would shear across the walls to annihilate the vacant sites (Fig. 2.3.9a) [115]. Anderson and Hyde proposed a model that the oxygen vacancies would aggregate into disks and then collapsed to shear-plane nucleus, bounded by a dislocation loop. The shear plane would grow by trapping vacancies on loop (Fig. 2.3.9b) [115]. The third model was proposed by Anderson and Wadsley where a layer of oxygen atoms is removed and a sheet of cations is displaced co-operatively into adjacent interstitial sites to form a crystallography shear plane at the surface. The crystallography shear plane at the surface would then diffuse into the crystal by a series of repetitive steps [115]. However, all these three models are not perfect.

When crystallographic shear planes are highly ordered on a large scale, they would be regarded as the so called Magnéli phases, which are represented as $Ti_nO_{2n-1}$, where n represents the number of $TiO_6$ octahedra between two consecutive shear planes [116].

### 2.3.4 Dielectric properties of $TiO_2$

$TiO_2$ exhibits anisotropy permittivity ($\varepsilon_c$=170 and $\varepsilon_a$=86 at 300K) and low loss. The dielectric permittivity in ceramics is *ca.* 100 in microwave range [117]. The refractive index *n* can be as high as 2.903 and 2.616 along the *c* and *a* axis, respectively. It has a negative temperature coefficient of dielectric constant of $-8.2\times10^{-4}$ /°C. Two mechanisms have been proposed to explain the high permittivity of $TiO_2$. One theory is proposed by Frank [118], in which the high permittivity is correlated with the simultaneously large electronic and atomic polarizability, according to the Clausius-Mossotti equation (2.3.9).

$$\mathrm{p} = \mathrm{p}_e + \mathrm{p}_a = (\varepsilon - 1)/(\varepsilon + 2) \tag{2.3.9}$$

where $\mathrm{p}$ is the total polarizability, $\mathrm{p}_e$ is the electronic polarizability, $\mathrm{p}_a$ is the atomic polarizability and $\varepsilon$ is the dielectric constant. The other theory proposed by Eucken *et al.* [119] considered only the contribution from the high atomic polarization, based on the linear relationship between the dielectric constant and the polarizability derived by Born [120]. Berberich *et al.* [121] pointed out that great discrepancy would appear between these two theories when the dielectric constant of the compound is large.

Table 2.3.2 lists the dielectric constant and polarizability of several materials. The $TiO_2$ owns high electronic polarizability of 0.681 and relatively low atomic polarizability of 0.293. As is shown, $PbCl_2$ and LiF have higher atomic polarizability while the dielectric constants are much lower compared to Rutile. The dielectric constant can be expressed by equation (2.3.10) based on the reorganization of equation (2.3.9).

$$\varepsilon = \frac{3}{1-p} - 2 \quad (2.3.10)$$

A small variation of the total polarizability $p$ would lead to a large change in $\varepsilon$ when $p$ is close to 1. Thus, the high permittivity of rutile can be expected due to its highest overall polarizability, including a high electronic polarizability (high refraction index) and a normal atomic polarizability.

Table 2.3.2 Dielectric constant and polarizability for certain compounds

| compound | $\varepsilon$ | P | $\varepsilon_0$ | $p_e$ | $p_a$ |
|---|---|---|---|---|---|
| Rutile | 114 | 0.974 | 7.42 | 0.681 | 0.293 |
| Brookite | 78 | 0.963 | 6.97 | 0.667 | 0.296 |
| $PbCl_2$ | 33.5 | 0.915 | 4.94 | 0.568 | 0.347 |
| Anatase | 31 | 0.909 | 6.33 | 0.64 | 0.269 |
| LiF | 9.3 | 0.735 | 1.94 | 0.238 | 0.497 |

### 2.3.5 Incipient ferroelectricity of $TiO_2$

Incipient ferroelectrics (also named quantum paraelectrics) refer to a kind of materials with polar soft mode, but no ferroelectric phase transition [122]. The phase transition is inhibited due to the stabilization of paraelectric phase by quantum fluctuation effect [123]. The soft mode, comparing to that of ferroelectrics, would never become unstable and the dielectric constant would not vary in the quantum-mechanical regime ($kT \ll \hbar\Omega$, where k is the Boltzmann's constant and $\hbar\Omega$ is the quantum energy) [123], as shown in Fig. 2.3.10 [124].

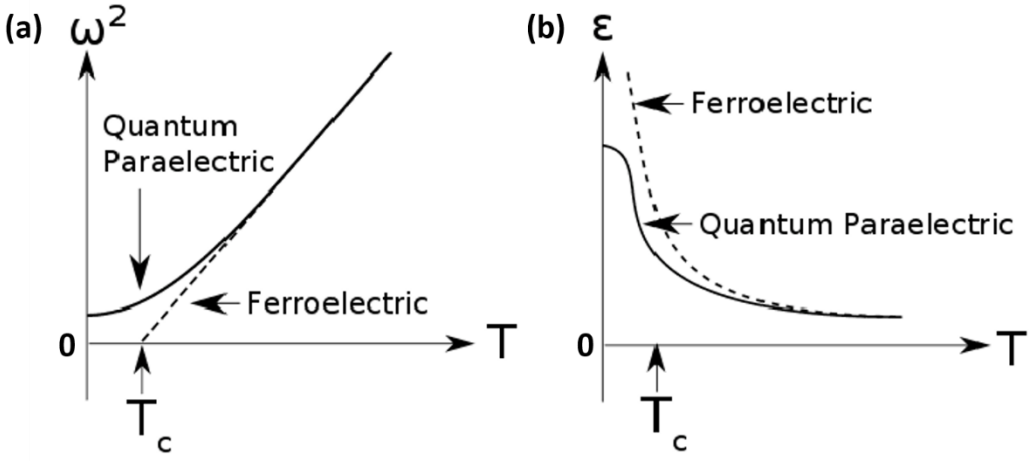


Fig. 2.3.10 Comparison between normal ferroelectric (dash line) and incipient ferroelectric (solid line) on (a) soft mode frequency as a function of temperature; (b) dielectric constant as a function of temperature [124].

The permittivity in the quantum-mechanical regime is stable because the ferroelectric fluctuations have been stabilized in paraelectric phase [123]. $SrTiO_3$ [125], $CaTiO_3$ [122], $KTaO_3$ [126], $TiO_2$ [127] are intrinsic incipient ferroelectrics. Their temperature dependent dielectric properties are shown in Fig. 2.3.11 [122]. The permittivity at room temperature and the maximum permittivity at low temperature are shown in Table 2.3.3 [122].

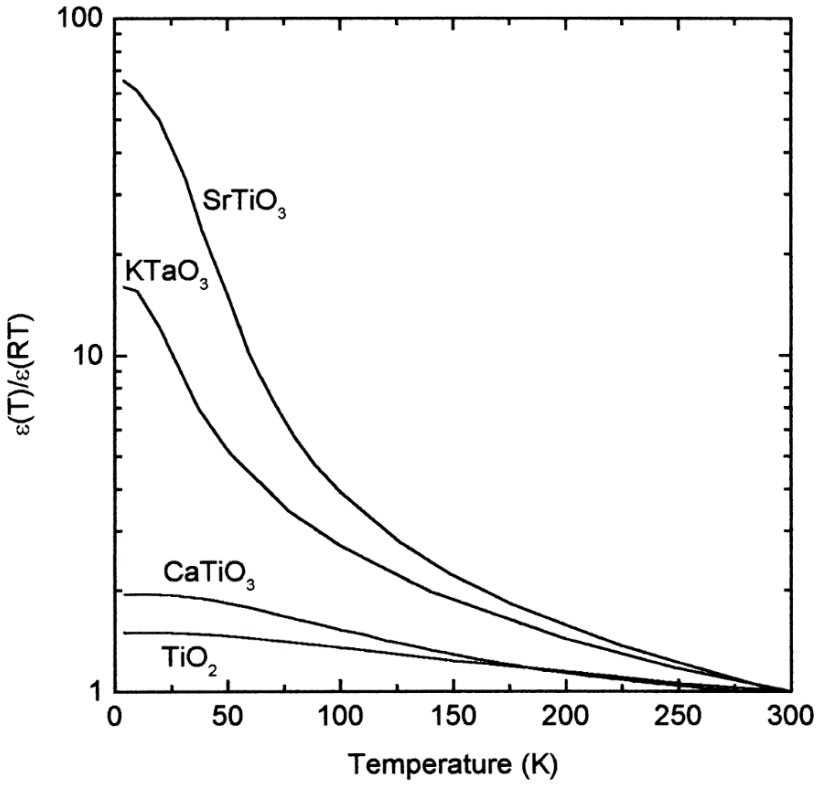


Fig. 2.3.11 The temperature dependent relative dielectric ε (T)/ε (RT) properties of $SrTiO_3$, $KTaO_3$, $CaTiO_3$, and $TiO_2$ ceramics [122].

Table 2.3.3 Room temperature permittivity ε (RT) and maximum permittivity $\varepsilon_{max}$ at low temperature [122]

| | $SrTiO_3$ | $CaTiO_3$ | $KTaO_3$ | $TiO_2$ |
|---|---|---|---|---|
| ε (RT) | 305 | 168 | 239 | 170 |
| $\varepsilon_{max}$ | 20 000 | 331 | 3840 | 251 |

## 2.4 Perspective of $TiO_2$ as high energy density storage capacitor

According to the equation (1.2.2), the volume energy density is governed by the electric breakdown field at a constant permittivity value. Higher electric breakdown field is expected to lead to high energy density. The rutile structured $TiO_2$ was selected due to its high electric breakdown strength (BDS) of *ca.* 350 kV $cm^{-1}$ and relative high permittivity of *ca.* 100 [128]. The BDS could be influenced by porosity, grain boundary, grain size and defect chemistry of dielectrics [129-131]. A reduced grain size would also improve BDS due to a higher grain boundary area-to-volume ratio. The defects contribute to the n-type behavior of $TiO_2$, would degrade dielectric properties and reduce the BDS [128].

Improved dielectric breakdown strength of 1400 kV $cm^{-1}$ could be expected in $TiO_2$ films with estimated energy density of 14 J $cm^{-3}$ [132]. However, as for commercial applications, $TiO_2$ ceramics require much lower cost and exhibit larger effective volume which is worthwhile developing as well. Efforts could be made to produce dense and high stoichiometric ceramics with minimum defects to enhance the electric breakdown strength.

# Chapter III. Experimental Process

## 3.1 Sample preparation

Powders with high purity were used as the raw materials. Table 3.1.1 lists all the powders used in the current work.

Table 3.1.1 Information on the raw materials

| Component | Purity | Manufacturer |
|---|---|---|
| $Bi_2O_3$ | 99.975% | Alfa Aesar |
| $Nb_2O_5$ | 99.9% | Alfa Aesar |
| $TiO_2$ | 99.7% | Aldrich |
| $TiO_2$ | 99.6% | Shantou, China |
| $Fe_2O_3$ | 99.9% | Alfa Aesar |
| $Sm_2O_3$ | 99.9% | Alfa Aesar |
| ZnO | 99.6% | Shantou, China |

The starting powders were weighed according to the stoichiometric formula of the final component and mixed using planetary ball milling machine (Nanjing machine factory, China). The Precursor powders were then put into a nylon pot with $ZrO_2$ balls in different size (5 mm and 10 mm in diameter) for mixing. Ethanol was used as the milling medium. The ratio of powders, ethanol and ball weight is about 1:2:3. Powders were mixed at a speed of 350 rpm for 4 h. Then the mixed powder was placed in a stainless steel pan and dried at 80 °C using a hot plate. The dried powder was sieved using a 250 μm (aperture diameter) stainless steel sieve to get finely ground powder.

The mixed powder was calcined using a muffle furnace (HTF1800, Carbolite) at an optimized temperature to get single phase material. A second ball milling was carried out at a speed of 350 rpm for 4 h to decrease the particle size. Ceramics were sintered using both sparking plasma sintering (SPS, HPD-25/1 FCT system GmbH) and solid state sintering using a box furnace (HTF1800, Carbolite).

The flow chart for the sample preparation is shown in Fig. 3.1.1.

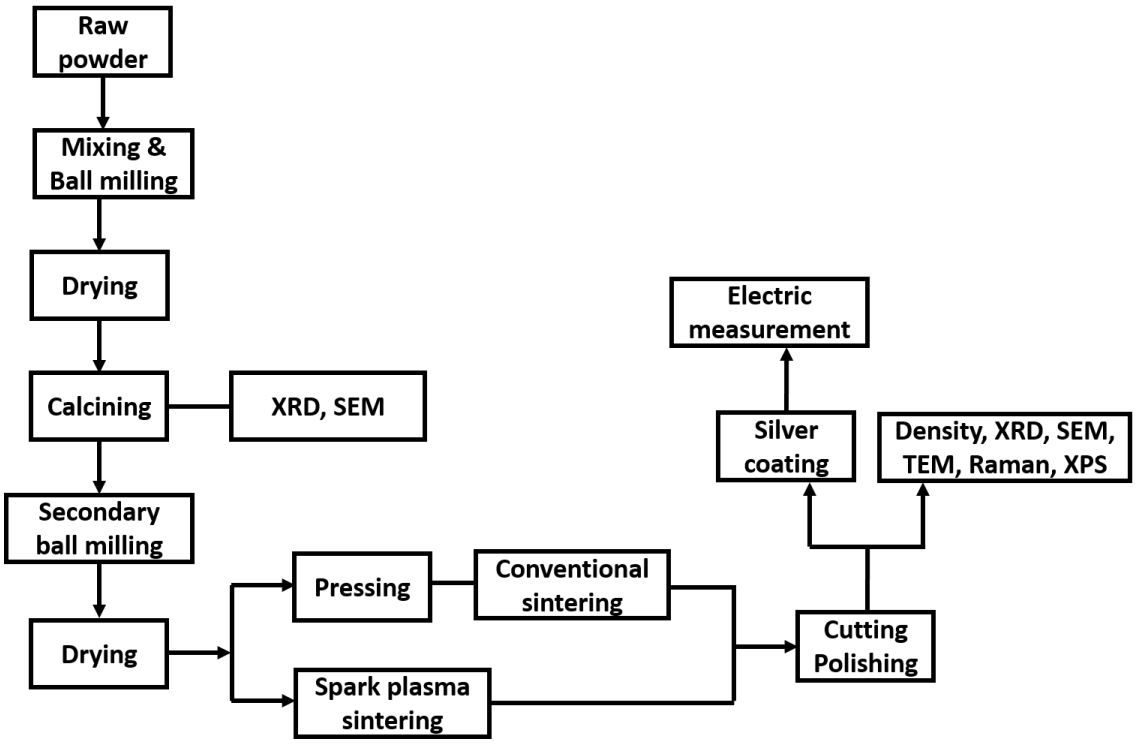


Fig. 3.1.1 Flow chart of the sample preparation.

## 3.2 Sintering methods

### 3.2.1 Solid state sintering

Solid state sintering, is one of the most applied conventional sintering method, due to its high output and simple processing procedure comparing to other methods. In this process that crystalline powder compact (green body) were densified in to a ceramic by heating. Sintering aids with low melting point could be used to fasten the sintering process, reduce the sintering temperature and densify the ceramics [1]. The driving force for the sintering is the reduction of the excess surface energy. The surface energy reduction can be fulfilled by both increasing the average grain size (coarsening) and eliminating the solid-vapor interfaces as well as creating grain boundary (densification) [1].

Sintering can be divided into three main stages. Fig. 3.2.1 displays the scheme of the three sintering stage [133].

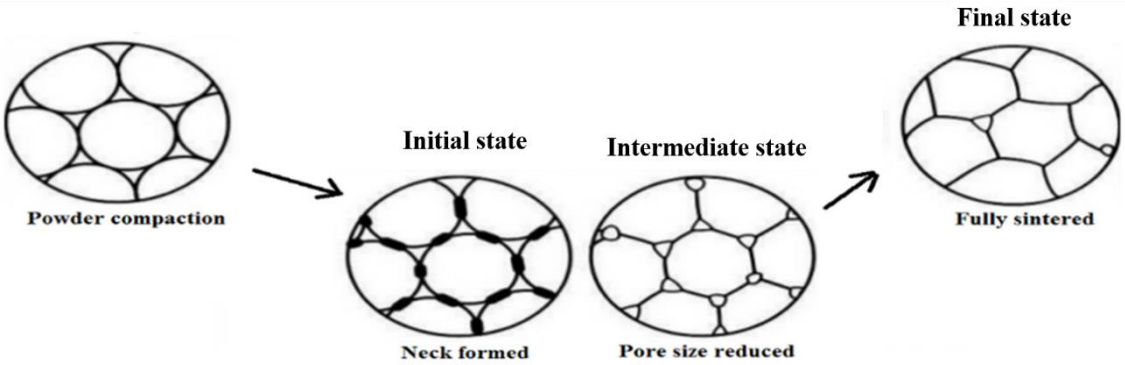


Fig. 3.2.1 The scheme of the three sintering stage during solid state sintering [133].

The initial stage involves a rapid growth of the inter-particle neck and the relative density of the ceramic can reach *ca.* 60-65%. The intermediate stage is characterized

by the smooth of the pore structure and the development of the interconnection among the pore structures. A relative density of 65%-90% can be achieved at this stage. The final stage is evidenced by the formation of the spherical and closed pores and grain growth. The continuous pore channel has been diminished and individual pores are located in either grain boundary or within the grains [1].

Although solid state sintering is of low cost, which is suitable for industrial production, it still suffers from several shortcomes. It is difficult to control the grain size and to avoid abnormal grain growth. The introduction of the sintering aids can be regarded as impurities and sometimes it could degrade the dielectric and electric properties of ceramics [134].

### 3.2.2 Sparking plasma sintering

Spark plasma sintering is a sintering method that utilizes pulsed DC current along with uniaxial pressure to consolidate powders [135]. The DC current is applied mainly to generate the required amount of resistive heat, while the spark or plasma has barely been observed so far [136]. Thus it is preferred to be named as field assisted sintering technique.

Fig. 3.2.2 shows the scheme of SPS equipment. The powder is placed in a graphite die between an upper and a bottom punch. The DC current is directly applied through the die, while high pressure is simultaneously applied on the punch against the powder to achieve high density [137].

SPS technique is capable of operating with high heating and cooling rate and requires short sintering time, which can be used to control the grain size and even preserve the initial powder grain size or nano structure [135]. Moreover, the lower sintering temperature can be achieved with the application of the high pressure, which is good for controlling the phase reactions and decomposition in the composites [135].

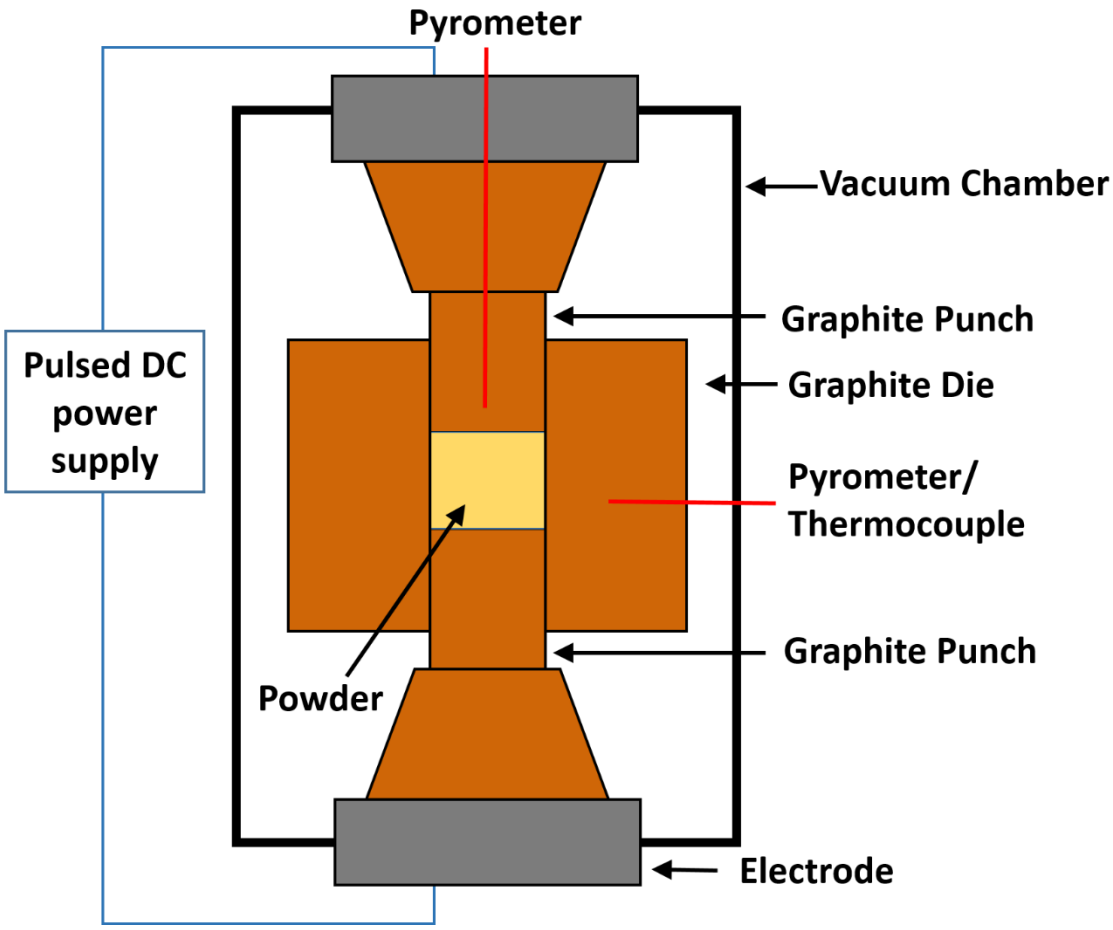


Fig. 3.2.2 The configuration of SPS equipment.

Moreover, SPS can fulfill a real time monitoring and adjusting all the operating parameters, such as pulse duration time, applied voltage, temperature and dwelling time [135]. Fig. 3.2.3 shows several operating parameters monitored during the SPS processing. The force can be applied at both room temperature and high temperature.

Normally it is preferred to apply to force at high temperature (as shown in Fig. 3.2.2a), as graphite exhibits an improved hardness with the increase of the temperature [138]. High pressure is effective to promote the plastic deformation of the particles in the last stage of sintering [135]. Sintering process can be optimized by monitoring of the relative piston traveling distance change (Fig. 3.2.2b) and piston speed variation (Fig. 3.2.2c), as information like when the green body starts sintering and how fast it shrinks and when the sintering process ends could be provided. The vacuum condition reveals the stability of the compound during the sintering processing and possibility of sample being volatilized or decomposed.

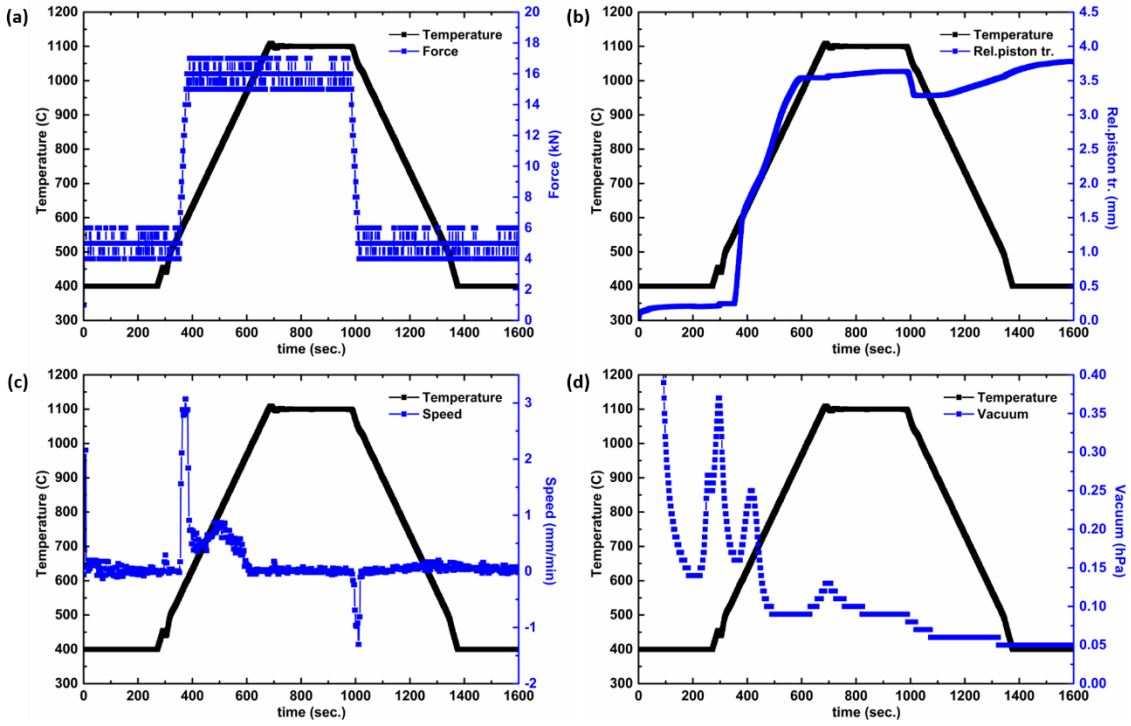


Fig. 3.2.3 The operating parameters monitored during the SPS processing (a) time vs. temperature and force; (b) time vs. temperature and relative piston traveling distance; (c) time vs. temperature and piston speed; (d) time vs. temperature and vacuum value.

## 3.3 Characterization

### 3.3.1 Density measurement

The density of the ceramics was measured by the Archimede's method. Dry samples were first weighed in air to obtain their weight $W_1$. The samples were then immersed in water where they experienced an upward Buoyancy force which equals the weight of the displaced liquid , as shown in equation (3.3.1) [139].

$$F_{float}=G=\rho_{liquid} \cdot g \cdot V_{displaced\ liquid} \quad (3.3.1)$$

and their Buoyancy weight $W_2$ was measured The density was then calculated based on Archimede's law shown in equation (3.3.2) [140].

$$d= (W_1 \times WDT)/(W_1-W_2) \quad (3.3.2)$$

Where WDT is the water density at room temperature.

The relative density (D) of the sample is shown in equation (3.3.3).

$$D=d/d_0 \times 100\% \quad (3.3.3)$$

Where $d_0$ is the theoretical density of the sample.

### 3.3.2 X-ray diffraction and neutron diffraction

X-ray diffraction (XRD, X'pert Pro, PANalytical, Almelo, Netherlands) is a common method to identify the structure of the sample. The crystal is formed of highly arranged atoms and the distance between these regularly arranged atoms (bond length) is in the same magnitude of the X-ray wavelength (Cu Kα= 1.54 Å). When a

beam of monochromatic X-ray diffracts in the crystal, the atomic lattice of the sample acts as a three dimensional diffraction grating, causing the X-ray beam to be diffracted at specific angles. Fig. 3.3.1 displays the schematic of X-ray diffracted from crystal lattice planes [141].

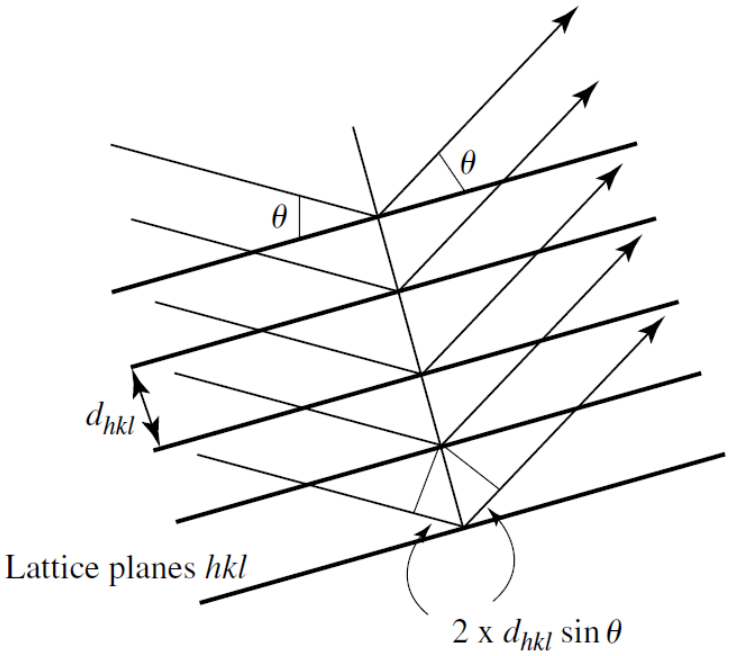


Fig. 3.3.1 The schematic of X-ray diffracted from crystal lattice planes [141].

The diffraction pattern, including the peak positions (angles), provides the specific information of the crystal according to Bragg Law (equation 3.3.4) [142]:

$$2d_{\mathrm{hkl}}\sin\theta = \mathrm{n}\lambda \qquad (3.3.4)$$

The angles are used to calculate the inter-planar atomic spacing ($d_{\mathrm{hkl}}$). The width of the diffraction peaks is used to determine crystallite size and micro-strain in sample.

Neutron diffraction method uses neutrons instead of X-ray to determine the structure. Neutrons are normally produced by nuclear reactor or spallation source. Neutrons

scatter from the atom nuclei while the X-rays or electrons scatter mainly from the electrons surrounding the nuclei. The advantage of neutron diffraction over X-ray diffraction is the sensitivity to light atoms like oxygen and hydrogen and the ability to distinguish isotopes and a penetration of several centimeters [143].

### 3.3.3 Rietveld method

Rietveld method, also known as the full pattern or full profile refinement, was proposed by Rietveld to determine the crystal structure [144]. The non-linear least squares minimization method is used in Rietveld method to calculate the theoretical line profile and to minimize the difference between theoretical and experimental profiles [145]. Non-linear least squares method requires reasonable initial free variables, like peak shape parameters, unit cell dimensions and coordinates of all the atoms, as starting structure model [145]. The minimized function is given in equation 3.3.5.

$$\Phi = \sum_{i=1}^{n} w_i \, (Y_i^{obs} - Y_i^{calc})^2 \qquad (3.3.5)$$

Where $w_i$ is the weight assigned to the $i^{th}$ data point; $Y_i^{obs}$ is the observed and $Y_i^{calc}$ is the calculated intensity of a point $i$ of the powder diffraction pattern; $n$ is the total number of measured data points [145].

In a practical refinement, the following least squares parameters are usually refined [145]. They are background parameters; sample displacement, zero-shift corrections; multiple peak shape function parameters (FWHM, asymmetry, etc.); cell dimension parameters; preferred orientation, absorption; Scale factor; atom positions of all

independent atoms; population parameters (when a certain site is partially occupied or co-occupied by different atoms) and atomic displacement parameters.

To quantify the quality of the fitting, figures of merit is introduced, including the profile residual factor ($R_p$); weighted profile residual ($R_{wp}$); Bragg residual ($R_B$); expected profile residual ($R_{exp}$) and the goodness of fit ($\chi^2$) [145].

$$R_p = \frac{\sum_{i=1}^{n} |Y_i^{obs} - Y_i^{calc}|}{\sum_{i=1}^{n} Y_i^{obs}} \times 100\% \quad (3.3.6)$$

$$R_{wp} = \left[\frac{\sum_{i=1}^{n} w_i (Y_i^{obs} - Y_i^{calc})^2}{\sum_{i=1}^{n} w_i (Y_i^{obs})^2}\right]^{1/2} \times 100\% \quad (3.3.7)$$

$$R_B = \frac{\sum_{j=1}^{m} |I_j^{obs} - I_j^{calc}|}{\sum_{j=1}^{m} I_j^{obs}} \times 100\% \quad (3.3.8)$$

$$R_{exp} = \left[\frac{n-p}{\sum_{i=1}^{n} w_i (Y_i^{obs})^2}\right]^{1/2} \times 100\% \quad (3.3.9)$$

$$\chi^2 = \left[\frac{R_{wp}}{R_{exp}}\right]^2 \quad (3.3.10)$$

Where $Y_i^{obs}$ is the observed and $Y_i^{calc}$ is the calculated intensity of a point $i$ of the powder diffraction pattern; $w_i$ is the weight assigned to the $i^{th}$ data point; $I_j^{obs}$ is the observed and $I_j^{calc}$ is the calculated intensity of the $j^{th}$ Bragg reflection ($1 < j < m$ and $m$ represents the number of overlapped individual Bragg peaks); $n$ is the total number of points measured in the experiment; and $p$ is the number of free least squares parameters.

### 3.3.4 Scanning electron microscopy

Scanning Electron Microscope (SEM, FEI Inspect F) is a technique to detect the morphology and microstructure of the sample on a nanometer (nm) to micrometer scale (μm). The electrons interact with the surface of the object, dislodging secondary electrons and backscattered electrons and other photons with varies energy from the surface of the specimen in unique patterns, when the electron beam traces over the sample. The sensor collects these signals and generate the 2-D image of the sample [146].

The secondary and backscattered electrons, carrying information about the specimen morphology and composition, are used as the principle signals for sample imaging [146]. Secondary electrons are the excited inner shell electrons that have been ejected from the sample during the inelastic scattering of the incident beam electrons. The secondary electrons own an energy less than 50 eV and could only travel very limited distance before they vanish [146]. As a result, the secondary electrons can be used to produce high resolution images of the sample surface.

Backscattered electrons are beam electrons that have been reflected from the sample by elastic scattering [146]. Backscattered electrons dominate most of the energy distribution over a range of 0 to $E_0$, where $E_0$ is the energy of the incident beam. The intensity of the backscattered electrons corresponds to the atomic number of the sample and can be used to identify the sample composition and the distribution of the elements [146]. Backscattering is quantified by the backscattered electron coefficient η. It is defined as the ratio of the number of backscattered electrons to that of the

incident beam of electrons. The representation of the backscattered electron coefficient is displayed in equation (3.3.11) [146].

$$\eta = \frac{n_{\mathrm{BSE}}}{n_{\mathrm{B}}} = \frac{i_{\mathrm{BSE}}}{i_{\mathrm{B}}} \tag{3.3.11}$$

where $n_{\mathrm{BSE}}$ is the number of backscattered electrons; $n_{\mathrm{B}}$ is the number of the incident beam electrons; $i_{\mathrm{BSE}}$ is the generated backscattered electron current and $i_{\mathrm{B}}$ is the ejected incident beam current.

Fig. 3.3.2 shows the variation of the backscattered electron coefficient η as a function of the atomic number [147].

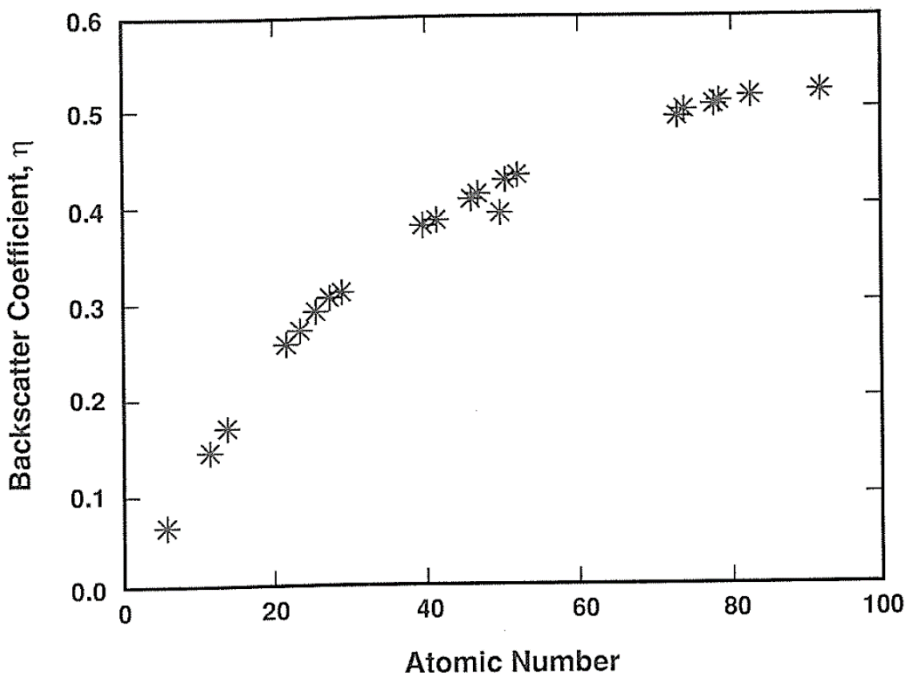


Fig. 3.3.2 The variation of the backscattered electron coefficient η as a function of the atomic number, at a beam energy $E_0$=20 keV [147].

### 3.3.5 Transmission electron microscopy

Transmission electron microscopy (TEM, JEOL 2010) is a technique to investigate the microstructure and lattice spacing in an atomic level resolution. The electrons would transmit through the ultra-thin sample while interacting with the sample at the same time. TEM images could be formed by collecting the information from the electron waves that have been exited from the sample.

The wavelength of the electrons is related to the electron energy, according to the Louis de Broglie's equation (3.3.12) [148].

$$\lambda = \frac{1.22}{E^{1/2}} \tag{3.312}$$

where λ (nm) is the wavelength of the electron and $E$ is the electron energy (eV). As a result, high energy electrons could exhibit a wavelength even smaller than the diameter of an atom, which is useful in obtaining significantly high resolution images [148].

There are different imaging modes. One is the bright field imaging mode, in which the image with different contrast is formed, due to the occlusion and absorption of the electrons (direct beam) in the sample. A darker contrast was observed in the thicker region or region involves higher atomic number, whereas regions with no sample in the beam path appear bright, hence the term bright field. The other one is dark field mode where the image is obtained from indirect beam using the objective aperture placed in back focal plane. The dark field mode is usually used to identify if the particles are crystalline or amorphous.

In diffraction mode, the electron beam undergoes Bragg scattering. Diffraction patterns from specific crystallography planes could be observed using selected area electron diffraction (SAED) aperture placed in the back focal plane. Diffraction patterns of a single crystal or thin crystalline samples were formed with aligned dots while those of a polycrystalline were in the form of a series of rings, which are useful to identify the sample space group symmetries.

### 3.3.6 Raman spectroscopy

Raman spectroscopy (Renishaw Ramascope, He-Neon Laser-633 nm) is an optical technique to obtain the atomic vibration, rotation information. Raman scattering is an inelastic scattering of the material in which the frequency of the incident light is different from that of the scattered light [149]. When the light interacts with the material, part of the photon energy would be transformed to the material, by which the atomic vibration or rotation would be excited. As a result, the energy of the scattering light would be decreased and the frequency would change as well [150]. The frequency difference is corresponding to the change of molecular vibration or rotation energy level and is called Raman shift. Raman scattering reflects the polarizability changes in molecular. When the electrons are excited with the incident light, they are excited into a virtual state. When the electrons move back to the ground state, there would be three possible situations. One state is that the energy of the scatted light is lower than the incident light, which is named Stokes. The second is that the energy of the scatted light is higher than the incident light, which is named anti-Stokes. Both of these are Raman scattering. The third is that the energy of the scatted light equals to

that of the incident light, which is the Rayleigh scattering [150]. The Raman scattering and Rayleigh are referred as Raman Effect. The schematic of the electron excitation states in both Raman and Rayleigh scattering is shown in Fig. 3.3.3.

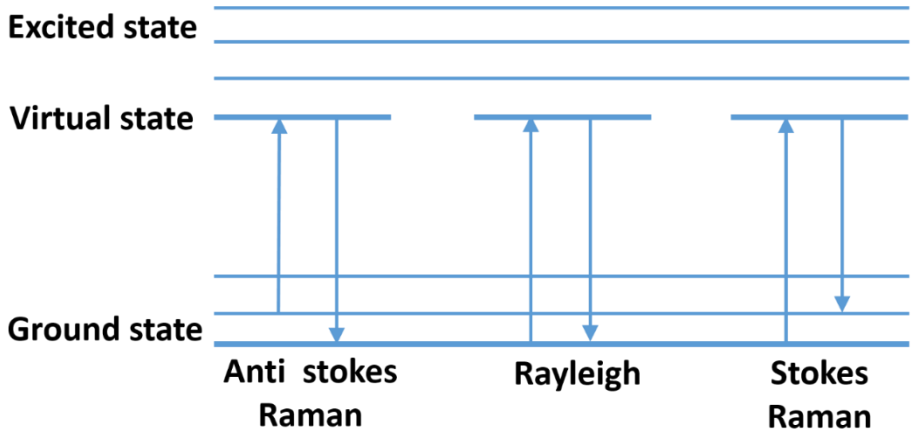


Fig. 3.3.3 Schematic of the electron excitation states in both Raman and Rayleigh scattering.

### 3.3.7 X-ray photoelectron spectroscopy

X-ray photoelectron spectroscopy (XPS, ESCALAB MK II, VG Scientific) is a surface technique to detect the elemental composition, chemical state and electronic state of material, *etc*. When the material is irradiated by the X-ray beam, electrons would be emitted from the material, from which their kinetic energy is measured [151]. The energy conservation for the photoemission process can be described by equation (3.3.12) [151].

$$E_{hv} = E_k + E_\Phi + E_B(i) \tag{3.3.12}$$

Where $E_{hv}$ is the X-ray energy; $E_k$ is the photoelectron kinetic energy; $E_\Phi$ is the correction for solid effects like work function; and $E_B(i)$ is the electron binding energy of the $i$ th level. The core electron binding energy of an atom is then obtained.

### 3.3.8 Differential scanning calorimetry

Differential Scanning Calorimeter (DSC, Rheometric Scientific STA 1500 H) is a thermal analysis technique which can reflect the physical or chemical processes happening in the material during heating or cooling process [152, 153]. DSC graph represents the temperature or heat flow changes associated with material transition along with temperature against time. Due to a different mechanism of operation, DSC can be divided into two types, one is power-compensated DSC, and the other is heat-flux DSC, also called DTA.

For heat-flux DSC, the sample and reference are set in one furnace. The power is stable and the temperature difference between the sample and the reference is measured. For power-compensated DSC, the sample crucible and reference crucible are placed in two separate furnaces with independent power supplement systems. To keep the sample and reference at the same temperature in process, the power of the sample furnace is adjusted and the relationship between difference power and temperature or time can be directly regarded as the heat flow against temperature or time [152-154].

As DSC can track the thermal capacity changes in a certain mass of material during heating and cooling, it is used in detection of transitions like melting, crystallization, glass transition, decomposition etc. [154]. The device used in the experiment is STA 1500 which is a combination of heat-flux DSC and thermal gravity analysis (TGA).

## 3.4 Electrical measurement

Silver or platinum paste was coated on both sides of the sample as electrodes. Samples with silver electrodes were fired at 800 °C for 0.5 h to and those with platinum electrodes were fired at above 1000°C for 0.5 h. The frequency dependence of dielectric properties has been measured using an Agilent 4294 precision impedance analyzer. The sample capacitance and loss were obtained from the test. The permittivity value could be calculated from the obtained capacitance, based on the equation (3.3.13).

$$\varepsilon = \frac{Cd}{\varepsilon_0 A} \tag{3.3.13}$$

where $C$ is the sample capacitance; $d$ is the sample thickness; $\varepsilon_0$ is the vacuum dielectric constant ($\varepsilon_0 \sim 8.854 \times 10^{-12}$ F/m) and $A$ is the sample surface area.

The temperature dependence of dielectric properties was obtained using an Agilent 4284A LCR meter connected to a furnace (Leton, LTF). The sample capacitance and loss in selected frequencies were obtained from the test.

The polarization-electric field (P-E) hysteresis loops and current-electric field (I-E) loops were measured by a ferroelectric hysteresis measurement tester (NPL, UK) at selected frequency. A triangular voltage ($E = \dot{\mathrm{E}}t$, where $\dot{\mathrm{E}}$ is the ratio of the electric to time) is applied on the material. The AC voltage that can be applied up to 10 kV in a frequency range of 1 to 200 Hz. Triangular voltage waveform, comparing to the others, has the advantages of distinguishing the contributions from the dielectric permittivity, electric conductivity and the domain switching [155]. The tester can give data from four

different parameters, namely current versus time (*I*-*t*), electric field versus time (*E*-*t*), current versus electric field (*I*-*E*), electric displacement versus electric field (*D*-*E*) loops [155]. The D-E loops of linear dielectric, ferroelectric and antiferroelectric is presented in Chapter 1, Fig. 1.2.1.

# Chapter IV The Antiferroelectric: Sm-doped $BiFeO_3$

## 4.1 Introduction

$BiFeO_3$ is a room temperature multiferroic material with rhombohedrally distorted *R*3*c* perovskite structure. $BiFeO_3$ has a spontaneous polarization of *ca.* 90-100 μC $cm^{-2}$ along the [111] direction [26]. However, it is difficult to obtain the saturated polarization hysteresis loop due to its high electrical conductivity. The high leakage current is attributed to the evaporation of Bi and the reduction of $Fe^{3+}$ to $Fe^{2+}$ during synthesis [31]. Secondary phases like $Bi_2Fe_4O_9$, $Bi_{25}FeO_{39}$ are easily formed due to the narrow compound formation temperature window [34]. A-site rare-earth elemental doping like $La^{3+}$ or $Nd^{3+}$ were reported to stabilize the Bi ions and suppress the formation of oxygen vacancies [40]. Karimi *et al.* reported that impurities ($Bi_2Fe_4O_9$ or $Bi_{25}FeO_{49}$) were always formed in $Bi_{1-x}Sm_xFeO_3$ ceramics at $x<0.1$, but disappeared at $x>0.1$, as a result of Sm doping [23].

Meanwhile, rare-earth doping induces as a chemical pressure in the lattice, which is able to manipulate the rhombohedral ferroelectric (FE) *R*3*c* structure into orthorhombic paraelectric *Pnma* phase, with the formation of the morphotropic phase boundary (MPB) [73, 156]. Moreover, an antiferroelectric (AFE) *Pbam* phase is reported to be formed in rare-earth-doped $BiFeO_3$ across the MPB region, with a complex coexistence of the *R*3*c* and *Pnma* phases at the nanoscale [17, 64]. Antiferroelectric materials exhibit higher energy density than linear dielectrics and ferroelectrics at a comparable electric field and they are suitable for energy storage devices. Lead-based

antiferroelectric materials, exhibiting high energy density, have to be expelled from the commercial application due to lead's toxicity [8]. Thus the development of lead-free materials such as rare-earth-doped $BiFeO_3$ as antiferroelectrics could be of great industrial interests.

The focus of the current work has been laid on Sm-substituted $BiFeO_3$ compounds due to the possible presence of an antiferroelectric order as evidenced by the double polarization-electric field hysteresis loops previously reported for thin films [17]. Additionally, the enhanced electromechanical properties nearby the MPB region may be also suited for the development of lead-free piezoelectrics. The MPB region is suggested to be located at x=0.14 in $Bi_{1-x}Sm_xFeO_3$ thin films [17].

It is agreed that the $Bi_{1-x}Sm_xFeO_3$ exhibits a *R*3*c* structure at x<0.1 [59, 73, 157]. However, the structure of $Bi_{1-x}Sm_xFeO_3$ at x>0.1 differs in films and ceramics. Cheng *et al.* suggested that the Sm-substitution in the $Bi_{1-x}Sm_xFeO_3$ ($x \geq 0.1$) thin film could destabilize the long-range FE state to form localized AFE clusters, which were found only locally within the parent FE matrix, without forming an intermediate single phase [158]. Kan *et al.* proposed that $Bi_{1-x}Sm_xFeO_3$ thin films exhibit an *R*3*c* phase with *Pbam* clusters at $0.1 \leq x \leq 0.14$ and a *Pnma* phase at x>0.14 [73]. Khomchenko [157] *et al.* reported that the XRD of $Bi_{0.85}Sm_{0.15}FeO_3$ ceramic can be fitted as a mixture of *Pbam* and *Pnma* phases while $Bi_{0.8}Sm_{0.2}FeO_3$ ceramic had a pure *Pnma* structure. Troyanchuk *et al.* found that the $Bi_{1-x}Sm_xFeO_3$ ceramics consisted of two phases, polar and antipolar, at x=0.11-0.13, while the antipolar dominated at x=0.13. Pure antipolar state *Pbam* ($\sqrt{2}a_c \times 2\sqrt{2}a_c \times 4a_c$) was only obtained at x=0.14, while traces of the *Pnma* phase were detected at x=0.15 and pure *Pnma* phase was obtained at x=0.18 [59].

The calcination temperature was also claimed to influence the phase distribution in $BiFeO_3$-$SmFeO_3$ system. Khomchenko *et al.* [66] found that a low calcination temperature of 850 °C leads to the coexistence of three phases in the $Bi_{0.85}Sm_{0.15}FeO_3$ ceramics, namely the *Pbam*, *Pnma* and *R*3*c* phases. The phase separation was attributed to an inhomogeneous distribution of $Bi^{3+}$ and $Sm^{3+}$ cations caused by the insufficient calcination temperature. The *R*3*c* phase was removed by a higher calcination temperature at 950 °C.

The double polarization-electric (P-E) hysteresis loop observed by Fujino *et al.* was explained as a result of antiferroelectric behavior [17]. Whereas, Kan *et al.* claimed that the double P-E loop is related to the electric field-induced paraelectric to ferroelectric phase transition, but not the field induced AFE to FE phase transition [58]. The AFE-related $\frac{1}{4}\{011\}$ reflections were found to reach a maximum intensity before the structural boundary ($Bi_{0.86}Sm_{0.14}FeO_3$) and further substitution resulted in lower intensity of the $\frac{1}{4}\{011\}$ reflections and the increase intensity of the paraelectric-related $\frac{1}{2}\{011\}$ reflections [73]. Double P-E hysteresis loops were obtained within the orthorhombic paraelectric structure region where the $\frac{1}{2}\{011\}$ reflections are dominant. The first principle analysis also indicated that the energy of the *Pnma* phase was closer to the energy of the ground *R*3*c* phase, comparing to that of the *Pbam* phase [58]. Thus it is easier for the *Pnma* phase to transit into the *R*3*c* phase under an external electric field. However, double hysteresis loops have never been obtained in Sm-doped $BiFeO_3$ ceramics, due to the high coercive field and high leakage current.

In this work, the effect of Sm-substitution on the structure of $Bi_{1-x}Sm_xFeO_3$ ceramics has been investigated. The coexistence of the ferroelectric *R*3*c* phase, antiferroelectric *Pbam* phase and the paraelectric *Pnma* phase was found. The phase fractions were affected by both calcination conditions and the Sm substitution. Phase transitions among the three phases at elevated temperatures are presented. Ceramics with low conductivity have been successfully produced. The polarization-electric field relationship of the Sm-doped $BiFeO_3$ compositions has been illustrated to investigate the possible presence of antiferroelectricity in $Bi_{1-x}Sm_xFeO_3$ ceramics and ultimately to assess their potential suitability in energy storage applications.

## 4.2 Experimental methods

### 4.2.1 Material synthesis

The starting materials $Bi_2O_3$ (Alfa Aesar, UK, 99.975%), $Sm_2O_3$ (Alfa Aesar, UK, 99.9%) and $Fe_2O_3$ (Alfa Aesar, UK, 99.9%) were mixed and milled in ethanol using a planetary ball mill (Nanjing machine factory, China) for 4 h. The dried powder was calcined at various temperatures (810 °C, 830 °C, 850 °C 910 °C or 950 °C) for 4 h. The synthesized powder was further milled in ethanol for 4 h to obtain fine homogenous particles. The $Bi_{1-x}Sm_xFeO_3$ ceramics (x=0.15, 0.16, 0.165, denoted as BSF15, BSF16 and BSF16.5, respectively) were sintered at 800 °C from powder calcined at 910 °C, using spark plasma sintering (SPS) (HPD-25/1 FCT systeme GmbH) at a pressure of 80 MPa, under vacuum, with a heating rate of 100 °C $min^{-1}$, with a dwell time of 5 min. The $Bi_{0.82}Sm_{0.18}FeO_3$ (denoted as BSF18) ceramic was sintered at 800 °C from powder calcined at 950 °C using the same sintering procedures. The SPS sintered samples were subsequently annealed in a muffle furnace (Carbolite HTF 1800, UK) at 700 °C in air for 15 h to remove the carbon diffused from the graphite die during SPS processing.

### 4.2.2 Structure analysis

The structure was determined by X-ray powder diffraction (XRD, X'pert Pro, PANalytical, Almelo, Netherlands) at room temperature over the $2\theta$ range 10° to 120°, in steps of 0.0167°, with an effective scan time of 200 s per step, using Ni filtered Cu-K$\alpha$ (1.5418 Å) radiation. Elevated temperature measurements were made using an Anton-Paar HTK-16 high-temperature camera. Data were collected at 25 °C and at 50 °C intervals from 100 to 950 °C. Diffraction patterns were acquired over the $2\theta$

range 5° to 120°, in steps of 0.0167°, with a scan time of 50 s per step. Temperature calibration was carried out by measuring the melting points of high purity $KNO_3$, CuCl, KI, NaCl, $K_2SO_4$ standards. Data analysis was carried by the Rietveld method using the General Structure Analysis System (GSAS) software [159, 160]. The structure was further studied using transmission electron microscopy (TEM, JEOL 2010) with electron diffraction. The microstructure was studied using scanning electron microscopy (SEM, FEI Inspect F).

### 4.2.3 Electric properties characterization

Electrodes for the $Bi_{1-x}Sm_xFeO_3$ ceramics were fabricated using Ag paste, fired at 800 °C for 0.5 h. Frequency dependent dielectric permittivity and loss were measured using an Agilent 4294 precision impedance analyzer. The temperature dependence of dielectric permittivity and loss was measured from 25 to 600 °C, with a heating and cooling rate of 5 °C $min^{-1}$, at selected frequencies (1, 10, 50, 100 and 500 kHz and 1 MHz), using an Agilent 4284A LCR meter connected to a furnace (Leton, LTF). The P-E hysteresis loops were measured by a ferroelectric hysteresis measurement tester (NPL, UK), at a frequency of 10 Hz.

## 4.3 Results and discussion

### 4.3.1 Crystal structure

The $Bi_{1-x}Sm_xFeO_3$ compositions ($0.15 \leq x \leq 0.18$) have been selected, as they have been suggested to be located in the MPB region characterized by the possible presence of an antiferroelectric structure. The BSF15 powder was calcined at different temperatures (810, 830, 850, 910 and 950 °C) to identify the optimum calcination condition. The XRD patterns of the resulting powder are shown in Fig. 4.3.1. The results indicate that a small amount of $Bi_2Fe_4O_9$ (JCPDS Nos. 25-0090) is formed as a secondary phase in powders calcined at low temperatures, but is removed at 910 °C and above.

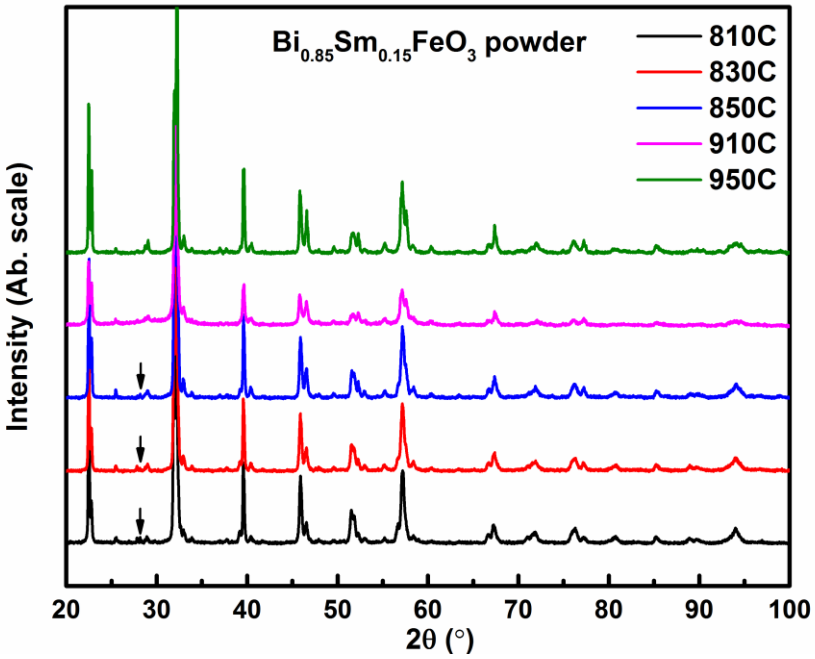


Fig. 4.3.1 X-ray diffraction patterns of $Bi_{0.85}Sm_{0.15}FeO_3$ powder calcined at different temperatures (as indicated). The secondary phase $Bi_2Fe_4O_9$ (JCPDS Nos. 25-0090) is marked by arrows.

All the XRD patterns have been fitted using the Rietveld refinement method. The fitted XRD of the BSF15 powder calcined at 910 °C is shown in Fig. 4.3.2 as an example. The structure has been fitted well with three phases, namely ferroelectric *R*3*c*, antiferroelectric *Pbam* and paraelectric *Pnma* phases. The refinement parameters are shown in Table 4.3.1.

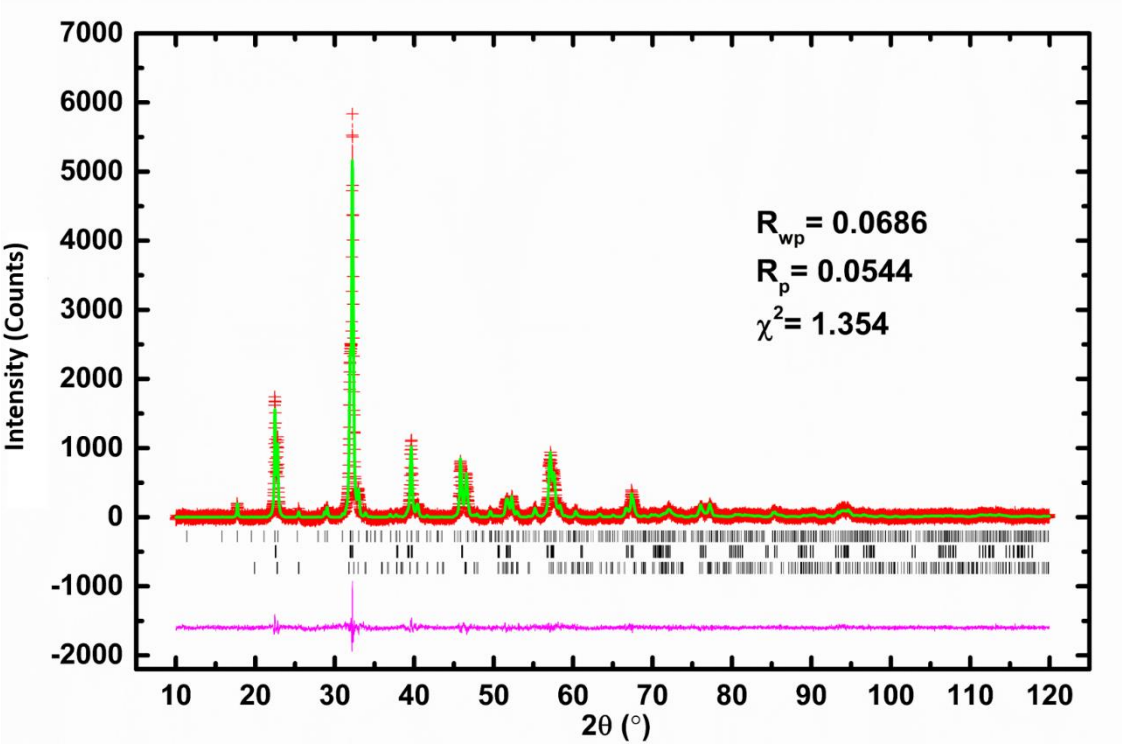


Fig. 4.3.2 X-ray diffraction profiles of the BSF15 powder calcined at 910 °C fitted using conventional Rietveld analysis. Observed (+) and calculated (line) profiles are shown, as well as the difference profile (lower), with reflection positions of *Pbam*, *R*3*c* and *Pnma* phases (from top to bottom) indicated by markers.

Fig. 4.3.3 shows the refined weight fractions of the *R*3*c*, *Pbam* and *Pnma* phases in BSF15 powder as a function of calcination temperature. Calcination conditions did affect the phase separation and homogeneity, as proposed by Khomchenko *et al.* [66] and Walker *et al.* [161].

The weight fraction of the *R*3*c* phase decreased, while that of the *Pbam* phase increased with the increase of the calcination temperature. The *Pnma* phase remained in a relative stable fraction with the increase of calcination temperature. It is indicated that high temperature was required for Sm cation to fit into the parent matrix. Meanwhile, the fraction of *Pnma* phase is mainly related to the Sm concentration.

Table 4.3.1 Crystal and refinement parameters of BSF15 powder (calcined at 910 °C)

| chemical formula | $Bi_{0.85}Sm_{0.15}FeO_3$ | | |
|---|---|---|---|
| crystal system | Orthorhombic | Rhombohedral | Orthorhombic |
| weight fraction | 0.797 (5) | 0.087 (5) | 0.116 (4) |
| formula weight | 304.03 g $mol^{-1}$ | 304.03 g $mol^{-1}$ | 304.03 g $mol^{-1}$ |
| Z | 8 | 6 | 4 |
| space group | *Pbam* | *R*3*c* | *Pnma* |
| unit cell dimension | *a* = 5.5908 (3) Å, *b* = 11.2219 (6) Å, *c* = 7.7973 (4) Å, $\alpha$ = 90 (0)° | *a* = 5.5583 (8) Å, *b* = 5.5583 (8) Å, *c* = 13.7780 (28) Å, γ = 120 (0)° | *a* = 5.6299 (10) Å, *b* = 7.8176 (14) Å, *c* = 5.4449 (8) Å, $\alpha$ = 90 (0)° |
| volume | 489.20 (6) $Å^3$ | 368.63 (9) $Å^3$ | 239.64 (5) $Å^3$ |
| density | 8.256 g $cm^{-3}$ | 8.217 g $cm^{-3}$ | 8.427 g $cm^{-3}$ |
| $R_p$ | | 0.0544 | |
| $R_{wp}$ | | 0.0686 | |
| $R_{ex}$ | | 0.0592 | |
| $R_B$ | | 0.0702 | |
| total number of variables | | 61 | |
| number of profiles points used | | 6580 | |

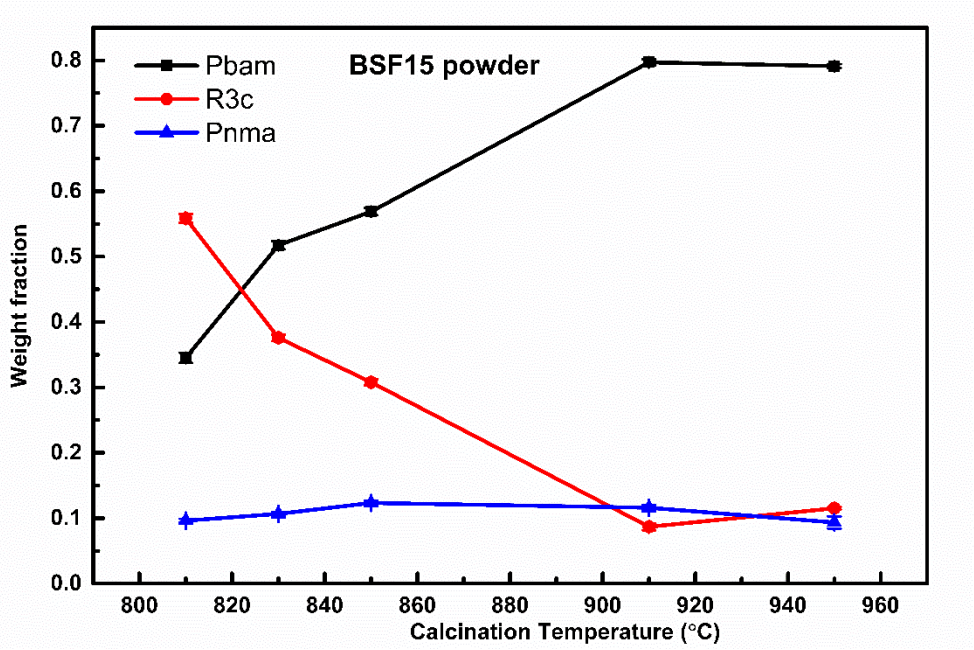


Fig. 4.3.3 The refined weight fractions of *R3c*, *Pbam* and *Pnma* phases fitted in $Bi_{0.85}Sm_{0.15}FeO_3$ powder at different calcination temperatures (810, 830, 850 910 and 950 °C).

The electron diffraction patterns of BSF15 powder are shown in Fig. 4.3.4. The $\frac{1}{4}\{110\}$ (Fig. 4.3.4a), $\frac{1}{4}\{001\}$ (Fig. 4.3.4b), $\frac{1}{2}\{011\}$ (Fig. 4.3.4c) and the $\frac{1}{2}\{111\}$ (Fig. 4.3.4c) reflections were observed. The $\frac{1}{4}\{110\}$ reflections have been previously observed in $PbZrO_3$, as a result of the unit cell quadrupling along the $<110>_p$ direction by antiparallel A-site cation displacement [162]. The $\frac{1}{2}\{011\}$ reflections are associated to the oxygen octahedral antiphase tilting [64, 158]. The existence of the $\frac{1}{4}\{001\}$ indicated the quadrupling of unit cell along the $<001>_p$ direction. The $\frac{1}{2}$ {11-1} reflections are related to the antiphase rotation of the [$FeO_6$] octahedron [72]. The observation of these superlattice reflections further supported the existence of the antiferroelectric *Pbam* phase in BSF15 powder.

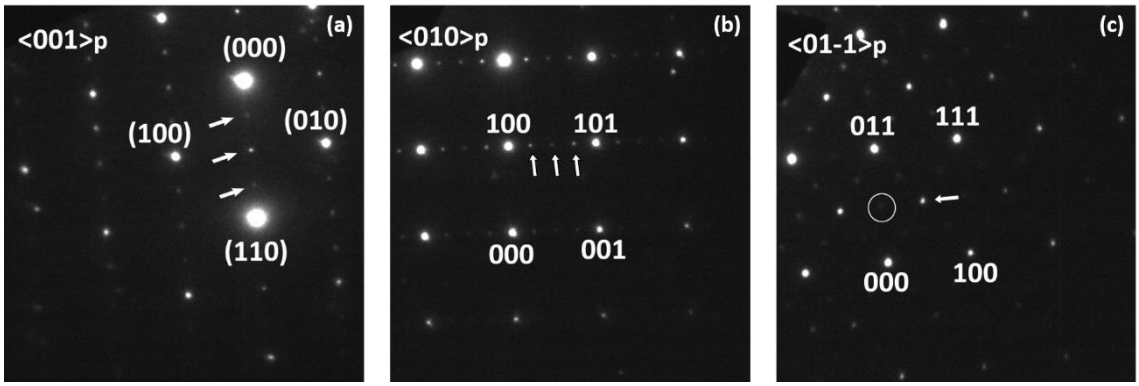


Fig. 4.3.4 Electron diffraction patterns of the BSF15 powder showing (a) $<001>_p$ zone axis with arrowed $\frac{1}{4}\{110\}$ reflections; (b) $<010>_p$ zone axis with arrowed $\frac{1}{4}\{001\}$ reflections; (b) $<01\text{-}1>_p$ zone axis with arrowed $\frac{1}{2}$ {111} and circled $\frac{1}{2}$ {011} reflections.

### 4.3.2 Structure evolution in the $Bi_{1-x}Sm_xFeO_3$

Calcination conditions were optimized for $Bi_{1-x}Sm_xFeO_3$ compositions to get the highest weight fraction of the *Pbam* phase with no impurities. The optimum calcination temperature of 910 °C was selected for $Bi_{1-x}Sm_xFeO_3$ (x=0.15, 0.16, 0.165) powders, while BSF18 was calcined at the optimized temperature of 950 °C. The related XRD patterns are shown in Fig. 4.3.5. All the patterns were fitted with the *R*3*c*, *Pbam* and *Pnma* phases. The variation of the weight fractions of three phases as function of Sm mol concentration is shown in Fig. 4.3.6. The weight fraction of *R*3*c* phase decreased with the increase of Sm concentration and vanished in BSF18. The fraction of the *Pbam* phase decreased and that of the *Pnma* phase increased with the increase of Sm concentration. This demonstrates that the present compositions experienced complex phase transition within the MPB region and that the Sm substitution would favor the formation of the *Pnma* phase at the expenses of the *R*3*c* and *Pbam* phases.

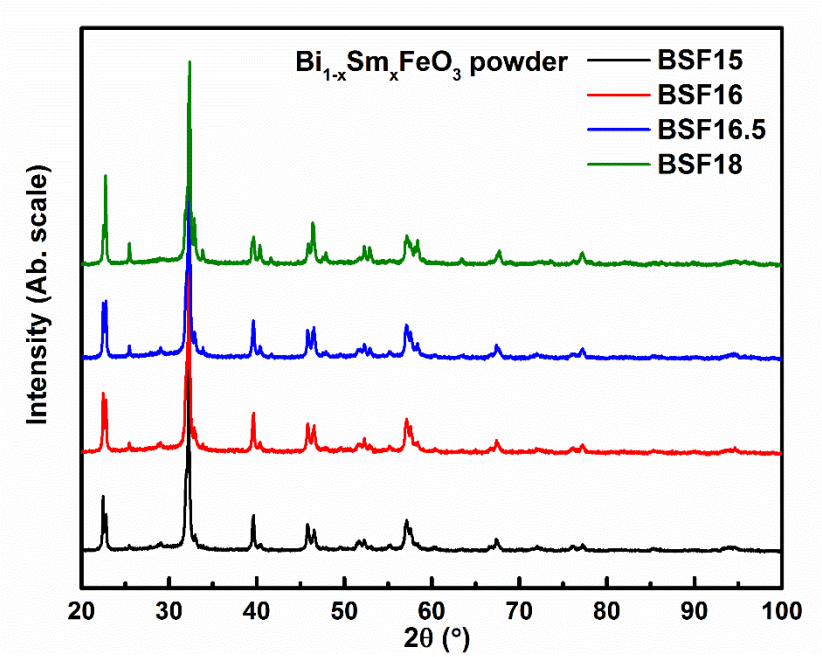


Fig. 4.3.5 XRD patterns of $Bi_{1-x}Sm_xFeO_3$ (x=0.15, 0.16, 0.165 and 0.18) powders.

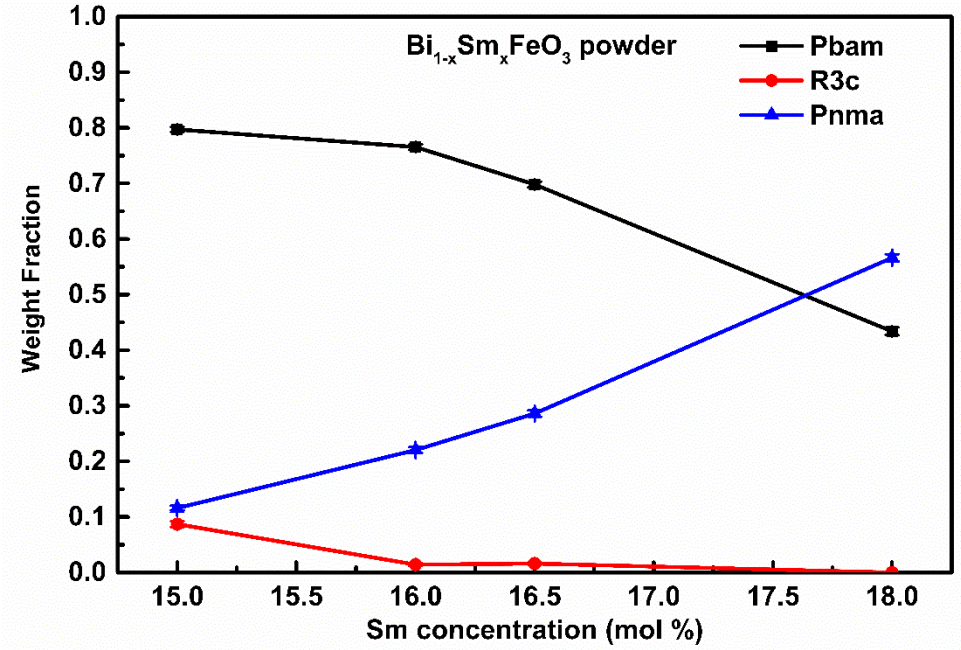


Fig. 4.3.6 The weight fractions of the *R*3*c*, *Pbam* and *Pnma* phases in $Bi_{1-x}Sm_xFeO_3$ (x=0.15, 0.16, 0.165 and 0.18) powder as a function of Sm mol concentration.

The XRD patterns of $Bi_{1-x}Sm_xFeO_3$ ceramics are shown in Fig. 4.3.7 and reveal weak additional peaks mainly attributable to $Bi_{25}FeO_{40}$ (JCPDS Nos. 46-0416). The $Bi_{25}FeO_{40}$ is reported to be thermodynamically more stable than $BiFeO_3$ in the temperature range 447 °C– 767 °C [34]. While the SPS sintering temperature was 800 °C, the annealing temperature was lower at 700 °C, which may account for the appearance of this secondary phase.

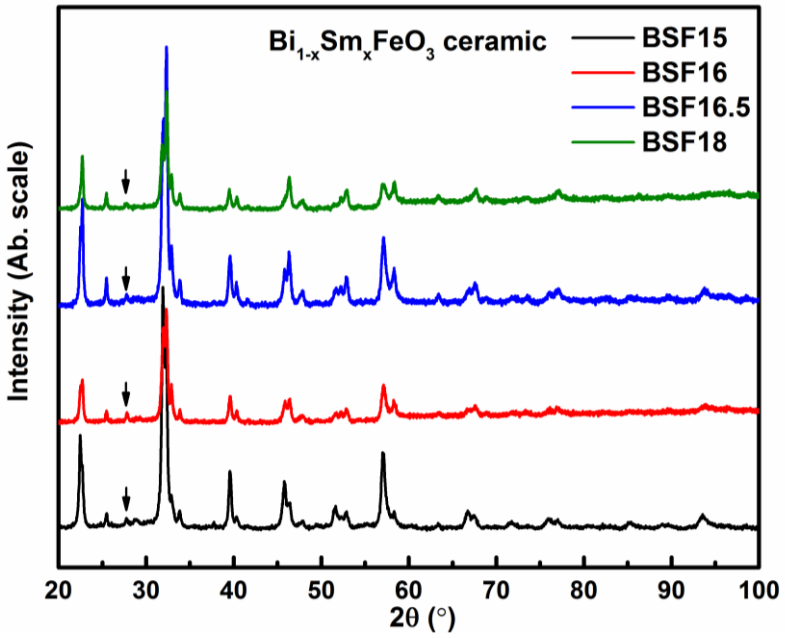


Fig. 4.3.7 X-ray diffraction patterns of $Bi_{1-x}Sm_xFeO_3$ (x = 0.150, 0.160, 0.165 and 0.180) ceramics (as indicated). The secondary phase $Bi_{25}FeO_{40}$ (JCPDS Nos. 46-0416) is marked by arrows.

The XRD patterns of $Bi_{1-x}Sm_xFeO_3$ ceramics were fitted using combination of the *R*3*c*, *Pbam* and *Pnma* phases (ignoring the weak $Bi_{25}FeO_{40}$ phase). The refined weight fractions are shown in Fig. 4.3.8. The fractions of the *R*3*c* phase increased in all the ceramics compared to those in the relative powders and simultaneously the fraction of the *Pbam* phase decreased. The fraction of the *Pnma* phase is relatively increased as

well. It is indicated that the applied pressure and the low sintering temperature would stabilize the *R*3*c* phase and suppress the *Pbam* phase.

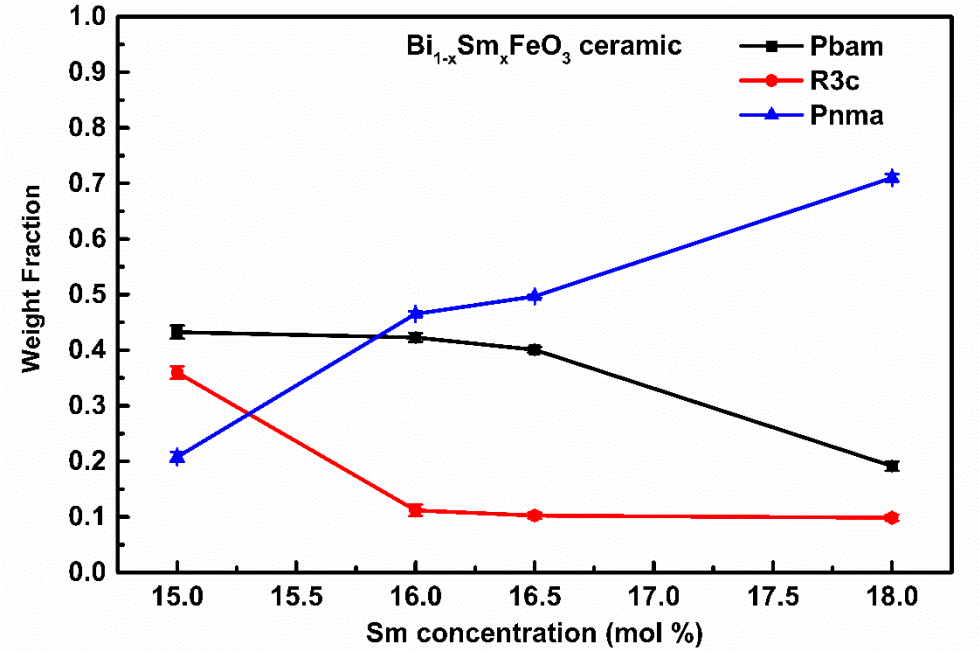


Fig. 4.3.8 The weight fractions of the *R*3*c*, *Pbam* and *Pnma* phases in $Bi_{1-x}Sm_xFeO_3$ (x=0.15, 0.16, 0.165 and 0.18) ceramics as a function of Sm mol concentration.

The SEM images of the $Bi_{1-x}Sm_xFeO_3$ (x=0.15, 0.16, 0.165 and 0.18) ceramics are shown in Fig. 4.3.9. The $Bi_2Fe_4O_9$ phase was mainly formed within the grains while the $Bi_{25}FeO_{39}$ phase was mainly presented at the grain boundaries. The $Bi_{25}FeO_{39}$ phase is easily formed in the contact boundaries [34]. The formation of the Fe-rich $Bi_2Fe_4O_9$ crystals is due to the $Bi_2O_3$ evaporation. Melting of the $Bi_{25}FeO_{39}$ phase (the peritectic temperature of $Bi_{25}FeO_{39}$ is 790 °C) is the main reason for the segregation of the Bi-rich and Fe-rich phases [34].

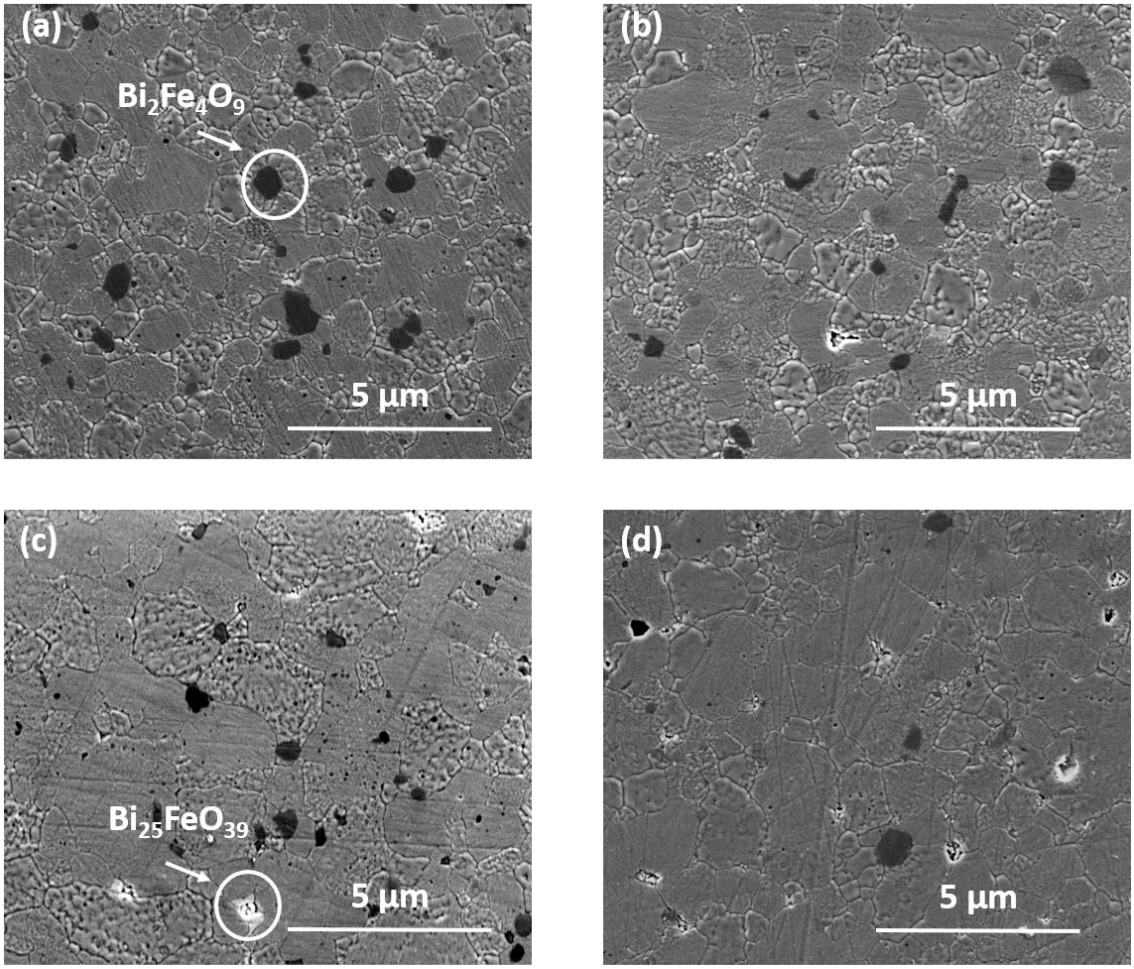


Fig. 4.3.9 SEM images of $Bi_{1-x}Sm_xFeO_3$ ceramics (a) BSF15; (b) BSF16; (c) BSF16.5; (d) BSF18. The $Bi_2Fe_4O_9$ (dark grey) and $Bi_{25}FeO_{39}$ (bright) phases were highlighted by circles.

Fig. 4.3.10a shows the frequency dependent dielectric properties of the $Bi_{1-x}Sm_xFeO_3$ (x=0.15, 0.16, 0.165 and 0.18) ceramics. The permittivity for $Bi_{1-x}Sm_xFeO_3$ ceramics increased in comparison to the pure $BiFeO_3$ [163]. The permittivity was enhanced due to the instability of polarization across the phase boundary and a significant polarization variation under external conditions (stress or electric field) [164]. The low dielectric loss has been achieved by minimizing the Bi evaporation and reduction of $Fe^{3+}$ ions. However, the loss value increased at high frequencies, indicating the electric heterogeneous of the ceramics which attributed to the electronic conductivity. The

permittivity value at a frequency of 1 MHz increased with the increase of Sm mol concentration. (Fig. 4.3.10b). The maximum permittivity value could not be identified due to a limited compositional variation, while it was reported to be located at x=0.14 in the thin films [73].

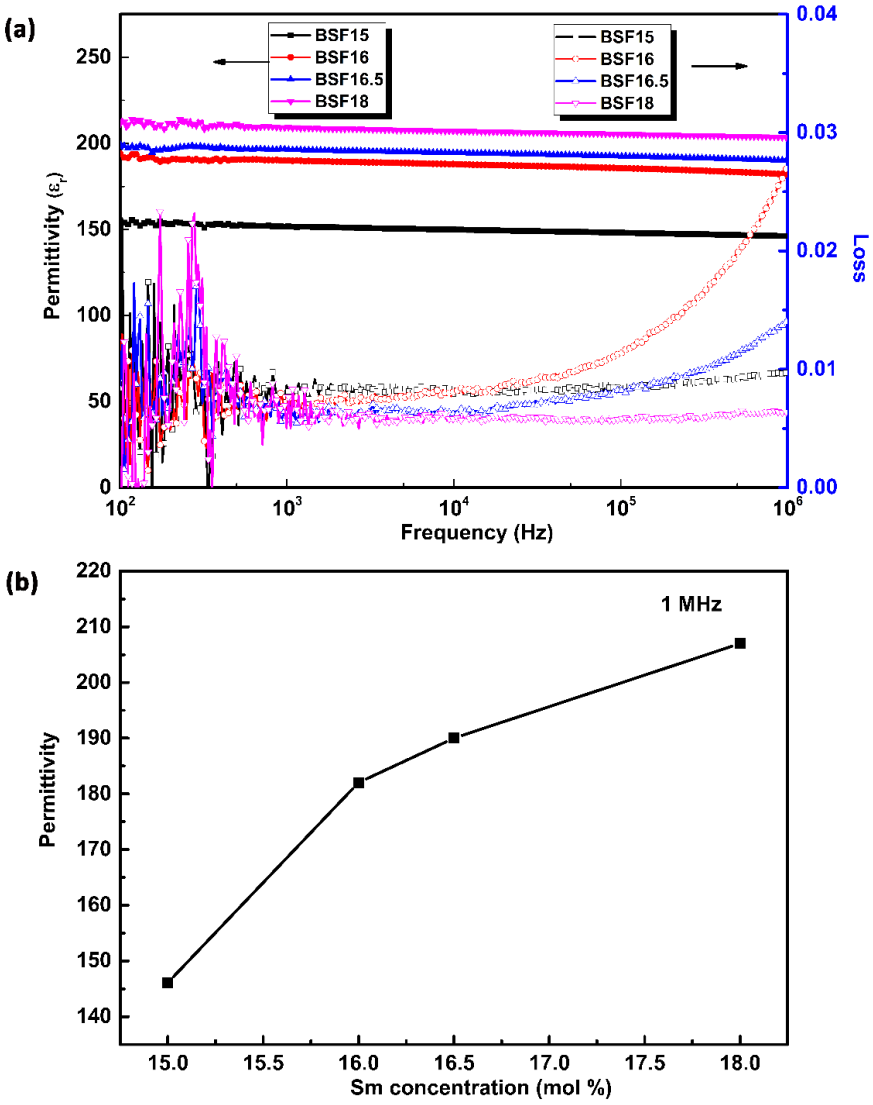


Fig. 4.3.10 (a) Frequency dependent dielectric properties of $Bi_{1-x}Sm_xFeO_3$ (x=0.15, 0.16, 0.165 and 0.18) ceramics; (b) permittivity values of $Bi_{1-x}Sm_xFeO_3$ ceramics at 1 MHz for various Sm mol %.

### 4.3.3 Phase transition

Phase transitions were investigated by XRD at different temperatures. Fig. 4.3.11 and 4.3.12 show the XRD patterns of BSF15 powder (calcined at 910 °C) and BSF18 powder (calcined at 950 °C) respectively, in the temperature range 25 - 950 °C, both in heating and cooling cycle. The peaks at *ca.* 25.4 °, 33.7 ° and 41.2 °, for example, belong to the paraelectric *Pnma* phase, whose intensity gradually increased with increasing temperature, as shown in Fig. 4.3.11. It states that the *Pnma* phase is the stable phase at high temperature. The peaks at 29.2 °, 45.9 ° and 55.3 °, for example, belong to the antiferroelectric *Pbam* phase. It can be seen that their intensity gradually reduces with increasing temperature. For the BSF18 powder, the peak at *ca.* 45.9 ° corresponds to the antiferroelectric *Pbam* phase, which gradually disappeared with increasing temperature.

Fig. 4.3.13 shows the weight fractions and normalized volumes of the *R*3*c*, *Pbam* and *Pnma* phases in BSF15 powder, as a function of temperature. Both the *Pbam* and *R*3*c* phases gradually transformed to the *Pnma* phase with increasing temperature, indicating that the *Pnma* phase is the high temperature stable phase. The transition to the *Pnma* phase should be completed at 450 °C. The normalized volume of the *Pnma* phase showed an almost linear increase with increasing temperature in the entire temperature range studied. However, the volume of the *R*3*c* and the *Pbam* phases is fluctuating within the temperature range, indicating the instability of the two phases with increasing temperature and the transitions to the *Pnma* phase.

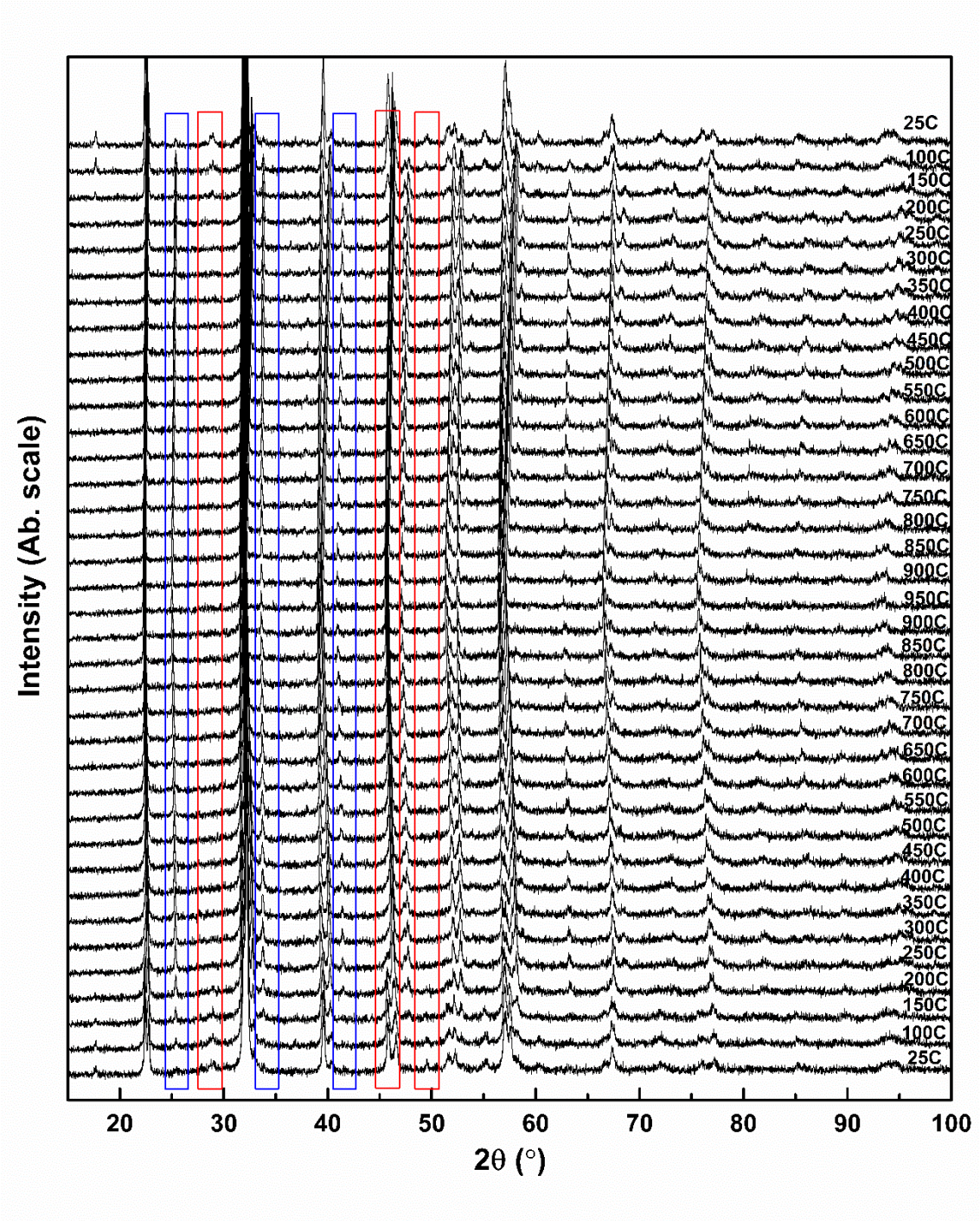


Fig. 4.3.11 High temperature XRD patterns of BSF15 powder on heating and cooling in a temperature range of 25 °C to 950 °C. The peaks belong to the *Pnma* phase were marked by blue circles and those of the *Pbam* phase were marked by red circles.

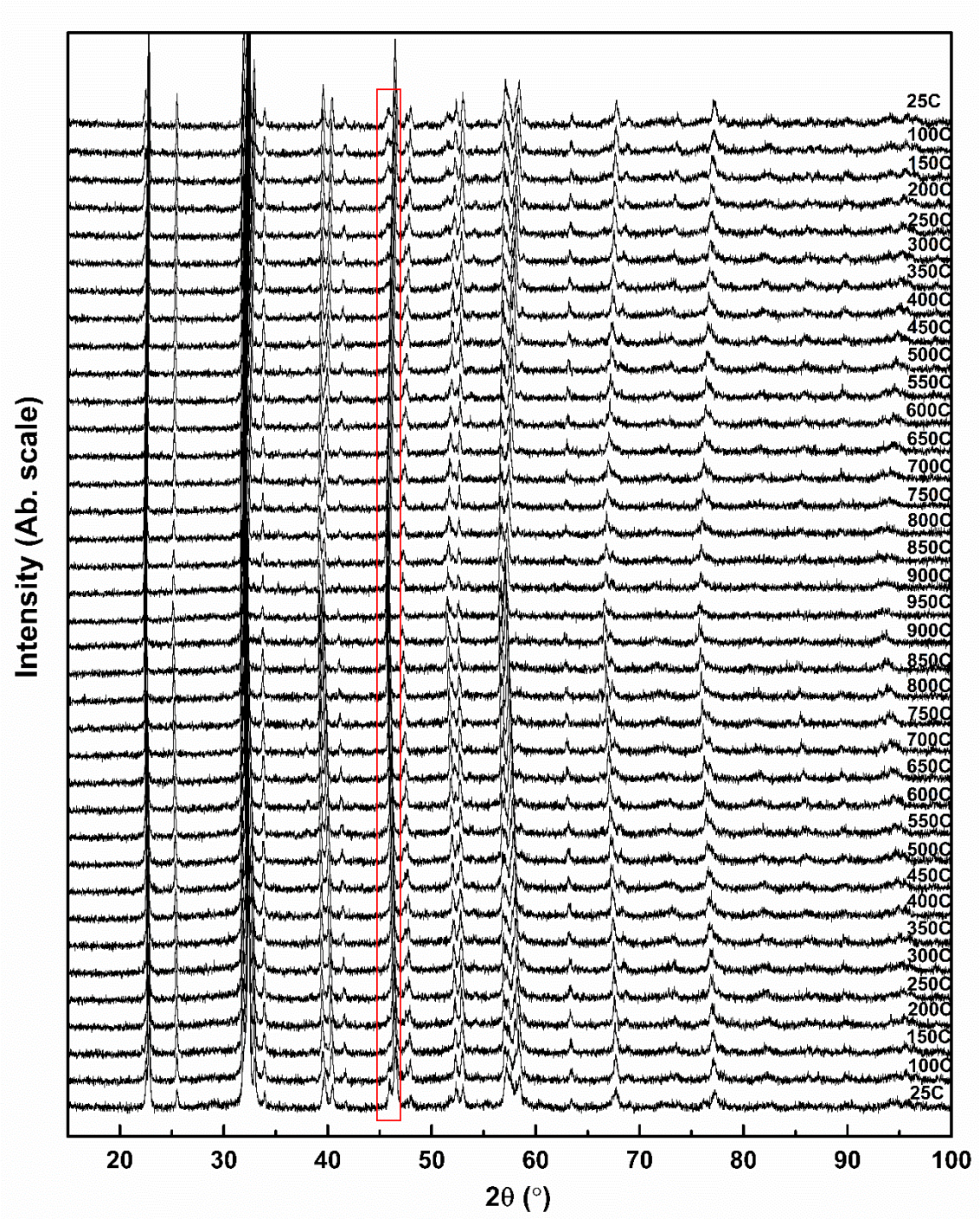


Fig. 4.3.12 High temperature XRD patterns of BSF18 powder on heating and cooling in a temperature range of 25 °C to 950 °C. The peak belongs to the *Pbam* phase was marked by red circle.

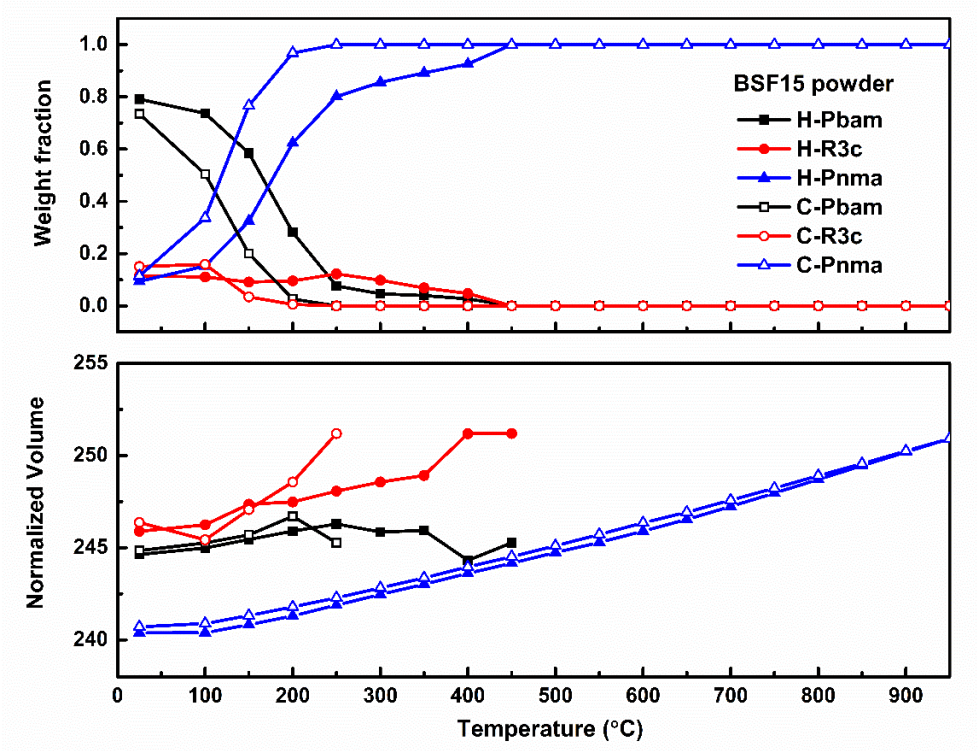


Fig. 4.3.13 The refined weight fractions and normalized volumes of the *R*3*c*, *Pbam* and *Pnma* phases in BSF15 powder, as a function of temperature.

Fig. 4.3.14 shows the fitted weight fractions and normalized volumes of the *Pbam* and *Pnma* phases in the BSF18 powder, as a function of temperature. The *Pbam* phase gradually transformed to the *Pnma* phase with increasing temperature. The transition to the *Pnma* phase was completed at 350 °C, which is significantly lower than the case of BSF15. The normalized volume of the *Pnma* phase showed an almost linear increase with the increase of the temperature, with a tiny discrepancy at 950 °C, which requires further examination. The normalized volume of the *Pbam* phase showed fluctuation within the temperature range, indicating the transition to the *Pnma* phase.

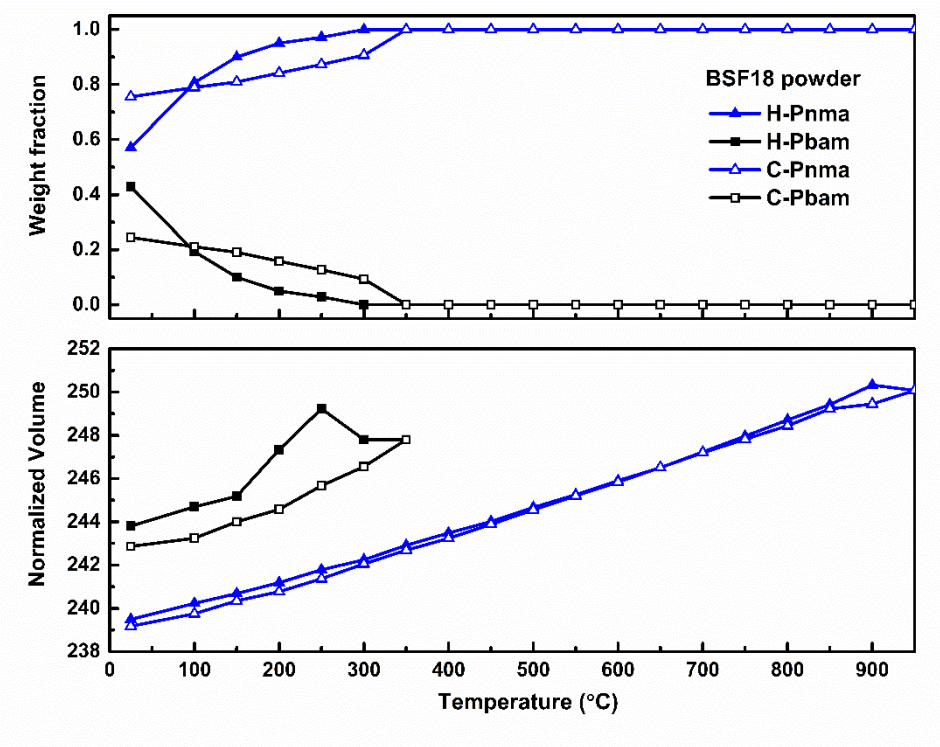


Fig. 4.3.14 The refined weight fractions and normalized volumes of the *Pbam* and *Pnma* phases in BSF18 powder, as a function of temperature.

Fig. 4.3.15 shows the temperature dependent dielectric properties of the BSF15 ceramic during heating. Frequency-independent permittivity peaks with the minimum loss were observed at 200 °C, which may correspond to the highest decrease rate of the *Pbam* phase, as observed in Fig. 4.3.13. The transition from the antiferroelectric *Pbam* phase to the paraelectric *Pnma* phase is suggested as the Curie transition of the *Pbam* phase with a Curie temperature of 200 °C. Relaxation behavior was also observed which could be related to the electronic conductivity attributed to the reduction of the $Fe^{3+}$. The second phase transition observed at 575 °C is probably related to the complete disappearance of the *R*3*c* phase. It is also suggested as a Curie transition for the ferroelectric *R*3*c* phase. Permittivity relaxation behavior was observed between 300 °C and 500 °C. The temperature discrepancy of the second

phase transition between the high temperature XRD and the temperature dependence of the dielectric properties may be related to the different stability level of the *R*3*c* phase in powder and ceramic.

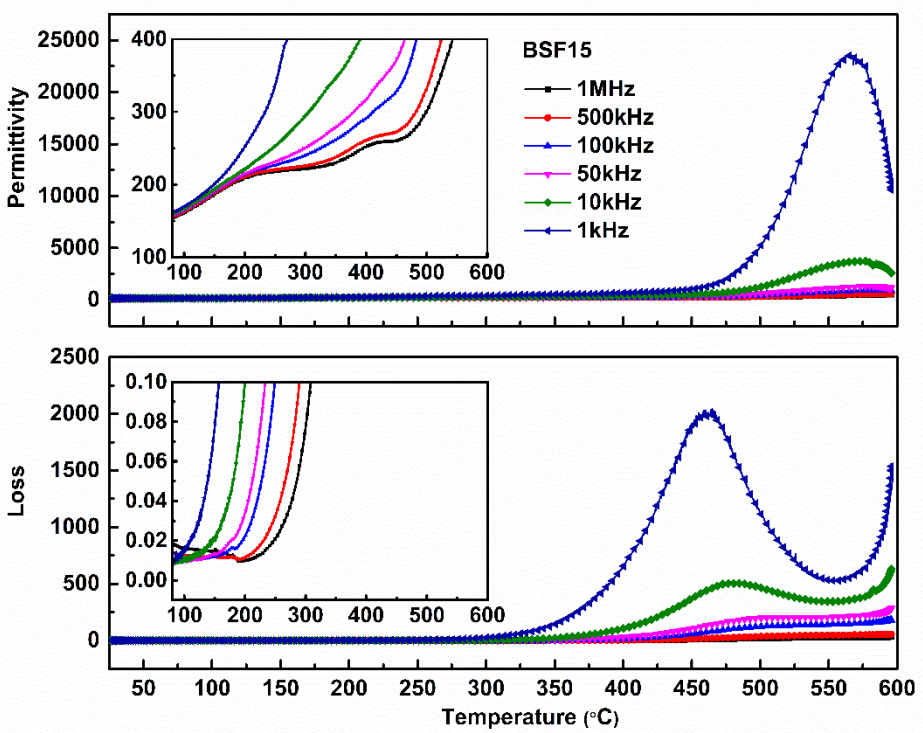


Fig. 4.3.15 Temperature dependent dielectric properties of BSF15 during heating cycle.

Fig 4.3.16 shows the temperature dependent dielectric properties of the BSF16 ceramic during heating. Fig. 4.3.17 shows the temperature dependent dielectric properties of the BSF16.5 ceramics during heating. The Curie temperature of the *Pbam* phase shifted towards the lower temperature with the increase of Sm concentration. The similar shift in Curie temperature was observed for the *R*3*c* phase as well.

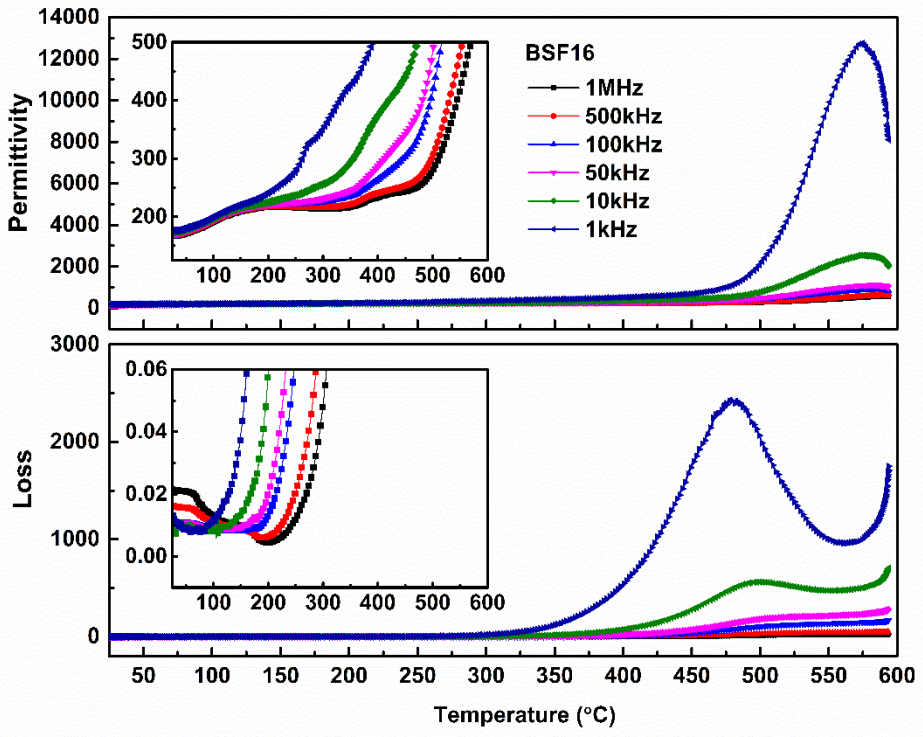


Fig. 4.3.16 Temperature dependent dielectric properties of BSF16 during heating cycle.

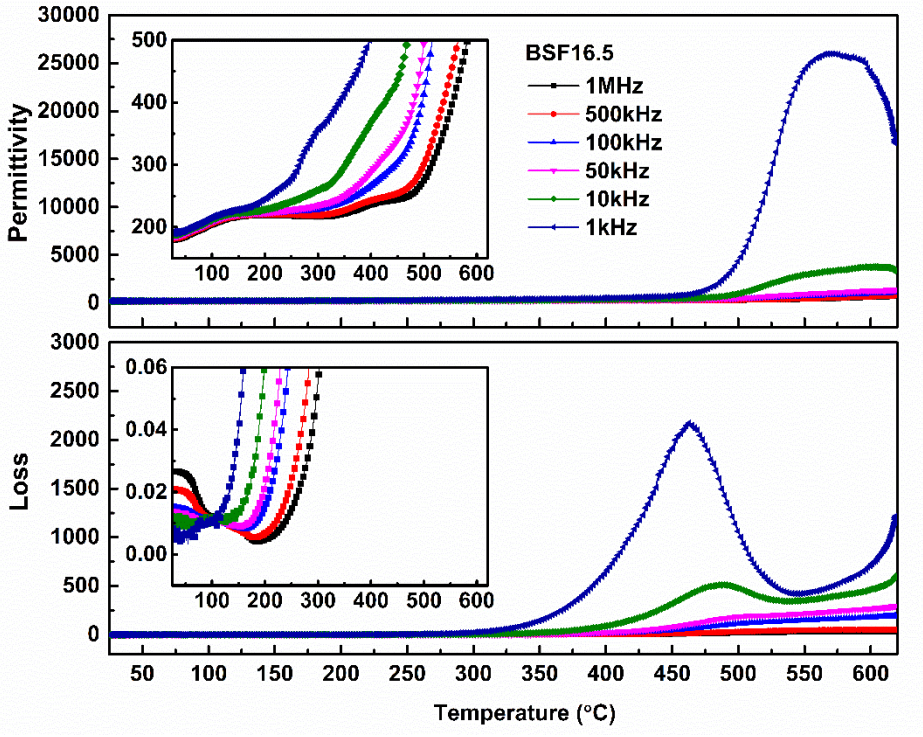


Fig. 4.3.17 Temperature dependent dielectric properties of BSF16.5 during heating cycle.

Fig. 4.3.18 shows the temperature dependent dielectric properties of BSF18 ceramic during heating cycle. The Curie temperature of the *Pbam* phase was shifted to 100 °C. This decrease in Curie temperature is related to the substitution of Bi ions by smaller Sm ions, resulting in a lattice distortion and unit cell volume reduction [165]. The Curie temperature of the *R*3*c* phase was observed at 525 °C, which was also lower than that in $Bi_{1-x}Sm_xFeO_3$ (x=0.15-0.165).

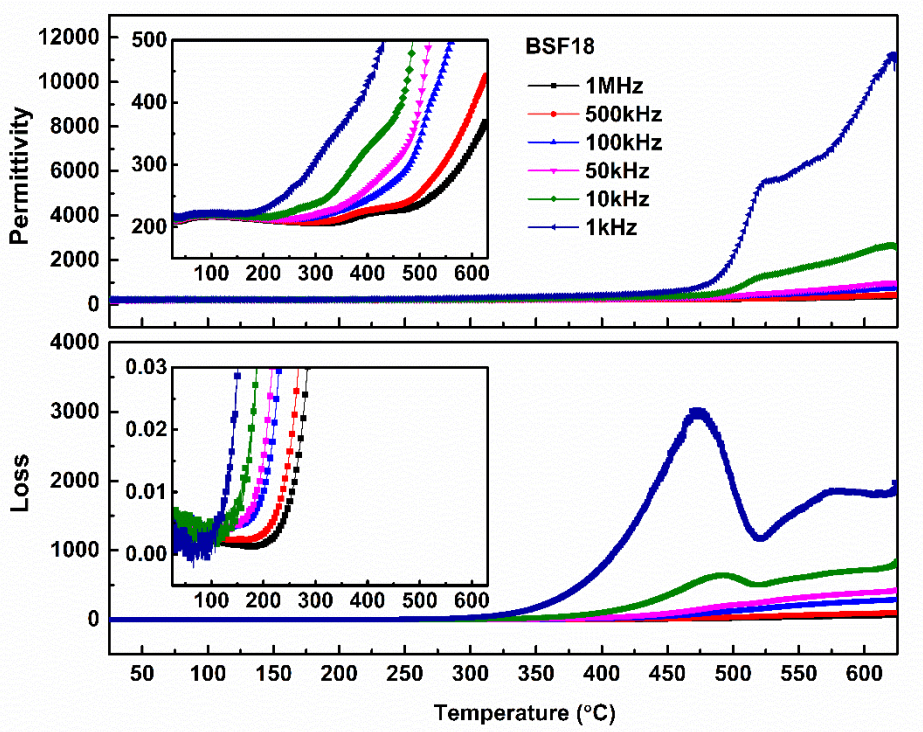


Fig. 4.3.18 Temperature dependent dielectric properties of BSF18 during heating cycle.

### 4.3.4 Electric properties

Fig. 4.3.19 shows the current-electric field (I-E) and the polarization-electric field (P-E) hysteresis loops of $Bi_{1-x}Sm_xFeO_3$ (x=0.15, 0.16, 0.165 and 0.18). The current peaks observed in the I-E loop for BSF15 indicate the domain switching taking place in ferroelectric R3c phase. The P-E loop of BSF15 is 'lossy' due to the activation of charge

carriers at high electric field. Linear P-E loops were obtained for the BSF16, BSF16.5 and BSF18. It is suggested that the ferroelectric behavior was suppressed. Double P-E hysteresis loops could not be obtained due to a high electric field required for the AFE-FE transition. The highest energy density of 0.64 J $cm^{-3}$ (error bar ±0.02) was obtained for the BSF18 ceramics.

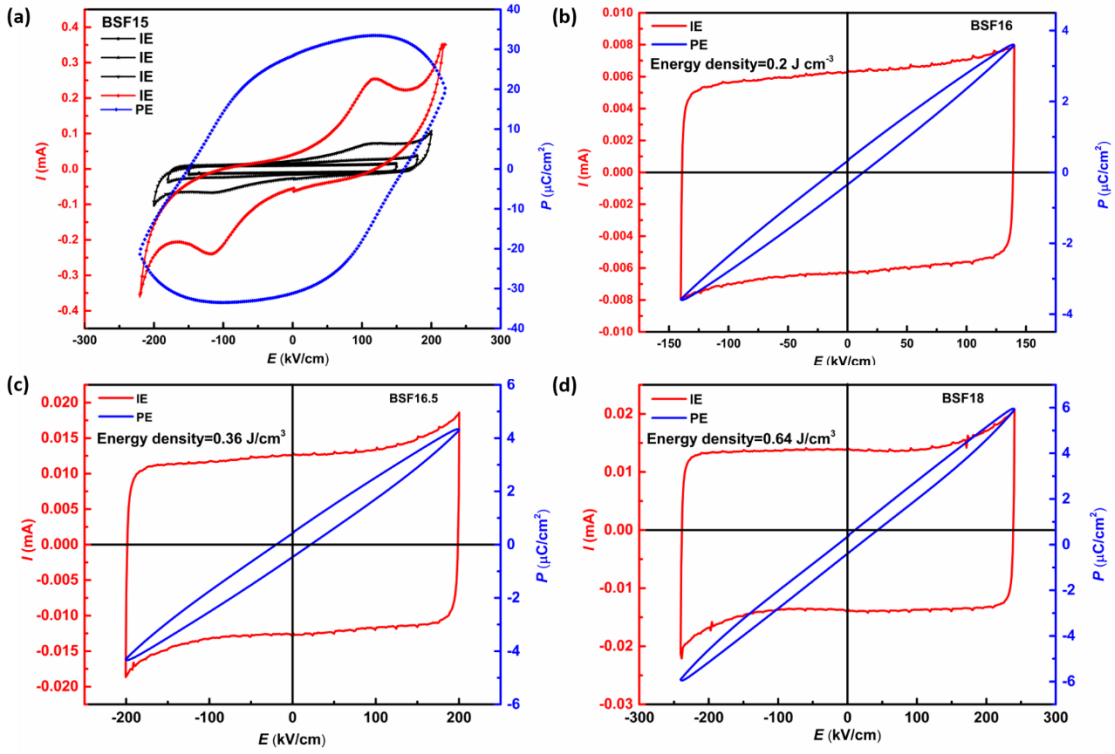


Fig. 4.3.19 Current-electric (I-E) loop and Polarization-electric (P-E) hysteresis loop of (a) BSF15; (b) BSF16; (c) BSF16.5; (d) BSF18.

## 4.4 Conclusions

The $Bi_{1-x}Sm_xFeO_3$ (x=0.15-0.18) powders have been successfully synthesized with no observed second phases at a calcination temperature above 910 °C. The $Bi_{1-x}Sm_xFeO_3$ ceramics have been produced using spark plasma sintering method for the first time. The structure of the Sm-doped $BiFeO_3$ compositions has been identified as the coexistence of the ferroelectric *R*3*c* phase, antiferroelectric *Pbam* phase and the paraelectric *Pnma* phase. The *Pbam* phase is competing with the *R*3*c* phase and their relative ratio is affected by the calcination conditions and the Sm concentration. The fraction of the *Pbam* phase increased and that of the *R*3*c* phase decreased with the increase in the calcination temperature. The fractions of the *R*3*c* phase and the *Pbam* phase both decreased with increasing the Sm concentration. The fraction of the *Pnma* phase is mainly derived by the Sm concentration with a gaining weight fraction on increasing the Sm concentration. Pure antiferroelectric *Pbam* phase could not be obtained in the current studied compositions. Nevertheless, both the *R*3*c* and the *Pbam* phases transform into the *Pnma* phase at high temperature. The Curie temperature of the *Pbam* phase in BSF15 ceramic is assumed to be 200 °C and that of the *R*3*c* phase is to be 575 °C. The Curie temperature of both phases decreased with the increase of Sm concentration. The conductivity has been largely reduced in the prepared ceramics, which is suitable for P-E tests. Ferroelectric hysteresis loops obtained in BSF15 is a result of domain switching in the *R*3*c* phase. Linear P-E loops were obtained for BSF16, BSF16.5 and BSF18 due to the suppression of the *R*3*c* and the enhancement of the *Pnma* phase. Double hysteresis loop of the antiferroelectric phase were not obtained due to absence of electric field-induced transitions in the

electric field range studied. The highest energy density of 0.64 J $cm^{-3}$ was obtained for the BSF18 ceramic. This is the highest value ever reported in the Sm-doped $BiFeO_3$ ceramics.

# Chapter V. The Linear Dielectric: $BiNbO_4$

## 5.1 Introduction

Bismuth Niobate ($BiNbO_4$) is an extensively studied dielectric material with two types of crystal structures, namely the $\alpha$- and $\beta$- phase. The $\alpha$-phase, with an orthorhombic structure and *Pnna* space group, is normally obtained below 1020 °C [75]. The $\beta$-phase, with a triclinic structure and *P*-1 space group, is normally formed above 1020 °C [76]. Both the $\alpha$- and $\beta$- phase $BiNbO_4$ are widely employed as multilayer RF and microwave components [166]. Meanwhile, both the $\alpha$- and $\beta$- phase $BiNbO_4$ were suggested as possible antiferroelectric (AFE) systems [81]. Lead-free antiferroelectrics, as environmental friendly materials, have the potential to replace lead-based antiferroelectric compounds to be applied in high energy storage capacitors, pulse power generators, micro-actuators [20, 22, 167].

However, the antiferroelectric nature of the $\alpha$- and $\beta$- phase $BiNbO_4$ is still under debate. Popolitov *et al.* [81], for the first time, pointed out that the $\alpha$-$BiNbO_4$ was possible antiferroelectric. The anomalies in the temperature dependent dielectric measurement of the $\alpha$ phase single crystal observed at 360 °C and 570 °C were suggested to be related to the antiferroelectric to ferroelectric (FE) transition and ferroelectric to paraelectric (PE) transition, respectively [22, 82]. It was mentioned that unsaturated polarization-electric field hysteresis loop was generated between 360 °C and 570 °C, which were regarded as evidence of a possible ferroelectric or ferrielectric state. However, the hysteresis loops were not shown. Additionally, the temperature

dependence of second harmonic generation failed to prove the existence of ferroelectric phase because the signal intensity dropped out of the instrument sensitivity from 360 to 570 °C [22]. Subsequently, Ayyub *et al.* [84, 85] reported the formation of double hysteresis loop in the α-$BiNbO_4$ thin film with thickness above 550 nm. It was suggested that the α-$BiNbO_4$ is antiferroelectric. The appearance of the ferroelectric hysteresis loop with a film thickness below 550 nm was related to the interfacial pinning effect by semiconductor substrate. However, no current-electric field loops were provided to further support the antiferroelectric nature in α-$BiNbO_4$. Moreover, no clear evidence of antiferroelectric behavior has ever been provided in studies of structure and properties of α-$BiNbO_4$ ceramics. The hypothetical antiferroelectric nature of β phase $BiNbO_4$ relies on the analogies with structure of $BaMnO_4$.

Moreover, the phase relationship between the α and the β phases is also still controversial. The β-$BiNbO_4$ is formed at a temperature higher than that in the α-$BiNbO_4$, thus it is considered that the α phase could transform to the β phase by heating. However, Keve *et al.* convinced that the β phase could not be transformed back to the α phase by annealing once it is generated, due to its lower symmetry and denser atom packing [20, 75]. However, in recent research, Zhou *et al*. [21] claimed that the β to α phase transformation can be observed by annealing the β-phase bulk in the temperature range 700 - 1030 °C. They proposed that such transition was stimulated by internal stresses, also the reason why the transition could not be observed in powder. Meanwhile, a longer dwelling time would further promote the transformation processing in bulk [21]. However, the XRD results reported by Zhou *et al.* were obtained

from crushed ceramics, which technically can only be regarded as powder instead of bulk (ceramic). Subsequently, Zhai *et al*. [91] synthesized the $BiNbO_4$ powder at 700 °C and 1050 °C respectively, by citrate method. The structure of powder calcined at 700 and 1050 °C were both identified as the β-phase and termed as low-temperature β-phase and high-temperature β-phase, respectively. It was additionally found that the powder produced between 700 and 900 °C was a combination of the low-temperature β phase and the α phase, while the powder synthesized between 900 and 1040 °C was pure α-phase. The low-temperature β-phase to the α-phase transition is assumed due to the thermodynamically metastable state of low-temperature β-phase.

Sleight *et al.* [94] studied the high temperature performance of the β-$BiNbO_4$ and the β-$BiTaO_4$. Transitions at 740 °C on heating and 715 °C on cooling were found in the β-$BiTaO_4$ by differential thermal analysis (DTA). Similar transitions were reported at 1009 °C on heating and 1002 °C on cooling in the β-$BiNbO_4$. High temperature XRD measurement of the β-$BiTaO_4$ confirmed the phase transformations observed in DTA and a high temperature phase, termed the γ-phase, was discovered. The cell dimensions of γ-$BiTaO_4$ were determined as *a*=7.681 Å, *b*= 5.627 Å, *c*=7.749 Å, α=90°, β=78.55°, γ=90°. The structure is isostructural to monoclinic $LaTaO_4$ [168]. The existence of a high temperature γ-phase was also claimed in the $BiNbO_4$, but the detailed structure has not been confirmed [94]. Meanwhile, no further investigation has been carried out on the high temperature γ-phase of either $BiTaO_4$ or $BiNbO_4$. The relationship of γ-phase to the α- and β- phase is also under development.

In this work, we demonstrate that the β-phase powder could be converted back to the α-phase by annealing β-phase powder at a temperature range of 800 °C to 1040 °C,

but with a slow kinetics. Both the α- and β-phase $BiNbO_4$ transform to the high temperature γ-phase whose structure has been identified as monoclinic with a $P2_1/c$ space group. The thermodynamic relationships among the α, β and γ-phases have been clarified.

## 5.2 Experimental procedures

### 5.2.1 Synthesis of $BiNbO_4$

The starting materials $Bi_2O_3$ (Alfa Aesar, UK, 99.975%) and $Nb_2O_5$ (Alfa Aesar, UK, 99.9%) were mixed in a 1:1 stoichiometric ratio and milled in ethanol using a planetary ball mill (Nanjing machine factory, China) for 4 h. The dried powder was calcined at 1000 or 1070 °C for 4 h to form pure $\alpha$ and $\beta$ phases, respectively. In each case, the synthesized powder was further milled in ethanol for 4 h to obtain fine homogenous particles. Spark plasma sintering (SPS) (HPD-25/1 FCT systeme GmbH) was used to fabricate dense ceramics. Pure $\alpha$-phase ceramics were sintered from $\alpha$-phase powder, using SPS at a pressure of 300 MPa, under vacuum, at a heating rate of 100 °C $min^{-1}$ to 900 °C, with a dwell time of 5 min at the highest temperature. Pellets were subsequently annealed in air using a box furnace (Carbolite HTF 1800, UK) at 850 °C for 15 h to remove surface and diffused carbon from the graphite die used in SPS. Pure $\beta$-phase ceramics were similarly prepared by SPS from pure $\beta$-phase powder with a maximum sintering temperature of 1050 °C and at a pressure of 50 MPa. As-sintered $\beta$ phase ceramics were annealed in air at 1050 °C for 15 h to remove diffused carbon. Pellet densities of 97.2% and 86.9% were achieved for the $\alpha$- and $\beta$- phases, respectively.

### 5.2.2 Structure analysis

Phase purity was determined by X-ray powder diffraction (XRD, X'pert Pro, PANalytical, Almelo, Netherlands) at room temperature over the $2\theta$ range 10° to 70°, in steps of 0.034°, with an effective scan time of 50 s per step, using Ni filtered Cu-K$\alpha$ (1.5418 Å)

radiation. Elevated temperature measurements were made using an Anton-Paar HTK-16 high-temperature camera. Data were collected at 25 °C and at 100 °C intervals from 100 °C to 1000 °C, 10 °C intervals from 1000 °C to 1050 °C and a final measurement at 1100 °C. Diffraction patterns were acquired over the $2\theta$ range 5° to 120°, in steps of 0.034°, with a scan time of 100 s per step, except for the 1100 °C data, which were scanned in steps of 0.0167°, with a scan time of 200 s per step. Temperature calibration was carried out by measuring the melting points of high purity $KNO_3$, CuCl, KI, NaCl, $K_2SO_4$ standards. The identities of the α- and β- phases were confirmed by comparison with their standard diffraction patterns (JCPDS 82-0348 and 71-1518, respectively).

### 5.2.3 Powder Neutron diffraction

High-resolution powder neutron diffraction data were acquired on the HRPD diffractometer at the ISIS Facility, Rutherford Appleton Laboratory, UK. Data were collected on backscattering (130°-160°), 90 (85°-95°) and low angle (28°-42°) detectors. Calcined $\alpha$- or β-$BiNbO_4$ powder was sealed in an evacuated silica glass tube (10 mm diameter), inside a vanadium can (11 mm diameter), which was placed in front of the backscattering detectors in an evacuated furnace. For the $\alpha$-phase, long data collections of *ca*. 150 $\mu$A h were made at room temperature, 400 and 700 °C, with shorter data collections of *ca*. 20 $\mu$A h at selected temperatures up to 950 °C. For the $\beta$-phase, long data collections of *ca*. 150 $\mu$A h were made at room temperature and at 1050 °C (the latter in the $\gamma$-phase region), with shorter data collections of *ca*. 10 $\mu$A h at other temperatures up to 1140 °C. Data analysis was carried out by the Rietveld method using the General Structure Analysis System (GSAS) software [159, 160]. The

initial structural models were based on those of Subramanian and Calabrese for the $\alpha$-phase with space group *Pnna* [77]; Keve and Skapski [20, 169] for the $\beta$-phase with space group *P*-1 and that of $LaTaO_4$ presented by Kurova and Aleksandrov [168] as an initial model for the $\gamma$-phase with space group $P2_1/c$.

### 5.2.4 Annealing investigation

The effect of temperature and annealing time on the $\beta$ to $\alpha$ phase transition was investigated. The $\beta$-$BiNbO_4$ powder (obtained by calcination at 1070 °C for 4 h) was annealed at selected temperatures (700, 800, 850 and 900 °C) for 5 h to study the effect of temperature. An additional annealing was carried out at 850 °C for 15 h to study the effect of annealing time. $\beta$-$BiNbO_4$ ceramics sintered by SPS and then annealed at 1050 °C to remove carbon were subsequently annealed at 700 °C, 800 °C, 900 °C and 950 °C for 5 h to study the temperature. Another sample was annealed at 900 °C for 15 h to examine the effect of annealing time. As-sintered (not annealed at 1050 °C) $\beta$-$BiNbO_4$ ceramics were annealed at 900 °C for 5 and 15 h to study the influence of residual carbon on the kinetics of $\beta$ to $\alpha$ transition. In each case the sample was characterized by X-ray diffraction prior to and post to heat treatment.

### 5.2.5 Thermal analysis

Thermal analysis was carried out on both powder and ceramics by differential scanning calorimetry (DSC, Rheometric Scientific STA 1500 H) in air from 25 °C to 1100 °C with a heating/cooling rate of 10 °C $min^{-1}$. Samples were further characterized by X-ray diffraction after the DSC analysis.

### 5.2.6 Electric properties characterization

Electrodes for the α and β-phase $BiNbO_4$ ceramics were fabricated using Pt paste, fired at 850 and 1050 °C for 0.5 h, respectively. Temperature dependence of dielectric permittivity and loss of the α and β-phase $BiNbO_4$ were measured from 25 °C to 1100 °C, with both heating and cooling rate of 5 °C $min^{-1}$, at selected frequencies (1, 10, 100 and 500 kHz and 1 MHz), using an Agilent 4284A LCR meter connected to a furnace.

The P-E hysteresis loops of the $\alpha$- and $\beta$-phase ceramics were measured by a ferroelectric hysteresis measurement tester (NPL, UK), at a frequency of 10 Hz.

## 5.3 Results and discussion

### 5.3.1 Ambient temperature structures

The fitted neutron diffraction profiles for the $\alpha$- and $\beta$- phases of $BiNbO_4$ at ambient temperature are shown in Fig. 5.3.1, with the corresponding crystal and refinement parameters of the $\alpha$- and β-phase $BiNbO_4$ in Table 5.3.1and 5.3.2. The structure of the $\alpha$-phase is based on that of the $SnWO_4$ and may be described as consisting of sheets of $[NbO_4]_n^{n3-}$ separated by $Bi^{3+}$ cations. The sheets are made up of a corner sharing array of niobate octahedra. Bismuth is in a four-pyramidal coordination with oxygen, typical for bismuth oxides and reflects the stereochemical activity of the Bi $6s^2$ lone pair of electrons (Fig. 5.3.2a). Two further non-bonding contacts to O atoms at around 2.74 Å, complete a distorted octahedral geometry for the site. The niobium coordination shows a degree of distortion away from regular octahedral geometry, with bond lengths ranging from 1.84 to 2.17 Å (Fig. 5.3.2b).

In the case of the $\beta$-$BiNbO_4$, the structure can again be described as consisting of sheets of corner sharing niobate octahedra separated by $Bi^{3+}$ cations. However, in this case the sheets are corrugated. The lower triclinic symmetry of the $\beta$-phase results in two crystallographically distinct sites each for $Bi^{3+}$ and $Nb^{5+}$ cations. The $Bi^{3+}$ cations adopt a five coordinate geometry, which may be described as a defect octahedron (Fig. 5.3.3), again reflecting the stereochemical activity of the Bi $6s^2$ lone pair.

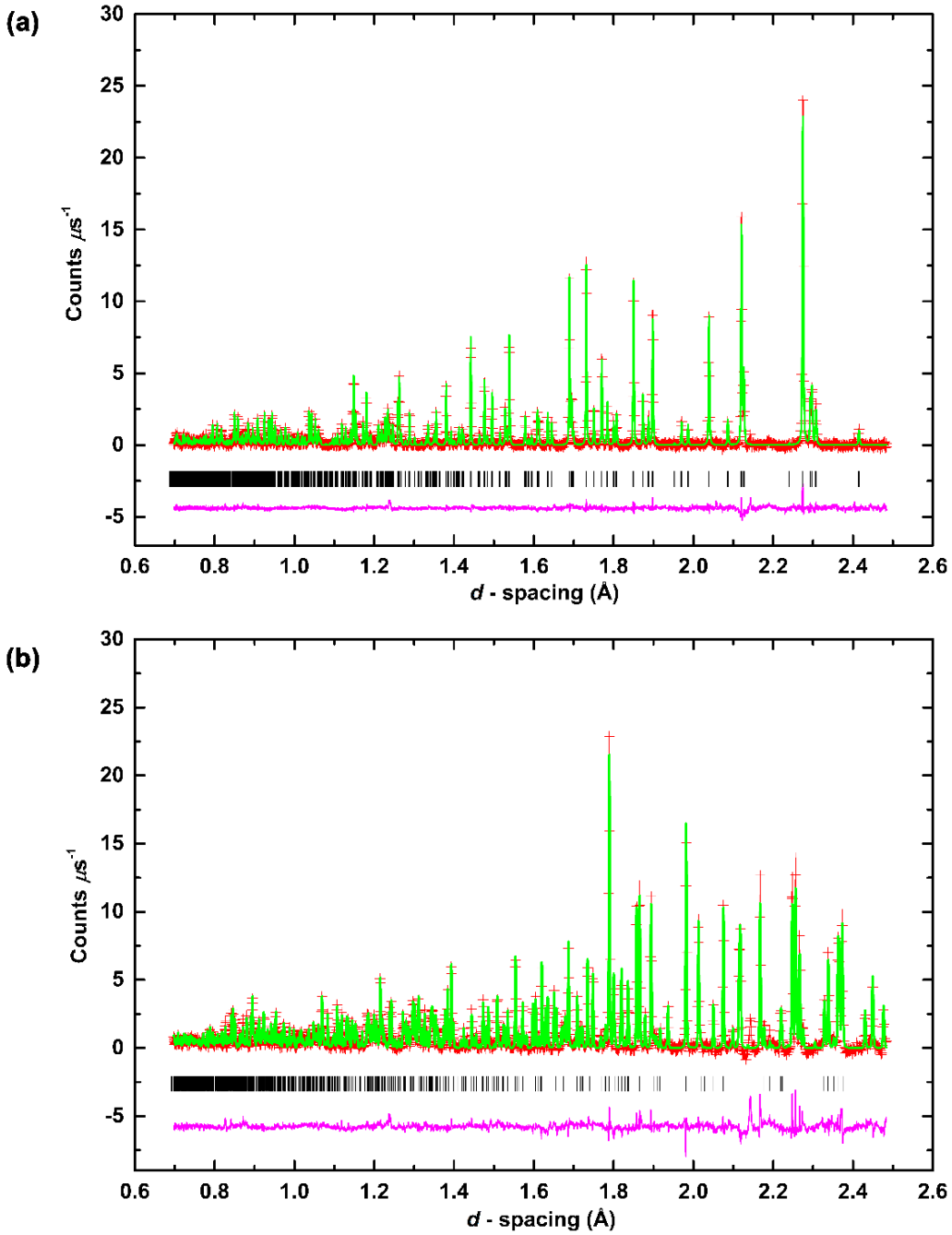


Fig. 5.3.1 Diffraction profiles of (a) the α-phase $BiNbO_4$; (b) the β-phase $BiNbO_4$, fitted using conventional Rietveld analysis. Neutron backscattering data is shown. Observed (+) and calculated (line) profiles are shown, as well as the difference profile (lower), with reflection positions indicated by markers.

Table 5.3.1 Crystal and refinement parameters of α and β-phase $BiNbO_4$ at 25 °C

| chemical formula | α-$BiNbO_4$ | β-$BiNbO_4$ |
|---|---|---|
| formula weight | 365.88 g $mol^{-1}$ | 365.88 g $mol^{-1}$ |
| crystal system | Orthorhombic | Triclinic |
| space group | *Pnna* | *P*-1 |
| unit cell dimension | *a* = 5.68059(2) Å,<br>*b* = 11.71356(5) Å,<br>*c* = 4.98333(2) Å,<br>α = 90(0)° | *a* = 5.54111(8) Å,<br>*b* = 7.62091(6) Å,<br>*c* = 7.93468(5) Å,<br>α = 102.517(1)°,<br>β = 90.163(1)°,<br>γ = 92.804(1)° |
| volume | 331.590 (3) $Å^3$ | 326.58 (1) $Å^3$ |
| Z | 4 | 4 |
| density | 7.329 g $cm^{-3}$ | 7.441 g $cm^{-3}$ |
| sample description | Colourless powder in sealed silica tube | Colourless powder in sealed silica tube |
| $R_p$ | 0.0191 | 0.0227 |
| $R_{wp}$ | 0.0209 | 0.0235 |
| $R_{ex}$ | 0.0152 | 0.0115 |
| $R_B$ | 0.0816 | 0.1079 |
| $\chi^2$ | 2.405 | 3.958 |
| total number of variables | 125 | 103 |
| number of profiles points used | | |
| neutron backscattering | 4234 | 4234 |

Table 5.3.2 Refined Parameters for α and β-phase $BiNbO_4$

| α-$BiNbO_4$ | | | | | | |
|---|---|---|---|---|---|---|
| Atom | Site | x | y | z | Occ. | Uiso (Å$^2$) |
| Bi | 4e | 0.25(0) | 0.5(0) | 0.78100(13) | 1 | 0.053(2) |
| Nb | 4e | 0.34593(17) | 0.25(0) | 0.25(0) | 1 | 0.021(2) |
| O1 | 4e | 0.13972(23) | 0.30549(12) | 0.50393(28) | 1 | 0.045(2) |
| O2 | 4e | 0.41557(22) | 0.09780(12) | 0.41427(24) | 1 | 0.022(2) |

| β- $BiNbO_4$ | | | | | | |
|---|---|---|---|---|---|---|
| Atom | Site | x | y | z | Occ. | Uiso (Å$^2$) |
| Bi1 | 4*e* | 0.28144(42) | 0.83281(31) | 0.62486(30) | 1 | 1.31(8) |
| Bi2 | 4*e* | 0.23691(43) | 0.87463(29) | 0.12807(30) | 1 | 1.26(9) |
| Nb1 | 4*e* | 0.22535(56) | 0.34366(40) | 0.17737(41) | 1 | 0.48(9) |
| Nb2 | 4*e* | 0.24100(60) | 0.32577(45) | 0.68011(48) | 1 | 0.856(95) |
| O1 | 4*e* | -0.00730(80) | 0.10477(62) | 0.18125(58) | 1 | 1.34 (12) |
| O2 | 4*e* | 0.45025(76) | 0.10522(59) | 0.67489(60) | 1 | 1.43 (12) |
| O3 | 4*e* | 0.16148(77) | 0.31970(56) | 0.94676(54) | 1 | 0.99(10) |
| O4 | 4*e* | 0.07393(74) | 0.55179(53) | 0.73150(54) | 1 | 0.99(11) |
| O5 | 4*e* | 0.29413(78) | 0.32778(59) | 0.45044(56) | 1 | 1.21(11) |
| O6 | 4*e* | 0.43853(72) | 0.54696 (51) | 0.22138(56) | 1 | 0.93(10) |
| O7 | 4*e* | 0.46530(74) | 0.15066(56) | 0.14361(56) | 1 | 1.12(11) |
| O8 | 4*e* | 0.03912(71) | 0.83534(55) | 0.36148(51) | 1 | 0.59(10) |

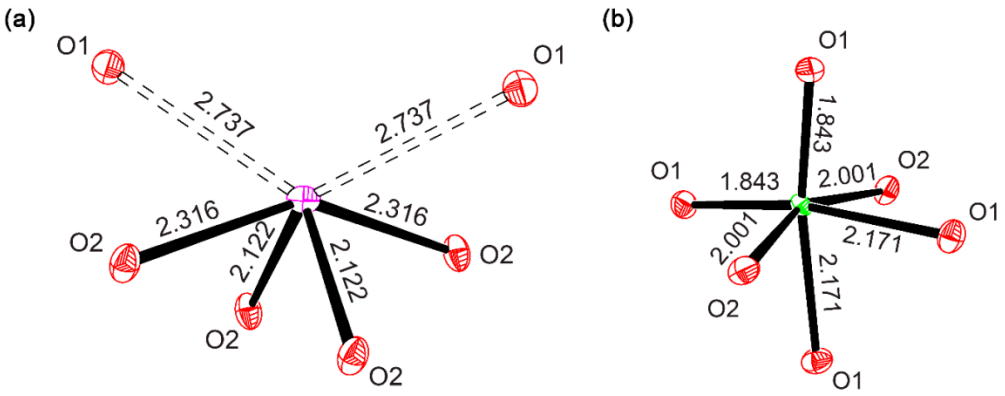


Fig. 5.3.2 Coordination geometries of (a) Bi and (b) Nb, in α-$BiNbO_4$ (red atoms denote oxygen, magenta atoms denote Bi and green atoms denote Nb).

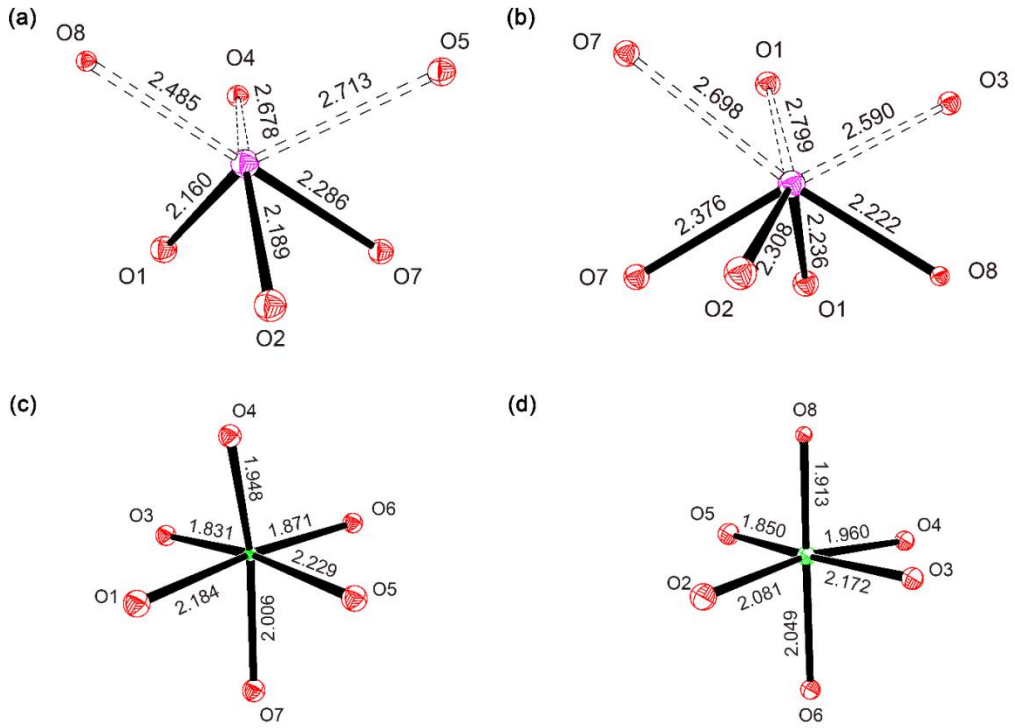


Fig. 5.3.3 Coordination geometries of (a) Bi1; (b) Bi2; (3) Nb1 and (4) Nb2, in the β-$BiNbO_4$ (red atoms denote oxygen, magenta atoms denote Bi and green atoms denote Nb).

### 5.3.2 Effect of annealing on the β to α phase transition

To study the relative temperature stabilities of the α- and β- phases of $BiNbO_4$ phase transition, annealing experiments were performed on the β-phase powder and ceramic. Fig. 5.3.4a shows the XRD data of the β-$BiNbO_4$ powder before and after heat treatment at 700, 800, 850 and 900 °C for 5 h. Additional Bragg peaks attributable to the α-phase are observed in the diffraction patterns for samples annealed at temperatures of 800 °C and above. The relative intensities of these peaks increase with increasing annealing temperature. Fig. 5.3.4b shows the effect of dwell time at 850 °C and clearly indicates that increased dwell time at this temperature leads to increased intensity of the α-phase peaks. The results suggest that the beta to alpha phase transition has relatively slow kinetics at this temperature.

Ceramic samples annealed at 1050 °C for 15 h post sintering showed XRD patterns corresponding to the pure β-phase. No evidence for the appearance of the α-phase was seen in the XRD traces after further annealing at 700, 800, 900 and 950 °C for 5 h (Fig. 5.3.5a). Moreover, annealing for up to 15 h could not stimulate the transition (Fig. 5.3.5b). As reported by Keve [20], the β-phase is more efficiently packed and thus the transformation to the α-phase involves a volume expansion. The generated stress impedes this volume increase and hence suppresses the β to α phase transition in ceramic samples. However, in as-sintered ceramic samples (*i.e.* those without the post annealing step at 1050 °C), complete conversion to the α-phase is observed following annealing at 900 °C for 15 h (Fig. 5.3.6). The reason for the different behavior of the as sintered ceramics may be associated with an initial reduction of $BiNbO_4$, due to the presence of surface and diffused C from the SPS die.

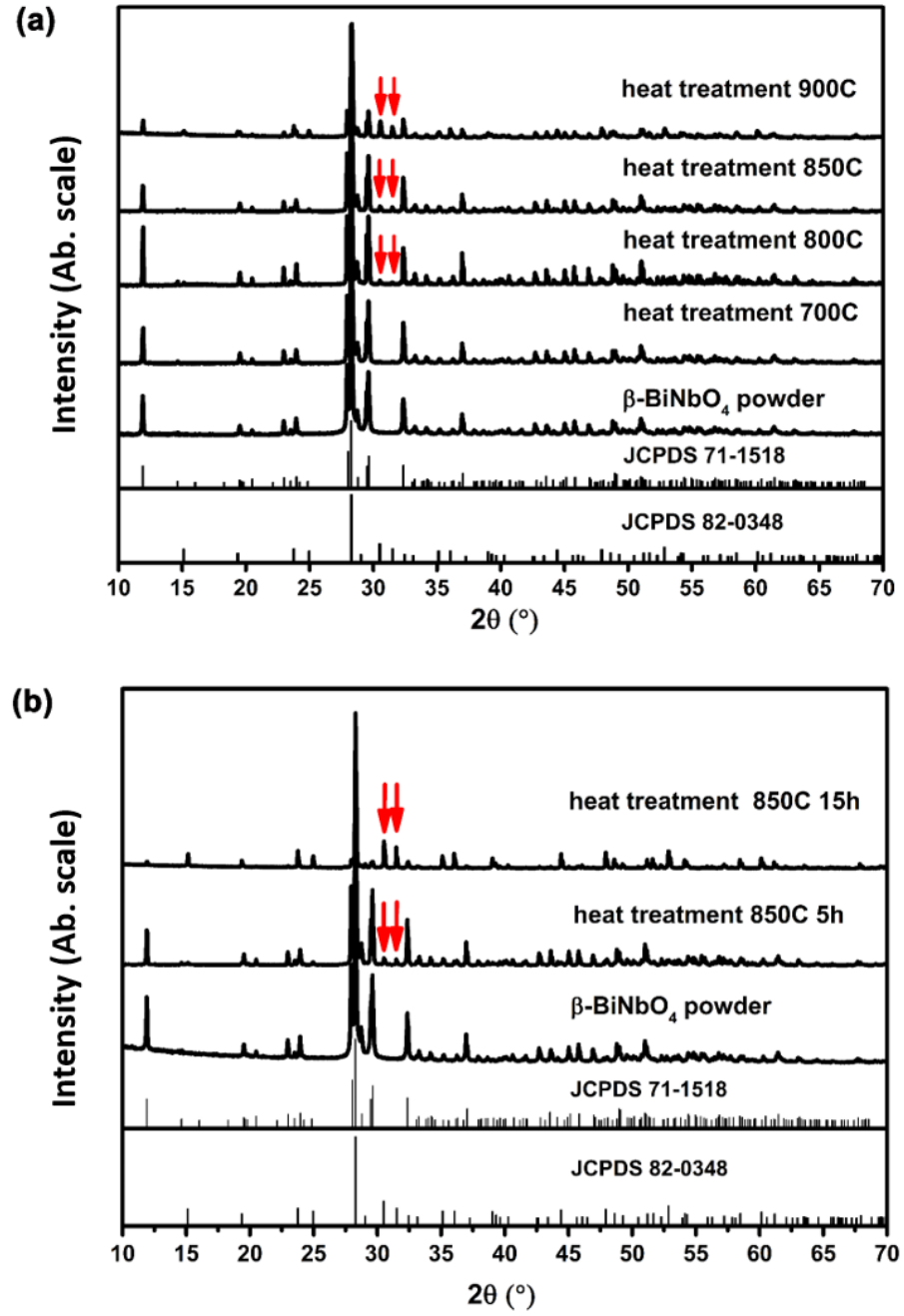


Fig. 5.3.4 XRD for the β-phase powder (a) annealed at 700, 800, 850, 900 °C for 5 h; (b) annealed at 850 °C for 5 h and 15 h. The JCPDS71-1518 and JCPDS 82-0348 correlated to the structures of the β and α phases, respectively.

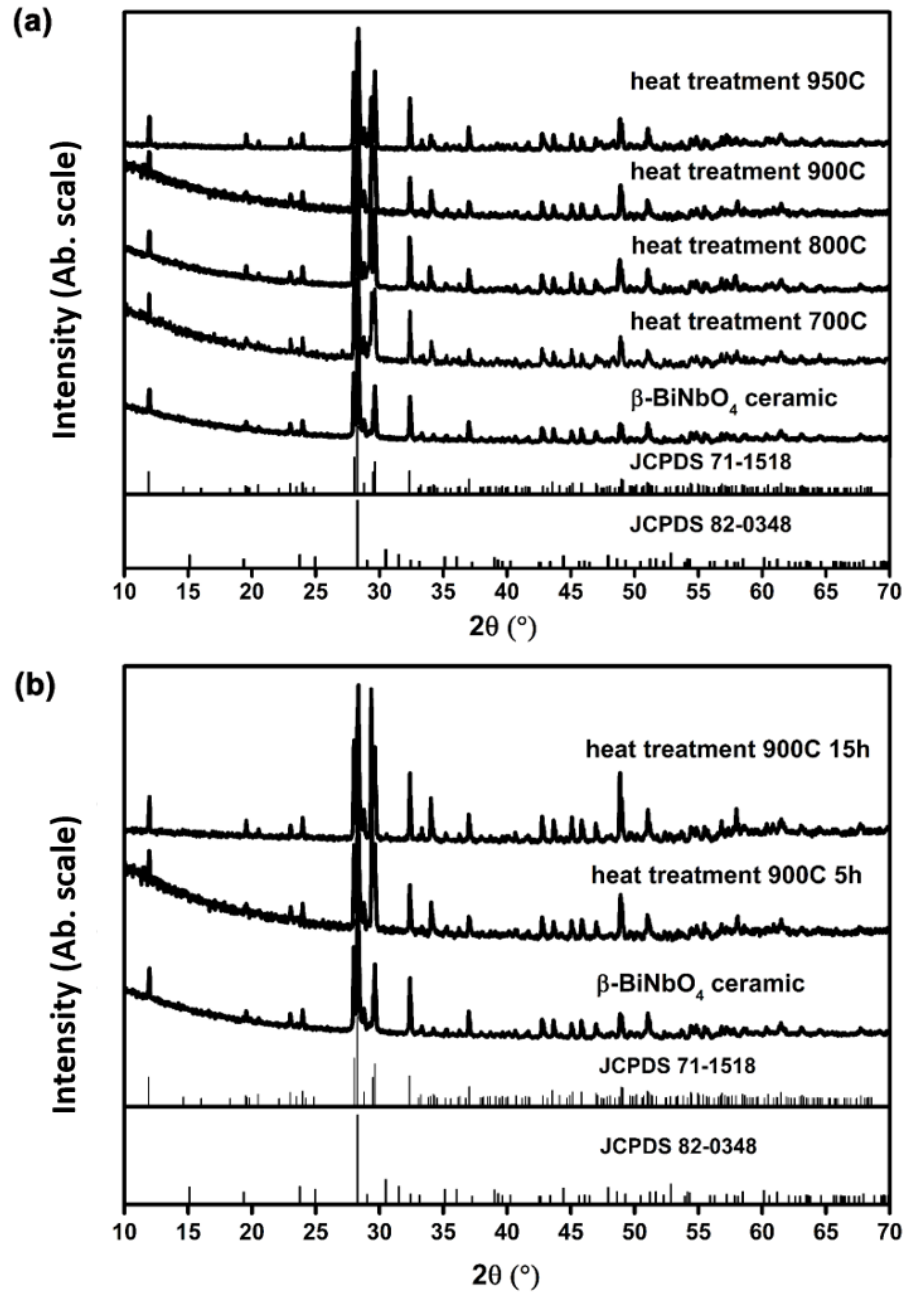


Fig. 5.3.5 XRD for the β-phase bulk ceramics (a) annealed at 700 °C, 800 °C, 900 °C, 950 °C for 5 h; (b) annealed at 900 °C for 5 h and 15 h. The JCPDS71-1518 and JCPDS 82-0348 correlated to the structures of the β and α phases, respectively.

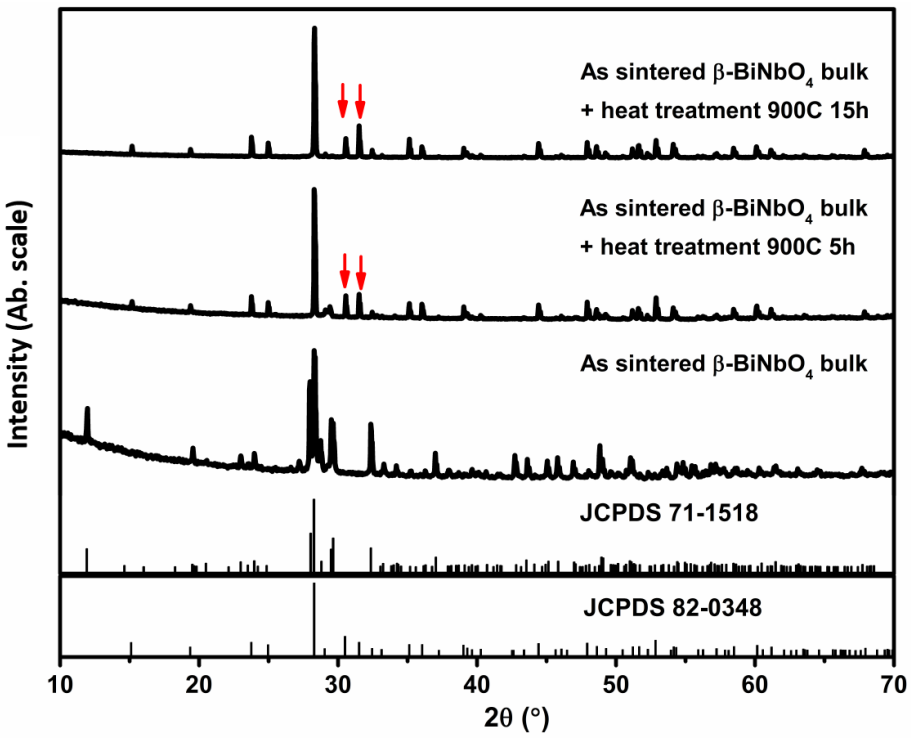


Fig. 5.3.6 XRD of as-sintered β-$BiNbO_4$ ceramic before and after heat treatment at 900 °C for 5 h and 15 h separately. The JCPDS71-1518 and JCPDS 82-0348 correlated to the structures of the β and α phases, respectively.

### 5.3.3 Thermal dependence of structure

Fig. 5.3.7 shows the DSC thermograms for α phase powder and ceramic on heating and cooling. The DSC curve of α-phase powder (Fig. 5.3.7a) showed an endothermic peak onset at 1040 °C on heating, with the corresponding exothermic onset on cooling at 1000 °C. On cooling the structure of the powder post measurement was identified as that of the β-phase (inset graph in Fig. 5.3.7a). Same transitions were observed in α phase ceramic (Fig. 5.3.7b), with the post-measurement structure identified as β-phase (inset graph in Fig. 5.3.7b). The observed thermal events appear to correspond to a phase transition. A high temperature polymorph γ-$BiNbO_4$ has been proposed by Sleight *et al.* [94].

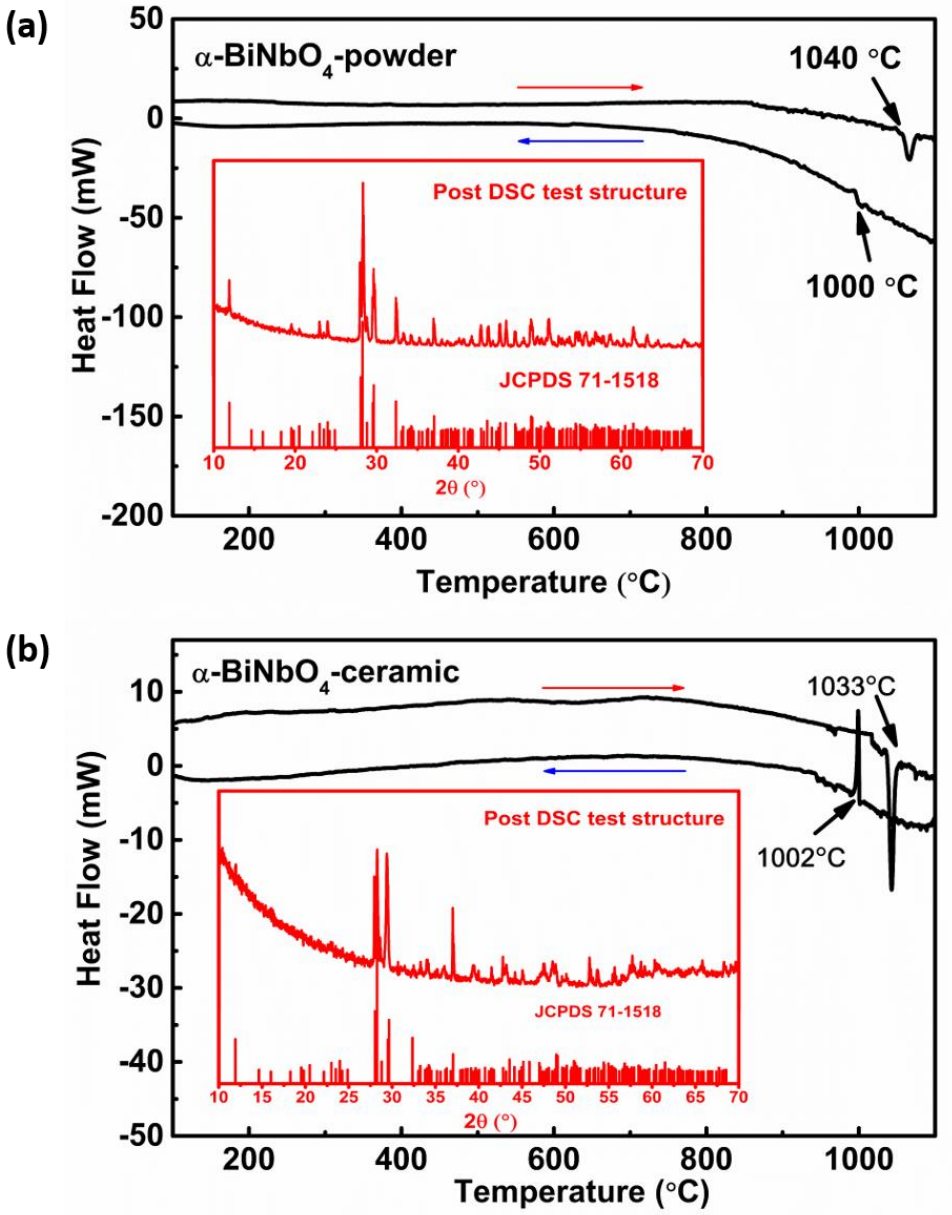


Fig. 5.3.7 DSC of α phase (a) powder and (b) ceramic, with inset XRD results of samples post DSC tests. The JCPDS71-1518 correlated to the structures of the β phase.

Evidence of a phase transition was also seen in the DSC thermogram for the β-phase powder, with the appearance of an endothermic peak at 1000 °C on heating and an exothermic peak at 997 °C on cooling (Fig. 5.3.8a). As for the α-phase powder, the structure of the sample post measurement was that of the β-phase (inset graph in Fig 5.3.8a). The results are consistent with a reversible β ↔ γ phase transition. The fact

that no evidence of the α-phase was seen in both samples post measurement appears to confirm the sluggish kinetics of the β→α transition. The same transition sequences were obtained in β-phase ceramic (Fig. 4.3.8b).

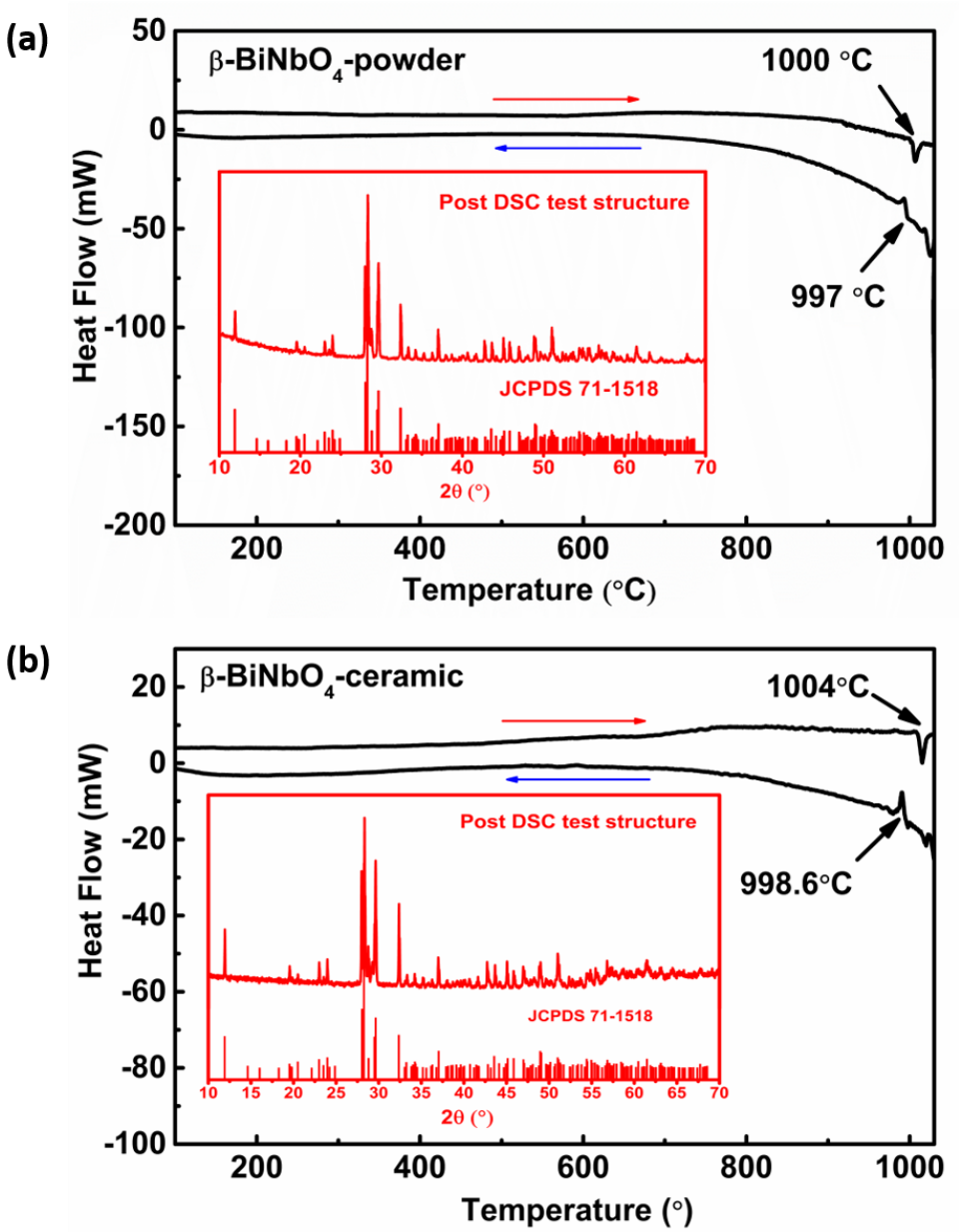


Fig. 5.3.8 DSC of β phase (a) powder and (b) ceramic, with inset XRD results of samples post DSC tests. The JCPDS71-1518 correlated to the structures of the β phase.

### 5.3.4 Variable temperature XRD analysis

Fig. 5.3.9 shows the XRD of the $\alpha$-$BiNbO_4$ powder at selected temperatures. It is observed that the $\alpha$-phase was stable below 1000 °C on heating, while a new phase termed $\gamma$ was revealed at 1100 °C. During cooling, this phase transforms into the β phase at 1000 °C, which remains to room temperature. As the $\gamma$ phase only exists at high temperature, it has been mistakenly considered that the $\alpha$-phase would transform into the β-phase above 1040 °C for decades [20, 21].

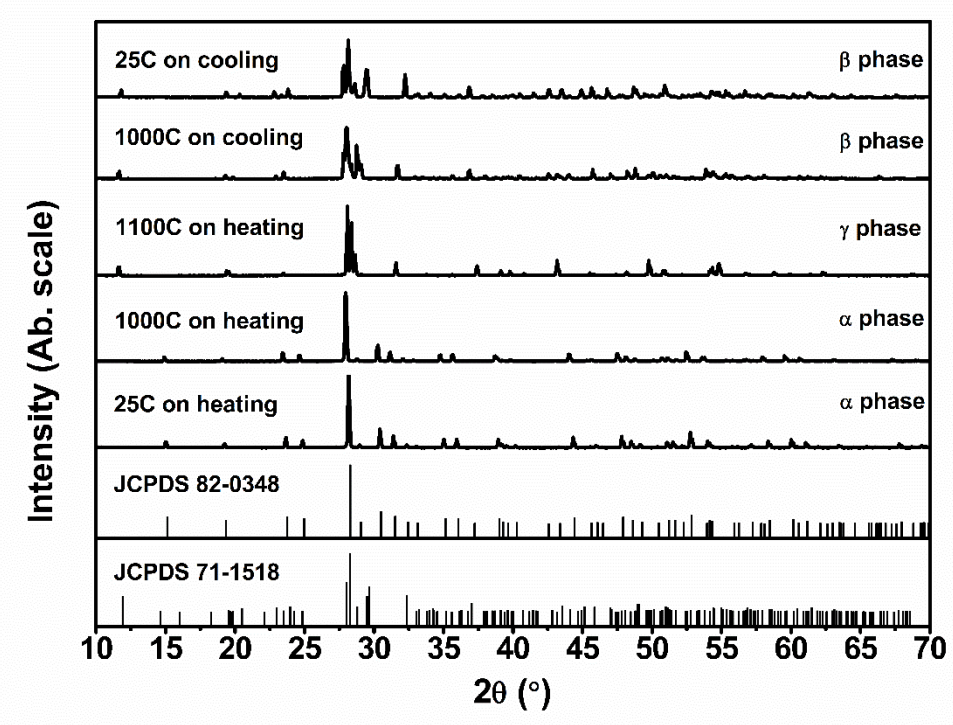


Fig. 5.3.9 High temperature XRD of $\alpha$-$BiNbO_4$ powder at 25, 1000 and 1100 °C on heating and 1000, 25 °C on cooling. The JCPDS71-1518 and JCPDS 82-0348 correlated to the structures of the β and α phases, respectively.

Fig. 5.3.10 shows the high temperature XRD of the β-$BiNbO_4$ powder at selected temperatures. It is observed that the β phase transforms into the $\alpha$ phase above

800 °C. The α-phase was stable up to 1040 °C, with a transition to the γ-phase at 1050 °C. During cooling, the γ-phase transforms back into the β-phase at 1000 °C. The observation of the β to α phase transition in the high temperature XRD was not evidenced in the DSC measurement, due to the sluggishness of the transition and the significant difference in time scales of the two experiments.

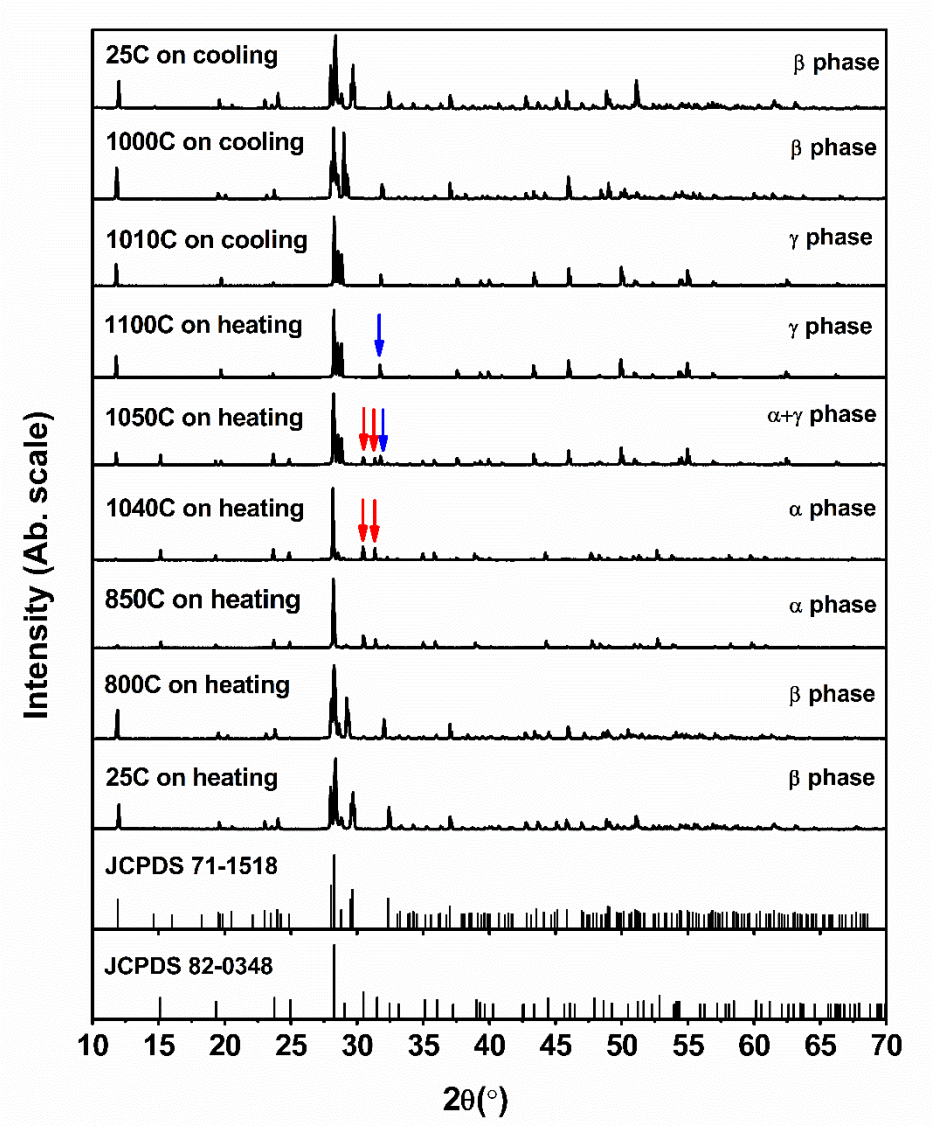


Fig. 5.3.10 High temperature XRD of β-$BiNbO_4$ at 25, 800, 850, 1040, 1050 and 1100 °C on heating and 1000, 25 °C on cooling.

### 5.3.5 Structure of γ-$BiNbO_4$

High resolution powder neutron diffraction of the β-$BiNbO_4$ powder in variable temperatures have been carried out to study the structure of the γ-$BiNbO_4$. Rietveld method was applied to solve the structure of the γ-$BiNbO_4$. The fitted neutron diffraction profiles for the γ-$BiNbO_4$ at 1050 °C is shown in Fig. 5.3.11, with the corresponding crystal and refinement parameters in Table 5.3.3, refined parameters in Table 5.3.4.

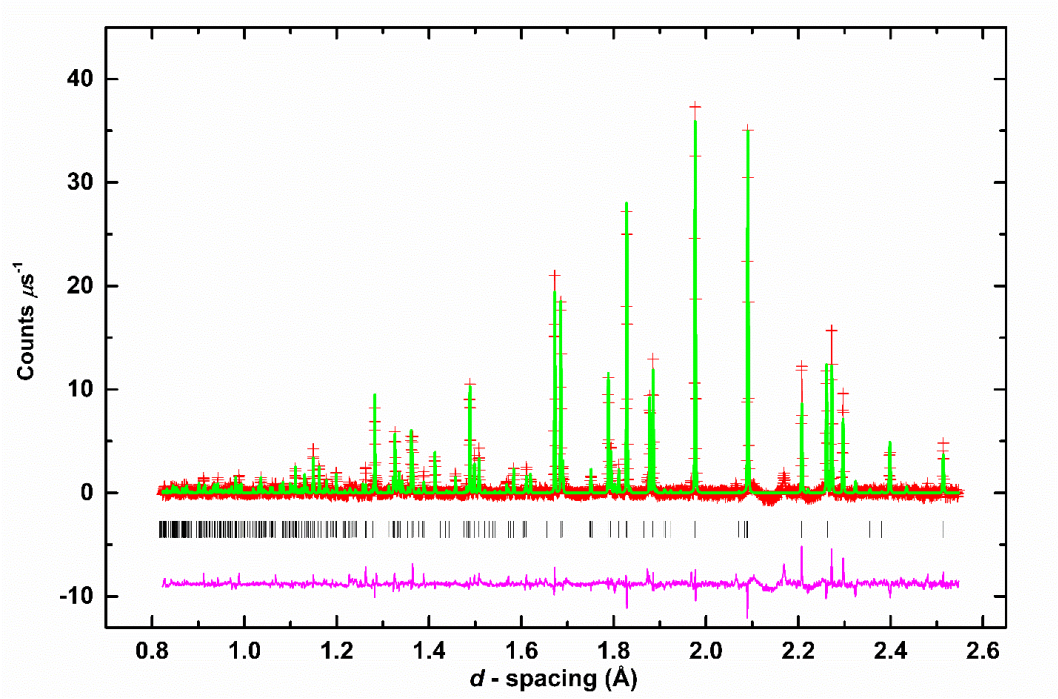


Fig. 5.3.11 Diffraction profiles of the γ-$BiNbO_4$ fitted using conventional Rietveld analysis. High resolution powder neutron diffraction data is shown. Observed (+) and calculated (line) profiles are shown, as well as the difference profile (lower), with reflection positions indicated by markers.

Table 5.3.3 Crystal and refinement parameters of the γ-phase $BiNbO_4$ at 1050 °C

| Chemical formula | $BiNbO_4$ |
|---|---|
| Formula weight | 365.88 g $mol^{-1}$ |
| Crystal system | Monoclinic |
| Space group | $P2_1/c$ |
| Unit cell dimensions | $a$ = 7.79508(14) Å, |
| | $b$ = 5.64993(9) Å, |
| | $c$ = 7.90480(13) Å, |
| | $\beta$ = 104.691(2)° |
| Volume | 336.76 (2) $Å^3$ |
| Z | 4 |
| Density (calculated) | 7.217 g $cm^{-3}$ |
| Sample description | Colourless powder in sealed silica tube |
| R-factors | |
| $R_p$ | 0.0198 |
| $R_{wp}$ | 0.0249 |
| $R_{ex}$ | 0.0110 |
| $R_B$ | 0.2953 |
| $\chi^2$ | 5.357 |
| total number of variables | 79 |
| number of profiles points used | |
| neutron backscattering | 3770 |

Table 5.3.4 Refined Parameters for the γ-phase $BiNbO_4$

| Atom | Site | x | y | z | Occ. | $U_{eqv}$ (Å$^2$) |
|---|---|---|---|---|---|---|
| Bi | 4*e* | 0.3661(5) | 0.7509(22) | 0.0838(9) | 1 | 0.053(2) |
| Nb | 4*e* | 0.1671(4) | 0.2602(17) | 0.3007(10) | 1 | 0.021(2) |
| O1 | 4*e* | 0.1828(7) | 0.2321(24) | 0.0476(15) | 1 | 0.045(2) |
| O2 | 4*e* | -0.0456(36) | 0.4133(37) | 0.2059(31) | 0.423 | 0.022(2) |
| O3 | 4*e* | 0.3948(19) | 0.4796(32) | 0.3464(34) | 0.577 | 0.026(3) |
| O4 | 4*e* | 0.3684(25) | 0.0079(29) | 0.3528(26) | 0.577 | 0.028(4) |
| O5 | 4*e* | 0.3614(17) | 0.1806(24) | 0.2498(18) | 0.423 | 0.028(4) |
| O6 | 4*e* | -0.0523(26) | 0.0977(27) | 0.2049(24) | 0.577 | 0.022(2) |
| O7 | 4*e* | 0.3428(33) | 0.4737(46) | 0.3502(43) | 0.423 | 0.026(3) |

The structure of the γ-$BiNbO_4$ is shown in Fig. 5.3.12. The structure is very closely related to that of the β-phase, showing similar corrugated sheets of corner sharing octahdra separated by $Bi^{3+}$ cations.

Bismuth adopts two types of octahedron. Fig. 5.3.13a shows that Bismuth is in a four-pyramidal coordination with oxygen. Fig. 5.3.13b shows that Bismuth is in a five-coordinate geometry with oxygen. The disorder in the oxide ion positions results in two types of niobate octahedra (Fig. 5.3.13c-d), with slightly different degrees of distortion (cf beta phase).

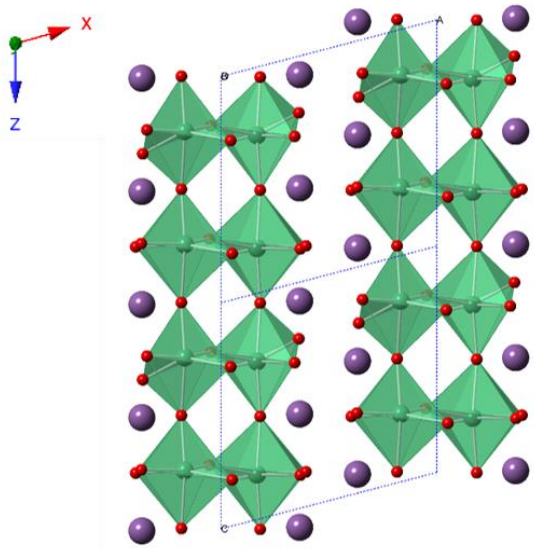


Fig. 5.3.12 The structure schematic of the γ-$BiNbO_4$ (green atoms denote Nb, purple atoms denote Bi and red atoms denote oxygen).

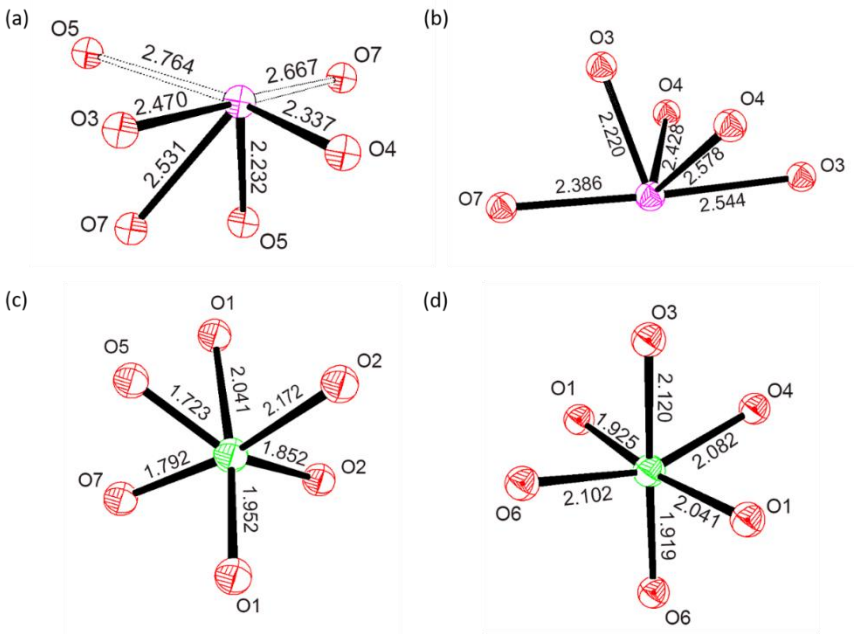


Fig. 5.3.13 Coordination geometries of (a) Bi1 and Bi2; (b) Bi3 and Bi4; (3) Nb1 and Nb2; (4) Nb3 and Nb4, in the γ-$BiNbO_4$ (red atoms denote oxygen, magenta atoms denote Bi and green atoms denote Nb).

### 5.3.6 Dielectric nature of the α- and β-phase

The temperature dependence of dielectric properties of the α-phase at different frequencies (1 kHz, 10 kHz, 100 kHz, 500 kHz and 1 MHz) is given in Fig. 5.3.14; (a) relative permittivity as a function of temperature on heating; (b) relative permittivity as a function of temperature on cooling; (c) loss as a function of temperature on heating; (d) loss as a function of temperature on cooling.

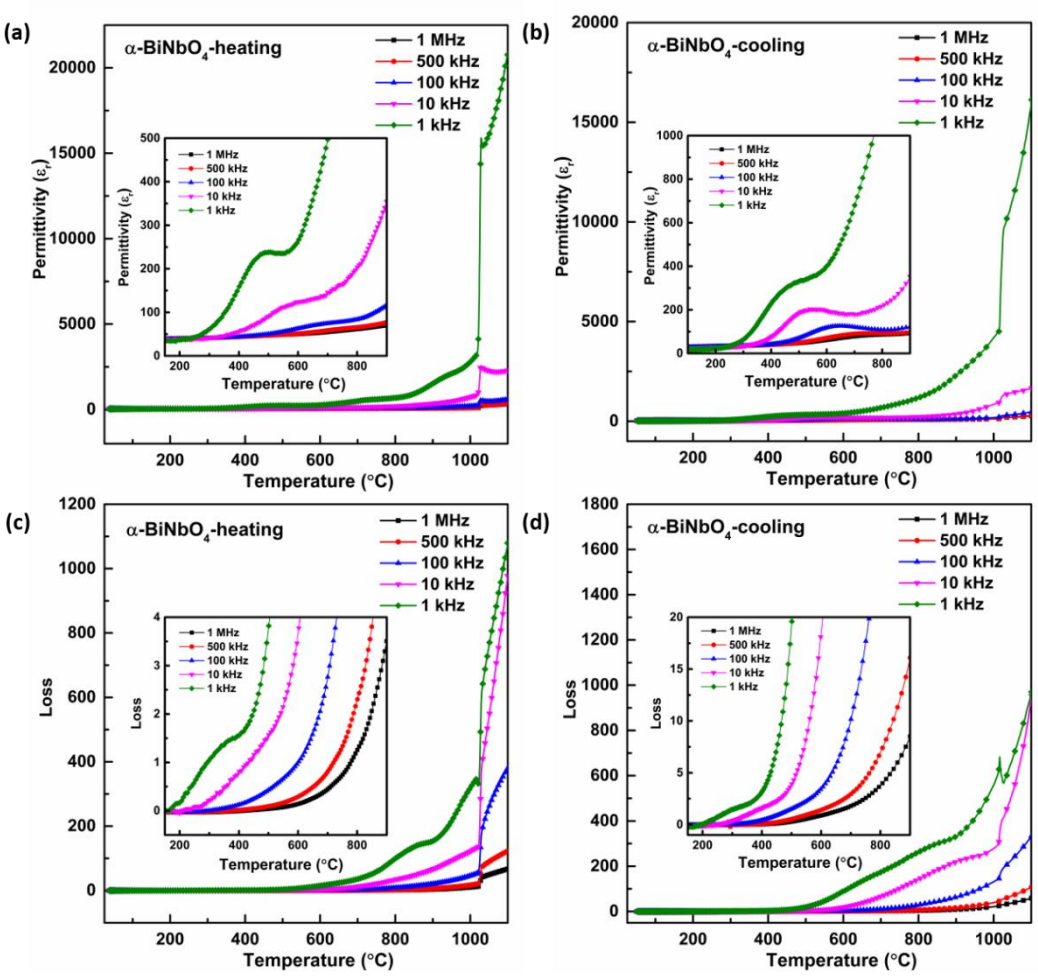


Fig. 5.3.14 Temperature dependent dielectric properties of the α-$BiNbO_4$ as (a) permittivity on heating; (b) permittivity on cooling; (c) loss on heating; (d) loss on cooling, at 1 kHz, 10 kHz, 100 kHz, 500 kHz and 1 MHz.

Frequency-independent peaks in permittivity peak and loss can be seen at *ca*. 1030 °C on heating, which correspond to the $\alpha$ to $\gamma$-phase transition as discussed in Fig. 5.3.7 and Fig. 5.3.9. The frequency-independent permittivity peak and loss peak were seen at 1000 °C on cooling and further support the $\gamma$ to β-phase transition. Meanwhile, a relaxation behavior was observed at temperature range of 400 °C to 700 °C.

The temperature dependence of dielectric properties of the β-phase at different frequencies (1 kHz, 10 kHz, 100 kHz, 500 kHz and 1 MHz) is given in Fig. 5.3.15; (a) relative permittivity as a function of temperature during heating; (b) relative permittivity as a function of temperature during cooling; (c) loss as a function of temperature during heating; (d) loss as a function of temperature during cooling.

A substantial rise in permittivity accompanied by a loss peak around 1000 °C on heating and a prominent descend in permittivity with a loss peak on cooling at a temperature lower than that observed on heating were responsible for the mentioned reversible $\beta$ to $\gamma$ phase transition. The thermal hysteresis observed is related to the first order transition. In addition, permittivity peaks with frequency dispersion were inspected between 300 to 800 °C on heating and cooling in β-$BiNbO_4$ ceramic as well. According to Zhou's explanation [170], the permittivity peak at 768.5 °C and related loss peak at 680 °C in 1 kHz were counted to the β to $\alpha$ phase transition, besides the visible frequency dispersion of permittivity and loss peak. However, considering the diffusive transition from β to $\alpha$ phase and stability of oxygen, electronic conductivity attributed to the reduction of $Nb^{5+}$ to $Nb^{4+}$ is more likely to account for the dielectric relaxation between 300 and 800 °C.

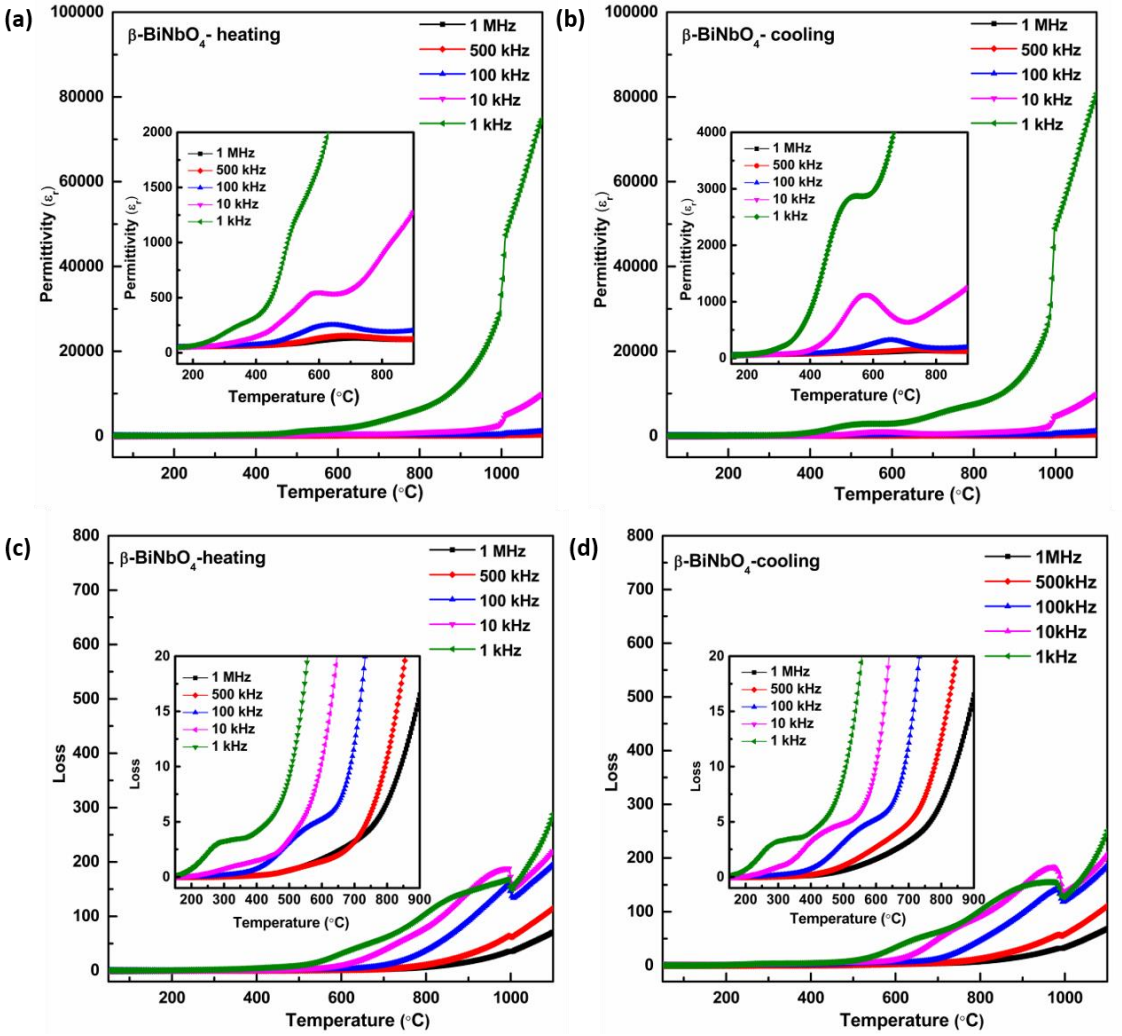


Fig. 5.3.15 Temperature dependent dielectric properties of the β-$BiNbO_4$ as (a) permittivity on heating; (b) permittivity on cooling; (c) loss on heating; (d) loss on cooling, at 1 kHz, 10 kHz, 100 kHz, 500 kHz and 1 MHz.

### 5.3.5 Antiferroelectric nature of the α and β phase

The hypothetical AFE characteristics [22] of the α phase $BiNbO_4$ were studied. In Fig. 5.3.7 no peak was detected around 360 and 570 °C, the temperature at which were assumed to be corresponding to the AFE to FE and the FE to PE phase transitions,

respectively [22]. Furthermore, the high temperature XRD (see Fig. 5.3.9) show that the structure remains to be α phase below 1000 °C. The broad permittivity peaks in the range 300 to 800 °C shift with increasing frequencies on both heating and cooling in agreement with Popolitov's results [171]. This dielectric relaxation is more likely related to the motion of oxygen vacancies [172] rather than to AFE to FE to PE transition series.

The current-polarization-electric field (I-P-E) hysteresis loops carried out on α phase $BiNbO_4$ ceramic are shown in Fig. 5.3.16. The I-E loop shows a square shape which was mainly contributed by capacitive current. The P-E loop is highly linear with no hysteresis and without evidences of AFE-FE transitions. The energy density obtained is 0.03 J $cm^{-3}$ (error bar ±0.001).

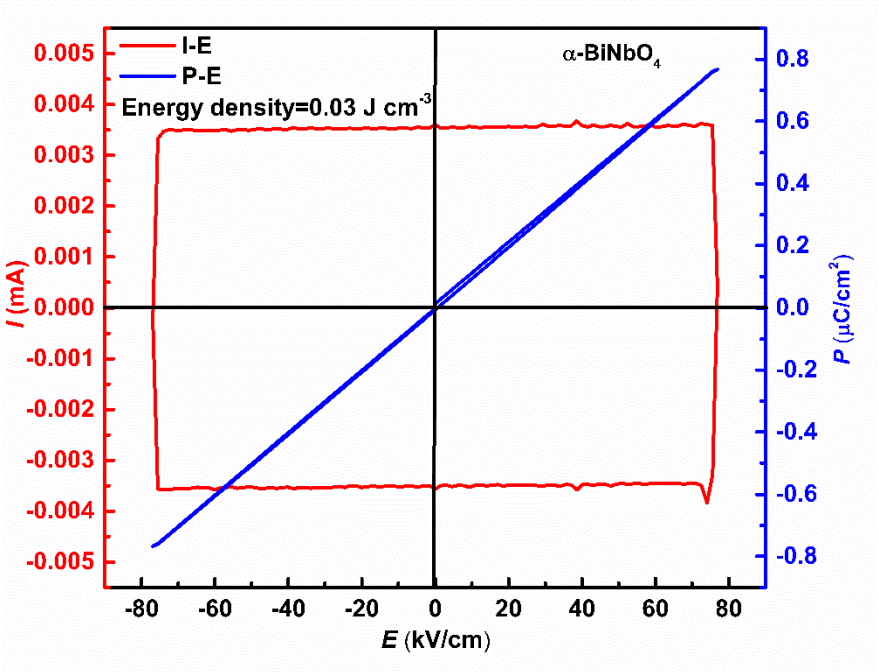


Fig. 5.3.16 The I-E and P-E hysteresis loop of the α-$BiNbO_4$.

To identify the AFE nature of the β phase $BiNbO_4$, thermal dynamic behavior and dielectric behavior of β-$BiNbO_4$ have been analyzed. No AFE to FE and FE to PE phase

transition was found in β-$BiNbO_4$ using DSC (see Fig. 5.3.8) and high temperature XRD (see Fig. 5.3.10). According to I-E loop and P-E loop of β-$BiNbO_4$ (see Fig. 5.4.17), no antiferroelectric like polarization-electric field hysteresis loop was formed either. It is known that most antiferroelectrics would break down before the critical field for electric field-induced antiferroelectric to ferroelectric transition [9, 173], which could be another possibility for the absence of the double hysteresis loop. The energy density obtained is 0.04 J $cm^{-3}$ (error bar ±0.001).

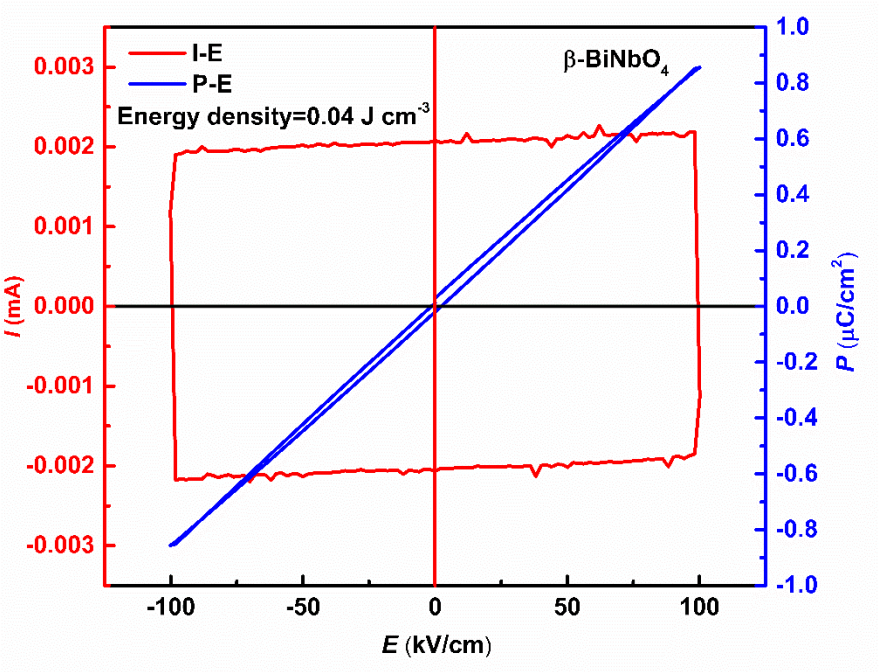


Fig. 5.3.17 The I-E and P-E hysteresis loop of the β-$BiNbO_4$.

## 5.4 Conclusions

In conclusion, we have generally studied the phase transitions in the α- and the β-$BiNbO_4$ and have successfully addressed this longstanding issue. Moreover, we revealed a high temperature γ phase, the structure of which is similar to that of the β phase, showing corrugated sheets of corner sharing octahdra separated by $Bi^{3+}$ cations. It has a monoclinic structure with a space group $P2_1/c$. The lattice parameters are: $a$= 7.795 Å, $b$=5.649 Å, $c$=7.904 Å, $\beta$ = 104.691(2)°.

The phase relationship among the α-, β- and γ- $BiNbO_4$ has been clarified as well. It is observed here that the α phase is stable until 1040 °C, while above 1040 °C, it first transforms into a high temperature γ phase, which in turn transforms into β phase at around 1000 °C during cooling. Meanwhile, a reversible first-order β to γ phase transition is observed at around 1000 °C for both powder and ceramic when no incubation processed on heating. On contrary, under the condition of incubation above 800 °C, it is found that β phase powder would transform into α phase at around 800 °C, followed by an α to γ transition at about 1040 °C, and thereafter, γ again converted into β phase on cooling. As a result, α phase is the low temperature stable phase while the γ phase is the high temperature stable phase. The β phase $BiNbO_4$ is a metastable phase according to the high thermo-coefficient obtained in the refinement.

It is therefore clarified that the β phase powder could be converted back to α phase by heating at a certain temperature range (800 °C-1000 °C) under a certain time. This is proved to be a diffusive transition, as it could be influenced by temperature and time. Higher temperature and longer dwelling time could accelerate the β to α transition in

powder. However, this transformation could not be obtained in the β phase ceramics. It is suggested the inner stress suppressed the phase transition to inhibit the volume change. It is interesting that reduced atmosphere and graphite could diminish the transition barrier in ceramic and prompt the transformation.

The energy density obtained in the ceramics was quite low, due to a low breakdown field, low permittivity value and absence of electric field-induced AFE-FE transformation.

# Chapter VI. The Incipient Ferroelectric: $TiO_2$

## 6.1 Introduction

The $TiO_2$ presents three crystal structures, namely anatase, brookite and rutile. The rutile structure , is the most stable and exhibits high static permittivity (*ca.* 100) and low dielectric loss [174]. Titanium oxide has been intensively studied for a wide range of applications, including photocatalysis [175, 176], solar cells [177, 178] and GHz radar microwave absorbing materials [179]. However, the synthesis of $TiO_2$ is very sensitive to temperature and oxygen partial pressure. It is easily reduced to oxygen-deficient non-stoichiometric $TiO_{2-x}$ (where x is the oxygen deficiency $O_d$) at high temperature and/or low oxygen partial pressure [180, 181]. Complex defect structures are formed due to the reduction [101]. They act as donor centers and contribute to the n-type semiconductor behavior of $TiO_2$ [113].

Here we studied wide range dielectric properties as well as the electric behavior of the $TiO_2$ ceramics using both conventional sintering method and spark plasma sintering method. The potential of the $TiO_2$ ceramics being applied in the high-data-rate THz communication field as well as high energy density storage capacitor has been further developed.

## 6.2 Experimental procedures

### 6.2.1 Sample preparation

$TiO_2$ (Aldrich, 99.9%) ceramics were produced by Spark Plasma Sintering (HPD 25/1 FCT, German) and conventional sintering method using a muffle furnace (SX2-5-12) separately. In SPS method, pure $TiO_2$ ceramics were sintered at 1050 °C, 1200 °C and 1250 °C with a mechanical pressure of 80 MPa for 3 min respectively. The heating rate and cooling rate were both 100°C $min^{-1}$. Samples were then annealed in air at 100 °C below their sintering temperature for 20 h to remove carbon contamination and compensate oxygen. In conventional sintering, $TiO_2$ powder (analytical reagent, Shantou, China) was mixed with 1 wt% ZnO (analytical reagent, Shantou, China) as sintering aid by planar ball milling (QM-3P2) for 4 h. 3 wt% Polyvinyl Acetate (PVA) was used as binding agent. Green pellets were prepared and then fired at 600 °C for 1 hour to remove the binder. Samples were sintered at different temperatures, namely, 1210, 1250 and 1300 °C for 3 h in air. Densities were obtained using the Archimede's method.

### 6.2.2 Characterization

The thermal etching temperature for each sample has been listed in Table 6.2.1. Each sample was etched for 15 min.

Table 6.2.1 The thermal etching temperature for each sample

| Sample | CS1210 | CS1250 | CS1300 | SPS1050 | SPS1200 | SPS1250 |
|---|---|---|---|---|---|---|
| Etching T (°C) | 1150 | 1100 | 1100C | 1000 | 1050 | 1100 |

The microstructure of the specimens was observed by scanning electron microscope (FEI, Inspect F, Hillsboro, OR). Phase purity was determined by X-ray diffraction (XRD, X'pert Pro, PANalytical, Almelo, Netherlands) at room temperature over the $2\theta$ range 10° to 70°, in steps of 0.034°, with an effective scan time of 50 s per step, using Ni filtered Cu-K$\alpha$ (1.5418 Å) radiation. Raman spectroscopy (Renishaw Ramascope, He-Neon Laser-633 nm) was performed on ceramics. The electron energy states of elements in the samples were determined by X-ray photoelectron spectroscopy (XPS, ESCALAB MK II, VG Scientific). The XPS peaks were fitted using Origin 9.0 software.

### 6.2.3 Dielectric measurement

The temperature dependence of dielectric behavior of the samples was measured from 25 °C to 850 °C at selected frequencies (1 MHz, 500 kHz, 100 kHz, 10 kHz, 1 kHz), using an Agilent 4284A LCR meter connected to a furnace (Lenton, LFT).

The THz dielectric behavior of the samples was measured at a frequency range of 0.22-0.325 THz using a VNA2-driven quasi-optical transmission meter [182].

## 6.3 Results and discussion

### 6.3.1 Structure

Rutile $TiO_2$ ceramics have been produced using both conventional sintering method and spark plasma sintering method. The structure was identified by XRD (Fig. 6.3.1).

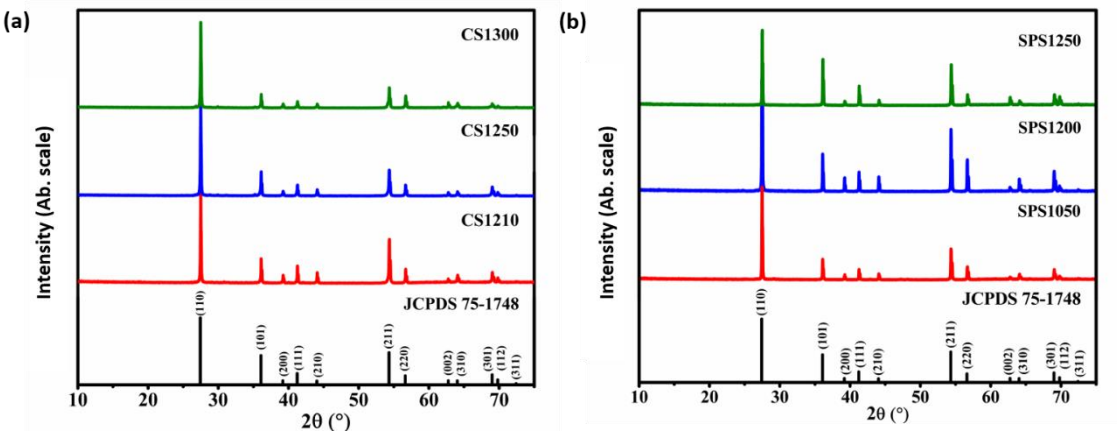


Fig. 6.3.1 XRD of (a) conventional sintering ceramics (CS1210, CS1250 and CS1300); (b) SPS ceramics (SPS1050, SPS1200 and SPS1250).

The densities of the samples are listed in Table 6.3.1. All the samples have a relative density above 95%. The density of the conventional sintered samples decreased with the increase of temperature to 1300 °C due to over-sintering. The density of SPS samples increased from SPS1050 to SPS1200, but decreased in SPS1250 due to over sintering.

Table 6.3.1 Density of samples sintered by both methods (with an error bar $\pm$0.02)

| | CS1210 | CS1250 | CS1300 | SPS1050 | SPS1200 | SPS1250 |
|---|---|---|---|---|---|---|
| Density ($g\ cm^{-3}$) | 4.18 | 4.17 | 4.12 | 4.038 | 4.17 | 4.13 |

### 6.3.2 Microstructure

Fig. 6.3.2 shows the SEM images of the $TiO_2$ ceramics. The microstructure of a fracture surface for the CS1210 sample is shown in Fig. 6.3.2a. There is a high density of trapped porosity, and sintering aid (marked as S) can be seen as second phase. Fig. 6.3.2b shows the microstructure of the CS1210 sample thermally etched at 1150 °C. The grain size is quite large (~25 μm). Pores can be seen within the grains and at the grain boundaries. The trapped pores were produced by abnormal grain growth. The observed precipitates (marked as P), were formed by thermal etching. [183, 184] Porosity, second phases (sintering aid), and interfaces (grain boundary) would increase dielectric loss [95].

Fig.6.3.2c shows the microstructure of the SPS1050 sample. It has a small grain (~1 μm) and pore size (~0.2 μm), and trapped porosity. Fig.6.3.2d shows the microstructure of the SPS1200 sample. It has a small and homogeneous grain size (~3 μm). Fig.6.3.2e shows the microstructure of the SPS1250 sample. The grain size (~7 μm) is larger than that of the SPS1200 sample. The sample is slightly over-sintered as evidenced by some abnormal grain growth. Trapped porosity was barely seen in the SPS1200 and SPS1250 samples, but precipitates were additionally observed. Fig.6.3.2f shows the

microstructure of a fracture surface of SPS1250. No precipitation was observed, since it only formed by the thermal etching.

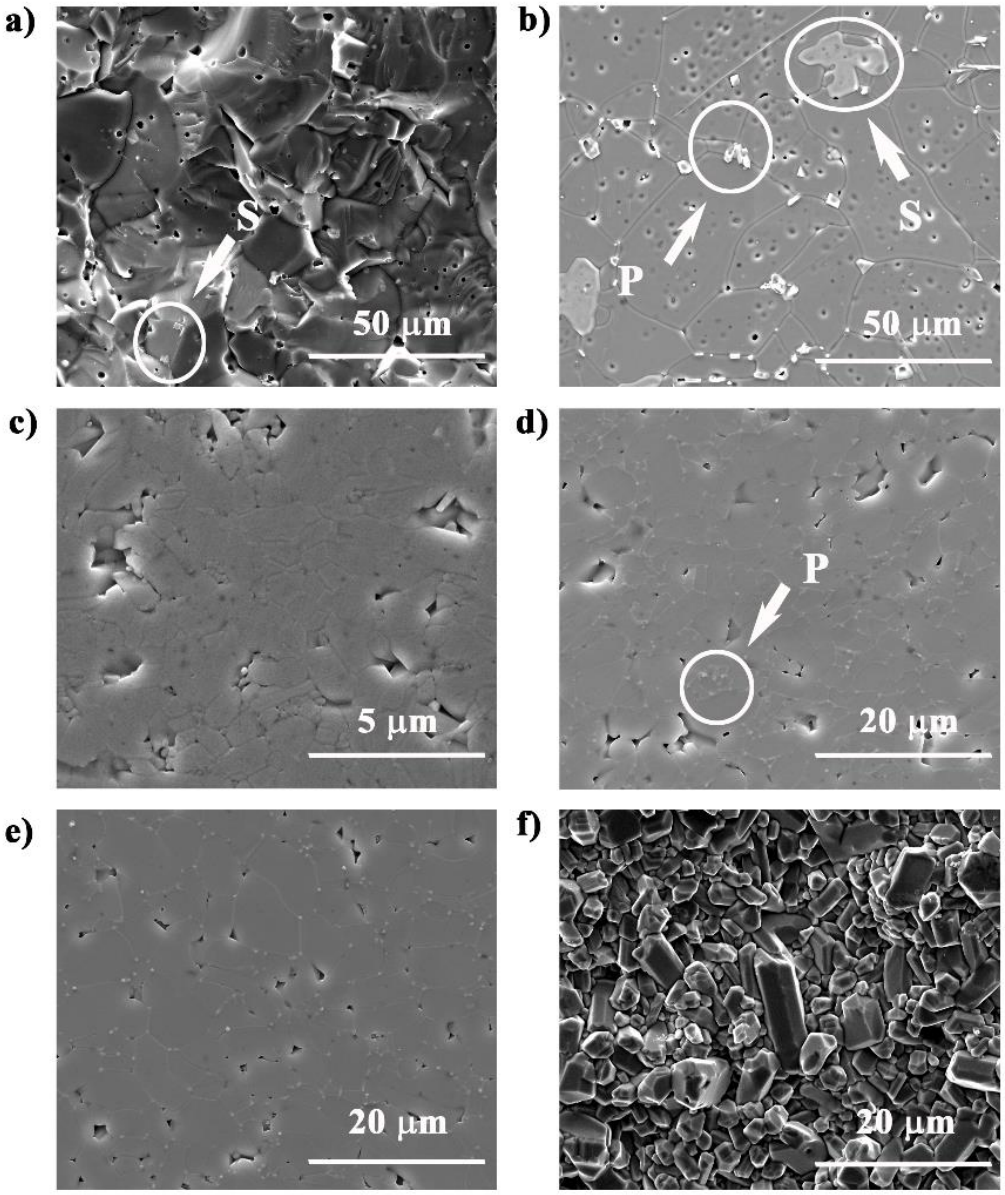


Fig. 6.3.2 The SEM images of a) fracture surface of CS1210; b) CS1210 thermally etched at 1150 °C; c) SPS1050 thermally etched at 1000 °C; d) SPS1200 thermally etched at 1050 °C; e) SPS1250 thermally etched at 1100 °C; f) fracture surface of SPS1250 (S denotes sintering aid; P, precipitation).

### 6.3.3 Defect chemistry

Fig. 6.3.3a shows the Ti 2p X-ray photoelectron spectroscopy (XPS) peaks of the CS samples. The Ti 2p3/2 peak shifts slightly towards a lower binding energy with increasing sintering temperature. Fig. 6.3.3b shows the O 1s peaks of the CS samples. The O 1s peak of CS1210, as an example, has been fitted with three peaks using the Lorentzian-Gaussian model [185]. The one at 529.98 eV represents oxygen in the intrinsic site; the peak at 531.5 eV is related to oxygen vacancies; and the peak at 532.65 eV corresponds to the oxygen absorbed on the surface of the sample [186]. The amount of oxygen vacancies decreased in CS1250 compared to that in CS1210 and then increased in CS1300. Fig. 6.3.3c shows the Ti peaks of the SPS samples. The Ti 2p3/2 peak positions of SPS1050 and SPS1200 are the same, but it tends to slightly shifts towards a lower binding energy in SPS1250. Fig. 6.3.3d shows the O 1s peaks of the SPS samples, with a fitted example of SPS1050. The amount of oxygen vacancies increased from SPS1050 to SPS1200 and then experienced a subtle decrease in SPS1250.

The shift of Ti 2p3/2 peaks in the CS samples to a lower binding energy is assumed to be due to the lowering of valence state of Ti cations from $Ti^{4+}$ to $Ti^{3+}$, which indicates the reduction of $TiO_2$ and formation of $Ti^{3+}$ interstitials at high sintering temperature [187]. The intensity of the oxygen vacancy peak increased with increasing sintering temperature, due to the higher thermal activity of oxygen. The formation of oxygen vacancies would lead to non-stoichiometry in the compound. However, a diminishing of oxygen vacancy is observed in CS1250 (Fig. 6.3.3b). The formation of crystallographic shear planes in $TiO_2$ is suggested to account for the elimination of

oxygen vacancy. According to the Anderson and Hyde model [115], oxygen vacancies would aggregate into disks and then collapse to a shear-plane nucleus bounded by a dislocation loop. The shear plane would grow by trapping vacancies on the loop. Crystal structure then changes from corner-shared octahedrals to edge-shared octahedrons or edge-shared octahedrons to plane-shared octahedrons [115]. It is reported that, in extremely reduced $TiO_2$, crystallographic shear planes would exist as an ordering structure with a regular spacing, resulting in a homologous series of stoichiometrically-defined intermediates with general formula $Ti_nO_{2n-1}$, also known as Magnéli phase [188]. However, crystallographic shear planes were also observed in pure $TiO_2$ ceramics, conventionally sintered in air [189]. Note that, in slightly reduced $TiO_2$, crystallographic shear planes could exist randomly in limited nano regions (bounded by dislocation rings) from the clustering of oxygen vacancies, [190].

The formation of crystallographic shear planes in CS1250 are due to the aggregation of oxygen vacancies by a high sintering temperature. However, the shortening of cation-cation distance by crystallographic shear planes leads to an enhancing cation-cation repulsion, which would impede the further growth of crystallographic shear planes [191]. Meanwhile, the formation of oxygen vacancies is temperature-dependent. As the sintering temperature increases, the rate of production oxygen vacancies outweighs that of eliminating oxygen vacancies by crystallographic shear planes. As a result, the amount of oxygen vacancy increased again in CS1300. The diminishing of oxygen vacancies was also observed in SPS1250 (Fig. 6.3.3d), suggests the formation of crystallographic shear planes at high temperature.

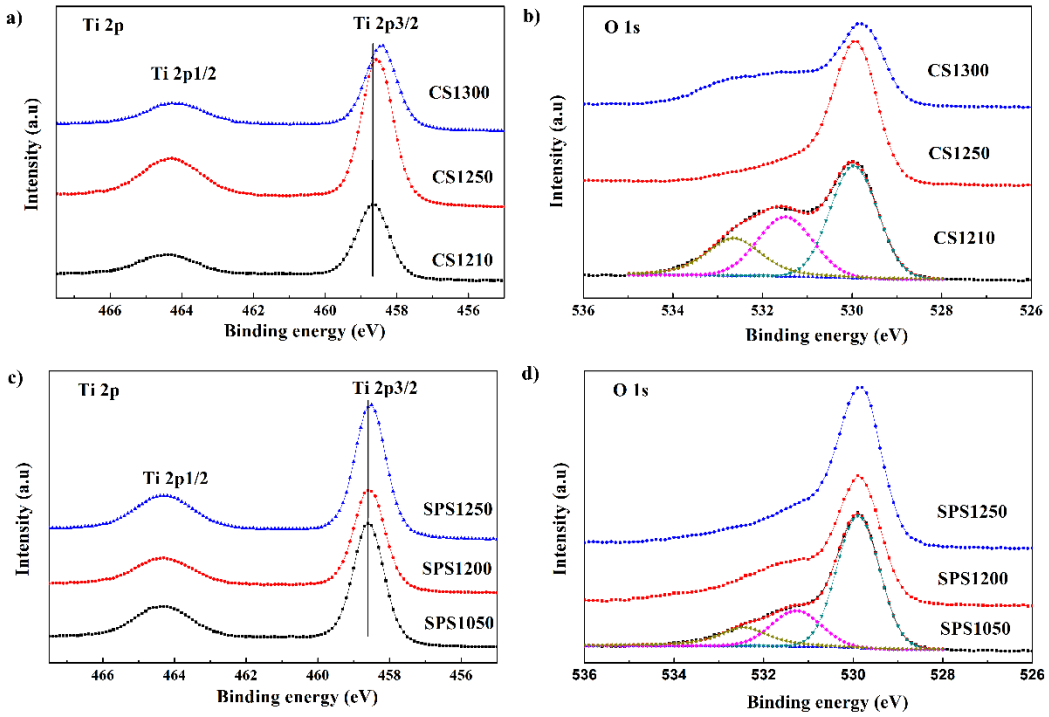


Fig. 6.3.3 XPS of (a) Ti 2p peaks of CS samples; (b) O 1s peaks of CS samples with fitted CS1210; (c) Ti 2p peaks of SPS samples; (d) O 1s peaks of SPS samples with fitted SPS1050.

Fig. 6.3.4a shows the Raman spectra of CS samples. The peak at *ca.* 142 $cm^{-1}$ is identified as the $B_{1g}$ mode, the peak at *ca.* 450 $cm^{-1}$ is the $E_g$ mode and the peak at *ca.* 608 $cm^{-1}$ is the $A_{1g}$ mode. The broad peak at 250 $cm^{-1}$ corresponds to a second order phonon mode [97]. The $E_g$ mode is associated with a planar O-O vibration mode, while the $A_{1g}$ and $B_{1g}$ modes are associated with a Ti-O stretching vibration. The oxygen deficiency in these planes would affect the $E_g$ mode more than the $A_{1g}$ and $B_{1g}$ modes [97, 192]. Therefore, only the change of the $E_g$ mode is considered here. The peak position of the $E_g$ mode was carefully identified and the full width of half maximum (FWHM) was calculated for CS samples (Fig. 6.3.4b). The peak position of the $E_g$ mode red shifted and the peak becomes broader as the sintering temperature increases [97]. Raman spectra of the SPS samples are shown in Fig. 6.3.4c. The $E_g$ peak position and

FWHM of the SPS samples are shown in Fig. 6.3.4d. The peak position blue shifts from SPS1050 to SPS1200, but it decreases again for SPS1250. The FWHMs keep decreasing as the sintering temperature increases.

The red shift of phonon energies (softening) and the broadening of phonon energies are due to anharmonic behavior of the crystals. Anharmonicity reduces crystal stability, degrades desired optical and dielectric and thermal transport properties and, cause phonon damping [193, 194]. Phonon softening of the CS samples, with increasing sintering temperature (Fig. 6.3.4b), indicated an increase of crystal instability linked with crystallography shear planes. The broadening of phonon energies was caused by the scattering of phonons by defects, which could further increase phonon damping, leading to high dielectric loss. The softening of $E_g$ mode and broadening of peak width in SPS1050 indicated the incomplete crystallization accompanied with anharmonicity. The decreasing of FWHM in the samples SPS1200 and SPS1250 could cause a lowering of dielectric loss. The phonon stiffening in SPS1200 demonstrates the increase of crystal stability and the diminishing effect of anharmonicity. SPS1250 experienced a phonon softening due to the appearance of crystallographic shear planes as mentioned in Fig. 6.3.4e.

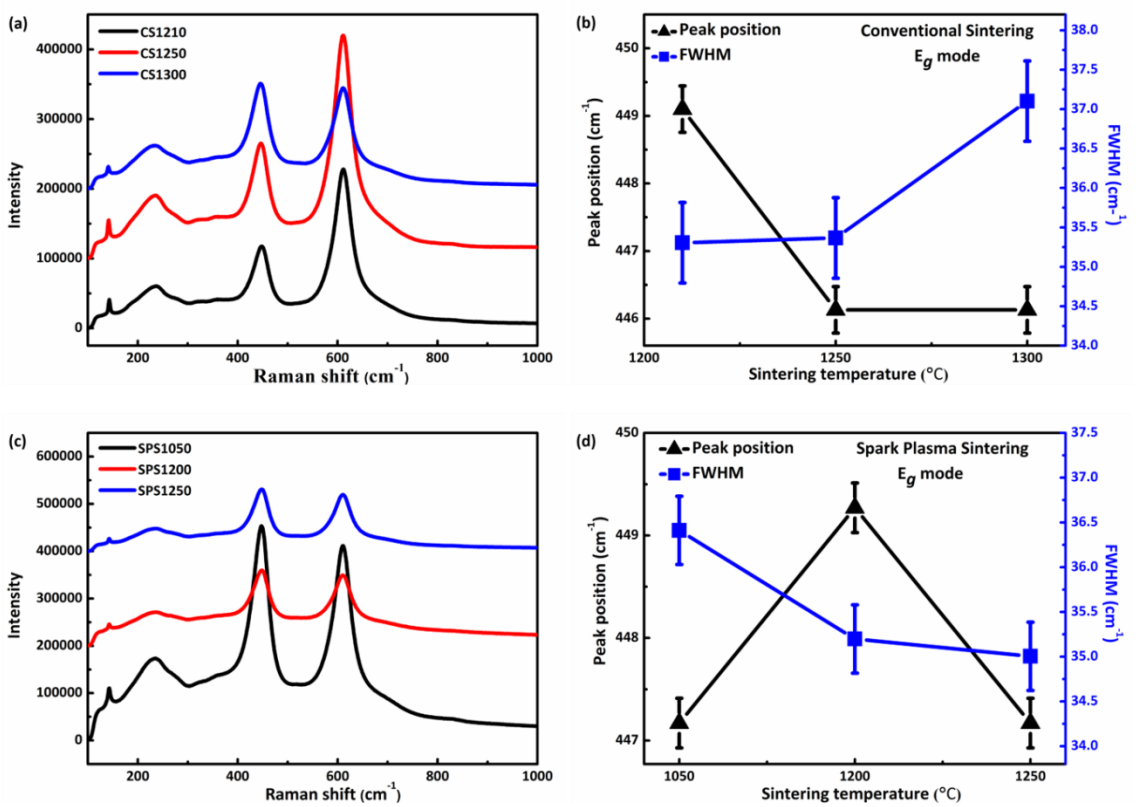


Fig. 6.3.4 (a) Raman spectra of conventional sintering samples; (b) peak position and FWHM of $E_g$ vibration mode of conventional sintering samples; (c) Raman spectra of SPS samples; (d) peak position and FWHM of $E_g$ vibration mode of SPS samples.

### 6.3.4 Dielectric properties

The CS1210 and SPS1200 ceramics were selected to study the temperature dependence of dielectric properties. Fig. 6.3.5 shows the temperature dependence of dielectric properties of CS1210. Relaxation behavior has been observed at a temperature range of 200 °C to 600 °C. It is indicated that the oxygen ions have been thermodynamically activated and are able to hop from one vacant site to another. The oxygen-ion hopping could contribute to the permittivity as well as the loss value [195]. Same relaxation behavior was observed in SPS1200, further supported the existence of the oxygen vacancies in the ceramics.

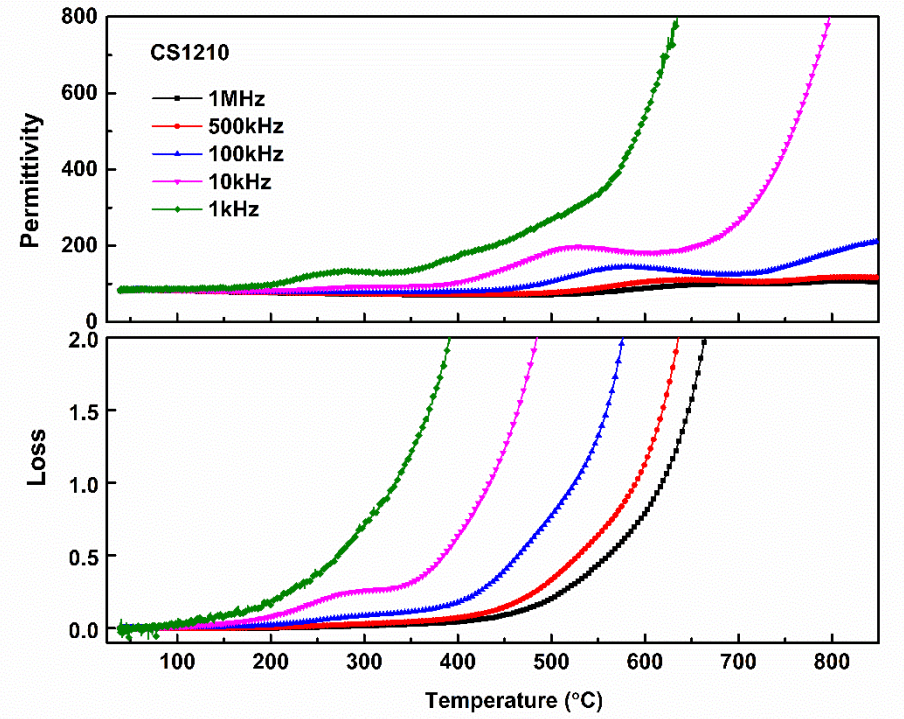


Fig. 6.3.5 Temperature dependence of dielectric properties in CS1210 ceramic.

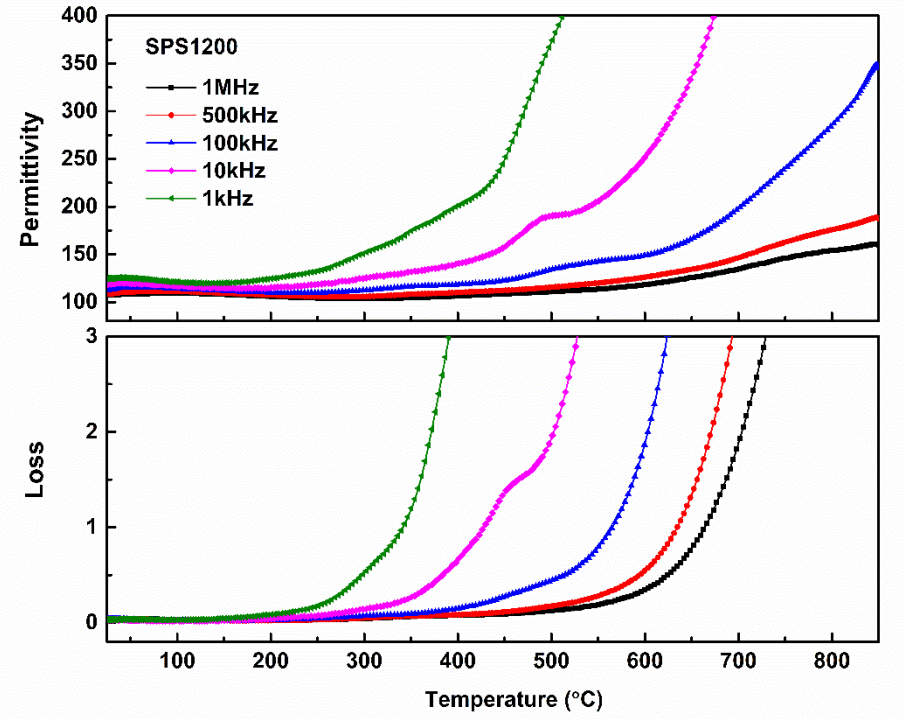


Fig. 6.3.6 Temperature dependence of dielectric properties in SPS1200 ceramic.

Fig. 6.3.7a shows the frequency dependence of dielectric response of the CS samples in THz band. The permittivity of CS1250 dropped compared to that of CS1210 and increased in CS1300 within the frequency band. Meanwhile, the loss tangent kept increasing with the increase of sintering temperature, especially for CS1300. The high permittivity is due to the large grain size (Fig. 6.3.2) and local vibration of oxygen-vacancy linked dipoles. The increase of grain size would relatively decrease the ratio of grain boundaries with low permittivity, which in turn would lead to increasing permittivity. Moreover, the local vibration of oxygen-vacancy linked dipoles would also contribute to the polarizability, and thus increase the measured permittivity [196]. The decrease of permittivity in CS1250 is suggested to be related to the diminishing of oxygen-vacancy linked dipoles, as discussed in Fig. 6.3.3b. Most of the oxygen vacancies would be eliminated by the formation of crystallographic shear planes, and as a result the contribution of permittivity from these defect-related dipoles would vanish. The higher amount of oxygen vacancies in CS1300 outweighed the formation of crystallography shear planes and thus the permittivity of CS1300 increased. The large dielectric loss in CS samples was mainly caused by the nonstoichiometry of the samples accommodated with oxygen vacancies and trapped porosity (Fig. 6.3.2).

For SPS samples, the dielectric permittivity increased with increasing sintering temperature (Fig. 6.3.7b). SPS1200 and SPS1250 exhibit extremely low loss (0.0053 and 0.0056, respectively), which are less than half of that in SPS1050 (0.0183) and CS1200 (0.012, and the lowest among the CS samples) at 0.22 THz. The increase of permittivity with the increase of sintering temperature in SPS samples is due to the densification of samples and the increase of grain size (Fig. 6.3.2). SPS1050 exhibited

trapped porosity and relative low density (Fig. 6.3.2c), leading to the high loss. Interest has been focused on the ultra-low loss found in SPS1200 and SPS1250. Trapped porosity, as a main mechanism for loss, were barely observed in SPS1200 and SPS1250 (Fig. 6.3.2), which resulted in low loss. Meanwhile, the increased crystal stability with less an harmonicity from defects in SPS1200 has been deduced from the Fig. 6.3.4d, which is also taken to account for the low-loss.

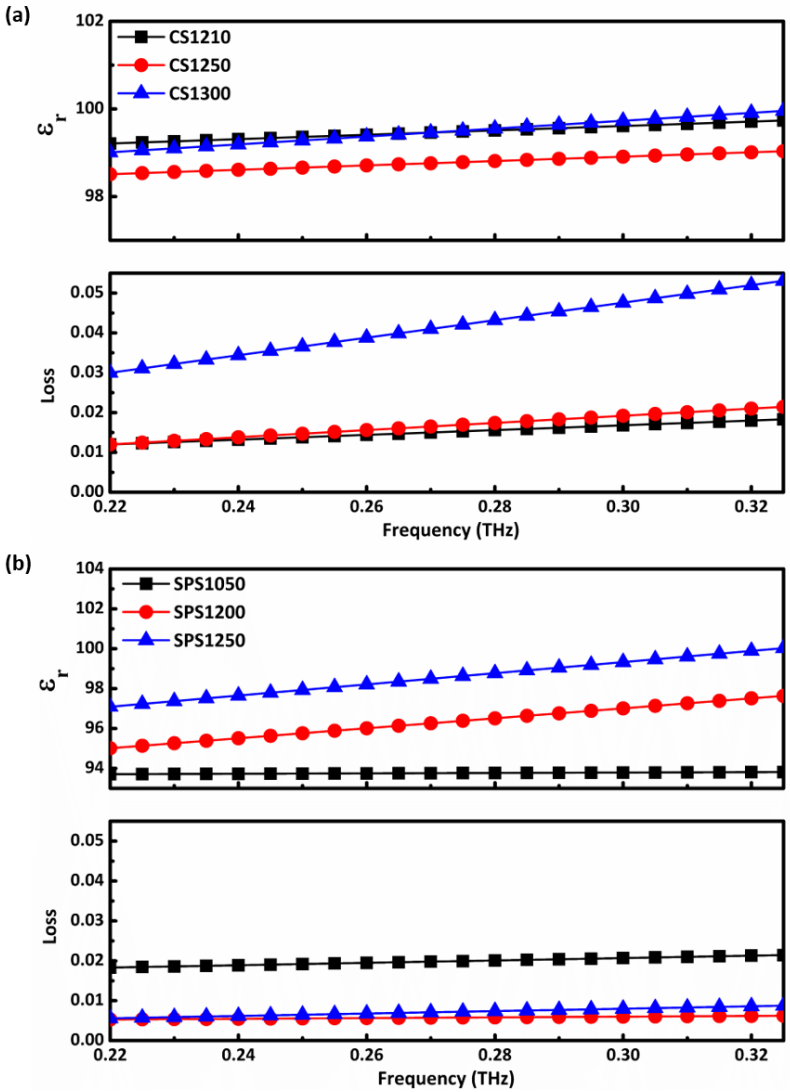


Fig. 6.3.7 Frequency dependence of dielectric properties in (a) the CS samples; (b) the SPS samples in THz domain (0.22-0.325 THz).

### 6.3.5 Electrical properties

Fig. 6.3.8 shows the current-electric field (I-E) and polarization-electric field (P-E) loops of selected samples CS1250 and SPS1250. Both samples exhibited high breakdown strength up to 30 kV $cm^{-1}$. The CS sample is quite lossy due to the high density of trapped porosity and point defects. The energy density of CS1250 ceramic is 0.08 J $cm^{-3}$. The P-E loop of the SPS1250 is relative linear. The obtained energy density in SPS1250 ceramic is 0.3 J $cm^{-3}$ (error bar ±0.01).

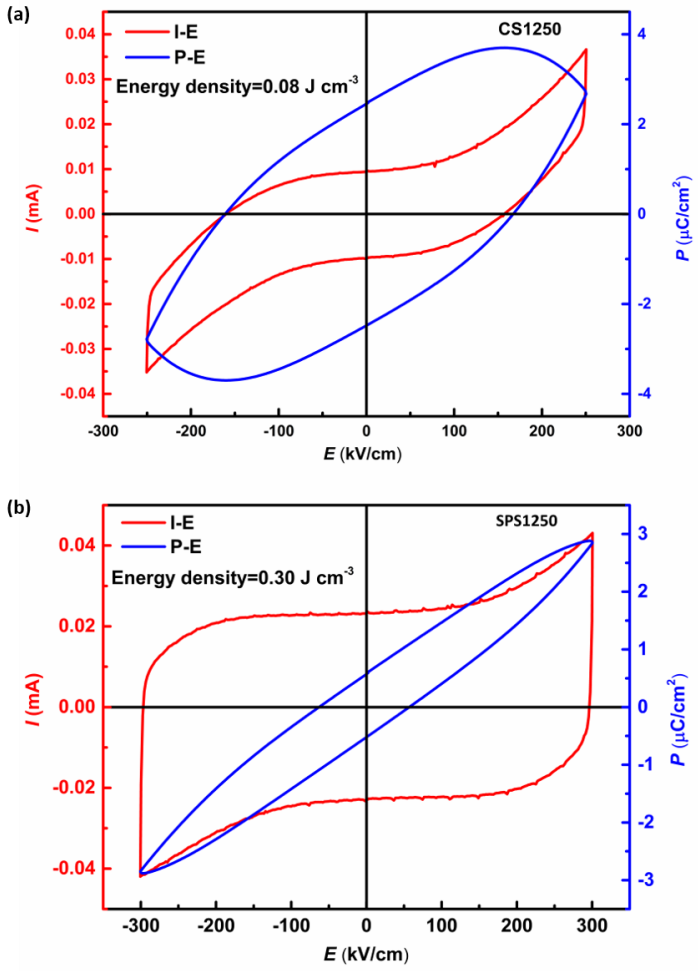


Fig. 6.3.8 Current-electric field (I-E) Polarization-electric field (P-E) hysteresis loop of (a) CS1250; (b) SPS1250.

## 6.4 Conclusions

In conclusion, we have studied the broad band dielectric properties of $TiO_2$. Abnormal grain growth and trapped porosities were observed in the conventional sintering samples. The SPS technique managed to control the grain size and the formation of the trapped porosity.

The oxygen vacancies contributed to the high permittivity with high dielectric loss in both the CS and SPS samples, in low frequency band. Crystallographic shear planes were found to degenerate the permittivity value. It is demonstrated that low density of trapped porosity, high ceramic density, and complete oxidation are the key factors to obtain improved dielectric properties.

The SPS samples achieved ultra-low loss in THz band, which is promising for THz communication application. The $TiO_2$ ceramics exhibited high breakdown strength with energy density as high as 0.3 J $cm^{-3}$.

# Chapter VII. Conclusions and Future work

## 7.1 Conclusions

In this research, systematic investigation has been carried out on antiferroelectric Sm-doped $BiFeO_3$, linear dielectric $BiNbO_4$ and incipient ferroelectric $TiO_2$.

### 7.1.1 The Antiferroelectric: Sm-doped $BiFeO_3$

The $Bi_{1-x}Sm_xFeO_3$ (x=0.15-0.18) powder has been successfully produced with no observed second phases. However, second phases $Bi_2Fe_4O_9$ and $Bi_{25}FeO_{39}$ were formed in the complement ceramics, during the annealing step. It is due to the close proximity of the impurity formation temperature and annealing temperature of $Bi_{1-x}Sm_xFeO_3$ resulted in the formation of impurities which are thermodynamically more stable. The Sm-doped $BiFeO_3$ structure has been identified as the coexistence of three phases, including ferroelectric *R*3*c* phase, antiferroelectric *Pbam* phase and paraelectric *Pnma* phase.

The phase distribution in $Bi_{1-x}Sm_xFeO_3$ powder is mainly affected by calcination and the Sm concentration. The fraction of the *Pbam* phase increased and the *R*3*c* phase decreased with the increase of calcination temperature. High calcination temperature above 910 °C is required to obtain the maximum weight fraction of the antiferroelectric *Pbam* phase. The weight fraction of the *Pnma* phase is mainly determined by the Sm concentration and is barely affected by the calcination temperature. The phase distribution in the ceramics differed from their parent powder, characterized by XRD. The weight fractions of the *R*3*c* phase increased and that of the

*Pbam* phase decreased in the ceramics comparing to those in the powder. This indicates that *R*3*c* phase has been stabilized with the application of pressure during the sintering process and at the low sintering temperature. Whereas, the fractions of the *R*3*c* phase and the *Pbam* phase decreased and the *Pnma* phase increased with the increase of the Sm concentration. The pure antiferroelectric *Pbam* phase could not be obtained in the current studied $Bi_{1-x}Sm_xFeO_3$ compositions (x=0.15, 0.16, 0.165 and 0.18).

The Curie temperature of the *Pbam* phase in BSF15 ceramic is assumed to be at 200 °C and that of the *R*3*c* phase is at 575 °C. The Curie temperature of both phases decreased with the increase of Sm concentration. The conductivity in the ceramics has been largely reduced. Ferroelectric hysteresis loop obtained in BSF15 is a results of domain switching in the ferroelectric *R*3*c* phase. Linear loops were obtained for BSF16, BSF16.5 and BSF18 due to the increased fraction of the *Pnma* phase and the suppression of the ferroelectric *R*3*c* phase. The antiferroelectric double hysteresis loops were not achieved due to the difficulty in obtaining the pure *Pbam* phase. Moreover, the forward field and backward field required for field induced antiferroelectric to ferroelectric phase transition are too high. An energy density of 0.64 J $cm^{-3}$ was obtained in BSF18 ceramic, which is the highest value that has ever been reported in the rare-earth-doped $BiFeO_3$ ceramics.

### 7.1.2 The Linear Dielectric: $BiNbO_4$

The longstanding issue on the phase relationship between the α- and the β- phase $BiNbO_4$ has been addressed. Moreover, a high temperature γ phase has been revealed,

the structure of which has been solved based on a $LaTaO_4$ monoclinic structure. The γ-$BiNbO_4$ has a monoclinic structure with a space group $P2_1/c$. The lattice parameters are: $a$= 7.795 Å, $b$=5.649 Å, $c$=7.904 Å, $\beta$ = 104.691(2)°. The structure of the γ-phase showed corrugated sheets of corner sharing octahedral separated by $Bi^{3+}$ cations.

The γ phase has been interpreted as a bridging phase between the α- and the β- phase. The α-phase would transform into the γ-phase at *ca.* 1040 °C on heating, which in turn transformed into β phase at *ca.* 1000 °C during cooling. A reversible first-order β to γ phase transition was observed at *ca.* 1000 °C for both powder and ceramic when no incubation processed on heating. On contrary, when β phase powder was annealed at a temperature range of 800 °C-1000 °C with certain incubation time, it could be transformed back to the α phase. Long incubation time would favor the β to α phase transition. However, the β to α phase transition could not be observed in the β-phase ceramics, even with long incubation time (up to 15 h). Whereas, the as-sintered β phase ceramics (those without the post annealing step at 1050 °C) could be transformed into α phase. It is deduced that the internal stress in the ceramics would suppress the volume expansion when the β phase transformed into the α phase, while the presence of the surface and diffused carbon would reduce the energy barrier and promote the transition processing.

The possibility of the α- and the β- phase of being antiferroelectric is still an open question. The energy density obtained in α- and β- phase ceramics was low (*ca*. 0.04 J $cm^{-3}$), due to the low dielectric breakdown field.

### 7.1.3 The Incipient Ferroelectric: $TiO_2$

The broad band dielectric properties of the rutile $TiO_2$ has been investigated. The microstructure, defect chemistry and Raman modes of the $TiO_2$ have been studied to better understand the dielectric properties. The $TiO_2$ exhibited ultra-low loss in Terahertz frequency band, which is good for high data rate communication application. The $TiO_2$ exhibited high dielectric breakdown strength while the energy density needed further improvement.

## 7.2 Future work

### 7.2.1 Structural investigation on Sm-doped $BiFeO_3$

The synthesis technique should be improved to produce monophasic *Pbam* phase in Sm-doped $BiFeO_3$. Techniques like Seebeck thermoelectric and impedance spectroscopy measurements could be used to further study the conductivity mechanism and electrical heterogeneous of the system. Differential scanning calorimetry could be carried out to study the phase transitions. The structural study using TEM and neutron diffraction are needed to further strengthen the present results. The breakdown strength should be improved and the forward field as well as the backward field should be decrease to get the double hysteresis loop and to study the electric nature.

### 7.2.2 Raman spectroscopy study on $BiNbO_4$

High temperature Raman spectroscopy should be carried out to study the structure of both α- and β- phase $BiNbO_4$ and relative phase transitions. Theoretical calculation on the optical phonon modes in α- and β- phase should be carried out to provide accurate vibration frequency for spectra fitting. The synthesis technique should be improved to get denser ceramics and to improve ceramic electric breakdown strength.

### 7.2.3 Element substitution in $TiO_2$

Dopant or solid solutions should be considered to increase the dielectric permittivity of $TiO_2$ but maintain the low dielectric loss. The synthesis procedures should be further investigated to improve the electric breakdown field and increase the energy density.

Systematic studied of the crystallographic planes and their effects on the dielectric properties should be carried out.

# List of Publications

1. J. Huang, B. Yang, **C. Yu**, G. Zhang, H. Xue, Z. Xiong, G. Viola, R. Donnan, H. Yan and M. Reece, Microwave and terahertz dielectric properties of $MgTiO_3$–$CaTiO_3$ ceramics, Mater*. Lett.*, 2015, 138, 225-227.

2. Y. Sun, Z. Li, H. Zhang, **C. Yu**, G. Viola, S. Fu, V. Koval and H. Yan, Lead free $Bi_3TaTiO_9$ ferroelectric ceramics with high Curie point, *Mater. Lett*., 2016, 175, 79-81.

3. **Chuying Yu**, Yang Zeng, Bin Yang, Jinbao Huang, Robert Donnan, Zhaoxian Xiong, Baogui Shi, Haitao Ye, Russell Binions, Mike J Reece and Haixue Yan, *Unique Terahertz Materials with High Permittivity and Ultra-Low Loss*, to be submitted.

4. **Chuying Yu**, Dou Zhang, Giuspeppe Viola, Salvatore Grasso, Rory Wilson, Kechao Zhou, Mike J Reece, Isaac Abrahams, Haixue Yan, *Phase transitions in $BiNbO_4$*, to be submitted.

5. **C. Yu**, G. Viola, D. Zhang, K. Zhou, R. Wilson, N.V. Tarakina, A. Mahajan, I. Abraham and H. Yan, *Phase evolution of Sm-doped $BiFeO_3$ across the morphotropic phase boundary*, to be submitted.

# Reference


1. Barsoum, M. and M. Barsoum, *Fundamentals of ceramics*. 2002: CRC press.
2. Damjanovic, D., *Ferroelectric, dielectric and piezoelectric properties of ferroelectric thin films and ceramics.* Reports on Progress in Physics, 1998. **61**(9): p. 1267.
3. O'Brien, M.C. and C. Chancey, *The Jahn–Teller effect: An introduction and current review.* American Journal of Physics, 1993. **61**(8): p. 688-697.
4. Golež, D., *Jahn-Teller effect.* 2011.
5. Chen, H., et al., *Progress in electrical energy storage system: A critical review.* Progress in Natural Science, 2009. **19**(3): p. 291-312.
6. Weinstock, I.B., *Recent advances in the US Department of Energy's energy storage technology research and development programs for hybrid electric and electric vehicles.* Journal of Power Sources, 2002. **110**(2): p. 471-474.
7. Ribeiro, P.F., et al., *Energy storage systems for advanced power applications.* Proceedings of the IEEE, 2001. **89**(12): p. 1744-1756.
8. Hao, X., *A review on the dielectric materials for high energy-storage application.* Journal of Advanced Dielectrics, 2013. **3**(01).
9. Jaffe, B., *Antiferroelectric ceramics with field-enforced transitions: a new nonlinear circuit element.* Proceedings of the IRE, 1961. **49**(8): p. 1264-1267.
10. Burn, I. and D. Smyth, *Energy storage in ceramic dielectrics.* Journal of materials science, 1972. **7**(3): p. 339-343.
11. Haertling, G.H., *Ferroelectric ceramics: history and technology.* J. Am. Ceram. Soc., 1999. **82**(4): p. 797-818.
12. Hackenberger, W., S. Kwon, and E. Alberta, *Advanced Multilayer Capacitors Using High Energy Density Antiferroelectric Ceramics.* CARTS USA, 2008: p. 192-204.
13. Ma, B., et al., *Fabrication and dielectric property of ferroelectric PLZT films grown on metal foils.* Materials Research Bulletin, 2011. **46**(7): p. 1124-1129.
14. Parui, J. and S. Krupanidhi, *Enhancement of charge and energy storage in sol-gel derived pure and La-modified $PbZrO_3$ thin films.* Applied Physics Letters, 2008. **92**(19): p. 192901_1-192901_3.
15. Hao, X., J. Zhai, and X. Yao, *Improved energy storage performance and fatigue endurance of Sr-doped $PbZrO_3$ antiferroelectric thin films.* Journal of the American Ceramic Society, 2009. **92**(5): p. 1133-1135.
16. Parliament, E. and E. Council, *Directive 2002/95/EC on the restriction of the use of certain hazardous substances in electrical and electronic equipment.* Official J Eur Union, 2003. **46**: p. 19-23.
17. Fujino, S., et al., *Combinatorial discovery of a lead-free morphotropic phase boundary in a thin-film piezoelectric perovskite.* Applied Physics Letters, 2008. **92**(20): p. 202904.
18. Arnold, D., *Composition-driven structural phase transitions in rare-earth-doped $BiFeO_3$ ceramics: a review.* Ultrasonics, Ferroelectrics, and Frequency Control, IEEE Transactions on, 2015. **62**(1): p. 62-82.

19. Kalantari, K., et al., *Ti-Doping to Reduce Conductivity in $Bi_{0.85}Nd_{0.15}FeO_3$ Ceramics.* Advanced Functional Materials, 2011. **21**(19): p. 3737-3743.
20. Keve, E. and A. Skapski, *The crystal structure of triclinic β-$BiNbO_4$.* Journal of Solid State Chemistry, 1973. **8**(2): p. 159-165.
21. Zhou, D., et al., *Phase transformation in $BiNbO_4$ ceramics.* Applied Physics Letters, 2007. **90**(17): p. 2910.
22. Popolitov, V., A. Lobachev, and V. Peskin, *Antiferroelectrics, ferroelectrics and pyroelectrics of a stibiotantalite structure.* Ferroelectrics, 1982. **40**(1): p. 9-16.
23. Karimi, S., et al., *Crystal chemistry and domain structure of rare-earth doped $BiFeO_3$ ceramics.* Journal of materials science, 2009. **44**(19): p. 5102-5112.
24. Wang, J., et al., *Epitaxial $BiFeO_3$ multiferroic thin film heterostructures.* Science, 2003. **299**(5613): p. 1719-1722.
25. Catalan, G. and J.F. Scott, *Physics and applications of bismuth ferrite.* Advanced Materials, 2009. **21**(24): p. 2463-2485.
26. Neaton, J., et al., *First-principles study of spontaneous polarization in multiferroic $BiFeO_3$.* Physical Review B, 2005. **71**(1): p. 014113.
27. Seshadri, R. and N.A. Hill, *Visualizing the role of Bi 6s "lone pairs" in the off-center distortion in ferromagnetic $BiMnO_3$.* Chemistry of materials, 2001. **13**(9): p. 2892-2899.
28. Palai, R., et al., *β phase and γ− β metal-insulator transition in multiferroic $BiFeO_3$.* Physical Review B, 2008. **77**(1): p. 014110.
29. Morozov, M., N. Lomanova, and V. Gusarov, *Specific features of $BiFeO_3$ formation in a mixture of bismuth (III) and iron (III) oxides.* Russian journal of general chemistry, 2003. **73**(11): p. 1676-1680.
30. Maitre, A., M. Francois, and J. Gachon, *Experimental study of the $Bi_2O_3$-$Fe_2O_3$ pseudo-binary system.* Journal of Phase Equilibria and Diffusion, 2004. **25**(1): p. 59-67.
31. Carvalho, T. and P. Tavares, *Synthesis and thermodynamic stability of multiferroic $BiFeO_3$.* Materials Letters, 2008. **62**(24): p. 3984-3986.
32. Lee, C.-C. and J.-M. Wu, *Studies on leakage mechanisms and electrical properties of doped $BiFeO_3$ films.* Electrochemical and solid-state letters, 2007. **10**(8): p. G58-G61.
33. Köferstein, R., T. Buttlar, and S.G. Ebbinghaus, *Investigations on $Bi_{25}FeO_{40}$ powders synthesized by hydrothermal and combustion-like processes.* Journal of Solid State Chemistry, 2014. **217**: p. 50-56.
34. Rojac, T., et al., *$BiFeO_3$ ceramics: Processing, electrical, and electromechanical properties.* Journal of the American Ceramic Society, 2014. **97**(7): p. 1993-2011.
35. Yu, B., et al., *Effects of ion doping at different sites on electrical properties of multiferroic $BiFeO_3$ ceramics.* Journal of Physics D: Applied Physics, 2008. **41**(6): p. 065003.
36. Zhang, Z., et al., *Density functional theory plus U study of vacancy formations in bismuth ferrite* 2010.
37. Achenbach, G., W. James, and R. Gerson, *Preparation of single‐phase polycrystalline $BiFeO_3$.* Journal of the American Ceramic Society, 1967. **50**(8): p. 437-437.
38. Silva, J., et al., *$BiFeO_3$: a review on synthesis, doping and crystal structure.* Integrated Ferroelectrics, 2011. **126**(1): p. 47-59.

39. Uchida, H., et al., *Fabrication of $M^{3+}$-substituted and $M^{3+}/V^{5+}$-cosubstituted bismuth titanate thin films [M= lanthanoid] by chemical solution deposition technique.* Japanese journal of applied physics, 2002. **41**(11S): p. 6820.
40. Uchida, H., et al., *Ion modification for improvement of insulating and ferroelectric properties of $BiFeO_3$ thin films fabricated by chemical solution deposition.* Japanese journal of applied physics, 2005. **44**(4L): p. L561.
41. Uchida, H., et al., *Crystal structure and ferroelectric properties of rare-earth substituted $BiFeO_3$ thin films.* Journal of applied physics, 2006. **100**(1): p. 4106.
42. Brinkman, K., T. Iijima, and H. Takamura, *Acceptor doped $BiFeO_3$ ceramics: A new material for oxygen permeation membranes.* Japanese Journal of Applied Physics, 2007. **46**(2L): p. L93.
43. Masó, N. and A.R. West, *Electrical properties of Ca-doped $BiFeO_3$ ceramics: from p-type semiconduction to oxide-ion conduction.* Chemistry of Materials, 2012. **24**(11): p. 2127-2132.
44. Singh, S., H. Ishiwara, and K. Maruyama, *Room temperature ferroelectric properties of Mn-substituted $BiFeO_3$ thin films deposited on Pt electrodes using chemical solution deposition.* Applied Physics Letters, 2006. **88**(26): p. 262908-262908.
45. Kittel, C., *Theory of antiferroelectric crystals.* Physical review, 1951. **82**(5): p. 729.
46. Rabe, K.M., *Antiferroelectricity in oxides: a reexamination*. 2012, Department of Physics and Astronomy, Rutgers University, Piscataway.
47. Lines, M.E. and A.M. Glass, *Principles and applications of ferroelectrics and related materials*. 1977: Oxford University Press.
48. Jona, F. and G. Shirane, *Ferroelectric crystals*. 1993: Dover Publications New York.
49. Shirane, G., E. Sawaguchi, and Y. Takagi, *Dielectric properties of lead zirconate.* Physical review, 1951. **84**(3): p. 476.
50. Shirane, G., K. Suzuki, and A. Takeda, *Phase transitions in solid solutions of $PbZrO_3$ and $PbTiO_3$ (II) X-ray study.* Journal of the Physical Society of Japan, 1952. **7**(1): p. 12-18.
51. Goldschmidt, V., *The laws of crystal chemistry.* Naturwissenschaften, 1926. **14**(21): p. 477-485.
52. Reaney, I.M., E.L. Colla, and N. Setter, *Dielectric and structural characteristics of Ba-and Sr-based complex perovskites as a function of tolerance factor.* Japanese Journal of Applied Physics, 1994. **33**(7R): p. 3984.
53. Jia, Y., *Crystal radii and effective ionic radii of the rare earth ions.* Journal of Solid State Chemistry, 1991. **95**(1): p. 184-187.
54. Jaffe B, C.J.W.J., and Jaffe H.L, *Piezoelectric ceramics*. Vol. 3. 1971: Academic Press.
55. Kuwata, J., K. Uchino, and S. Nomura, *Dielectric and piezoelectric properties of $0.91Pb(Zn_{1/3}Nb_{2/3})O_3$-$0.09PbTiO_3$ single crystals.* Japanese Journal of Applied Physics, 1982. **21**(9R): p. 1298.
56. Guo, R., et al., *Origin of the high piezoelectric response in $PbZr_{1-x}Ti_xO_3$.* Physical Review Letters, 2000. **84**(23): p. 5423.
57. Ye, Z.-G., *Crystal chemistry and domain structure of relaxor piezocrystals.* Current Opinion in Solid State and Materials Science, 2002. **6**(1): p. 35-44.

58. Kan, D., et al., *Universal Behavior and Electric‐Field‐Induced Structural Transition in Rare‐Earth‐Substituted $BiFeO_3$.* Advanced Functional Materials, 2010. **20**(7): p. 1108-1115.
59. Troyanchuk, I.O., et al., *Phase Transitions, Magnetic and Piezoelectric Properties of Rare‐Earth‐Substituted $BiFeO_3$ Ceramics.* Journal of the American Ceramic Society, 2011. **94**(12): p. 4502-4506.
60. Rusakov, D.A., et al., *Structural Evolution of the $BiFeO_3$–$LaFeO_3$ System.* Chemistry of materials, 2010. **23**(2): p. 285-292.
61. Cheng, Z., et al., *Structure, ferroelectric properties, and magnetic properties of the La-doped bismuth ferrite.* 2008.
62. Gabbasova, Z., et al., *$Bi_{1-x}R_xFeO_3$ (R= rare earth): a family of novel magnetoelectrics.* Physics Letters A, 1991. **158**(9): p. 491-498.
63. Troyanchuk, I., et al., *Structural transformations and magnetic properties of $Bi_{1-x}Ln_xFeO_3$ (Ln= La, Nd, Eu) multiferroics.* physica status solidi (b), 2009. **246**(8): p. 1901-1907.
64. Cheng, C.-J., et al., *Structural transitions and complex domain structures across a ferroelectric-to-antiferroelectric phase boundary in epitaxial Sm-doped $BiFeO_3$ thin films.* Physical Review B, 2009. **80**(1): p. 014109.
65. Sawaguchi, E., H. Maniwa, and S. Hoshino, *Antiferroelectric structure of lead zirconate.* Physical review, 1951. **83**(5): p. 1078.
66. Khomchenko, V., et al., *Structural, ferroelectric and magnetic properties of $Bi_{0.85}Sm_{0.15}FeO_3$ perovskite.* Crystal Research and Technology, 2011. **46**(3): p. 238-242.
67. Viehland, D., et al., *Incommensurately Modulated Polar Structures in Antiferroelectric Sn-Modified Lead Zirconate Titanate: The Modulated Structure and Its Influences on Electrically Induced Polarizations and Strains.* Journal of the American Ceramic Society, 1995. **78**(8): p. 2101-2112.
68. He, H. and X. Tan, *Electric-field-induced transformation of incommensurate modulations in antiferroelectric $Pb_{0.99}Nb_{0.02}[(Zr_{1-x}Sn_x)_{1-y}Ti_y]_{0.98}O_3$.* Physical Review B, 2005. **72**(2): p. 024102.
69. Schönau, K.A., et al., *Nanodomain structure of $Pb[Zr_{1-x}Ti_x]O_3$ at its morphotropic phase boundary: Investigations from local to average structure.* Physical Review B, 2007. **75**(18): p. 184117.
70. Kan, D., V. Anbusathaiah, and I. Takeuchi, *Chemical Substitution‐Induced Ferroelectric Polarization Rotation in $BiFeO_3$.* Advanced Materials, 2011. **23**(15): p. 1765-1769.
71. Yuan, G., et al., *Structural transformation and ferroelectromagnetic behavior in single-phase $Bi_{1-x}Nd_xFeO_3$multiferroic ceramics.* Applied Physics Letters, 2006. **89**(5): p. 1-3.
72. Karimi, S., et al., *Nd-doped BiFeO ceramics with antipolar order.* Applied Physics Letters, 2009. **94**(11).
73. Kan, D., et al., *Composition and temperature-induced structural evolution in La, Sm, and Dy substituted $BiFeO_3$ epitaxial thin films at morphotropic phase boundaries.* Journal of Applied Physics, 2011. **110**(1): p. 014106.
74. Walker, J., et al., *Temperature dependent piezoelectric response and strain–electric-field hysteresis of rare-earth modified bismuth ferrite ceramics.* Journal of Materials Chemistry C, 2016.

75. Roth, R. and J. Waring, *Phase equilibrium relations in binary system bismuth sesquioxide-niobium pentoxide.* Journal of Research of the National Bureau of Standards Section A-Physics and Chemistry, 1962. **66**(6): p. 451-+.
76. Aurivillius, B., *X-ray investigations on $BiNbO_4$, $BiTaO_4$ and $BiSbO_4$.* Arkiv for Kemi, 1951. **3**(2-3): p. 153-161.
77. Subramanian, M. and J. Calabrese, *Crystal structure of the low temperature form of bismuth niobium oxide [α-$BiNbO_4$].* Materials research bulletin, 1993. **28**(6): p. 523-529.
78. Ayyub, P., et al., *Vibrational spectroscopic study of ferroelectric $SbNbO_4$, antiferroelectric $BiNbO_4$, and their solid solutions.* Physical Review B, 1986. **34**(11): p. 8137.
79. Yu, Y., et al., *The crystal growth of $BiNbO_4$.* Ferroelectrics, 1990. **107**(1): p. 225-228.
80. Sathyanarayana, D.N., *Vibrational spectroscopy: theory and applications*. 2015: New Age International.
81. Popolitov, V., et al., *Ferroelectrics $ABO_4$: Synthesis of single crystals and ceramics; dielectric and nonlinear optical properties.* Ferroelectrics, 1974. **8**(1): p. 519-520.
82. Popolitov, V., et al., *Synthesis and Study of Single Crystals and Ceramics of the Bismuth Niobate ($BiNbO_4$) and Bismuth Tantalate ($BiTaO_4$) Compositions.* Kristallografiya, 1975. **20**(4): p. 783-787.
83. Venevtsev, Y.N., et al., *Ferro-and antiferroelectrics with the stibiotantalite type structure.* Ferroelectrics, 1978. **21**(1): p. 417-419.
84. Ayyub, P., et al., *Ferroelectric behavior in thin films of antiferroelectric materials.* Physical Review B, 1998. **57**(10): p. R5559.
85. Chattopadhyay, S., et al., *Synthesis of thin films of polycrystalline ferroelectric $BiNbO_4$ on Si by pulsed laser ablation.* Journal of materials research, 1998. **13**(05): p. 1113-1116.
86. Ayyub, P., *Finite Size Effects in Ferroelectric Nanomaterials and Thin Films.* Proceedings-Indian national secience academy part A 2001. **67**(1): p. 71-84.
87. Keve, E. and A. Skapski, *The structure of triclinic $BiNbO_4$ and $BiTaO_4$.* Chemical Communications (London), 1967(6): p. 281-283.
88. Keve, E., S. Abrahams, and J. Bernstein, *Crystal Structure of Pyroelectric Paramagnetic Barium Manganese Fluoride, BaMnF.* The Journal of Chemical Physics, 1969. **51**: p. 4928.
89. Keve, E., S. Abrahams, and J. Bernstein, *Crystal structure of pyroelectric paramagnetic barium manganese fluoride, $BaMnF_4$.* The Journal of Chemical Physics, 1969. **51**(11): p. 4928-4936.
90. Roth, R. and J. Waring, *Phase equilibrium relations in the binary system bismuth sesquioxide–niobium pentoxide.* J. Res. Natl. Bur. Stand., Sect. A, 1962. **66**: p. 451-63.
91. Zhai, H.-F., et al., *Abnormal phase transition in $BiNbO_4$ powders prepared by a citrate method.* Journal of Alloys and Compounds, 2011. **509**(42): p. 10230-10233.
92. Xu, C., et al., *High pressure and high temperature study the phase transitions of $BiNbO_4$.* Solid State Communications, 2013. **156**: p. 21-24.

93. Zhou, D., et al., *Dielectric properties and phase transitions of $BiNbO_4$ ceramic.* Scripta Materialia, 2014. **81**: p. 40-43.
94. Sleight, A. and G. Jones, *Ferroelastic transitions in-$BiNbO_4$ and-$BiTaO_4$.* Acta Crystallographica Section B: Structural Crystallography and Crystal Chemistry, 1975. **31**(11): p. 2748-2749.
95. Templeton, A., et al., *Microwave dielectric loss of titanium oxide.* Journal of the American Ceramic Society, 2000. **83**(1): p. 95-100.
96. Sugiyama, K. and Y. Takeuchi, *The crystal structure of rutile as a function of temperature up to 1600C.* Zeitschrift für Kristallographie-Crystalline Materials, 1991. **194**(1-4): p. 305-314.
97. Betsch, R.J., H.L. Park, and W.B. White, *Raman spectra of stoichiometric and defect rutile.* Materials research bulletin, 1991. **26**(7): p. 613-622.
98. Frank, O., et al., *Raman spectra of titanium dioxide (anatase, rutile) with identified oxygen isotopes (16, 17, 18).* Physical Chemistry Chemical Physics, 2012. **14**(42): p. 14567-14572.
99. Matsumoto, N., et al., *Analysis of dielectric response of $TiO_2$ in terahertz frequency region by general harmonic oscillator model.* Japanese journal of applied physics, 2008. **47**(9S): p. 7725.
100. Von Hippel, A., J. Kalnajs, and W. Westphal, *Protons, dipoles, and charge carriers in rutile in rutile.* Journal of Physics and Chemistry of Solids, 1962. **23**(6): p. 779-799.
101. Hurlen, T., *On the defect structure of rutile.* Acta chem. scand, 1959. **13**(2).
102. Nowotny, J., et al., *Defect chemistry and electrical properties of titanium dioxide. 1. Defect diagrams.* The Journal of Physical Chemistry C, 2008. **112**(2): p. 590-601.
103. Iguchi, E. and K. Yajima, *Diffusion of oxygen vacancies in reduced rutile ($TiO_2$).* Journal of the Physical Society of Japan, 1972. **32**(5): p. 1415-1421.
104. Akse, J. and H. Whitehurst, *Diffusion of titanium in slightly reduced rutile.* Journal of Physics and Chemistry of Solids, 1978. **39**(5): p. 457-465.
105. Li, X., et al., *Energetics of charged point defects in rutile $TiO_2$ by density functional theory.* Acta Materialia, 2009. **57**(19): p. 5882-5891.
106. Bak, T., J. Nowotny, and M. Nowotny, *Defect disorder of titanium dioxide.* The Journal of Physical Chemistry B, 2006. **110**(43): p. 21560-21567.
107. Kofstad, P., *Thermogravimetric studies of the defect structure of rutile ($TiO_2$).* Journal of Physics and Chemistry of Solids, 1962. **23**(11): p. 1579-1586.
108. Yahia, J., *Dependence of the electrical conductivity and thermoelectric power of pure and aluminum-doped rutile on equilibrium oxygen pressure and temperature.* Physical Review, 1963. **130**(5): p. 1711.
109. Haul, R. and G. Dümbgen, *Sauerstoff-selbstdiffusion in rutilkristallen.* Journal of Physics and Chemistry of Solids, 1965. **26**(1): p. 1-10.
110. Blumenthal, R., et al., *Electrical conductivity of nonstoichiometric rutile single crystals from 1000 to 1500C.* Journal of Physics and Chemistry of Solids, 1966. **27**(4): p. 643-654.
111. Chester, P., *Electron spin resonance in semiconducting rutile.* Journal of Applied Physics, 1961. **32**(10): p. 2233-2236.

112. Kingsbury Jr, P.I., W. Ohlsen, and O. Johnson, *Defects in rutile. I. Electron paramagnetic resonance of interstitially doped n-type rutile.* Physical Review, 1968. **175**(3): p. 1091.
113. Hasiguti, R.R., *The structure of defects in solids.* Annual Review of Materials Science, 1972. **2**(1): p. 69-92.
114. Yagi, E., et al., *Investigation of Ti Interstitials in Slightly Reduced Rutile ($TiO_2$) by Means of Channeling Method.* Journal of the Physical Society of Japan, 1977. **42**(3): p. 939-946.
115. Anderson, J., et al., *Surface and Defect Properties of Solids.* Vol. 1 The Chemical Society, London, 1972: p. 1.
116. Magnéli, A., *Non-stoichiometry and structural disorder in some families of inorganic compounds.* Pure and Applied Chemistry, 1978. **50**(11-12): p. 1261-1271.
117. Grant, F., *Properties of rutile (titanium dioxide).* Reviews of Modern Physics, 1959. **31**(3): p. 646.
118. Frank, F., *On high dielectric constants.* Transactions of the Faraday Society, 1937. **33**: p. 513-523.
119. Büchner, A., *Die Dielektrizitätskonstante schwach polarer Kristalle und ihre Temperaturabhängigkeit*. 1935: Akademische Verlag-Ges.
120. Born, M. and M. Goppert-Mayer, *Dynamic lattice theory in crystals.* Handb. Phys, 1933. **24**: p. 623.
121. Berberich, L. and M. Bell, *The dielectric properties of the rutile form of $TiO_2$.* Journal of Applied Physics, 1940. **11**(10): p. 681-692.
122. Lemanov, V., et al., *Perovskite $CaTiO_3$ as an incipient ferroelectric.* Solid State Communications, 1999. **110**(11): p. 611-614.
123. Müller, K.A. and H. Burkard, *$SrTiO_3$: An intrinsic quantum paraelectric below 4 K.* Physical Review B, 1979. **19**(7): p. 3593.
124. Psi-k-ed, *Frequency and dielectric susceptibility as a function of temperature for a quantum paraelectric material*. 2012.
125. Itoh, M. and R. Wang, *Quantum ferroelectricity in $SrTiO_3$ induced by oxygen isotope exchange.* Applied Physics Letters, 2000. **76**.
126. Singh, D.J., *Stability and phonons of $KTaO_3$.* Physical Review B, 1996. **53**(1): p. 176.
127. Grünebohm, A., P. Entel, and C. Ederer, *First-principles investigation of incipient ferroelectric trends of rutile $TiO_2$ in bulk and at the (110) surface.* Physical Review B, 2013. **87**(5): p. 054110.
128. Ye, Y., et al. *Influence of nanocrystalline grain size on the breakdown strength of ceramic dielectrics*. in *Pulsed Power Conference, 2003. Digest of Technical Papers. PPC-2003. 14th IEEE International*. 2003. IEEE.
129. Wang, X., et al., *Glass additive in barium titanate ceramics and its influence on electrical breakdown strength in relation with energy storage properties.* Journal of the European Ceramic Society, 2012. **32**(3): p. 559-567.
130. Tunkasiri, T. and G. Rujijanagul, *Dielectric strength of fine grained barium titanate ceramics.* Journal of materials science letters, 1996. **15**(20): p. 1767-1769.

131. Liebault, J., et al., *How the trapping of charges can explain the dielectric breakdown performance of alumina ceramics.* Journal of the European Ceramic Society, 2001. **21**(3): p. 389-397.
132. Chao, S. and F. Dogan, *Processing and Dielectric Properties of TiO2 Thick Films for High‐Energy Density Capacitor Applications.* International Journal of Applied Ceramic Technology, 2011. **8**(6): p. 1363-1373.
133. Prakasam, M., et al., *Fabrication, properties and applications of dense hydroxyapatite: a review.* Journal of functional biomaterials, 2015. **6**(4): p. 1099-1140.
134. Rahaman, M.N., *Ceramic processing*. 2006: Wiley Online Library.
135. Grasso, S., Y. Sakka, and G. Maizza, *Electric current activated/assisted sintering (ECAS): a review of patents 1906–2008.* Science and Technology of Advanced Materials, 2016.
136. Hulbert, D.M., et al., *The absence of plasma in "spark plasma sintering".* Journal of Applied Physics, 2008. **104**(3): p. 033305.
137. Munir, Z., U. Anselmi-Tamburini, and M. Ohyanagi, *The effect of electric field and pressure on the synthesis and consolidation of materials: a review of the spark plasma sintering method.* Journal of materials science, 2006. **41**(3): p. 763-777.
138. Malmstrom, C., R. Keen, and L. Green Jr, *Some mechanical properties of graphite at elevated temperatures.* Journal of Applied Physics, 1951. **22**(5): p. 593-600.
139. Hughes, S.W., *Archimedes revisited: a faster, better, cheaper method of accurately measuring the volume of small objects.* Physics Education, 2005. **40**(5): p. 468.
140. Roman, P. and J.M. Gutierrez-Zorrilla, *A quick method for determining the density of single crystals.* J. Chem. Educ, 1985. **62**(2): p. 167.
141. Blake, A.J. and W. Clegg, *Crystal structure analysis: principles and practice*. Vol. 13. 2009: Oxford University Press.
142. Bragg, W.H. and W.L. Bragg, *The reflection of X-rays by crystals.* Proceedings of the Royal Society of London. Series A, Containing Papers of a Mathematical and Physical Character, 1913. **88**(605): p. 428-438.
143. Piccoli, P.M., T.F. Koetzle, and A.J. Schultz, *Single crystal neutron diffraction for the inorganic chemist–a practical guide.* Comments on Inorganic Chemistry, 2007. **28**(1-2): p. 3-38.
144. Rietveld, H., *Line profiles of neutron powder-diffraction peaks for structure refinement.* Acta Crystallographica, 1967. **22**(1): p. 151-152.
145. Pecharsky, V.K. and P.Y. Zavalij, *Fundamentals of powder diffraction and structural characterization of materials*. Vol. 69. 2009: Springer.
146. Goldstein, J., et al., *Scanning electron microscopy and X-ray microanalysis*. 2003: Springer.
147. Heinrich, K., *Electron probe microanalysis by specimen current measurement.* X-ray Optics and Microanalysis, 1966: p. 159-167.
148. Williams, D.B. and C.B. Carter, *The transmission electron microscope*, in *Transmission electron microscopy*. 1996, Springer. p. 3-17.

149. Efremov, E.V., F. Ariese, and C. Gooijer, *Achievements in resonance Raman spectroscopy: Review of a technique with a distinct analytical chemistry potential.* Analytica chimica acta, 2008. **606**(2): p. 119-134.
150. Colthup, N., *Introduction to infrared and Raman spectroscopy*. 2012: Elsevier.
151. Hollander, J.M. and W.L. Jolly, *X-ray photoelectron spectroscopy.* Accounts of chemical research, 1970. **3**(6): p. 193-200.
152. Gill, P., T.T. Moghadam, and B. Ranjbar, *Differential scanning calorimetry techniques: applications in biology and nanoscience.* Journal of biomolecular techniques: JBT, 2010. **21**(4): p. 167.
153. Gabbott, P., *Principles and applications of thermal analysis*. 2008: John Wiley & Sons.
154. Elmer, P., *Introduction to dynamic mechanical analysis (DMA): a beginner's guide.* 2008.
155. Yan, H., et al., *The contribution of electrical conductivity, dielectric permittivity and domain switching in ferroelectric hysteresis loops.* Journal of Advanced Dielectrics, 2011. **1**(01): p. 107-118.
156. Sun, W., et al., *Phase transition and piezoelectricity of sol-gel-processed Sm-doped $BiFeO_3$ thin films on Pt(111)/Ti/$SiO_2$/Si substrates.* Journal of Materials Chemistry C, 2015. **3**(9): p. 2115-2122.
157. Khomchenko, V., et al., *Effect of Sm substitution on ferroelectric and magnetic properties of $BiFeO_3$.* Scripta Materialia, 2010. **62**(5): p. 238-241.
158. Cheng, C.-J., et al., *Nanoscale structural and chemical properties of antipolar clusters in Sm-doped BiFeO3 ferroelectric epitaxial thin films.* Chemistry of materials, 2010. **22**(8): p. 2588-2596.
159. Larson, A. and R. Von Dreele, *GSAS General Structure Analysis System, Report LAUR 86-748.* Los Alamos National Laboratory, Los Alamos, NM, 1986.
160. Larson, A.C. and R.B. Von Dreele, *Gsas.* General Structure Analysis System. LANSCE, MS-H805, Los Alamos, New Mexico, 1994.
161. Walker, J., et al., *Temperature dependent piezoelectric response and strain–electric-field hysteresis of rare-earth modified bismuth ferrite ceramics.* Journal of Materials Chemistry C, 2016. **4**(33): p. 7859-7868.
162. Tanaka, M., R. Saito, and K. Tsuzuki, *Electron microscopic studies on domain structure of $PbZrO_3$.* Japanese journal of applied physics, 1982. **21**(2R): p. 291.
163. Kumar, M.M., et al., *Ferroelectricity in a pure BiFeO3 ceramic.* Applied Physics Letters, 2000. **76**(19): p. 2764-2766.
164. Yao, Y., et al., *Large piezoelectricity and dielectric permittivity in BaTiO3-xBaSnO3 system: The role of phase coexisting.* EPL (Europhysics Letters), 2012. **98**(2): p. 27008.
165. Berenov, A., F. Le Goupil, and N. Alford, *Effect of ionic radii on the Curie temperature in Ba1-x-ySrxCayTiO3 compounds.* Scientific Reports, 2016. **6**.
166. Shlyakhtin, O.A. and Y.J. Oh, *A Chemical Route to $BiNbO_4$ Ceramics.* International Journal of Applied Ceramic Technology, 2009. **6**(2): p. 312-323.
167. Hao, X., et al., *A comprehensive review on the progress of lead zirconate-based antiferroelectric materials.* Progress in Materials Science, 2014. **63**: p. 1-57.
168. Kurova, T. and V. Aleksandrov. *Crystal Structure of $LaTaO_4$*. in *Soviet Physics Doklady*. 1971.

169. Skapski, A. and D. Rogers, *The structure of $SbNbO_4$, α-$Sb2O_4$, and $SbTaO_4$.* Chemical Communications (London), 1965(23): p. 611-613.
170. Zhou, D., et al., *Phase transformation in $BiNbO_4$ ceramics.* Applied Physics Letters, 2007. **90**(17): p. 172910-172910-3.
171. Popolitov, V., et al., *Synthesis and Study of Single Crystals and Ceramics of the Bismuth Niobate (BiNbO 4) and Bismuth Tantalate (BiTaO 4) Compositions.* Kristallografiya, 1975. **20**(4): p. 783-787.
172. Ang, C., Z. Yu, and L. Cross, *Oxygen-vacancy-related low-frequency dielectric relaxation and electrical conduction in B i: S r T i O 3.* Physical Review B, 2000. **62**(1): p. 228.
173. Tan, X., et al., *The Antiferroelectric↔ Ferroelectric Phase Transition in Lead-Containing and Lead-Free Perovskite Ceramics.* Journal of the American Ceramic Society, 2011.
174. Frederikse, H., *Recent studies on rutile (TiO2).* Journal of Applied Physics, 1961. **32**(10): p. 2211-2215.
175. Soni, S.S., et al., *Visible‐Light Photocatalysis in Titania‐Based Mesoporous Thin Films.* Advanced Materials, 2008. **20**(8): p. 1493-1498.
176. Hashimoto, K., H. Irie, and A. Fujishima, *$TiO_2$ photocatalysis: a historical overview and future prospects.* Japanese journal of applied physics, 2005. **44**(12R): p. 8269.
177. Tiwana, P., et al., *Ultrafast terahertz conductivity dynamics in mesoporous $TiO_2$: influence of dye sensitization and surface treatment in solid-state dye-sensitized solar cells.* The Journal of Physical Chemistry C, 2009. **114**(2): p. 1365-1371.
178. O'regan, B. and M. Grätzel, *A low-cost, high-efficiency solar cell based on dye-sensitized colloidal $TiO_2$ films.* Nature, 1991. **353**(6346): p. 737-740.
179. Xia, T., et al., *Hydrogenated $TiO_2$ nanocrystals: a novel microwave absorbing material.* Advanced Materials, 2013. **25**(47): p. 6905-6910.
180. Janotti, A., et al., *Hybrid functional studies of the oxygen vacancy in $TiO_2$.* Physical Review B, 2010. **81**(8): p. 085212.
181. Hendry, E., et al., *Electron transport in $TiO_2$ probed by THz time-domain spectroscopy.* Physical Review B, 2004. **69**(8): p. 081101 (R)-081101 (R).
182. Wang, Y., et al., *Micromachined thick mesh filters for millimeter-wave and terahertz applications.* IEEE Transactions on Terahertz Science and Technology, 2014. **4**(2): p. 247-253.
183. Wijaranakula, W., *Effect of point defect reactions on behavior of boron and oxygen in degenerately doped Czochralski silicon.* Applied physics letters, 1993. **62**(23): p. 2974-2976.
184. Yin, Q., B. Zhu, and H. Zeng, *Microstructure, Property and Processing of Functional Ceramics*. 2010: Springer Science & Business Media, USA.
185. Hesse, R., P. Streubel, and R. Szargan, *Product or sum: comparative tests of Voigt, and product or sum of Gaussian and Lorentzian functions in the fitting of synthetic Voigt‐based X‐ray photoelectron spectra.* Surface and Interface Analysis, 2007. **39**(5): p. 381-391.
186. Chen, M., et al., *X-ray photoelectron spectroscopy and auger electron spectroscopy studies of Al-doped ZnO films.* Applied Surface Science, 2000. **158**(1): p. 134-140.

187. Santara, B., et al., *Evidence for Ti interstitial induced extended visible absorption and near infrared photoluminescence from undoped $TiO_2$ nanoribbons: an in situ photoluminescence study.* The Journal of Physical Chemistry C, 2013. **117**(44): p. 23402-23411.
188. Reece, M. and R. Morrell, *Electron microscope study of non-stoichiometric titania.* Journal of materials science, 1991. **26**(20): p. 5566-5574.
189. Pullar, R.C., et al., *Dielectric loss caused by oxygen vacancies in titania ceramics.* Journal of the European ceramic society, 2009. **29**(3): p. 419-424.
190. Bursill, L. and B. Hyde, *Crystallographic shear in the higher titanium oxides: structure, texture, mechanisms and thermodynamics.* Progress in solid state chemistry, 1972. **7**: p. 177-253.
191. Sørensen, O.T., *Nonstoichiometric oxides*. 2012: Elsevier.
192. Parker, J. and R. Siegel, *Raman microprobe study of nanophase $TiO_2$ and oxidation-induced spectral changes.* Journal of Materials Research, 1990. **5**(06): p. 1246-1252.
193. Lubchenko, A. and N.K. Nyap, *Anharmonic effects in the dispersion of the permittivity tensor of solid solutions.* Theoretical and Mathematical Physics, 1974. **19**(3): p. 593-599.
194. Lan, T., X. Tang, and B. Fultz, *Phonon anharmonicity of rutile $TiO_2$ studied by Raman spectrometry and molecular dynamics simulations.* Physical Review B, 2012. **85**(9): p. 094305.
195. Shulman, H.S., D. Damjanovic, and N. Setter, *Niobium doping and dielectric anomalies in bismuth titanate.* Journal of the American Ceramic Society, 2000. **83**(3): p. 528-532.
196. Hu, W., et al., *Electron-pinned defect-dipoles for high-performance colossal permittivity materials.* Nature materials, 2013. **12**(9): p. 821-826.